Dipl.Ing. Philipp Lehner, BSc

Ultra Trace Oxygen Sensors

DISSERTATION

zur Erlangung des akademischen Grades

Doktor/in der technischen Wissenschaften/Naturwissenschaften

eingereicht an der

Technischen Universität Graz

Betreuer/in:
Univ.-Prof. Dipl.-Chem. Dr.rer.nat. Ingo Klimant
Institut für analytische Chemie und Lebensmittelchemie

Graz, March, 2015

Abstract

This work details the development of trace and ultra trace oxygen sensors and some of the artifacts encountered when using such sensors. Most oxygen sensors are designed to resolve oxygen in the range of 20 % to 1 % oxygen. For some applications in marine biology much lower detection limits are required, as a result trace sensors (measuring oxygen in the nM region) and ultra trace sensors (measuring in the pM region) had to be developed. The Lumos, a miniaturized phase fluorimeter is presented, that can read-out special sensing chemistry to quantify oxygen in the range of 10.000 to 0.5 nM. For measurements below 1 nM, a novel ultra trace sensing material is presented that –because of its exceptionally long phosphorescence decay times – features a detection limit of 5 pM, which corresponds to a 20-fold increase in sensitivity compared to other state-of-the-art sensor materials. Such high sensitivities are accompanied by some problems though, as the unique conditions present in ultra trace measurements result in the manifestation of non-linearities that result in a dependence of the read-out parameter on excitation light intensity. These non-linearities are also thoroughly tested and described in this work.

Kurzfassung

In dieser Arbeit ist die Entwicklung von Spuren- und Ultra Spurensensoren beschrieben, sowie einige Messartefakte die bei Messungen mit Ultra Spuren Sensoren auftreten können. Die meisten Sauerstoff Sensoren sind entwickelt um Sauerstoff in dem Bereich von Luftsättigung bis etwa 1 % zu detektieren. Für einige Anwendungen, for allem in marinebiologischen Anwendungsgebieten werden jedoch wesentlich sensitivere Sensoren benötigt. Deswegen mussten Sensoren entwickelt werden die Sauerstoff im Spurenbereich (nM Bereich) oder sogar im Ultra Spurenbereich (pM Bereich) messen können. Der Lumos, ein miniaturisiertes Phasenfluorimeter, wird in dieser Arbeit vorgestellt. Dank spezieller kompatibler Sensormaterialien kann er Sauerstoff in einem Bereich von 10.000 bis 0.5 nM messen. Für Messungen unter 1 nM wird ein neuartiges Sensormaterial vorgestellt, dass dank seiner außerordentlich langen Phosphorezenzlebenzeit über eine Nachweisgrenze von bis zu 5 pM verfügt. Dies entspricht einer zwanzigfachen Steigerung der Sensitivität verglichen mit anderen derzeitig verfügbaren Sensormaterialien. Solch hohe Sensitivitäten gehen jedoch einher mit einigen neuen Problemen. Die einzigartigen Bedingungen denen das Sensormaterial bei solchen Ultra Spurenmessungen ausgesetzt ist führen zu Nichtlinearitäten die sich in einer Abhängigkeit der Sensorantwort von der Anregungslichtintensität bemerkbar machen. Diese Nichtlinearitäten werden in dieser Arbeit ebenfalls ausführlich untersucht und erklärt.

EIDESSTATTLICHE ERKLÄRUNG

Ich erkläre an Eides statt, dass ich die vorliegende Arbeit selbstständig verfasst, andere als die angegebenen Quellen/Hilfsmittel nicht benutzt, und die den benutzten Quellen wörtlich und inhaltlich entnommenen Stellen als solche kenntlich gemacht habe. Das in TUGRAZonline hochgeladene Textdokument ist mit der vorliegenden Dissertation identisch.

Datum/Date

Unterschrift/Signature

Acknowledgement

I have numerous people to thank for for their help, assistance and guidance that has enabled me to finally complete my phd thesis and become a doctor. My first and biggest gratitude goes to my wife Karin, who has not only made me a better person but also always supported me in my decisions even if she had to make some sacrifices. Without her I might still have acquired my degree eventually, but I would have been a much different person. I'd also like to thank the whole working group for the friendliest, funniest and most comfortable work environment possible that I had the luxury of enjoying the last four years. I especially like to thank Sergey, who has guided me throughout my thesis and was always available for valuable discussion and feedback on any matter. My gratitude goes towards Christoph and Christoph, both of them were great colleagues and without them I couldn't have got all the work done. And, of course, I'd like to thank Ingo, who I had countless fruitful discussions with and who gave me the great opportunity to work on a very interesting and challenging project that helped me acquire many new skills. A great Thank You also goes to all the people in Aarhus and Odense, it was a great pleasure working with you guys and I hope you will profit for quite a while from the work that we've done together.

Dipl.Ing. Philipp Lehner, BSc Graz, March, 2015

Contents

1 Introduction

Light brings us the news of the Universe.

– Sir William Bragg, *The Universe of Light*

1.1 Scope of this Thesis

Optical oxygen sensing is a large field with multiple research groups working on different implementations. Among luminescence based sensors oxygen sensors are possibly the closest to being established in the market as a viable alternative to other, often electrochemical, detection systems. However, most commercialized sensing schemes are designed to resolve oxygen concentrations in the physiological range (0-20 % O_2, 0-284 μM (dissolved oxygen, (DO))), with a few exceptions of sensors that measure up to oxygen saturation (0-100 % O_2, 0-1.35 mM (DO)) or measure what is usually called trace oxygen (0-5 % O_2, 0-68 μM (DO)). The dynamic range of optical oxygen sensors usually spans three to four orders of magnitude, though resolution is not linear over the entire range. This means that detection limits of systems are rarely below 50 nM (DO), even for the above mentioned trace sensors. However, there are certain applications where oxygen concentrations in the low nano molar (DO) range are of interest, for example in marine biology. Some measurements might even benefit from pico molar detection limits. In this thesis the work done on designing, creating, calibrating, testing and integrating optical oxygen sensors that operate in this very low concentration regions is described. We also present some of the obstacles encountered in this new territory of ultra trace oxygen sensing and the knowledge we gained from overcoming them. This work consists of mainly three publications which directly resulted from the work done during Project Oxygen. The first one presented in chapter 2 details the development of boron di-fluoride and aluminium complex based sensor materials that offer detection limits in the low pico molar range. The second publication dealt with in chapter 3 details some of the important artefacts that can have a significant influence on measurements in this very low concentration region. And the third publication in chapter 4 describes the Lumos, a miniature phase fluorimeter with matching sensing chemistry that is designed for detection limits slightly below 1 nM and is the measurement "workhorse" of project oxygen.

1.2 Project Oxygen

Project Oxygen is an ERC Advanced Grant that aims to investigate the importance of oxygen on the early evolution of life. It is conducted in cooperation with marine biologists of two Danish universities in Aarhus and Odense, with the principal investigator Donald Eugene Canfield, Head of the Nordic Center for Earth Evolution (NordCEE) of Sydansk University in Odense and a leading expert in the field. Other notable participants are Niels Peter Revsbech, professor at the Institute of Bioscience in the University of Aarhus who has devised and built a electrochemical sensor called the "STOX" sensor that achieves the lowest detection limits of any

electrochemical oxygen sensor through repeated zero calibration after each data point. It was the hope of these two universities and their teams that Ingo Klimant, Head of the Institute of Analytical Chemistry and Foodchemistry, who is a leading expert on optical sensor technology and the supervisor of this thesis, would be able to provide the trace and ultra trace oxygen sensors required for further investigating the origins of aerobic life. After more than three years of working on project oxygen, Ingo Klimant, Sergey M. Borisov, Christoph Larndorfer, Christoph Staudinger and the author have succeeded in providing these two teams of marine biologists with the tools required to monitor oxygen concentrations in the low nM and even pM region.

1.3 Theoretical Background

1.3.1 Interaction of Light and Matter

The range of light a human can see is just a small but crucial band in the large continuous energy spectrum of electromagnetic radiation. The gauge boson of electromagnetism is the photon, which according to quantum principles can be interpreted as both a particle and a wave. Its discovery was crucial to the understanding of quantum physics and chemistry we have today. Photons are mass- and chargeless particles that travel at a constant maximum relativistic speed, the speed of light ($\sim 3{\times}10^8$ m/s in vacuum). Their energy is therefore not determined by mass times velocity but rather by their frequency, which can be imagined as a oscillation of the photon wave function in the plane normal to the travel direction. A photon's frequency can be converted to its energy and wavelength through equation 1.1.[1]

$$E = h \cdot \nu = \frac{h \cdot c}{\lambda} \tag{1.1}$$

Photons can be created in multiple ways, but one of the most important ones is emission of a photon through transition of an electron to a lower energy level. The energy of the emitted photon exactly matches the energy of the transition. Generated photons can interact with matter in different ways, one of them is absorption. In an absorption event the energy of the photon is used for an electron to transition to a higher energy state, the photon is consumed in the process. Comparable to emission, the energy of the photon exactly matches the energy required for the transition. In reverse this means that absorption can only occur if a specific atom or molecule has an electron transition that requires exactly that energy. These principles form the basis of many spectrometric methods.[2]

As the energy of emitted and absorbed photons matches the transition energy of various states it is interesting to know which different transitions correspond to which regions in the electromagnetic spectrum of light. Table 1.1 gives an overview over various energy regions and their associated transitions.

The visible (VIS) region roughly spans wavelengths from 400 to 700 nm. As shown in table 1.1 this region corresponds to the transition of a molecular electron from the highest occupied orbital into higher unoccupied orbitals. The spectrum of possible transition energies varies greatly for most molecular compounds and allows differentiation of different types of matter. Electrons that were excited into higher energy states can normally return to their ground state through relaxation, often involving the emission of a photon, a process generally referred to as luminescence. As the excited states usually have very different chemical properties from the ground state they may not be inherently stable, so another possibility for the energy to

Name	Wavelength	Energy mol^{-1}	Transitions
Gamma Rays	1 - 10 pm	100 - 2 GJ	Excitation and dissociation of nuclei
X-Rays	0.05 - 1 nm	1000 - 100 MJ	Excitation and ejection of core electrons
UV	1 - 400 nm	200 - 0.3 MJ	Excitation and ejection of valence electrons
Visible	400 - 700 nm	300 - 170 kJ	molecular electron excitation
Infrared	1 - 100 μm	120 - 1 kJ	molecular vibration

Table 1.1: A non exhaustive list of different regions of the electromagnetic spectrum and associated approximate energies and transitions in atoms and molecules.

dissipate is through chemical reaction e.g. bond formation or breaking. The field describing these events is called photo chemistry.

1.3.2 Lambert-Beer Law

Absorption of photons through matter is macroscopically described by the Lambert-Beer law (equation 1.2), which correlates the intensity (I_0) of the incident light and the intensity (I) of the light transmitted through a solution of path length d to the amount of the substance in solution ($[C]$). The logarithm of the fraction of initial and transmitted intensity is called the Absorbance (A).[1]

$$A = \log \frac{I_0}{I} = \epsilon_\lambda \cdot [C] \cdot d \tag{1.2}$$

The proportionality factor ϵ is called the absorption coefficient, or molar absorption coefficient if the amount of absorbing substance is given in mol. It is valid only for a given wavelength and therefore is usually given with the corresponding wavelength as a subscript.

The Lambert-Beer law can easily be derived by representing a sample as a number of infinitely thin cross sections which absorb photons depending on the concentration through a proportionality factor (ϵ^*). The difference in intensity over the sample length is then described by the differential equation 1.3.

$$\begin{aligned} \frac{\mathrm{d}I}{\mathrm{d}d} &= -\epsilon^* \cdot [C] \cdot I \\ \frac{\mathrm{d}I}{I} &= -\epsilon^* \cdot [C] \cdot \mathrm{d}d \end{aligned} \tag{1.3}$$

One may recognize equation 1.3 as very similar to the equation of exponential decay, and the solution is accordingly:

$$\ln I = -\epsilon^* \cdot [C] \cdot d + C \tag{1.4}$$

By setting the boundary condition to $I(t = 0) = I_0$ and multiplying the conversion factor from the natural logarithm to the decimal logarithm into ϵ^* one gets the absorption coefficient ϵ_λ ($\approx 0.434 \cdot \epsilon^*$) and the following equation:

$$-\log \frac{I}{I_0} = \epsilon^* \cdot [C] \cdot d \tag{1.5}$$

This can be rearranged into equation 1.2. As the Lambert-Beer equation ignores the possibility of other influences such as reemission of light, scattering, and molecular interactions it is only valid vor very diluted samples that have negligible turbidity.

1.3.3 Franck-Condon Principle

The potential energy well of a diatomic molecule can be expressed as a function of nucleus distance for any given electron configuration. This is possible because of the Born-Oppenheimer approximation, which states that the large difference in mass between a nucleus and an electron ($m_e \approx 9.1 \times 10^{-31} kg$, $m_p \approx 1.7 \times 10^{-27} kg$) means that the nuclei have a much larger inertia and can be considered stationary when solving the Schrödinger equation for the electrons. Plotting the energy solutions versus the nucleus distance results in the curves in figure 1.1 for the ground state and an excited state (denoted by $*$) respectively.

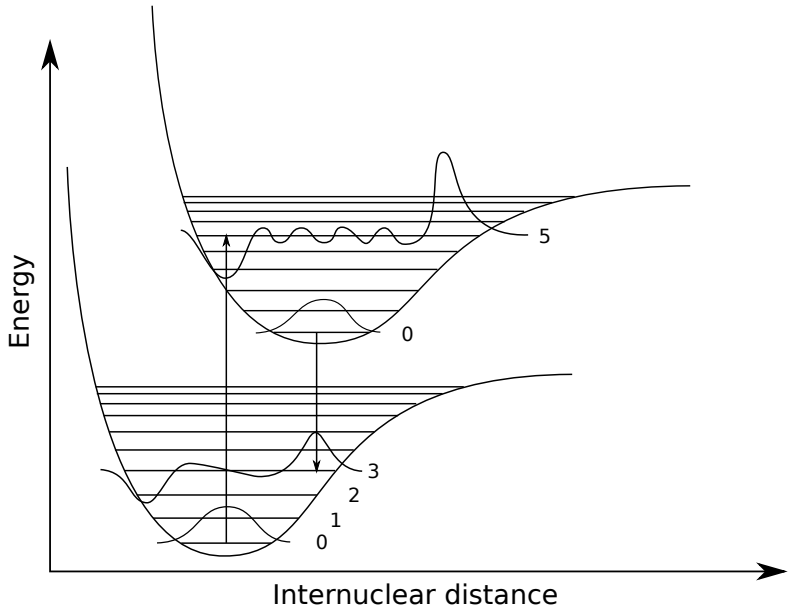

Figure 1.1: Franck-Condon diagram of the potential energy curves as a function of nucleus distance for a diatomic molecule. Because electron transitions happen much faster than nucleus movement, the absorption of a photon leads to a vertical transition. The probability of a transition is given by the Franck-Condon factor $|S_{v',v}|^2$.

As the timeframe in which electronic transitions happen is much faster than the oscillation of the nuclei, absorption of a photon is always represented as a straight line. This fact is called the Franck-Condon principle. The quantum-mechanical interpretation of this principle predicts probabilities for transitions of a specific energy. The probability of a given transition is represented by the square of the transition dipole moment $|\mu_{GE}|^2$ which is given for a single electron by equation 1.6.[1]

$$\mu_{GE} = -e \int \Psi_E^* r \Psi_A \mathrm{d}\tau \tag{1.6}$$

Ψ_A and Ψ_E^* are the wave functions of the molecule before and after the transition, r are the electrons coordinates and e its charge. As the total wave function of both states can be

approximated by the product of electronic and vibrational wave functions, it is possible to write:

$$\mu_{GE} = -e \int \Psi^*_{e'}(r)\Psi_e(r)\mathrm{d}\tau_e \int \Psi^*_{v'}(R)\Psi_v(R)\mathrm{d}\tau_N \tag{1.7}$$

The first integral is a measure of the change in electron density while the second integral is a measure for the orbital overlap of ground and excited state wave functions. The square of this second integral $|S_{v',v}|^2$, which is called the Franck-Condon factor is therefore proportional to $|\mu_{GE}|^2$ and the probability of a transition. This fact is represented in figure 1.1 by the schematic wave functions superimposed over the vibrionic states.

1.3.4 Jablonski Diagram

To better visualize the various processes that can be observed during the absorption and the emission of light by molecular orbital electrons, a Jablonski diagram is often used. It is a one dimensional representation of the energy levels involved in excitation and de-excitation processes and is a more convenient abstract representation than the Franck-Condon diagram. The Jablonski diagram in figure 1.2 shows a typical representation of the various processes that can be observed.[2]

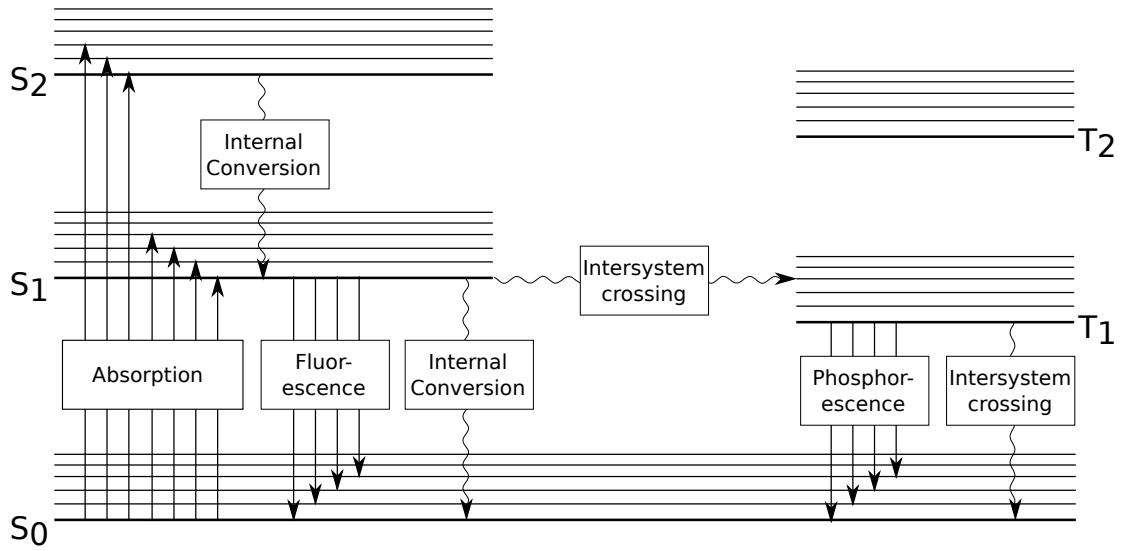

Figure 1.2: Example of a Jablonski diagram. Horizontal lines represent the different energy states and their vibrational levels. Arrows depict electron transitions similar to the ones shown in a Franck-Condon diagram.

In this diagram the horizontal solid lines represent some of the possible energy states of a given molecule, S_0 is the ground state and S_1, S_2 and T_1 are the excited singlet and triplet states, respectively. S and T denote the multiplicity of the states, as per equation 1.8.

$$M = 2\sum m_s + 1 \tag{1.8}$$

Where $\sum m_s$ is the sum of all electron spins, in agreement with Hunds rule this number is usually equal to the number of unpaired electrons divided by two (though exceptions exist, most notably $^1\Sigma_g^+$ singlet oxygen). Therefore the multiplicity can often be obtained by adding

one to the number of unpaired electrons. Note that excitation is shown to always start at the vibrational base level, which is a result of most compounds residing predominantly in that state at room temperature. Emission also starts at the base vibrational level of the excited state. This is a simple result of change between vibrational levels of a state being much faster than a transition between states.[1]

Process or Lifetime	Timescale
absorption	10^{-15} s
vibrational relaxation	10^{-12} - 10^{-10} s
S_1 excited state lifetime	10^{-10} - 10^{-7} s
inter system crossing	10^{-10} - 10^{-5} s
T_1 excited state lifetime	10^{-5} - 1 s

Table 1.2: Characteristic timescales for various energy states and processes

Table 1.2 shows different characteristic timescales at which the various processes can happen. It is important to understand that the relative observable intensity of these transitions and processes is governed directly by the probability distribution of the underlying quantum mechanical representation. If a specific transition becomes more probable, its rate and therefore observed intensity increases.

1.3.5 Non Radiative De-Excitation Processes

Internal Conversion

Internal conversion is an iso-energetic, non-radiative transition between two energy states that have the same spin-multiplicity. After excitation a molecule can reach the lowest vibrational state by dissipating the excess energy through vibrational relaxation (if thermal dissipation, e.g. collision with other molecules, is possible). If the electron is excited into an energy state higher than S_1 (for example S_2) it can transition into the S_1 vibrational state through internal conversion. For higher level excited states, which have a smaller relative energy difference, this transition is very fast, but for the transition of $S_1 \rightarrow S_0$ it is in the timescale of fluorescence and inter system crossing, and can therefore compete with those processes.[2]

Inter System Crossing

Just like internal conversion, inter system crossing is an iso-energetic, non-radiative transition between two energy states. However, in the case of inter system crossing, the two states are of different spin-multiplicity. This transition is generally spin-forbidden (the inversion of the electron spin is not allowed in a transition). It can, however, still be observed due to spin orbit coupling, which is the interaction of magnetic fields created by the electron's orbit and its spin. Spin orbit coupling results in the singlet or triplet wave function to always include a small fraction of either triplet or singlet character, which enables the overlapping integral to be non-zero. The magnitude of this effect is dependent on the atomic number to the power of 4, which results in inter system crossing to be a favored transition in many molecules containing heavy atoms.[2]

1.3.6 Types of Luminescence

Fluorescence

Fluorescence is the $S_1 \rightarrow S_0$ relaxation of a molecule through the emission of a photon. In most cases the vibrational relaxation of higher states is faster than fluorescence so that the emission almost always occurs from the S_1 vibrational base state. This means that the wavelength of emitted photons is not dependent on the wavelength of absorbed photons. Because of the similarity of vibrational levels a fluorescence spectrum usually looks like a redshifted mirrored version of the absorption spectrum. The shift (in wave numbers) between the absorption and emission maximum is called the Stokes Shift. Very often absorption and emission spectra have a small spectral overlap, this is because of the fact that not all molecules will actually reside in the vibrational ground state at room temperature. Although fluorescence itself is a very fast process comparable in speed to absorption (10^{-15} s), the S_1 state has a certain stability which leads to an observed exponential decay of fluorescence intensity not unlike the one observed for radioactive decay, which is dependent on the average lifetime of the excited state.[2]

Phosphorescence

Phosphorescence is the relaxation of an excited state by emission of a photon into a state of different spin multiplicity, usually a transition of type $T_1 \rightarrow S_0$. As the T_1 excited state is the result of inter system crossing from the S_1 state to an equienergetic triplet vibrational level and the T_1 state is of lower energy than the S_1 state, the phosphorescence emission spectrum is even further redshifted than the fluorescence spectrum. As the relaxation from the T_1 state involves a spin-forbidden transition it usually has avery long lifetime. In solution and/or at high temperatures non-radiative de-excitation processes are usually preferred over phosphorescence. If temperatures are very low, however, or the molecule is embedded in a rigid matrix, phosphorescence can be observed. Due to the stable triplet state, phosphorescence lifetimes are in the range of milliseconds up to multiple seconds.[2]

Stimulated Emission

Stimulated emission is comparable to spontaneous emission (fluorescence), but is instead triggered by interaction of the excited state with a photon of exactly the energy of the transition. The result of this interaction is the emission of a second photon that has the same energy as the stimulating photon and travels in the same direction. While stimulated emission is difficult to observe in nature, lasers are a common example. In lasers inversion of the system ($[S_1] > [S_0]$) is achieved by pumping and the cascading effect results in high intensity coherent light.[2]

Delayed Fluorescence

Just like inter system crossing allows the transition of S_1 to T_1, the reverse is also possible. In a process called thermal or e-type delayed fluorescence, vibrationally excited triplet states can transition back to the singlet excited state through reverse inter system crossing. This is followed by regular relaxation of the S_1 state including fluorescence, because the $T_1 \rightarrow S_1$ transition is the rate limiting step and fluorescence is very fast compared to phosphorescence. Delayed fluorescence exhibits the same lifetime as accompanying phosphorescence. Because the population of the vibrationally excited triplet states depends strongly on temperature, delayed fluorescence is also heavily temperature dependent. The intensity of this type of delayed fluorescence therefore increases with temperature. Another phenomenon also called delayed

fluorescence is the result of triplet triplet annihilation. In this bimolecular process two excited state molecules are involved in an energy transfer where one molecule returns to the ground state while the other returns to the excited singlet state. This process is therefore strongly dependent on excited triplet state concentration and lifetime and the observed delayed fluorescence lifetime is half that of phosphorescence observed without triplet-triplet annihilation. Its intensity has a characteristic square dependence on triplet state concentration.[2]

1.3.7 Quantum Yields

The Quantum Yield is defined as the number of photons absorbed per corresponding "event". The fluorescence quantum yield is therefore defined as the ratio of emitted photons to absorbed photons and approaches unity if fluorescence is the dominant relaxation method. Equation 1.9 shows the representation of the steady state equation for a simple system with fluorescence as the only radiative relaxation process.[2]

$$k_a S_0 = k_f S_1 + \sum k_{nr} S_1 \tag{1.9}$$

Where S_0 and S_1 are ground- and excited state concentrations and k_a is the absorption rate constant, k_f is the fluorescence rate constant and $\sum k_{nr}$ is the sum of all non-radiative rate constants. As the number of emitted photons is defined by $k_f S_1$ and the number of absorbed photons is represented by the left hand side of equation 1.9 the fluorescence quantum yield can be given as:

$$\Phi_f = \frac{k_f}{k_f + \sum k_{nr}} = k_f \cdot \tau_f \tag{1.10}$$

Relative QY Determination

There are two ways quantum yields can be determined experimentally, either in relation to a compound of known quantum yield or absolutely by using a so called integrating sphere. In the relative approach the fluorescence spectrum of a fluorophore with known quantum yield is obtained and the experiment is then repeated with exactly the same settings and the compound of which the quantum yield is to be determined. The quantum yield can then be calculated by equation 1.11:

$$\Phi_f = \Phi_R \times \frac{\int em - 10^{-A_R}}{\int em_R - 10^{-A}} \cdot \frac{n^2}{{n_R}^2} \tag{1.11}$$

Where em and em_R are the photons emitted at different wavelengths, A and A_R are the absorbances at the excitation wavelength and n and n_R are the refractive indices of the used solvents for sample and reference, respectively.

Absolute QY Determination

For the absolute method of quantum yield determination an integrating sphere (often called Ulbricht sphere) is used. It consists of a spherical cavity whose walls are coated with a diffuse, highly reflective material and it has two small holes for incident and emission light. Because light rays can undergo numerous diffuse scattering processes at the walls, the intensity of light is conserved but any spatial information is destroyed. If a sample is introduced into the sphere and excited by light source, the intensity spectra of both absorption and emission can be measured

with and without sample. By integrating and subtracting the measured data, the quantum yield can be determined directly as per equation 1.12.

$$\Phi_f = \frac{\int \frac{\lambda}{hc}(I_{em}^S - I_{em}^R)\mathrm{d}\lambda}{\int \frac{\lambda}{hc}(I_{ex}^R - I_{ex}^S)\mathrm{d}\lambda} \tag{1.12}$$

1.3.8 Quenching

In addition to the intra molecular processes of relaxation there is the possibility of relaxation involving a second molecule. This method of relaxation is called quenching and the compound involved is called a quencher. There are various different methods by which inter molecular quenching can occur. In sensor applications the luminophore is typically referred to as the dye and the quenching species as the analyte or quencher. Macroscopically two types of quenching can be differentiated: static and dynamic quenching.[2]

Static Quenching

In static quenching the quencher is forming a non-luminescent complex with the luminophore thereby reducing luminescence intensity. The measured luminescence lifetime is not affected, though, as complex formation "switches off" the luminophore and the complex therefore does not contribute to the observed lifetime. Another effect that is often also called static quenching is if quencher and dye cannot change their positions relative to each other during the excited state lifetime of the dye and the quencher is close enough to the dye to be inside the so called sphere of effective quenching.[2]

Dynamic quenching

In dynamic or collisional quenching the quencher collides with the excited state luminophore and the energy is transferred, resulting in a non radiative decay of the excited state. As this process competes directly with luminescence intensity it is affected by quencher concentration, just like in static quenching, but this time the measured luminescence lifetime is also proportionally reduced. Dynamic quenching is the process by which oxygen can quench various luminophores.[2]

Photoinduced Electron Transfer

Photoinduced electron transfer (PET) is an important process in many organic photochemical reactions whenever charges need to be separated such as in photosynthesis or artificial systems for the conversion of solar energy. Because the intramolecular PET effect is very efficient it is also often responsible for fluorescence quenching. Many optical chemical sensors employ switchable PET groups such as amines that have their PET efficiency reduced when protonated, resulting in enhanced fluorescence.[3]

Resonance Energy Transfer

Resonance energy transfer (RET) is also often called FRET for fluorescence resonance energy transfer (which is a misnomer as fluorescence is not involved in the process). RET is a blanket term describing a number of different energy transfer mechanisms. They have in common that the energy is transmitted without generation and subsequent absorption of a photon. It is therefore a non-radiative energy transfer. The transfer requires donor and acceptor transitions

to have the same energy, they are therefore coupled, i.e. they are in resonance. The mechanisms behind RET are dipole-dipole interactions (Förster's mechanism, also sometimes called FRET for Förster Resonance Energy Transfer) and short range multi-polar interactions. Both of which are coulombic in nature and require a spectral but no orbital overlap. Orbital overlap mechanisms are only important at short ranges and are the predominant transition method when the transfer is between triplet states, e.g. ${}^3D^* + {}^1A \rightarrow {}^1D + {}^3A^*$, as Coulomb interactions are negligibly small in that case. For allowed transitions the Coulomb interactions are dominant and can be effective at ranges up to 100 Å. Fluorescence quenching by these long range dipole-dipole interactions can be used to measure distances between donor and acceptor and is an important tool for microbiological applications, where it can help to determine e.g. protein and DNA binding and folding characteristics.[2]

Singlet Oxygen

When molecular oxygen quenches a luminophore through collision, the energy is transferred and the oxygen molecule is excited into its first excited singlet state (note that ground state oxygen is in the triplet state). The excited singlet state of oxygen may then undergo relaxation comparable to previously described processes, either by photon emission (λ_{max}= 1270 nm) or through non-radiative de-excitation. Singlet oxygen is, however, a very reactive species that readily oxidizes various electron rich organic compounds. Therefore singlet oxygen may also undergo chemical deactivation by reaction.[2]

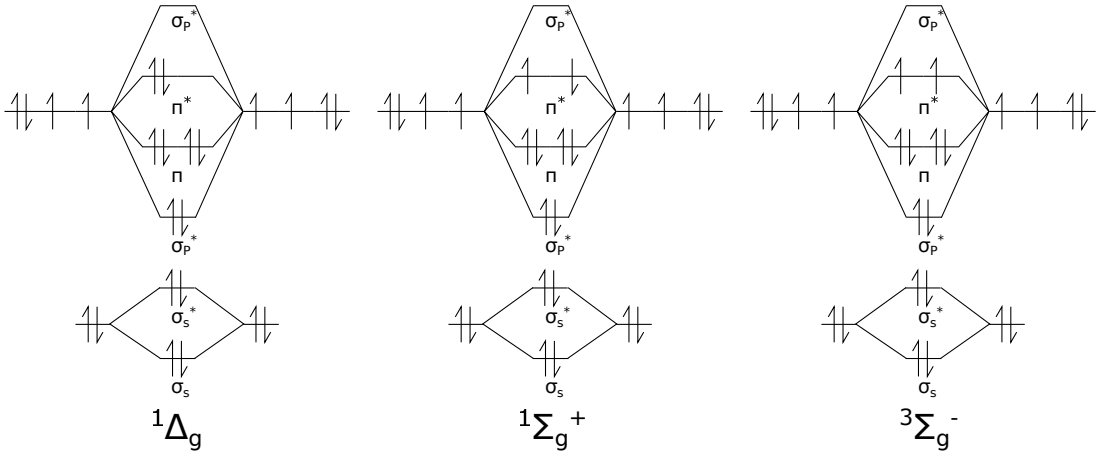

Figure 1.3: Molecular orbital scheme of the different dioxygen species. ${}^3\Sigma_g^-$ is the triplet ground state of molecular oxygen and ${}^1\Delta_g$ is the excited singlet state, the second excited singlet state ${}^1\Sigma_g^+$ is very short lived and therefore often neglected when considering possible reactions of the singlet state.

1.3.9 Stern-Volmer Equation

The ideal process of dynamic quenching is described by the Stern-Volmer relation (equation 1.13). It describes the relation between steady state intensity or lifetime and quencher concentration. K_{SV} is called the Stern-Volmer constant and is equal to $k_q \cdot \tau_0$ with k_q being the bimolecular quenching constant. $[Q]$ is the concentration of the quencher and I_0, I and τ_0, τ are steady

state intensity and lifetime with and without quencher, respectively.[4]

$$\frac{I_0}{I} = \frac{\tau_0}{\tau} = 1 + K_{SV} \cdot [Q] \tag{1.13}$$

One way to derive equation 1.13 is by examining the time evolution of the system's response to a short excitation pulse and subsequent decay of the luminescence signal:

$$\frac{\mathrm{d}S_1}{\mathrm{d}t} = -S_1(k_f + \sum k_{nr} + k_q \cdot [Q]) \tag{1.14}$$

Which results in (in much the same way as the derivation of equation 1.2):

$$S_1(t) = S_{1,0} \cdot \mathrm{e}^{-(k_f + \sum k_{nr} + k_q \cdot [Q])t} \tag{1.15}$$

Which is a mono exponential decay with the lifetime: $1/(k_f + \sum k_{nr} + k_q \cdot [Q])$. Substituting $\tau_0 = 1/(k_f + \sum k_{nr})$ yields the equation:

$$\tau = \frac{\tau_0}{1 + \tau_0 k_q \cdot [Q]} \tag{1.16}$$

This is easily transformed into equation 1.13. Additionally the Stern-Volmer relation can be derived from the fluorescent quantum yields with and without quencher. If equation 1.10 is expanded to include relaxation through quenching, the ratio of unquenched and quenched quantum yields is given by:

$$\frac{\Phi_0}{\Phi} = \frac{k_f \tau_0}{\frac{k_f}{k_f + \sum k_{nr} + k_q \cdot [Q]}} \tag{1.17}$$

which can be rearranged and simplified to:

$$\frac{\Phi_0}{\Phi} = \frac{I_0 \cdot I_a}{I \cdot I_a} = 1 + \frac{k_q \cdot [Q]}{k_f + \sum k_{nr}} \tag{1.18}$$

This can once again easily be converted to equation 1.13. It is important to understand that the Stern-Volmer relation describes an ideal system. In a plot of experimentally determined values of I_0/I versus the quencher concentration should result in a linear relation with K_{SV} as the slope. However, there are various ways in which a real calibration may deviate from this ideal behavior. The addition of static quenching would result in an upward curvature of the line for example, whereas an inhomogeneous system with multiple K_{SV}s would result in a downward curvature. Regardless of the actual form of the curve, K_{SV} is a direct measure for the sensitivity of a luminophore or dye to a specific quencher. In all these approaches K_{SV} is comprised of the unquenched lifetime and the bimolecular quenching constant k_q. The sensitivity of a sensor based on luminescence quenching is therefore dependent on the lifetime of the used luminophore and the bimolecular quenching constant. Importantly, as the system describes dynamic quenching, k_q is actually defined as $k_q = p \cdot k_d$, with p a proportionality factor describing the success rate of a collision and k_d the diffusion rate constant, which itself is given by equation 1.19.

$$k_d = 4\pi R^* D_O \tag{1.19}$$

With R^* being the effective radius at which quenching takes place and D_O being the diffusion coefficient of oxygen. This is given by the Einstein-Stokes equation as:

$$D_O = \frac{k_B T}{6\pi\eta a} \tag{1.20}$$

By assuming that $R^* = 2a$ and combining equation 1.19 and 1.20, one can arrive at the expression usually given for the rate constant of diffusion for one species to a stationary second reaction species:

$$k_d = \frac{4k_B T}{3\eta} \cdot N_A = \frac{4RT}{3\eta} \tag{1.21}$$

As a result, a sensor's sensitivity may also be improved by increasing the diffusion coefficient for oxygen of the surrounding medium.

1.3.10 Two-Site Model

As the Stern-Volmer relation describes an ideal system, a variation – the two site model – is often used to fit experimental data instead. The two site model assumes that instead of a homogenous dye environment, the dye is embedded in at least two distinct environments with their own set of K_{SV} values.[5, 6] A simple example would be a polymer with crystalline and amorphous regions that feature very different diffusion properties. Even though there are usually not just two distinct regions, but rather a continuum of different environments, two is quite often enough to achieve reasonable fits to experimental data. The formula of the two site model is shown in equation 1.22.

$$\frac{I}{I_0} = \frac{f}{1 + K_{SVa} \cdot [Q]} + \frac{1 - f}{1 + K_{SVb} \cdot [Q]} \tag{1.22}$$

Note that the left hand side fraction is reversed compared to the Stern-Volmer relation (1.13). As mentioned this simplified model of just two sites is often sufficient to describe experimental systems. However, in some cases this equation can be even further simplified by assuming that K_{SVb} is zero (the second domain is not permeable to oxygen at all). This assumption greatly simplifies solving equation 1.22 for the quencher concentration which can now be given by:

$$[Q] = \frac{1 - \frac{I}{I_0}}{k_{SVa}(f - 1 + \frac{I}{I_0})} \tag{1.23}$$

While this simplification makes calculations easy, one has to be careful to note that this simplification leads to the fitting curve to show an asymptote at $I/I_0 = 1 - f$ where it is not defined, which is quite obviously not the behavior expected of an actual sensor. This approximation therefore only fits data which are reasonably far away from the asymptote.

1.3.11 Sensor Characteristics

A chemical sensor is defined as a device that transforms chemical information into an analytically useful signal.[7] They generally consist of two integral parts, the receptor and transducer. The receptor reacts to a change in the measurement system and may be based on various principles such as physical quantities like absorbance, conductivity or temperature. It can also be based on chemical or biochemical quantities where the participation of the receptor in a chemical reaction generates the signal. The second part – the transducer – transforms the receptor's

change of state into a usable signal. Its operation principle is often used to classify different sensors and some common operating principles are: optical, electrochemical, mass sensitive, thermometric and magnetic.[7] The oxygen sensors described in this work exclusively belong to the optical family of sensors, specifically luminescence based sensors.

An ideal sensor measures the intended property selectively and does not alter the measured system in any way.[8] Optical oxygen sensors deviate from this ideal behavior in multiple ways that have to be accounted for.

- Temperature cross-talk: Most optical sensors show a cross sensitivity to temperature, because some physical properties of the sensor system are affected by it, like oxygen diffusion speed and abundance and the probability of non-radiative decay pathways.
- Pressure cross-talk: The sensors might be influenced by high pressure environments, like deep sea applications.
- Excitation light: As is demonstrated in this work, sensors show an intrinsic dependence on excitation light intensity, for simple photochemical reasons, especially if high photon fluxes are involved.[9]
- Chemical degradation of the sensor: While a key effort in sensor development is to make probes and matrices chemically stable, sensors can show degradation and chemical aging over time.
- Quenching through other chemical species: Besides oxygen, there exist a number of other small compounds that can quench probe molecules. These have to be kept away from the probes by a suitable matrix.
- Photobleaching: The excited state of a molecule is often very different in its chemical properties from its ground state. It often more readily reacts with other compounds. Another effect that is also referred to as photobleaching is if singlet oxygen created in the quenching process oxidizes the probe and thereby alters its photo physical properties.

1.3.12 Sensor Matrix

Many of the unintended influences on a sensor's response can be eliminated or minimized by choosing an appropriate matrix. The matrix is a polymer or other substrate that contains the oxygen sensitive dye either by physical or chemical entrapment and acts a a defined environment for the dye. It has a constant permeability and thereby makes the sensor largely independent from the composition of the measured system. It also acts as a physical and chemical barrier that is often hydrophobic to prevent penetration of charged compounds. It can act as physical protection and sometimes aids in the gathering of emission light. Matrices can be chosen for an optimal combination of a variety of properties, like their resistance to biofouling, chemical- and especially oxidation stability but most importantly their permeability. A matrix's permeability is a very important property for any sensor system as it is directly proportional to the sensor's sensitivity, as per equation 1.24.

$$Sensitivity \propto \tau_0 * P \tag{1.24}$$

where P is the permeability and τ_0 is the dye's lifetime in absence of quencher. This means that selecting a polymer matrix with a specific permeability can be used to tune the resulting

sensor's sensitivity. The permeability of polymers is defined in equation 1.25[10].

$$P = D * S \tag{1.25}$$

where D is the diffusion coefficient and S is the Solubility of the quencher. The resulting proportionality of a sensor's sensitivity on both diffusion coefficient of the quencher and its solubility can also be derived from equations 1.13 and 1.19. D is contained in k_q and thusly in K_{SV} and the solubility can be understood as being contained in $[Q]$, as the measured oxygen concentration in the sensor $[Q]_S$ is proportional to the bulk quencher concentration $[Q]$ through a solubility ratio.

1.3.13 Sensor Geometries

Planar Optodes

Planar optodes consist of a thin sensor material evenly covering a substrate surface. They are easy to manufacture through knife-, spray- or spin coating and can be used for both conventional sensing and imaging applications. Readout geometries for planar optodes can be very simple and some ratio metric sensors can be read out with a simple consumer grade photo camera. If analyte concentration differences at the sensing layer surface are representative for bulk concentration differences, such planar sensors can be used for imaging applications such as in micro fluidics, cell cultures or even to indirectly detect flow changes in a wind tunnel.

Fibre Optodes

Fibre optodes consist of a glass or polymer fibre that has its tip coated in the respective sensor material. They are mostly manufactured by dip-coating. They require more sophisticated readout devices because excitation and emission light has to be coupled into and out of the fibre, respectively. They are easy to manipulate, as the sensor is situated at the end of a flexible fibre and they are usually quite robust and can even be contained in a hollow needle to pierce membranes. They are also prevalently used in deep sea applications as fibre optical feedthroughs are easier to realize in a pressure container than a larger transparent window. Due to their very thin sensor film and small cross section they usually offer superior response times and are indeed employed in Eddy Correlation Experiments.

Nanobeads

In many cases the sensor material can also be precipitated and emulgated to form micro or even nanometer sized particles instead of being bound to a substrate. Such nano beads are very well suited for imaging applications and can be used to measure analytes directly in single cellular organisms or micro fluidic channels. Their fabrication is more complicated than the other two methods and readout is also more difficult, because concentration cannot be guaranteed to be constant over a whole sample. Ratio-metric measurements employing e.g. core-shell designs or using lifetime imaging are required for reliable results.

1.3.14 Readout Methods

As described in section 1.3.11 the transducer part of an optical chemical sensor converts the change of physical properties of the probe in a useable signal. In the case of luminescence based optical sensors there are different possible strategies to obtain such a signal. The

extrinsic property of the system that is directly dependent on the oxygen concentration is the concentration of dye in the excited triplet state. Both luminescence intensity and -lifetime are proportional to that concentration and can therefore be used as readout parameters.

Ratiometric Readout

Measuring intensity directly is often complicated and unreliable as it has to be guaranteed that no other influences, like changes in optical geometry or variation in dye concentration or emission intensity, are responsible for a change in signal intensity. A common way to address this issue is ratiometric readout, where a second dye whose luminescence properties are not influenced by the analyte is also immobilized in the sensor material and the emission of this reference dye is in a sufficiently different wavelength region from the indicator dye so that it can be used to normalize the emission signal in a dual wavelength measurement setup.

A different way to obtain normalized signal intensities using a reference dye is to use dual lifetime referencing.[11] This method is however not very relevant for the optical oxygen sensors employed in this work which are not based on fluorescence quenching, still, for completeness an explanation is provided in the appendix in section 9.1.

Frequency Domain

One possible method to experimentally determine lifetime information is by phase fluorometry in the frequency domain. As illustrated in figure 1.4, the sensor system is excited by sinusoidally modulated excitation light and the harmonic response of the system is recorded.[2] The equation

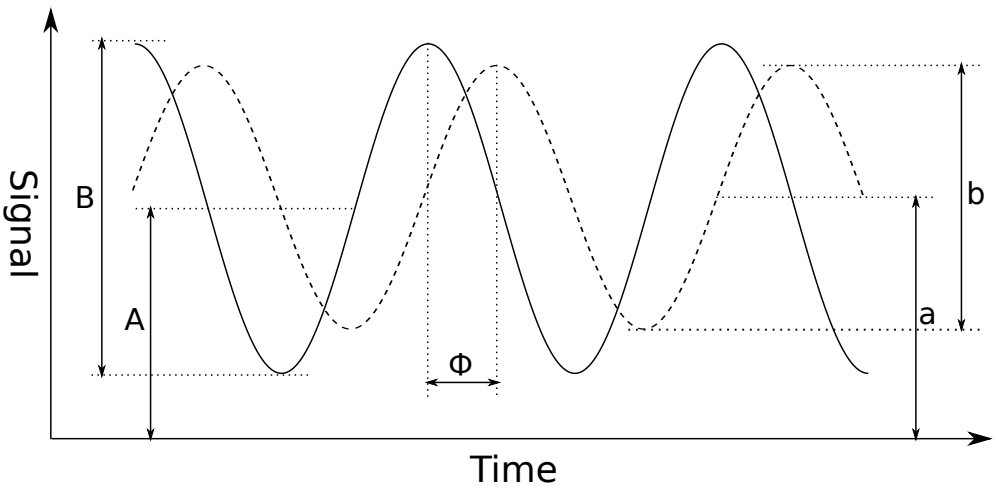

Figure 1.4: Diagram of principle of phase fluorometry, a sinusoidally modulated excitation light source results in a sensor response that is shifted in phase by the angle Φ.

for the excitation light intensity $E(t)$ and the response $R(t)$ are given in equation 1.26. The response is partially demodulated and the phase is shifted in respect to the excitation function by the phase angle Φ.

$$\begin{aligned} E(t) &= A + B \cdot \sin \omega t \\ R(t) &= a + b \cdot \sin (\omega t - \Phi) \end{aligned} \tag{1.26}$$

t being the time and ω being the angular frequency ($2\Pi f$). In measurements, the phase shift Φ can be determined either by direct fitting or performing a single frequency fast fourier

transformation of the response. The phase angle is related to the lifetime of the used dye through an equation that can be determined by convoluting the excitation function with the theoretical δ-pulse response of the dye.

$$I(t) = I_0 \cdot e^{\frac{-t}{\tau}} \tag{1.27}$$

In the case of ideal mono-exponential behavior that response is given by equation 1.27. The resulting convolution product is therefore defined as:

$$R(t) = I(t) \otimes E(t) = \int_0^\infty E(t_i) \cdot I(t - t_i)\mathrm{d}t_i \tag{1.28}$$

Inserting from equations 1.26 and 1.27 yields equation 1.29 which can be simplified according to integral factoring and addition rules to yield an addition of three separate defined integrals.

$$\begin{aligned} R(t) &= I_0 \int_0^\infty e^{\frac{-t_i}{tau}} \cdot [A + B\cos(\omega t - \omega t_i)]\mathrm{d}t_i \\ &= I_0[A \int_0^\infty e^{\frac{-t_i}{tau}}\mathrm{d}t_i + b\cos\omega t \int_0^\infty \cos\omega t_i \cdot e^{\frac{-t_i}{tau}}\mathrm{d}t_i + b\sin\omega t \int_0^\infty \sin\omega t_i \cdot e^{\frac{-t_i}{tau}}\mathrm{d}t_i] \end{aligned} \tag{1.29}$$

These solutions to the integrals in equation 1.29 are given in equation 1.30. Substituting these results into the original equation and factoring out τ and b yields equation 1.31.

$$\begin{aligned} \int_0^\infty e^{\frac{-t_i}{tau}}\mathrm{d}t_i &= \tau \\ \int_0^\infty \cos\omega t_i \cdot e^{\frac{-t_i}{tau}}\mathrm{d}t_i &= \frac{\tau}{\omega^2\tau^2 + 1} \\ \int_0^\infty \sin\omega t_i \cdot e^{\frac{-t_i}{tau}}\mathrm{d}t_i] &= \frac{\omega\tau^2}{\omega^2\tau^2 + 1} \end{aligned} \tag{1.30}$$

$$R(t) = I_0\tau[a + b(\frac{\cos\omega t + \omega\tau\sin\omega t}{\omega^2\tau^2 + 1})] \tag{1.31}$$

Comparing equation 1.31 to the function $R(t)$ defined in equation 1.26 shows a lot of similarities and it stands to reason that by choosing appropriate values for A, B and Φ, $R(t)$ from equation 1.26 can be rearranged to yield equation 1.31. As a first step the rules of trigonometric addition can be used to expand the expression $cos(\omega t - \Phi)$, and by substitution of $\tan\Phi = \sin\Phi/\cos\Phi$:

$$\begin{aligned} \cos(\omega t - \Phi) &= \cos\omega t \cdot \cos\Phi + \sin\omega t \cdot \sin\Phi \\ &= (\cos\omega t + \tan\Phi \cdot \sin\omega t) \cdot \cos\Phi \end{aligned} \tag{1.32}$$

If one is further aware of the trigonometric identity of $\cos\Phi = (\tan^2\Phi + 1)^{-\frac{1}{2}}$ then equation 1.32 may be substituted to yield the final form:

$$\cos(\omega t - \Phi) = \frac{\cos\omega t + \tan\Phi \cdot \sin\omega t}{\sqrt{tan^2\Phi + 1}} \tag{1.33}$$

Thus, finally equation 1.31 can be substituted and rearranged (by factoring out $(\tan^2\Phi+1)^{-\frac{1}{2}}$) to yield the result:

$$B \cdot \frac{\cos\omega t + \tan\Phi \cdot \sin\omega t}{\sqrt{tan^2\Phi + 1}} = \frac{b}{\sqrt{\omega^2\tau^2 + 1}} \cdot (\frac{\cos\omega t + \omega\tau\sin\omega t}{\sqrt{\omega^2\tau^2 + 1}}) \tag{1.34}$$

and therefore:

$$\begin{aligned} \tan\Phi &= \omega\tau \\ \tau &= \frac{\tan\Phi}{2\Pi f} \end{aligned} \tag{1.35}$$

Equation 1.35 is the important basis of phase fluorometric measurements, though one has to be aware that the above described solution is only valid for mono exponential behavior. The same result can, of course, be obtained by measuring the demodulation, and indeed if the results of these two methods diverge that is a strong indication for multi-exponential behavior (or instrument problems).

Time Domain

The second approach to lifetime determination is measuring the lifetime directly in the time domain. Unlike frequency measurements, the dye is excited by a pulse or steady irradiation and the decay curve is captured in real-time after the excitation source has been switched off. The acquired decay curve can then be fitted directly to obtain the indicator dye's lifetime. Depending on the lifetime of the dye, this method can be very straight-forward for indicators with long living luminescence, or rather complex for indicators with short lived luminescence that require specialized time-resolved detection methods and may require deconvolution of the excitation pulse decay. Generally time-domain measurements are preferable to frequency domain measurements as they are truly unaffected by excitation light changes and, because the actual decay curve is captured, multi-exponential behavior is easily detected and can still be fitted quite well. Still, frequency domain measurements are often preferred because the method is much easier to implement. A common experimental setup for time-domain measurements

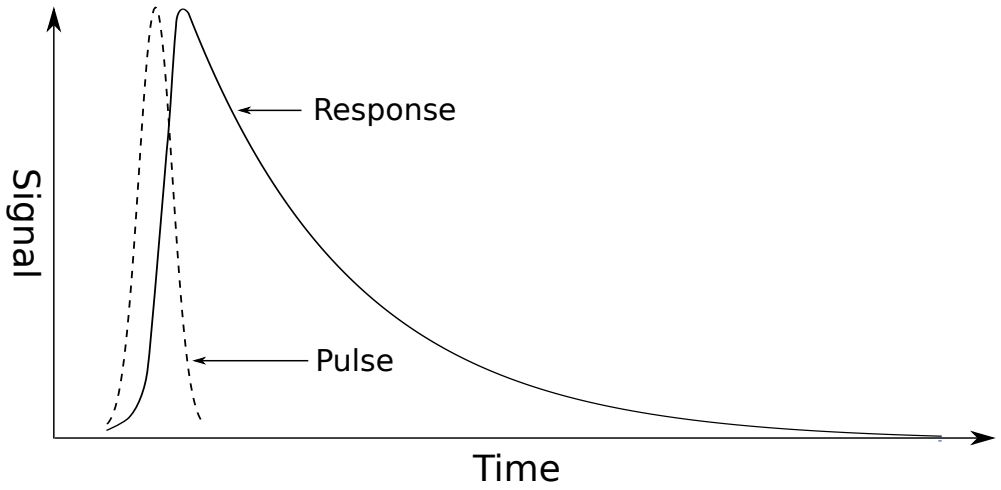

Figure 1.5: Diagram of the principle of time domain measurements, an excitation light pulse results in a response of the sensor system that can be directly fitted with single or multi-exponential decay functions after deconvolution.

is single-photon-counting (SPC). In an SPC setup the delay between a start and and a stop trigger is measured by a time-to-amplitude converter (TAC). The stop signal triggers as soon as a photon is detected at the photo-multiplier tube. The experiment is repeated many times until a probability distribution of the various detection times leads to the desired response

decay curve as pictured in figure 1.5. This curve may then be fitted by different algorithms, for example with least squares optimization. Another possible approach is the so called rapid lifetime determination, in which the lifetime is calculated by equation 1.36.

$$\tau = \frac{-\Delta t}{\ln(D_1/D_0)} \tag{1.36}$$

where D_0 and D_1 are equally spaced areas over which the signal is integrated, and their starting point is separated by Δt. This approach is, as the name suggests, very fast because it does not rely on an optimization algorithm to find a solution and it is widely used in lifetime imaging applications because integrating signal intensity over two defined windows is easy with gated cameras. For single exponential decay the agreement with the least squares method is quite good,[12] but for more complex decays the obtained value will deviate from the true value. In most cases it is still proportional to the lifetime, though, and can therefore be used for calibrations as well.

1.4 State-of-the-art Luminescent Oxygen Sensor Probes and Matrices

Oxygen sensing materials for trace and ultra trace regions are not very numerous, but for higher oxygen concentrations a multitude of different probes and matrix combinations are established. This section gives a short overview over the most important categories.

1.4.1 Organic Probes

Polycyclic aromatic hydrocarbons generally exhibit strong fluorescence, though the exact luminescent properties also largely depend on substituents. Some aromatic compounds exhibit luminescence lifetimes of up to 200 ns, which makes them suitable for sensing oxygen through collisional quenching.[13] Especially perylene, pyrene and their derivates are common examples of organic oxygen sensing probes. A group of organic oxygen probes relevant to trace sensing are fullerenes, specifically fullerene C_{70} which exhibits strong e-type delayed fluorescence with a lifetime of about 25 ms at room temperature. Though quantum yields are rather low, the comparably long lifetime and the large size and resulting high collision probability make fullerene C_{70} well suited for use in trace oxygen sensors.[14]

1.4.2 Metal Ligand Complexes

Metal ligand complexes are commonly employed in oxygen sensing because of their generally high photo stability, large Stokes shift and their usually long luminescence lifetimes. The spectral properties of these complexes can be tuned by changing substituents on the ligands or by partially exchanging ligands. Excitation and emission wavelengths as well as lifetime and solubility might be tuned in this way to suit specific needs, substituents that allow covalent grafting to a matrix material are also often employed. It was found that complexes of e.g. ruthenium(II), iridium(III), osmium(II), rhenium(I) and some lanthanides are strongly quenched by oxygen. These transition metal complexes can undergo metal-ligand charge transfer upon photo-excitation and form slow decaying triplet or higher multiplicity states that are readily quenched by oxygen. Ruthenium complexes are well investigated and form the largest group of oxygen sensing probes. The most common ones are readily available commercially, such as Ru(bipyridine)$_3$, Ru(1,10-phenanthroline)$_3$ and Ru(4,7 -diphenyl-1,10 -phenanthroline)$_3$.[13] Among iridium based probes iridium coumarin complexes are of special interest. They show excellent molar absorption coefficients, lifetimes comparable to Ru(II) complexes and exceptional brightness which makes them useful to applications where high signal to noise ratios (SNR)s are required.[15]

Porphyrins

Oxygen sensors that use porphyrins – especially metalloporphyrins – as probes are also very common and well investigated. Platinum(II), palladium(II) and zinc(II) metallated porphyrins all show strong quenching by molecular oxygen. Most porphyrins have excellent molar absorption coefficients and show two distinct bands in which absorption is the highest. The so-called Soret band, usually in the blue or UV region, exhibits very high absorption coefficients of up to 300 000 M^{-1} cm^{-1}, and the second, weaker band (the Q-Band) still shows absorption coefficients that are usually in the range of 10 000 M^{-1} cm^{-1} to 10 000 M^{-1} cm^{-1} with the exception of benzoporphyrins which feature much higher absorption coefficients in the Q-Band.

Metalloporphyrins generally have long luminescence lifetimes. Pt(II) complexes usually have lifetimes in the range of tens of microseconds and Pd(II) complexes generally posses lifetimes that are about a magnitude longer than their platinum counterparts.[16] Because of their high molar absorption coefficients and long lifetimes Pd(II)porphyrins are excellent candidates for trace sensing applications.[17] A further distinction has to be made between regular porphyrins and benzoporphyrins. While porphyrins mostly emit light in the visible range, the emission of benzoporphyrins is commonly shifted into the NIR region. This can lead to advantageous SNRs because interference from the visible range can be largely removed by choosing appropriate optical filters. Also, strong absorption in the corresponding region allows excitation with red light which has the benefit of reducing background fluorescence as most fluorescent molecules in natural samples are excited in the UV or blue region. Benzoporphyrins also generally exhibit superior chemical and photo-stability.

1.4.3 Some Common Matrix Materials

As mentioned earlier the matrix material – though often not as carefully optimized – is just as important to an oxygen sensing material as the probe is. Choosing the appropriate matrix offers an easy way to tune a sensors sensitivity, and a matrix' compatibility with the probe ensures low leaching and therefore low drift and high stability of the sensor. A chemically stable matrix is usually a requirement for sensors that exhibit robust calibrations and long shelf life. Among the most popular matrices is polystyrene which has good oxygen permeability (8.8×10^{-16} mol m^{-1} s^{-1} Pa^{-1}) and is often cited for its chemical stability and wide compatibility with various probes. In conjunction with sensitive probes it is a good starting point for trace sensors, although its inherent oxygen consumption limits its capabilities. Other polymer choices with moderate or good permeabilities are poly(methyl methacrylate) (PMMA, $P = 0.53 \times 10^{-16}$ mol m^{-1} s^{-1} Pa^{-1}) and ethylcellulose (EC, $P = 50.94 \times 10^{-16}$ mol m^{-1} s^{-1} Pa^{-1}). Especially EC has already been applied to create trace sensors.[18].[13] Some other matrices like poly(vinylidene dichloride) (PVDC, $P = 0.018 \times 10^{-16}$ mol m^{-1} s^{-1} Pa^{-1}) and polyacrylonitrile (PAN, $P = 0.0007 \times 10^{-16}$ mol m^{-1} s^{-1} Pa^{-1}) are usually applied as oxygen barrier material, in conjunction with very long decaying probes like the ones introduced in chapter 2 they can, however, also be used for oxygen sensor materials with moderate sensitivity. Suitable matrix materials are not limited organic polymers though, silica based matrices like poly(phenylsilsesquioxane) (PPSQ) and other ormosils offer very good permeabilites that are usually 5 to 10 times higher than that of polystyrene. They are also very chemically stable, but processing is often a challenge. In addition to these materials there exist a number of polymers that have high intrinsic free volume and therefore high permeability. Examples of such usually perfluorinated polymers are Hyflon AD ($P \approx 170 \times 10^{-16}$ mol m^{-1} s^{-1} Pa^{-1}) and Teflon AF($P \approx 1\ 200 \times 10^{-16}$ mol m^{-1} s^{-1} Pa^{-1}). In addition to their high permeabilities they are chemically inert due to their high degree of fluorination. This combination makes them ideally suitable for trace oxygen sensing. However, not all probes are readily soluble in these types of polymers and may require synthetic modification for optimal compatibility.

1.5 References

[1] Peter W Atkins and Julio de Paula. *Physikalische Chemie*. 4th ed. WILEY-VCH Verlag, Jan. 2008.

[2] Bernard Valeur. *Molecular Fluorescence*. 1st ed. Principles and Applications. Wiley-VCH, Nov. 2001.

[3] Daniel Aigner, Stefan A Freunberger, Martin Wilkening, Robert Saf, Sergey M Borisov, and Ingo Klimant. "Enhancing photoinduced electron transfer efficiency of fluorescent pH-probes with halogenated phenols." In: *Analytical Chemistry* 86.18 (Sept. 2014), pp. 9293–9300.

[4] Otto Stern and Max Volmer. "Über die Abklingzeit der Fluoreszenz". In: *Physikalische Zeitschrift* 20 (Sept. 1919), pp. 183–188.

[5] ER Carraway and JN Demas. "Photophysics and Photochemistry of Oxygen Sensors Based on Luminescent Transition-Metal Complexes". In: *Analytical Chemistry* 63 (1991), pp. 337–342.

[6] J N Demas, B A DeGraff, and Wenying Xu. "Modeling of Luminescence Quenching-Based Sensors: Comparison of Multisite and Nonlinear Gas Solubility Models". In: *Analytical Chemistry* 67.8 (Apr. 1995), pp. 1377–1380.

[7] A Hulanicki, S Glab, and F Ingman. "Chemical sensors: definitions and classification". In: *Pure and Applied Chemistry* 63.9 (1991).

[8] Otto S Wolfbeis. "Editorial: Probes, Sensors, and Labels: Why is Real Progress Slow?" In: *Angewandte Chemie International Edition* 52.38 (Aug. 2013), pp. 9864–9865.

[9] Christoph Larndorfer, Sergey M Borisov, Philipp Lehner, and Ingo Klimant. "The effect of high light intensities on luminescence lifetime based oxygen sensing". In: *Analyst* (2014), pp. –.

[10] J Crank and G S Park. *Diffusion in Polymers*. Ed. by P Neogi. Marcel Dekker Inc., Feb. 1996.

[11] Christian Huber, Ingo Klimant, Christian Krause, and Otto S Wolfbeis. "Dual Lifetime Referencing as Applied to a Chloride Optical Sensor". In: *Analytical Chemistry* 73.9 (May 2001), pp. 2097–2103.

[12] R M Ballew and J N Demas. "Error analysis of the rapid lifetime determination method for single exponential decays with a non-zero baseline". In: *Analytica Chimica Acta* 245 (Jan. 1991), pp. 121–127.

[13] Xu-Dong Wang and Otto S Wolfbeis. "Optical methods for sensing and imaging oxygen: materials, spectroscopies and applications." In: *Chemical Society Reviews* 43.10 (May 2014), pp. 3666–3761.

[14] Stefan Nagl, Carlos Baleizão, Sergey M Borisov, Michael Schäferling, Mário N Berberan-Santos, and Otto S Wolfbeis. "Optical sensing and imaging of trace oxygen with record response." In: *Angewandte Chemie (International ed. in English)* 46.13 (2007), pp. 2317–2319.

[15] Sergey M Borisov and Ingo Klimant. "Ultrabright Oxygen Optodes Based on Cyclometalated Iridium(III) Coumarin Complexes". In: *Analytical Chemistry* 79 (2007), pp. 7501–7509.

[16] Y Amao and T Miyashita. "Novel optical oxygen sensing material: platinum octaethylporphyrin immobilized in a copolymer film of isobutyl methacrylate and tetrafluoropropyl methacrylate". In: *Reactive and Functional Polymers* 47 (2001), pp. 49–54.

[17] M Trinkel. “Optical sensors for trace oxygen analysis”. PhD thesis. Karl Franzens University Graz: University of Graz, Jan. 1998.

[18] Sven Kochmann, Carlos Baleizão, Mário N Berberan-Santos, and Otto S Wolfbeis. “Sensing and imaging of oxygen with parts per billion limits of detection and based on the quenching of the delayed fluorescence of (13)C70 fullerene in polymer hosts.” In: *Analytical Chemistry* 85.3 (Feb. 2013), pp. 1300–1304.

2 Ultra-sensitive optical oxygen sensors for characterization of nearly anoxic systems

Philipp Lehner[1], Christoph Staudinger[1], Sergey M. Borisov[1] and Ingo Klimant[1]

[1]Institute of Analytical Chemistry and Food Chemistry, Graz University of Technology, NAWI Graz, Stremayrgasse 9, 8010 Graz, Austria.

Corresponding Author:
Sergery M. Borisov
tel: +43 316 873 32516
email: sergey.borisov@tugraz.at

Published in: **Nature Communications**
Recieved: 27 Feb. 2014
Accepted: 19 Jun. 2014
Published: 21 Jul. 2014
doi: 10.1038/ncomms5460

2.1 Abstract

Oxygen quantification in trace amounts is essential in many fields of science and technology. Optical oxygen sensors proved invaluable tools for oxygen measurements in a broad concentration range, but until now neither optical nor electrochemical oxygen sensors were able to quantify oxygen in the sub-nanomolar concentration range. Herein we present new optical oxygen-sensing materials with unmatched sensitivity. They rely on the combination of ultra-long decaying (several 100 ms lifetime) phosphorescent boron- and aluminium- chelates, and highly oxygen-permeable and chemically stable perfluorinated polymers. The sensitivity of the new sensors is improved up to 20-fold compared with state-of-the-art analogues. The limits of detection are as low as 5 ppbv in gas phase under atmospheric pressure or 7 pM in solution. The sensors enable completely new applications for monitoring of oxygen in previously inaccessible concentration ranges.

2.2 Introduction

Oxygen undoubtedly belongs to the most important analytes on earth. Traditionally, most oxygen sensors were designed for the physiological range. However, numerous applications require monitoring of oxygen at significantly lower concentrations, for example, corrosion protection[1], surface treatment[2], the semiconductor industry[3] and biological research. For instance, it was demonstrated that bacteria can show respiration and potentially aerobic growth far below the

Pasteur point (10mM dissolved oxygen (DO))[4, 5, 6]. Recently, sensors that quantify DO in concentration ranges of 100 nM and below have gained special interest as biologists explore aerobic life in areas very close to anoxic conditions[7]. Unfortunately, few sensors are capable to resolve at such low concentration[8, 9], and measurements below 0.5 nM are currently impossible. Optical sensors proved to be indispensable tools for oxygen quantification that have mostly replaced the more conventional Clark electrode. Their advantages include minimal invasiveness, simplicity, suitability for miniaturization, versatility of formats (planar optodes, fibre-optic sensors, micro- and nanoparticles, paints and so on) and suitability for imaging of oxygen distribution on surfaces or in volume. Moreover, optical oxygen sensors are tuneable over a wide range of concentrations. Optical oxygen sensors rely on quenching of a phosphorescent indicator by the analyte. Both the nature of the indicator and the matrix (which acts as a solvent and support for the dye and as a permeation-selective barrier) are of great importance since the sensitivity of an oxygen sensor is roughly proportional to the luminescence decay time of the indicator and to the oxygen permeability of the matrix[10]. State-of-the-art indicators are dominated by phosphorescent complexes with platinum group metals that possess decay times varying from microseconds to a few milliseconds[11, 12, 13, 14]. Dyes with significantly longer decay times are extremely rare and are so far limited to fullerenes[9, 15] (which have rather low luminescence brightness at ambient temperatures) and some phosphorescent BF_2-chelates[16, 17, 18, 19]. Both classes are not inherently compatible with highly oxygen- permeable matrices (for example, silicone and Teflon AF). Hence, the sensors based on these indicators and other matrices (for example, ethylcellulose and polystyrene (PS))[9] are not drastically more sensitive than sensors relying on more conventional dyes (for example, Pd(II) porphyrins) immobilized in highly oxygen-permeable polymers[20]. Herein, we present a new type of oxygen-sensing materials that show sensitivities well beyond state-of-the-art trace oxygen sensors. They rely on new blue light-excitable BF_2 and Al(III) chelates featuring ultra-long room temperature phosphorescence. The chelates are modified with perfluoroalkyl chains to ensure compatibility with highly oxygen-permeable and chemically inert perfluorinated polymers. The resulted ultra-sensitive sensors are ideally suitable for characterization of nearly anoxic systems.

2.3 Results

2.3.1 Photophysical properties

The new-sensing materials rely on novel difluoroboron- and aluminium chelates of 9-hydroxyphenalenone (HPhN; Fig. 2.1)[21] and its benzannelated derivative 6-hydroxybenz[de]anthracene-7-on (HBAN; 2.1)[22]. In contrast to the common fluorescent difluoroboron chelates of dipyrromethenes and tetraarylazadipyrromethenes[23, 24], the new difluoroboron-based dyes simultaneously show prompt fluorescence, delayed fluorescence and phosphorescence when embedded in polymers (2.2a, b). Room temperature phosphorescence is an extremely rare phenomenon for compounds with no heavy atoms. It was previously observed for BF_2-chelates of aliphatic β-diketones coupled to polylactic acid[16, 17] or physically entrapped in the same polymer[19]. This work and our results indicate that phosphorescence of aliphatic and aromatic BF_2-chelates of β-diketones appears to be a general phenomenon. As can be seen, the extension of p-conjugation in HPhN derivatives results in bathochromic shifts of absorption, fluorescence and phosphorescence compared with the reported aliphatic diketonate chelates. In fact, the absorption of the HPhN and HBAN difluoroboron chelates peaks at 450 and 459 nm, respectively, ($\epsilon_{450} = 10.2 \times 10^3$ M^{-1} cm^{-1} and $\epsilon_{459} = 12.9 \times 10^3$ M^{-1} cm^{-1}). This enables excitation with bright blue 450 and 470 nm LEDs and with conventional white light sources. Temperature affects the quantum yields of

all three emissions. As expected, the phosphorescence QYs decrease at higher temperature and the delayed fluorescence becomes stronger (Fig. 2.2b). Since both phosphorescence and delayed fluorescence possess virtually identical decay times (Fig. 2.12) and are quenched by oxygen to the same extent, their ratio can be used to eliminate temperature crosstalk. Importantly, prompt fluorescence is suitable for referencing purposes, as it is not affected by oxygen. However, the most outstanding property of these dyes is their extraordinary long phosphorescence decay time of 360 and 730 ms for BF_2(HPhN) and BF_2(HBAN), respectively (in PS at 20 °C), which, to the best of our knowledge, are the longest decay times recorded for visible light-excitable dyes. This is likely due to the rigid aromatic backbone structure of the dyes. Despite those long decay times, the phosphorescence quantum yields are fairly high (Table 2.1 and Table 2.2).

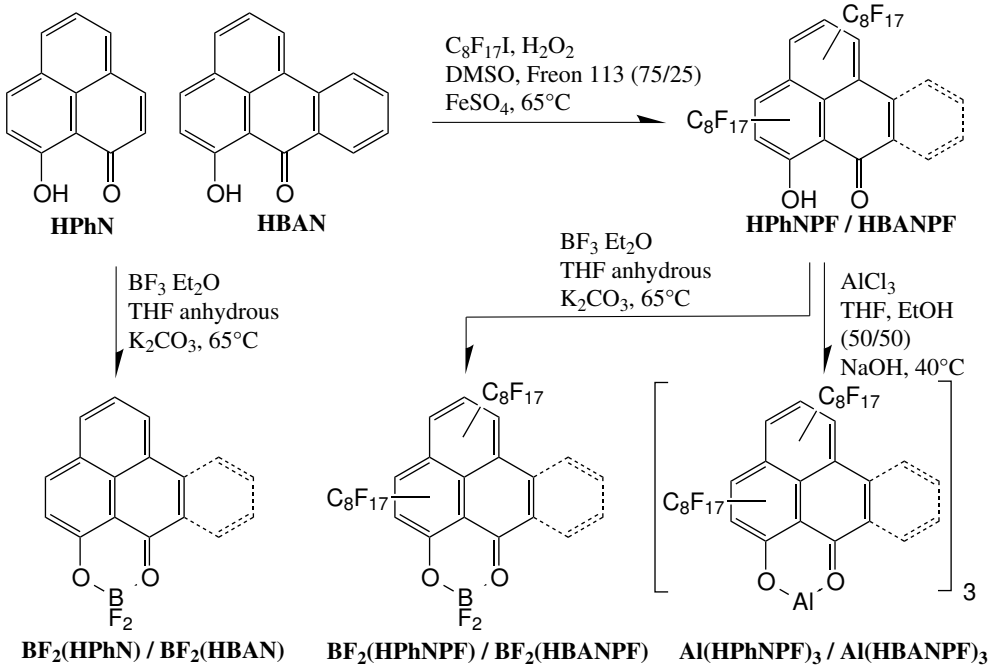

Figure 2.1: Synthesis of the borondifluoride chelates and aluminium complexes.

2.3.2 Ultra-sensitive oxygen-sensing materials

Owing to the exceptionally long lifetimes of these chelates, resulting sensing materials are expected to have sensitivities orders of magnitude above those based on conventional sensing chemistries. Indeed, sensors composed of difluoroboron chelates in PS show very high sensitivities, even though PS has only moderate oxygen permeability ($P \approx 8.8 \times 10^{-16}$ mol m^{-1} s^{-1} Pa^{-1})[25] K_{SV} for BF_2(HPhN)- and BF_2(HBAN)-based sensors was 60×10^{-3} and 120×10^{-3} ppmv^{-1}, respectively, (Fig. 2.3), which makes them suitable for monitoring sub-nanomolar DO concentrations. The limit of detection for the BF_2(HBAN)-based material, assuming a resolution of 0.5 % I_0, is in fact 45 ppbv (gas phase) or 60 pM (DO). Both sensing materials surpass the sensitivity of nearly all previously published sensors.

Still, highly permeable matrices such as Hyflon, Teflon AF and poly(- trimethylsilylpropyne) can potentially be used to create even more sensitive materials. Poly(trimethylsilylpropyne) has the highest known oxygen permeability ($P \approx 23{,}000 \times 10^{-16}$ mol m^{-1} s^{-1} Pa^{-1})[27] but was not considered because of poor chemical stability and possession of double bonds that are prone to

Sensor material	Abs. max. (nm)[a]	Em. max. (nm)	Φ (%)[b]	τ_0 (ms)	K_{SV}(10^{-3}) ppmv^{-1}	References
Pd-TPFPP in silica gel	410	670	ND	0.978	7	[26]
C_{70} in ethylcellulose	470	710	1[c]	20-25	75	[15]
$^{13}C_{70}$ in ethylcellulose[d]	470	710	ND	28	48	[9]
BF_2(HPhN) in polystyrene	450	552	4.6	360	60	This work
BF_2(HBAN) in polystyrene	459	565	9.1	730	120	This work
Al(HPhNPF)$_3$ in Hyflon AD 60	465	570	ND	270	420	This work
Al(HBANPF)$_3$ in Hyflon AD 60	459	565	ND	400	590	This work
Al(HPhNPF)$_3$ in Teflon AF 1600	465	570	5.4	250	920	This work
Al(HBANPF)$_3$ in Teflon AF 1600	459	575	3.2	350	960	This work

Table 2.1: Photophysical and sensing properties of trace oxygen sensors at 20 °C. HBAN, 6-hydroxybenz[de]anthracene-7-on; HPhN, 9-hydroxyphenalenone; max., maximum; ND, not determined; Pd-TPFPP, Pd(II)-5,10,15,20-meso-tetrakis-(2,3,4,5,6-pentafluorphenyl)-porphyrin. [a]The maximum for the longest wavelength absorption. [b]Phosphorescence quantum yields. [c]Quantum yield of the delayed fluorescence. [d]At 25 °C.

oxidation and thus analyte consumption[28, 29]. Hyflon and Teflon AF are amorphous, glassy, perfluorinated copolymers that combine high free volume and unmatched chemical stability. In this work we used Hyflon AD 60 (P ≈ 170 × 10^{-16} mol m^{-1} s^{-1} Pa^{-1})[30] and Teflon AF 1600 (P ≈ 1,200 × 10^{-16} mol m^{-1} s^{-1} Pa^{-1})[31]. Unfortunately, most conventional dyes, as well as BF_2(HPhN) and BF_2(HBAN), show extremely poor solubility in these matrices and aggregate readily. We failed to obtain usable sensors based on the BF_2-chelates due to poor luminescence in perfluorinated polymers at any relevant concentration (0.01–1 *wt*% of the dyes in respect to the polymer).

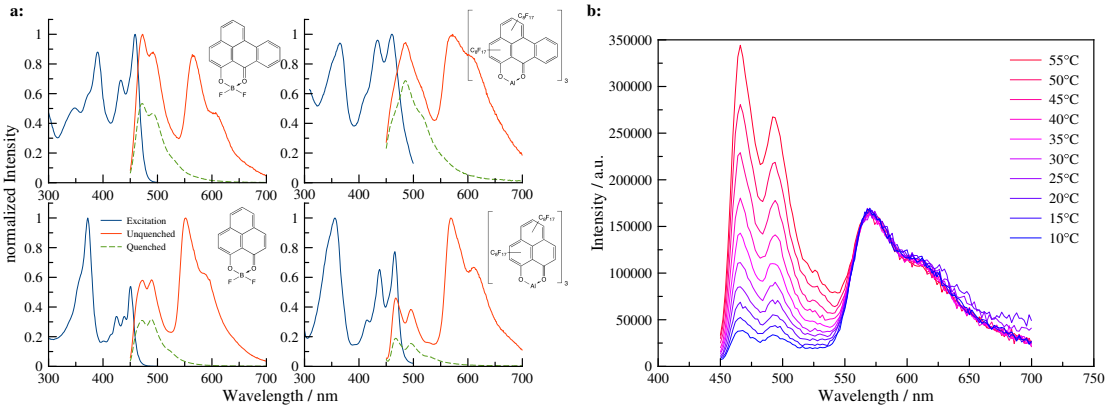

Figure 2.2: Spectral properties of the oxygen indicators. (a) Excitation and emission spectra of HBAN and HPhN difluoroboron chelates in PS and aluminium complexes in Teflon AF 1600. (b) Temperature-dependent emission spectra of Al(HPhNPF)3 in Hyflon AD 60 under deoxygenated conditions acquired with a delay of 0.5 ms after excitation.

Therefore, in order to render the indicators soluble in Hyflon and Teflon AF, HPhN and

HBAN were perfluoroalkylated with perfluorooctyl iodide (Fig. 2.1). The resulting ligands 9-hydroxy-4,7-diperfluorooctyl-1H-phenalenone (HPhNPF) and 6-hydroxy-1,4-diperfluorooctyl-7H-benzo[de]anthracen-7-one (HBANPF) bear two C_8F_{17} chains each, although in the case of HBANPF there is some impurity of tri-substituted ligand (Figs 2.21 and 2.22). As indicated by nuclear Overhauser effect spectroscopy (NOESY) and hetero-nuclear multiple-bond correlation spectroscopy (HMBC) spectra (Figs 2.31 and 2.32), a single isomer appears to be the predominant product for HPhNPF (Fig. 2.30). The ^{1}H nuclear magnetic resonance (NMR) and correlation spectroscopy (COSY) spectra for HBANPF (Figs 2.18 and 2.19) showed no significant substitution in the benzannelated ring. Complete separation of the tri-substituted derivate is very challenging owing to the very high similarity; however, both tri- and disubstituted derivates are expected to have very similar photophysical properties und solubility. It was found that perfluoroalkylated derivates of the difluoroboron chelates have low chemical stability and dissociate in solution in presence of traces of water (Fig. 2.9). Hence, aluminium complexes (Al(HPhNPF)$_3$ and Al(HBANPF)$_3$; Fig. 2.1) were prepared in an attempt to obtain more stable indicators. Indeed, dissociation was not observed for the aluminium chelates and they dissolve readily in fluorinated solvents (octafluorotoluene and perfluorodecalin) and also in Hyflon and Teflon AF. Owing to the octahedral structure of the Al(III) complexes and unsymmetric substitution pattern of the ligands four sterioisomers are possible, which are inseparable because of their extreme similarity. The photophysical properties of the isomers are expected to be virtually identical. Similar to the BF_2-chelates, the Al(III) complexes possess prompt fluorescence, delayed fluorescence and phosphorescence (Fig. 2.2). The phosphorescence decay times (250 ms for Al(HPhNPF)$_3$ and 350 ms for Al(HBANPF)$_3$ at 20 °C in Teflon AF 1600) are slightly shorter than those of the BF_2-chelates, and the Al(III) complexes possess higher molar absorption coefficients ($\epsilon_{465} = 23.2 \times 10^3$ M^{-1} cm^{-1} and $\epsilon_{459} = 27.1 \times 10^3$ M^{-1} cm^{-1} for Al(HPhNPF)$_3$ and Al(HBANPF)$_3$, respectively). The oxygen- sensing materials based on these Al(III) complexes embedded in Hyflon show extremely high sensitivities (Fig. 2.3b). In fact, the K_{SV} values are as high as 590×10^{-3} ppmv^{-1} (for Al(HBANPF)$_3$, Table 2.1) and the sensors resolve up to 10 ppbv or 12 pM (DO). They are about one order of magnitude more sensitive than the state-of-the-art sensors based on fullerenes (Table 2.1)citeNagl:2007wa. The sensors based on Teflon AF 1600 show a twofold increase in sensitivity compared with the Hyflon-based ones. Al(HBANPF)$_3$ in Teflon AF 1600 is the most sensitive sensor material presented, with a K_{SV} of 960×10^{-3} ppmv^{-1} and a detection limit of 5 ppbv or 7 pM (DO). Potentially, even more sensitive sensor materials based on Teflon AF 2400 ($P \approx 3000 \times 10^{-16}$ mol m^{-1} s^{-1} Pa^{-1})[31] showed signs of aggregation and were therefore not further investigated. Importantly, the Stern–Volmer plots for the phosphorescence decay time are similar to those obtained for the intensity measurements (Figs 2.3 and 2.13) so both read-out schemes (ratiometric intensity or decay time) can be used. It should be mentioned that sensitivities are so high that obtaining reliable calibrations becomes rather challenging. Even high-purity nitrogen contains oxygen impurities in the low ppmv range, hence all aluminium complex-based sensor materials were calibrated using a standard addition method described in the experimental section.

Temperature is known to affect the response of all optical sensors; thus the temperature dependence of the new sensors was investigated (Supplementary Fig. 2.11). In contrast to most oxygen sensors, the Stern–Volmer constants K_{SV} decrease at higher temperature. This can be explained by a relatively strong effect of temperature on the phosphorescence decay time τ_0 (280, 250 and 220 ms at 5, 20 and 35 °C, respectively, for Al(HPhNPF)3 in Hyflon AD 60) and a negligible influence on the bimolecular quenching constant kq (1.65, 1.65 and 1.69 ppmv^{-1} ms^{-1} at 5, 20 and 35 °C, respectively). This indicates that in contrast to most polymers, the oxygen permeability of Hyflon AD 60 appears to be barely affected by temperature.

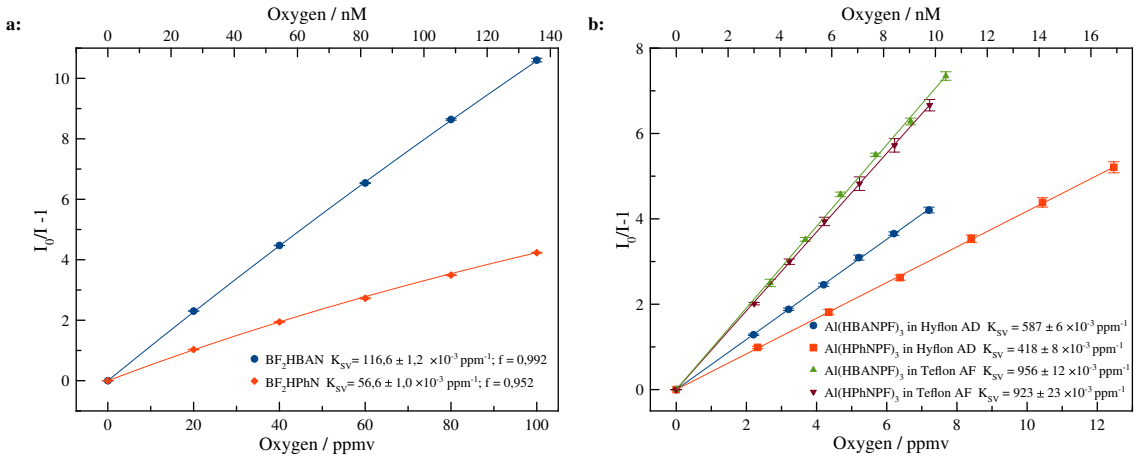

Figure 2.3: Oxygen sensitivity of the trace sensors at 20 °C. (a) Stern–Volmer plots for BF_2HBAN and BF_2HPhN in PS. (b) Stern–Volmer plots for the aluminium complexes. (c) Photographic images of the Al(HPhNPF)$_3$/Hyflon AD 60 sensor under illumination with a 366 nm line of a ultraviolet lamp. Bluish prompt fluorescence remains constant, and the intense yellow phosphorescence slowly appears for the areas covered with anaerobic sodium sulphite solution (5 *wt*%, containing traces of Co^{2+} as a catalyst).

2.3.3 Application example

To illustrate potential applications of these trace oxygen sensors, the kinetics of oxygen consumption during enzymatic oxidation of glucose was monitored as it approached anoxic conditions (Fig. 2.4). Aqueous solutions of glucose oxidase, catalase and glucose were combined in a closed stirred vessel, and the oxygen concentration was monitored with a set of sensors with overlapping ranges. In addition to the Al(HPhNPF)$_3$/Hyflon sensor, two other oxygen sensors were used: a commercially available trace sensor from Pyroscience GmbH and a sensor based on Pd(II)-5,10,15,20-meso-tetrakis-(2,3,4,5,6-pentafluorphenyl)-porphyrin in Hyflon, which is comparable in sensitivity to previously published sensors[26]. Figure 2.4 shows the high resolution of the new sensors in the ultra-trace region, whereas the other sensors fail to resolve oxygen concentrations below 1nM. The insert shows a mono-exponential fit of the ultra-trace region corresponding to purely diffusion-controlled depletion of oxygen.

Precise quantification of oxygen impurity in inert gases represents another potential application of the new sensors. The Al(HPhNPF)$_3$/Hyflon sensor was used to quantify oxygen content in high-purity gases obtained from Linde (Austria). For example, two samples of compressed nitrogen 5.0 (99.999 %, $<$ 10 ppmv O_2) contained 3.7 and 2.5 ppmv O_2, whereas compressed nitrogen 6.0 (99.9999 %, $<$ 1 ppmv O_2) contained 0.52 ppmv O_2, which is within the specifications of the gas manufacturer.

2.4 Discussion

We prepared new optical oxygen-sensing materials with unmatched sensitivity. The most sensitive shows an 20-fold increase in sensitivity compared with state-of-the-art materials. Such extraordinary high-sensitivity results from the combination of extremely long phosphorescence decay times of the indicators and very high oxygen permeability of the matrix. Novel heavy metal-free chelates of rigid aromatic analogues of β-diketones represent unique indicators for

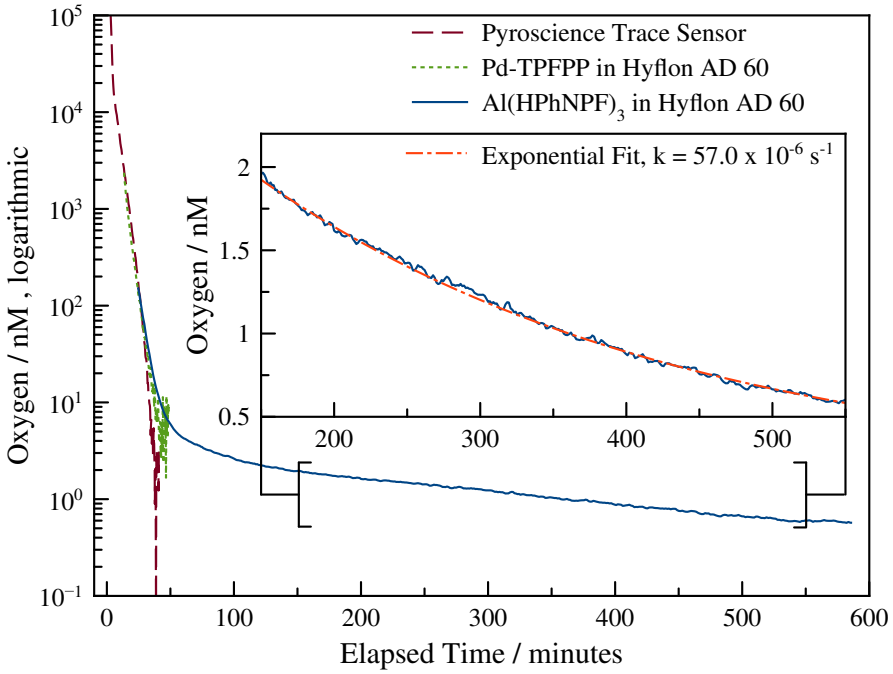

Figure 2.4: Real-time monitoring of oxygen levels during enzymatic oxygen consumption. Three trace sensors with overlapping ranges are used to monitor oxidation of glucose catalysed by glucose oxidase. A running average of 3 data points was used for all sensors. Whereas, the reference sensors fail to resolve below 2–10 nM; the new ultra-trace sensor can reliably monitor oxygen even at much lower concentrations (insert).

oxygen sensors that feature absorption in the blue part of the electromagnetic spectrum, very long-decaying room temperature phosphorescence, good molar absorption coefficients and adequate quantum yields. The unique dual emission of the chelates (delayed fluorescence and phosphorescence) can be used for intrinsic temperature compensation. These sensors enable completely new applications for monitoring of oxygen in previously inaccessible concentration regions, and are likely to become invaluable tools in various fields of science and technology.

2.5 Methods

2.5.1 Materials

Nitrogen (99.9999 % purity) and test gases (1,000 ppmv O_2, rest N_2; and 20 ppmv O_2, rest N_2) were obtained from Linde Gas (Austria; www.linde.at), PS (molecular weight (MW) 250,000) and hydrogen peroxide (60 %) were obtained from Fisher Scientific. Perfluorooctyl iodide and aquaphobe CF were bought from ABCR (Germany; www.abcr.de). Teflon AF 1600 was acquired from DuPont (USA; www.dupont.com). Hyflon AD 60 was obtained from Solvay (USA; www.solvay- plastics.com). Sodium sulphite was obtained from Carl Roth (www. carlroth.com). Boron trifluoride diethyl etherate, aluminium oxide (activated, neutral Brockmann I), aluminium(III) chloride, 1,1,2-trichloro-1,2,2- trifluoroethane (Freon 113), glucose oxidase from Aspergillus niger, catalase from bovine liver, anhydrous tetrahydrofuran (THF) and anhydrous dimethylsulphoxide were obtained from Aldrich, iron(II) sulphate heptahydrate from Merck, sodium hydroxide from Lactan (Austria; www.lactan.at) and silicon E4 from Wacker (Germany; www.wacker.de). Acetone and ethanol were acquired from Brenntag (Germany; www.brenntag.de), and other solvents including the deuterated solvents were from VWR (Austria; www.at.vwr.com). HPhN was obtained from Ramidus (Sweden; www.ramidus.se) and HBAN was synthesized according to the literature procedure[22].

2.5.2 Synthesis of the BF_2 chelate of HPhN

An amount of 294 mg (1.5 mmol) of HPhN were dissolved in 50 ml of anhydrous THF and 1.92 g (13.5 mmol) of boron trifluoride diethyl etherate were added. The solution was stirred for 1 h at 65 °C, the solvent was removed under vacuum and the product was purified on an aluminium oxide column using dichloromethane as an eluent. Yield: 300 mg (67 %) of orange crystals. ^{1}H NMR (300 MHz, DMSO-d_6, δ): 8.94 (d, J = 9.1 Hz, 2H), 8.70 (d, J = 7.7 Hz, 2H), 8.03 (t, J = 7.7 Hz, 1H), 7.62 (d, J = 9.1 Hz, 2H). Electron impact- direct injection-time of flight (EI-DI-TOF) (m/z): found 244.0499, calculated 244.0510.

2.5.3 Synthesis of the BF_2 chelate of HBAN

A quantity of 369 mg (1.5 mmol) of HBAN were dissolved in 60 ml of anhydrous THF, and 1.7 g (12 mmol) of boron trifluoride diethyl etherate were added. The solution was stirred at 65 °C for 2 h, and 69 mg (0.5 mmol) of potassium carbonate were added and the stirring was continued for 2 h. The solvent was removed under vacuum and the product was purified on an aluminium oxide column using dichloromethane as an eluent. Yield: 340 mg (77 %) of orange crystals. ^{1}H NMR (300 MHz, DMSO-d_6, δ): 9.26 (d, J = 7.7Hz, 1H), 9.04 (d, J = 8.3Hz, 1H), 8.91 (d, J = 9.2Hz, 1H), 8.69 (d, J = 8.2Hz, 1H), 8.50 (d, J = 7.6Hz, 1H), 8.21 (t, J = 8.3Hz, 1H), 7.97 (dt, J = 21.2, 7.6Hz, 2H), 7.61 (d, J = 9.1 Hz, 1H). EI-DI-TOF (m/z): found 294.0671, calculated 294.0667.

2.5.4 Synthesis of HPhNPF

HPhN (1 g, 5.1 mmol) and $FeSO_4$ 7 H_2O (2.5 g, 9.0 mmol) were dissolved in 120 ml dimethylsulfoxide (DMSO) and 40 ml 1,1,2-trichloro- 1,2,2-trifluoroethane in a 200 ml Schlenk flask. The whole reaction was conducted under argon atmosphere. The solution was heated to 40 °C and perfluorooctyl iodide (3.4 ml, 7.03 g, 12.9 mmol) was added. 60 % H_2O_2 (1.4 ml, 1.67 g, 49 mmol) was added drop-wise over 5 min. The solution turned red and formed black foam. After 30 min, 20 ml 1,1,2-trichloro-1,2,2-trifluoroethane were added and the foam dissolved. One hour after the start of the reaction, a second portion perfluorooctyl iodide (3.4 ml, 7.03 g, 12.9 mmol) was added and 60 % H_2O_2 (1.4 ml, 1.67 g, 49 mmol) was added drop-wise over 5 min. The reaction was continued for 1 h, then the reaction mixture was cooled to room temperature, and the DMSO and 1,1,2-trichloro-1,2,2-trifluoroethane phases were separated. The 1,1,2-trichloro-1,2,2-trifluoroethane phase was washed three times with 36 % hydrochloric acid, once with water, and was dried over Na_2SO_4. After removing the solvent, 9.3 g reddish-brown oil were obtained. The product was purified on a silica-gel column with hexane and toluene as eluents. Yield: 700 mg (13 %). R_F 0.57 with toluene. ^{1}H NMR (300 MHz, $CDCl_3$ + Freon 113 (1:1 v/v), δ): 16.75 (s, 1H), 8.77 (s, 1H), 8.15-8.00 (m, 2H), 7.86 (d, J = 7.9 Hz, 2H), 7.24 (d, J = 9.3 Hz, 2H). DI-EI (*m/z*): 1,031.98 found, 1,031.98 calculated.

2.5.5 Synthesis of HBANPF

HBANPF was prepared using the same procedure as HPhNPF, but with a fivefold excess of perfluorooctyl iodide, and the reaction mixture was stirred stirred for 2 h at 40 °C and then overnight at room temperature. Yield 500 mg (23 %) starting from 0.5 g HBAN. R_F 0.69 with hexane/toluene 2/1. ^{1}H NMR (300 MHz, $CDCl_3$ + Freon 113 (1:1 v/v), δ): 17.01 (s, 1H), 8.94 (s, 1H), 8.79 (d, J = 8.2Hz, 1H), 8.71 (d, J = 7.9Hz, 1H), 8.52 (d, J = 8.3Hz, 1H), 8.03 (d, J = 8.2Hz, 1H), 7.89 (t, J = 7.6Hz, 1H), 7.73 (t, J = 7.5Hz, 1H). DI-EI (*m/z*): 1,081.99 found, 1,081.99 calculated.

2.5.6 Synthesis of the aluminium complex of HPhNPF

HPhNPF (100 mg, 0.097 mmol) was dissolved in 20 ml THF and 20 ml ethanol. NaOH (5.9 mg, 0.15 mmol) and $AlCl_3$ (3.9 mg, 29 μmol) were added and the reaction mixture was stirred for 2.5 h at 40 °C. Then the reaction was stopped the product was extracted with 1,1,2-trichloro-1,2,2-trifluoroethane and the organic phase was washed twice with water. The organic layer was dried over Na_2SO_4 and evaporated in vacuum. Five millilitres THF were added to the raw product and the mixture was placed in the freezer for a few hours. The THF phase was removed and new THF was added. The product was washed seven times following this procedure. Yield: 68.4 mg (74 %). ^{1}H NMR (300 MHz, $CDCl_3$ + Freon 113 (1:1 v/v), δ)): 8.87-8.55 (m, 3H), 8.15-7.84 (m, 6H), 7.84-7.54 (m, 3H), 7.42-7.04 (m, 3H); matrix assisted laser desorption ionisation (MALDI) (*m/z*): $[M + Na]^+$: 3,142.93 found, 3,142.90 calculated.

2.5.7 Synthesis of the aluminium complex of HBANPF

$Al(HBANPF)_3$ was prepared and purified with the same procedure as $Al(HPhNPF)_3$. Yield 19.5 mg (31 %) starting from 80 mg HBANPF. ^{1}H NMR (300 MHz, $CDCl_3$, δ): 9.2-8.2 (m, 9.9H), 8.06 (s, 3H), 8.0-7.2 (m, 7.2H); MALDI (*m/z*): $[MH]^+$: 3,271.11 found, 3,270.96 calculated, [MH(with one additional C_8F_{17}-group)]$^+$: 3,689.02 found, 3,688.92 calculated.

2.5.8 Preparation of the PS-based sensing materials

The sensor 'cocktails' contained the dyes (0.02 *wt*% in respect to the polymer), PS (5 *wt*% in respect to the solvent) and chloroform. These were knife-coated on a glass slide using a 175-μm spacer. The resulting thickness for the dried layer is estimated to be 6 μm.

2.5.9 Preparation of the Hyflon AD 60-based sensing materials

Before coating, the glass slides were rendered hydrophobic with aquaphobe CF. The dyes (0.05 *wt*% in respect to the polymer) and the polymer (6 *wt*% in respect to the solvent) were dissolved in octafluorotoluene. Knife-coating on the glass slides using a 175-μm spacer yielded a layer thickness of $\sim$ 12 μm. After a second coating with a 275-μm spacer and evaporation of the solvent an $\sim$ 31-μm-thick layer was obtained.

2.5.10 Preparation of the Teflon AF 1600-based sensing materials

The sensors were prepared analogously to those based on Hyflon, but a 5 *wt*% solution of the polymer in octafluorotoluene was used. The thickness of the sensing layer was estimated to be 24 μm.

2.5.11 Measurements

^{1}H NMR spectra were recorded on a 300 MHz instrument (Bruker). NOESY and HMBC spectra were acquired on an INOVA 500 MHz NMR spectrometer (Varian). DMSO-d_6 was used for HPhN and HBAN and the respective BF_2 chelates and a mixture of 1,1,2-trichloro-1,2,2-trifluoroethane and $CDCl_3$ (1:1, v/v) was used for perfluorinated ligands and the respective chelates. Electron impact (EI; 70 eV) and MALDI-TOF mass spectra were recorded on a Waters GCT Premier equipped with direct insertion (DI) and on a Micromass TofSpec 2E, respectively. Absorption spectra were acquired on a Cary 50 UV-VIS spectrophotometer from Varian and the emission spectra on a Fluorolog 3 fluorescence spectrometer from Horiba Scientific equipped with a R2658 photo- multiplier from Hamamatsu. The absolute luminescence quantum yields were determined using an integrating sphere from Horiba. The luminescence decay times for the sensing materials were measured with the Fluorolog 3 spectrometer in kinetic acquisition mode. Calibrations were obtained using a temperature-controlled flow-through cell combined with a gas-mixing device from Voegtlin (Switzerland; www.red-y.com), which was used to mix nitrogen with 0.1 % O_2 test gas (for the boron chelates) and nitrogen with 20 ppmv O_2 test gas (for the aluminium complexes). Calibrations for the aluminium complexes were further corrected for impurities in the nitrogen gas using a standard addition method, by measuring decay times under nitrogen und in oxygen-free sodium sulphite solution. The measured intensities under nitrogen were multiplied with the lifetime ratio (nitrogen/oxygen-free) to obtain the actual value for I_0. All calibration points were corrected by the obtained intrinsic oxygen contamination. For additional information on photophysical properties of the dyes, see Supplementary Figs 2.5 - 2.13. For NMR and mass spectroscopy analysis of the compounds in this article, see Supplementary Figs 2.14 - 2.32.

2.6 Acknowledgements

The work was financially supported by the European Research Council (Project 'Oxygen', N 267233). We thank Professor R. Saf (Institute for Chemistry and Technology of Materials,

Graz University of Technology) for acquiring mass spectra and Professor H. Weber (Institute of Organic Chemistry) for acquiring and analysis of the NOESY and HMBC NMR spectra.

2.7 References

[1] Kazuo Tanno. “An Automatic Recording Analyzer for the Determination of Dissolved Oxygen in Boiler Feed Water”. In: *Bulletin of the Chemical Society of Japan* 37.6 (Feb. 1964), pp. 804–810.

[2] Takeo Nakano, Ken’ichiroh Hoshi, and Shigeru Baba. “Effect of background gas environment on oxygen incorporation in TiN films deposited using UHV reactive magnetron sputtering”. In: *Vacuum* 83.3 (Oct. 2008), pp. 467–469.

[3] Henry Berger. “Contamination due to process gases”. In: *Microelectronic Engineering* 10.3-4 (Feb. 1991), pp. 259–267.

[4] I S Longmuir. “Respiration rate of bacteria as a function of oxygen concentration.” In: *The Biochemical journal* 57.1 (May 1954), pp. 81–87.

[5] F J Bergersen and G L Turner. “Bacteriods from Soybean Root Nodules: Respiration and NFormula-Fixation in Flow-Chamber Reactions with Oxyleghaemoglobin”. In: *Proceedings of the Royal Society B: Biological Sciences* 238.1293 (Jan. 1990), pp. 295–320.

[6] M J Johnson. “Aerobic microbial growth at low oxygen concentrations.” In: *Journal of bacteriology* 94.1 (July 1967), pp. 101–108.

[7] Daniel A Stolper, Niels Peter Revsbech, and Donald E Canfield. “Aerobic growth at nanomolar oxygen concentrations.” In: *Proceedings of the National Academy of Sciences of the United States of America* 107.44 (Nov. 2010), pp. 18755–18760.

[8] N P Revsbech, L H Larsen, J Gundersen, T Dalsgaard, O Ulloa, and B Thamdrup. “Determination of ultra-low oxygen concentrations in oxygen minimum zones by the STOX sensor”. In: *Limnol Oceanogr Methods* 7 (2009), pp. 371–381.

[9] Sven Kochmann, Carlos Baleizão, Mário N Berberan-Santos, and Otto S Wolfbeis. “Sensing and imaging of oxygen with parts per billion limits of detection and based on the quenching of the delayed fluorescence of (13)C70 fullerene in polymer hosts.” In: *Analytical Chemistry* 85.3 (Feb. 2013), pp. 1300–1304.

[10] J Crank and G S Park. *Diffusion in Polymers*. Ed. by P Neogi. Marcel Dekker Inc., Feb. 1996.

[11] Michela Quaranta, Sergey M Borisov, and Ingo Klimant. “Indicators for optical oxygen sensors.” In: *Bioanalytical reviews* 4.2-4 (Dec. 2012), pp. 115–157.

[12] Otto S Wolfbeis. “Materials for flourescence-based optical chemical sensors”. In: *Journal of Materials Chemistry* 15 (July 2005), pp. 2657–2669.

[13] Yutaka Amao. “Probes and Polymers for Optical Sensing of Oxygen”. In: *Microchimica Acta* 143.1 (Sept. 2003), pp. 1–12.

[14] Xu-Dong Wang and Otto S Wolfbeis. “Optical methods for sensing and imaging oxygen: materials, spectroscopies and applications.” In: *Chemical Society Reviews* 43.10 (May 2014), pp. 3666–3761.

[15] Stefan Nagl, Carlos Baleizão, Sergey M Borisov, Michael Schäferling, Mário N Berberan-Santos, and Otto S Wolfbeis. "Optical sensing and imaging of trace oxygen with record response." In: *Angewandte Chemie (International ed. in English)* 46.13 (2007), pp. 2317–2319.

[16] G Zhang, J Chen, S J Payne, and S E Kooi. "Multi-Emissive Difluoroboron Dibenzoylmethane Polylactide Exhibiting Intense Fluorescence and Oxygen-Sensitive Room-Temperature Phosphorescence - Journal of the American Chemical Society (ACS Publications)". In: *Journal of the ...* (2007).

[17] Guoqing Zhang, Gregory M Palmer, Mark W Dewhirst, and Cassandra L Fraser. "A dual-emissive-materials design concept enables tumour hypoxia imaging." In: *Nature materials* 8.9 (Sept. 2009), pp. 747–751.

[18] Songpan Xu, Ruffin E Evans, Tiandong Liu, Guoqing Zhang, J N Demas, Carl O Trindle, and Cassandra L Fraser. "Aromatic difluoroboron β-diketonate complexes: effects of π-conjugation and media on optical properties." In: *Inorganic chemistry* 52.7 (Apr. 2013), pp. 3597–3610.

[19] Xuepeng Zhang, Tongqing Xie, Minxin Cui, Li Yang, Xingxing Sun, Jun Jiang, and Guoqing Zhang. "General design strategy for aromatic ketone-based single-component dual-emissive materials." In: *ACS applied materials & interfaces* 6.4 (Feb. 2014), pp. 2279–2284.

[20] S M Borisov, A S Vasylevska, Ch Krause, and O S Wolfbeis. "Composite Luminescent Material for Dual Sensing of Oxygen and Temperature". In: *Advanced Functional Materials* 16.12 (Aug. 2006), pp. 1536–1542.

[21] R C Haddon, R Rayford, and A M Hirani. "2-Methyl-and 5-methyl-9-hydroxyphenalenone". In: *The Journal of Organic Chemistry* 46.22 (1981), pp. 4587–4588.

[22] R C Haddon. "Benzannelated 9-hydroxyphenalenones". In: *Australian Journal of Chemistry* 35.8 (1982), p. 1733.

[23] Aurore Loudet and Kevin Burgess. "BODIPY dyes and their derivatives: syntheses and spectroscopic properties." In: *Chemical reviews* 107.11 (Nov. 2007), pp. 4891–4932.

[24] Noël Boens, Volker Leen, and Wim Dehaen. "Fluorescent indicators based on BODIPY". In: *Chemical Society Reviews* 41.3 (2012), p. 1130.

[25] J Brandrup, E H Immergut, and E A Grulke, eds. *Polymer Handbook*. Wiley: New York, 1999.

[26] Sergey M Borisov, Philipp Lehner, and Ingo Klimant. "Novel optical trace oxygen sensors based on platinum(II) and palladium(II) complexes with 5,10,15,20-meso-tetrakis-(2,3,4,5,6-pentafluorphenyl)-porphyrin covalently immobilized on silica-gel particles." In: *Analytica Chimica Acta* 690.1 (Mar. 2011), pp. 108–115.

[27] Toshio Masuda, Eiji Isobe, Toshinobu Higashimura, and Koichi Takada. "Poly[1-(trimethylsilyl)-1-propyne]: a new high polymer synthesized with transition-metal catalysts and characterized by extremely high gas permeability". In: *Journal of the American Chemical Society* 105.25 (Nov. 1983), pp. 7473–7474.

[28] Kazukiyo Nagai and Tsutomu Nakagawa. "Oxidation of poly(1-trimethylsilyl-1-propyne)". In: *Journal of Applied Polymer Science* 54.11 (Dec. 1994), pp. 1651–1658.

[29] Kazukiyo Nagai and Tsutomu Nakagawa. “Effects of aging on the gas permeability and solubility in poly (1-trimethylsilyl-1-propyne) membranes synthesized with various catalysts”. In: *Journal of Membrane Science* 105.3 (Sept. 1995), pp. 261–272.

[30] Vincenzo Arcella, Alessandro Ghielmi, and Giulio Tommasi. “High Performance Perfluoropolymer Films and Membranes”. In: *Annals of the New York Academy of Sciences* 984.1 (Mar. 2003), pp. 226–244.

[31] Stuart M Nemser and Ian C Roman. “Perfluorodioxole Membranes”. Pat. Sept. 1991.

2.8 Supplementary Information

2.8.1 Methods

Synthesis of the BF_2 chelate of 9-hydroxyphenalenone

294 mg (1.5 mmol) of 9-hydroxyphenalenone were dissolved in 50 ml of anhydrous tetrahydrofuran and 1.92 g (13.5 mmol) of boron trifluoride diethyl etherate were added. The solution was stirred for 1 h at 65 °C, the solvent was removed under vacuum and the product was purified on an aluminium oxide column using dichloromethane as an eluent. Yield: 300 mg (67 %) of orange crystals. ^{1}H NMR (300 MHz, DMSO-d_6, δ): 8.94 (d, J = 9.1 Hz, 2H), 8.70 (d, J = 7.7 Hz, 2H), 8.03 (t, J = 7.7 Hz, 1H), 7.62 (d, J = 9.1 Hz, 2H). EI-DI-TOF (m/z): found 244.0499, calcd 244.0510.

Synthesis of the BF_2 chelate of 6-hydroxybenz[de]anthracene-7-on

369 mg (1.5 mmol) of 6-hydroxybenz[de]anthracene-7-on were dissolved in 60 ml of anhydrous tetrahydrofuran and 1.7 g (12 mmol) of boron trifluoride diethyl etherate were added. The solution was stirred at 65 °C for 2 h, 69 mg (0.5 mmol) of potassium carbonate were added and the stirring was continued for 2h. The solvent was removed under vacuum and the product was purified on an aluminium oxide column using dichloromethane as an eluent. Yield: 340 mg (77 %) of orange crystals. ^{1}H NMR (300 MHz, DMSO-d_6, δ): 9.26 (d, J = 7.7 Hz, 1H), 9.04 (d, J = 8.3 Hz, 1H), 8.91 (d, J = 9.2 Hz, 1H), 8.69 (d, J = 8.2 Hz, 1H), 8.50 (d, J = 7.6 Hz, 1H), 8.21 (t, J = 8.3 Hz, 1H), 7.97 (dt, J = 21.2, 7.6 Hz, 2H), 7.61 (d, J = 9.1 Hz, 1H). EI-DI-TOF (m/z): found 294.0671, calcd 294.0667.

Synthesis of C_8F_{17} substituted 9-hydroxyphenalenone

HPhN (1g, 5.1mmol) and $FeSO_4 \cdot 7\ H_2O$ (2.5g, 9.0mmol) were dissolved in 120 mL DMSO and 40 mL 1,1,2-trichloro-1,2,2-trifluoroethane in a 200 mL Schlenk flask. The whole reaction was conducted under argon atmosphere. The solution was heated to 40 °C and perfluorooctyl iodide (3.4 mL, 7.03 g, 12.9 mmol) was added. 60 % H_2O_2 (1.4 mL, 1.67 g, 49 mmol) was added drop-wise over 5 min. The solution turned red and formed black foam. After 30 min 20 mL 1,1,2-trichloro-1,2,2-trifluoroethane were added and the foam dissolved. 1h after the start of the reaction a second portion perfluorooctyl iodide (3.4mL, 7.03g, 12.9mmol) was added and 60 % H_2O_2 (1.4 mL, 1.67 g, 49 mmol) was added drop-wise over 5 min. The reaction was continued for 1 h, then the reaction mixture was cooled to room temperature and the DMSO and 1,1,2-trichloro-1,2,2-trifluoroethane phases were separated. The 1,1,2-trichloro-1,2,2-trifluoroethane phase was washed 3 times with 36 % hydrochloric acid, once with water and was dried over Na_2SO_4. After removing the solvent 9.3 g reddish-brown oil were obtained. The

product was purified on a silica-gel column with hexane and toluene as eluents. Yield: 700 mg (13 %). R_F 0.57 with toluene. NMR spectroscopy: ^{1}H NMR (300 MHz, $CDCl_3$, δ: 16.75 (s, 1H), 8.77 (s, 1H), 8.15-8.00 (m, 2H), 7.86 (d, J = 7.9 Hz, 2H), 7.24 (d, J = 9.3 Hz, 2H). DI-EI (*m/z*): 1031.98 found, 1031.98 calcd

Synthesis of C_8F_{17} substituted 6-hydroxybenz[de]anthracene-7-on

HBANPF was prepared using the same procedure as HPhNPF, but with a fivefold excess of perfluorooctyl iodide and the reaction mixture was stirred stirred for 2 h at 40 °C and then overnight at room temperature. Yield 500 mg (23 %) starting from 0.5 g HBAN. R~subF 0.69 with hexane/toluene 2/1. ^{1}H NMR (300MHz, $CDCl_3$, δ): 17.01 (s, 1H), 8.94 (s, 1H), 8.79 (d, J = 8.2 Hz, 1H), 8.71 (d, J = 7.9 Hz, 1H), 8.52 (d, J = 8.3 Hz, 1H), 8.03 (d, J = 8.2Hz, 1H), 7.89 (t, J = 7.6Hz, 1H), 7.73 (t, J = 7.5Hz, 1H). DI-EI (*m/z*): 1081.99 found, 1081.99 calcd

Synthesis of the aluminium complex of di-perfluorooctyl-9-hydroxyphenalenone

HPhNPF (100 mg, 0.097 mmol) was dissolved in 20 mL THF and 20 mL ethanol. NaOH (5.9 mg, 0.15 mmol) and AlCl3 (3.9 mg, 29 μmol) were added and the reaction mixture was stirred for 2.5 h at 40 °C. Then the reaction was stopped the product was extracted with 1,1,2-trichloro-1,2,2-trifluoroethane and the organic phase was washed twice with water. The organic layer was dried over Na_2SO_4 and evaporated in vacuum. 5 mL THF were added to the raw product and the mixture was placed in the freezer for a few hours. The THF phase was removed and new THF was added. The product was washed 7 times following this procedure. Yield: 68.4 mg (74 %. ^{1}H NMR (300 MHz, $CDCl_3$, δ): 8.87-8.55 (m, 3H), 8.15-7.84 (m, 6H), 7.84-7.54 (m, 3H), 7.42-7.04 (m, 3H); MALDI (*m/z*): $[M+Na]^+$: 3142.93 found, 3142.90 calcd

Synthesis of the aluminium complex of di-perfluorooctyl-6-hydroxybenz[de]anthracene-7-on

$Al(HBANPF)_3$ was prepared and purified with the same procedure as $Al(HPhNPF)_3$. Yield 19.5 mg (31 %) starting from 80 mg HBANPF. ^{1}H NMR (300MHz, $CDCl_3$, δ): 9.2-8.2 (m, 9.9H), 8.06 (s, 3H), 8.0-7.2 (m, 7.2H); MALDI (*m/z*): $[MH]^+$: 3271.11 found, 3270.96 calcd, [MH(with one additional C8F17-Group)]$^+$: 3689.02 found, 3688.92 calcd

2.8.2 Additional photo physical information

Figure 2.5 to 2.8 show absorption spectra as well as molar absorption coefficients for the various indicator dyes used in this work.

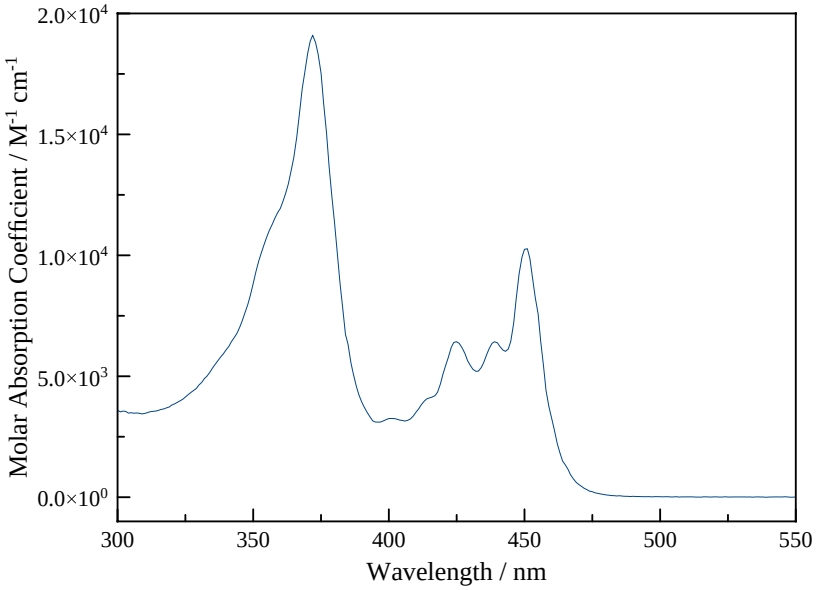

Figure 2.5: Absorption spectra of BF_2(HPhN)

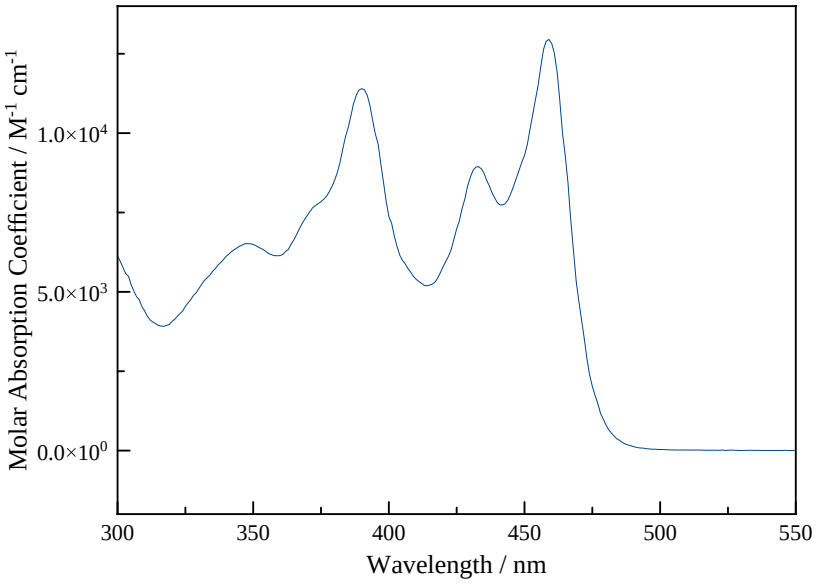

Figure 2.6: Absorption spectra of BF_2(HBAN)

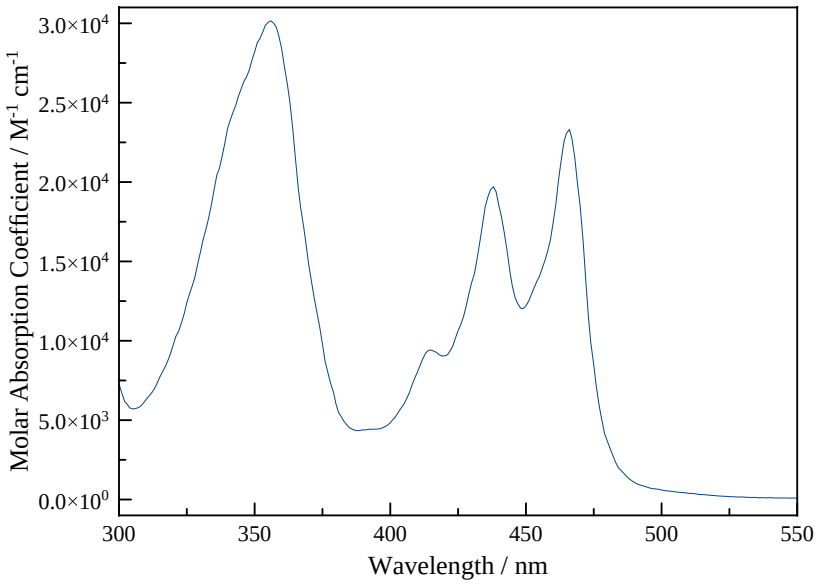

Figure 2.7: Absorption spectra of $Al(HPhNPF)_3$

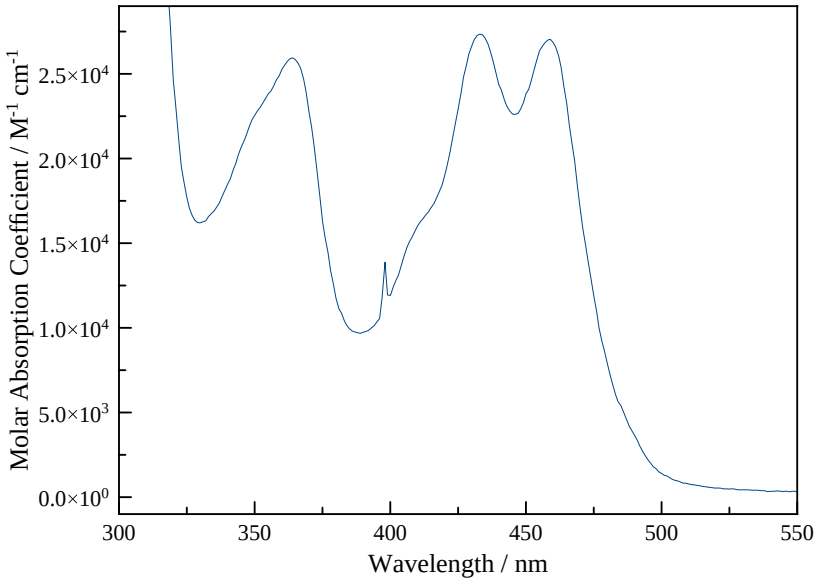

Figure 2.8: Absorption spectra of $Al(HBANPF)_3$

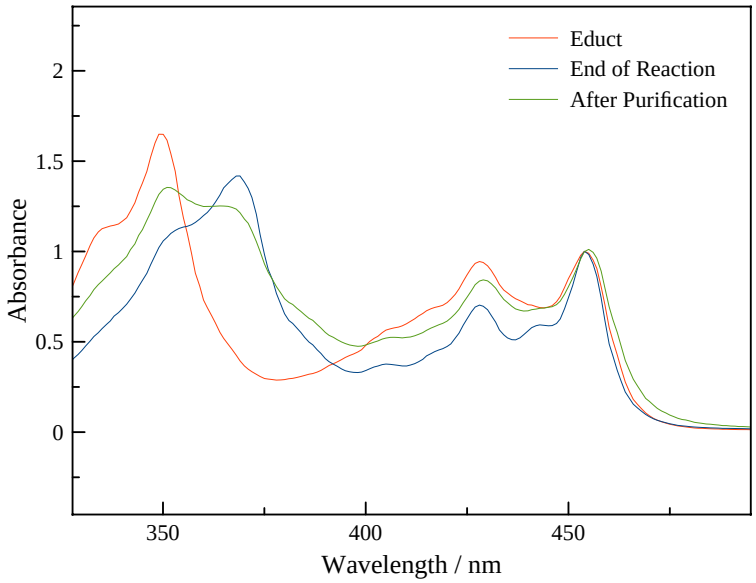

Figure 2.9: Absorption spectra used to monitor the synthesis of BF_2(HPhNPF). Some dissociation of BF_2(HPhNPF) occurs during purification. BF_2(HBANPF) was found to be more stable but showed inferior photophysical properties (lower phosphorescence quantum yields and decay times) in Teflon AF 1600 probably due to aggregation.

Due to very high sensitivity of the sensors sufficient deoxygenation of the integrating sphere is extremely challenging. Therefore, the quantum yields of delayed fluorescence and phosphorescence were calculated from the comparison of the emission spectra under deoxygenated conditions (sodium sulfite; prompt fluorescence + delayed fluorescence + phosphorescence) and air-saturated conditions (prompt fluorescence). The quantum yield of the prompt fluorescence obtained in the integrating sphere under air saturation was used as a reference.

Dye	wavelength / nm[a]	ϵ_{max} [m^{-1} cm^{-1}] (VIS)	FΦ[%]	DFΦ [%]	PΦ[%]	τ_0 [ms][b]
BF_2(HPhN)	450	$10.2 times 10^3$	1.4	1.2	4.6	310
BF_2(HBAN)	459	$12.9 times 10^3$	5.5	4.6	9.1	640
Al(HPhNPF)$_3$	465	$23.2 times 10^3$	0.9	1.3	5.4	266
Al(HBANPF)$_3$	459	$27.1 times 10^3$	2.0	0.8	3.2	396

Table 2.2: Photophysical properties of the new dyes at 25 °C. [a] of respective molar absorption coefficient values, [b] Decay times are given for 0.01 *wt*% dye in polystyrene in the case of non-perfluoroalkylated dyes and for 0.05 *wt*% dye in Teflon AF 1600 for perfluoroalkylated dyes

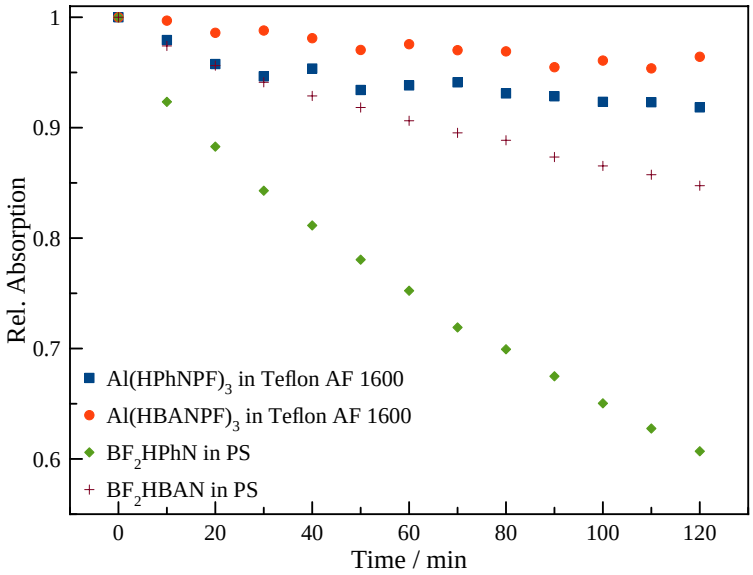

Figure 2.10: Photobleaching of the sensors was investigated using a high power blue LED array (Germany, www.led-tech.de) operated at 7.4 W input power; photon flux about 4000 μmol $s^{-1}m^{-2}$ of photons as estimated by a Li-250A Light meter from Li-COR®. The absorption changes were monitored on a Cary 50 UV-VIS spectrophotometer.

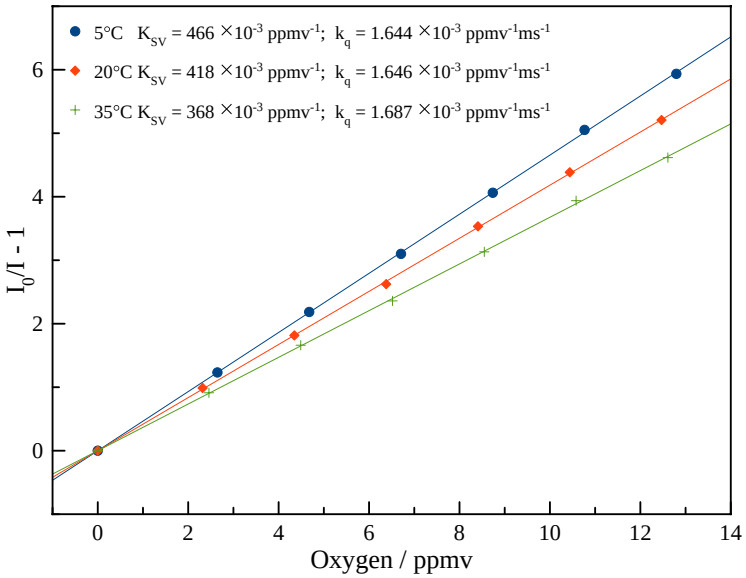

Figure 2.11: Temperature dependence of the $Al(HPhNPF)_3$ calibration

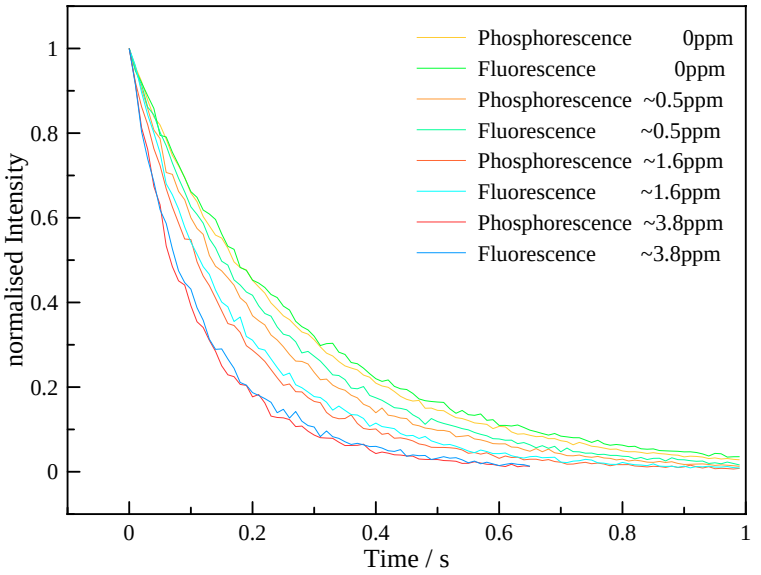

Figure 2.12: Decay curves of $Al(HPhNPF)_3$ in Hyflon AD 60 at different oxygen concentrations

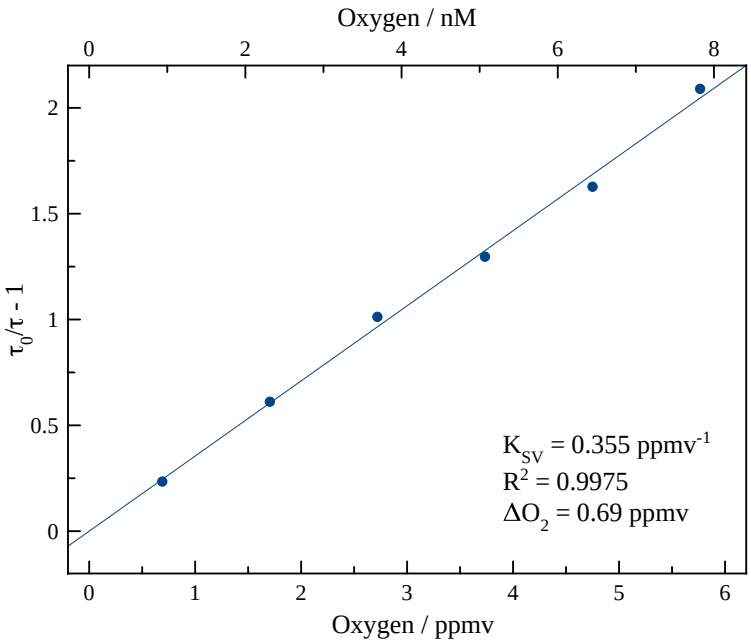

Figure 2.13: Decay time calibration of $Al(HPhNPF)_3$ in Hyflon AD 60

2.8.3 Compound Characterisation

The ^{1}H-NMR spectra of Al(HPhNPF)$_3$ and Al(HBANPF)$_3$ show weak peaks of impurities whereof the peaks at 1.34, 1.47, 2.01 and 5.13 ppm can be attributed to impurities in the added trichlorotrifluoroethane which is necessary to dissolve the perfluoroalkylated dyes but was not available in NMR quality (see Figure 2.28 for solvent background) and water (1.18 ppm). The remaining impurities in the dyes account for only 0.5 $wt\%$ (assuming a chemical formula of the impurities similar to $(CH_2)_n$ with 7 amu / hydrogen). Their relatively high visibility can be attributed to the very high molar mass (3120 for Al(HPhNPF)$_3$ and 3270 for Al(HBANPF)$_3$) of the dyes compared with their hydrogen content (208 amu / hydrogen and 156 amu / hydrogen for Al(HPhNPF)$_3$ and Al(HBANPF)$_3$ respectively). In both cases no OH-peaks ($\sim$ 17 ppm) from the free ligands could be observed.

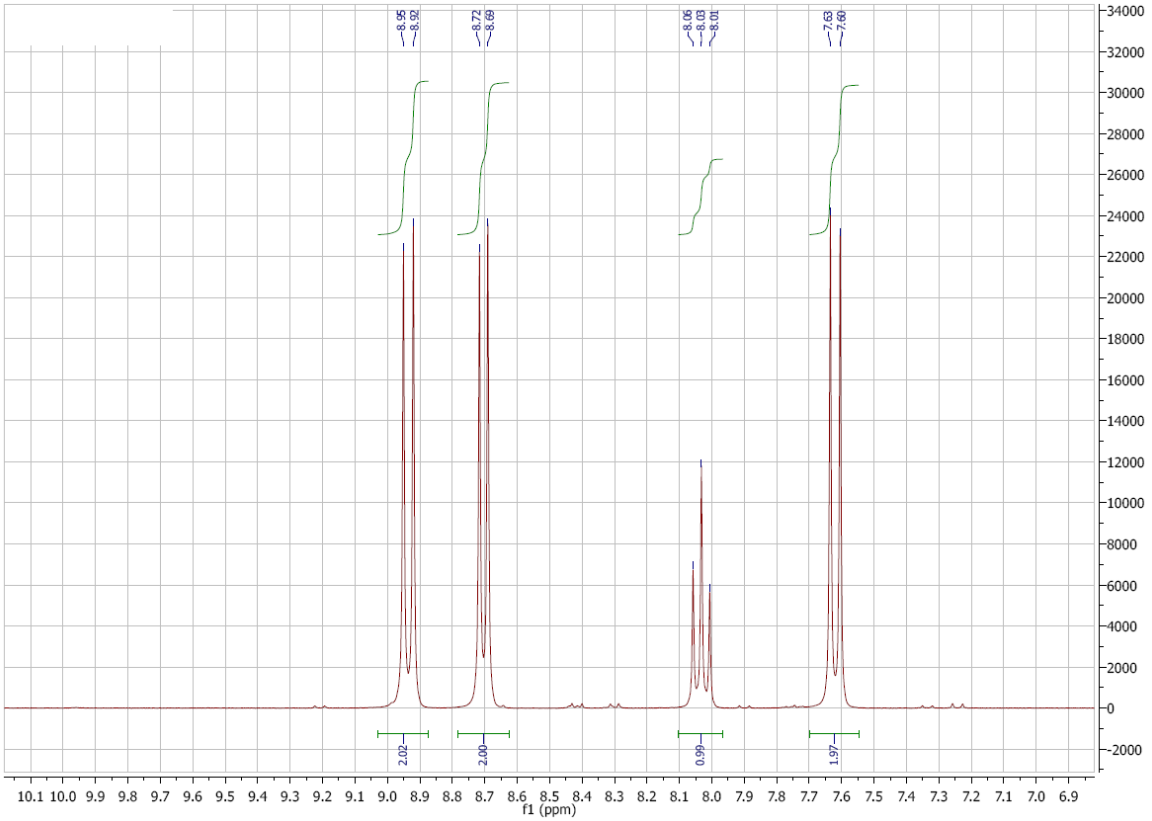

Figure 2.14: ^{1}H NMR spectrum (300 MHz, DMSO-d$_6$) of BF_2(HPhN)

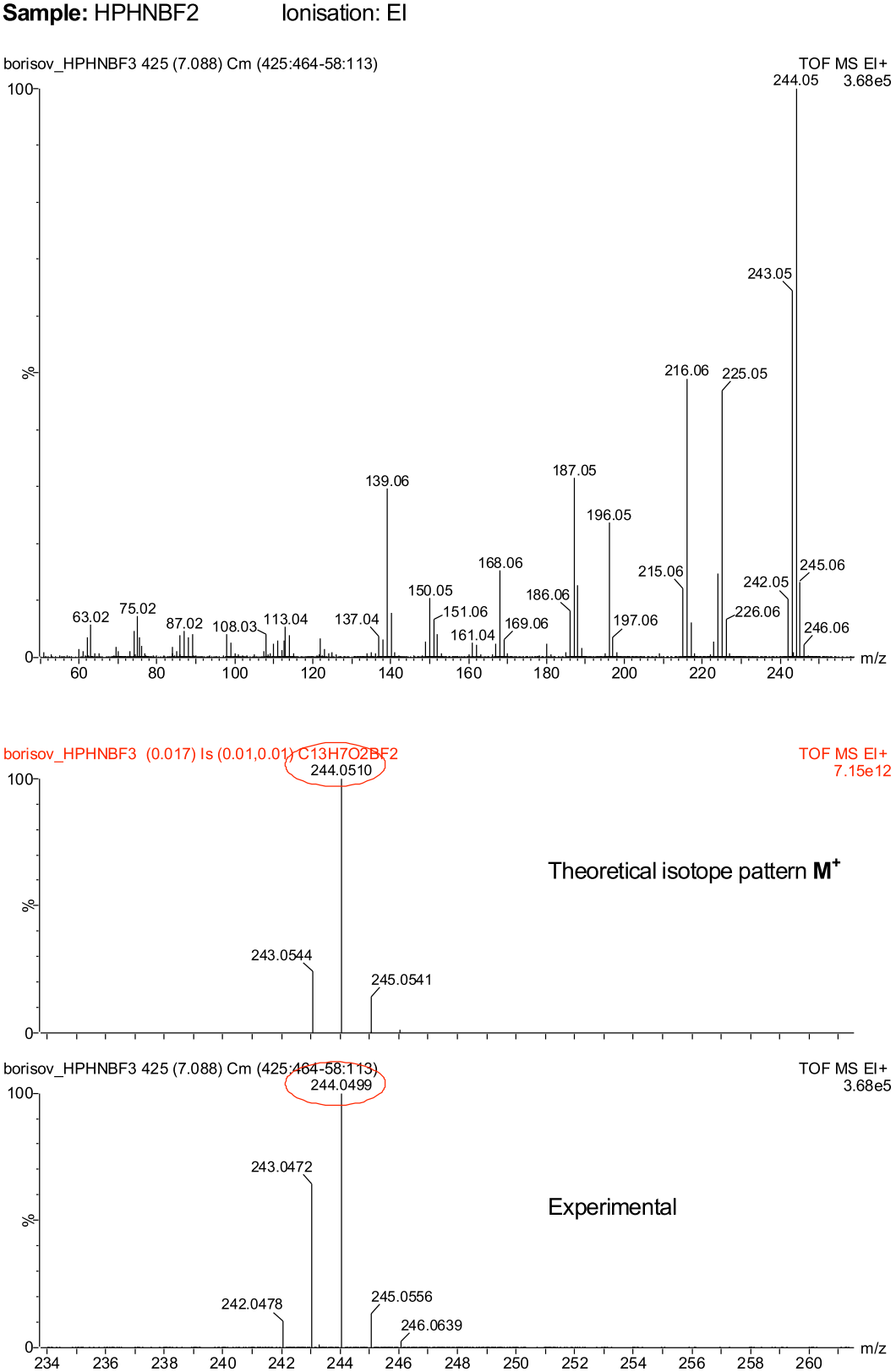

Figure 2.15: EI-DI-TOF spectrum of BF_2(HPhN)

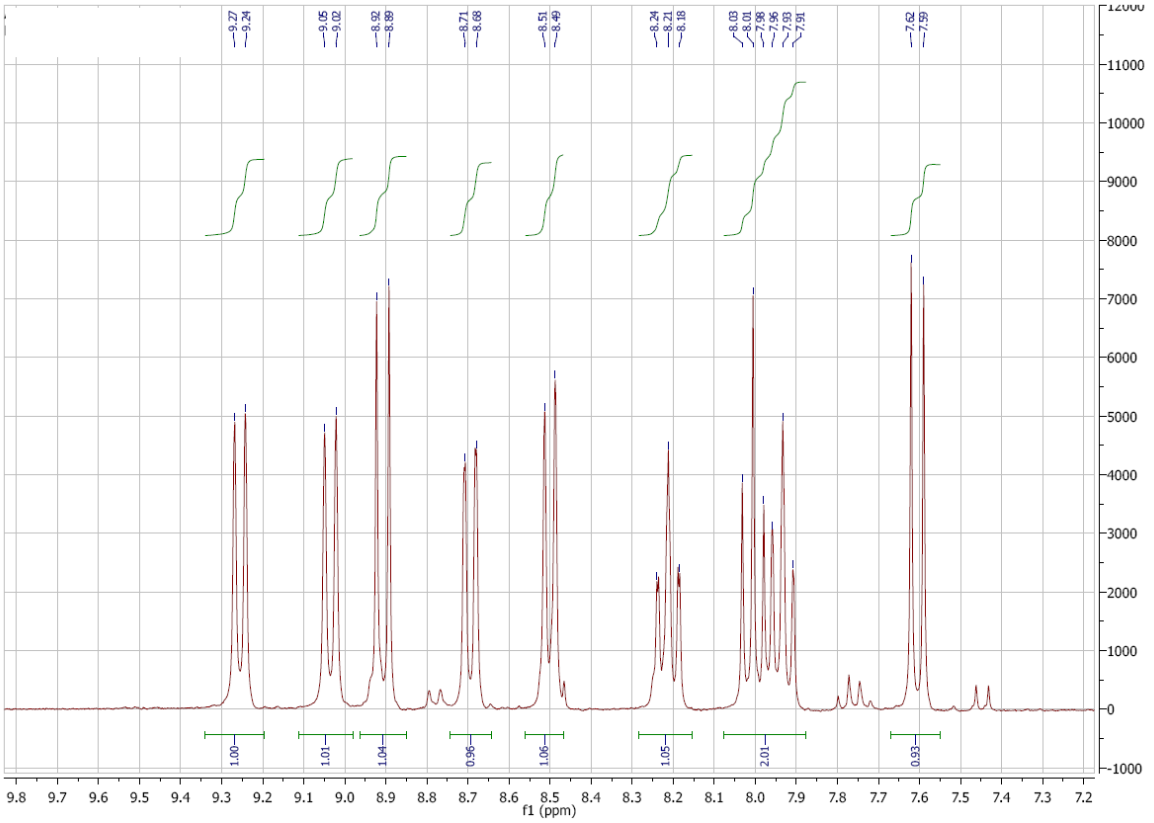

Figure 2.16: ^{1}H NMR spectrum (300 MHz, DMSO-d_6) of BF_2(HBAN)

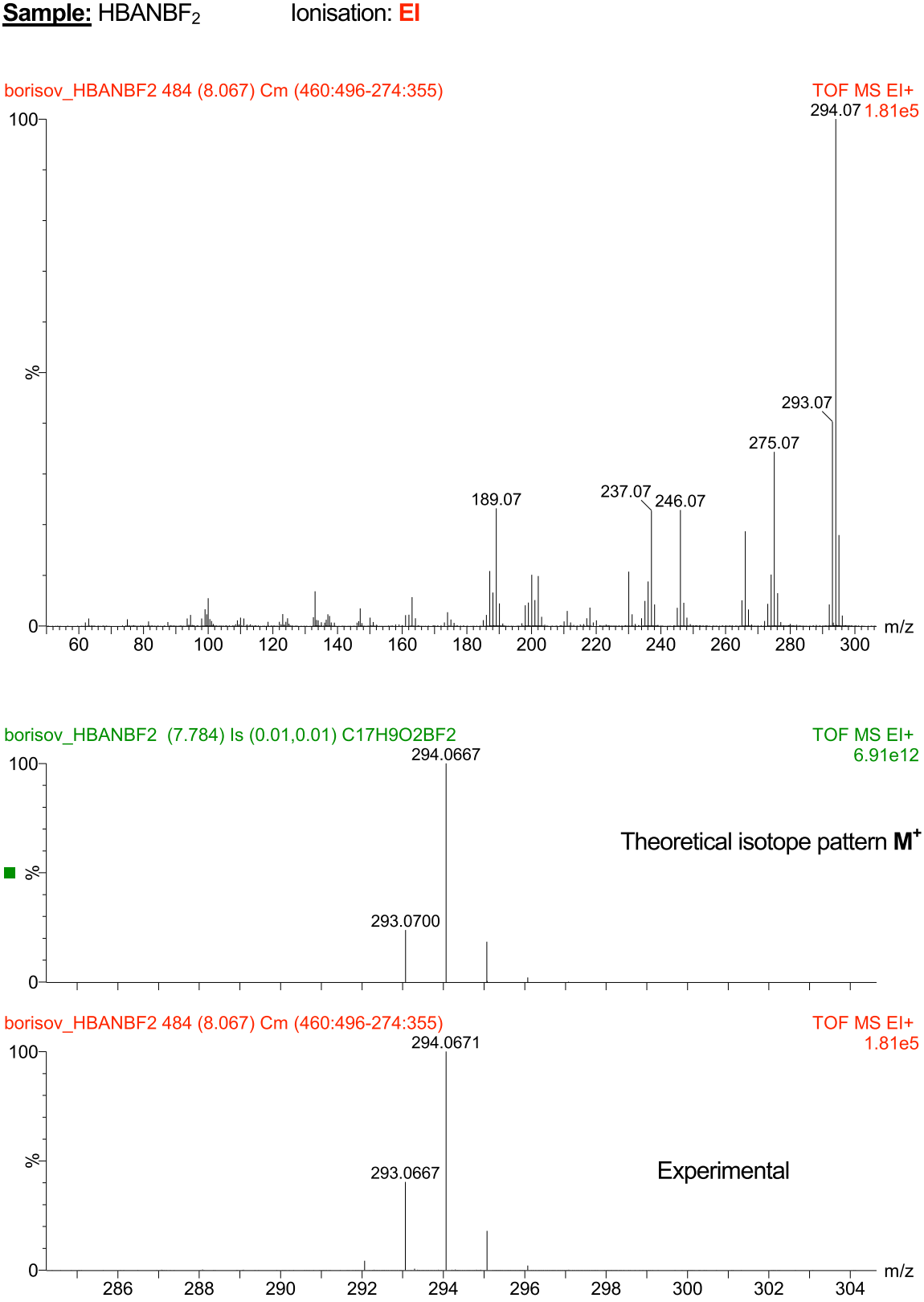

Figure 2.17: EI-DI-TOF spectrum of BF_2(HBAN)

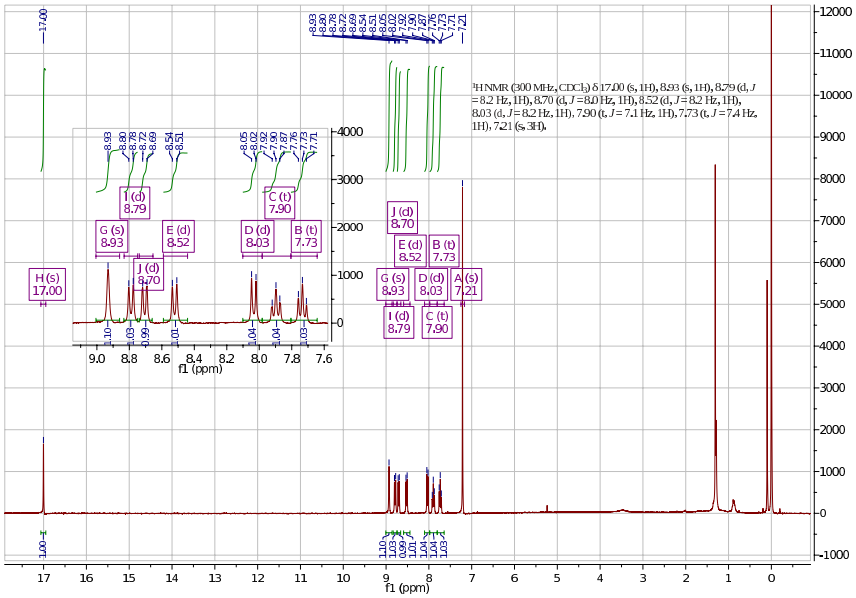

Figure 2.18: ^{1}H NMR spectrum (300 MHz, 112-trichlortrifluoroethan + $CDCl_3$) of HBANPF (Free Ligand)

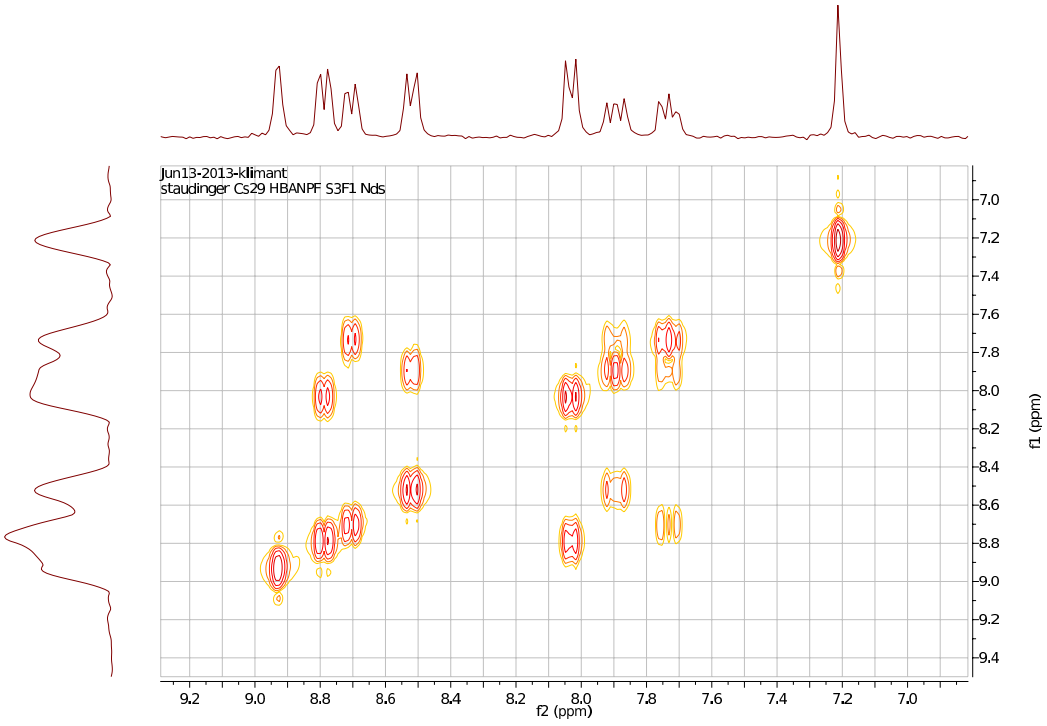

Figure 2.19: ^{1}H cosy NMR spectrum (300 MHz, 112-trichlortrifluoroethan + $CDCl_3$) of HBANPF (Free Ligand)

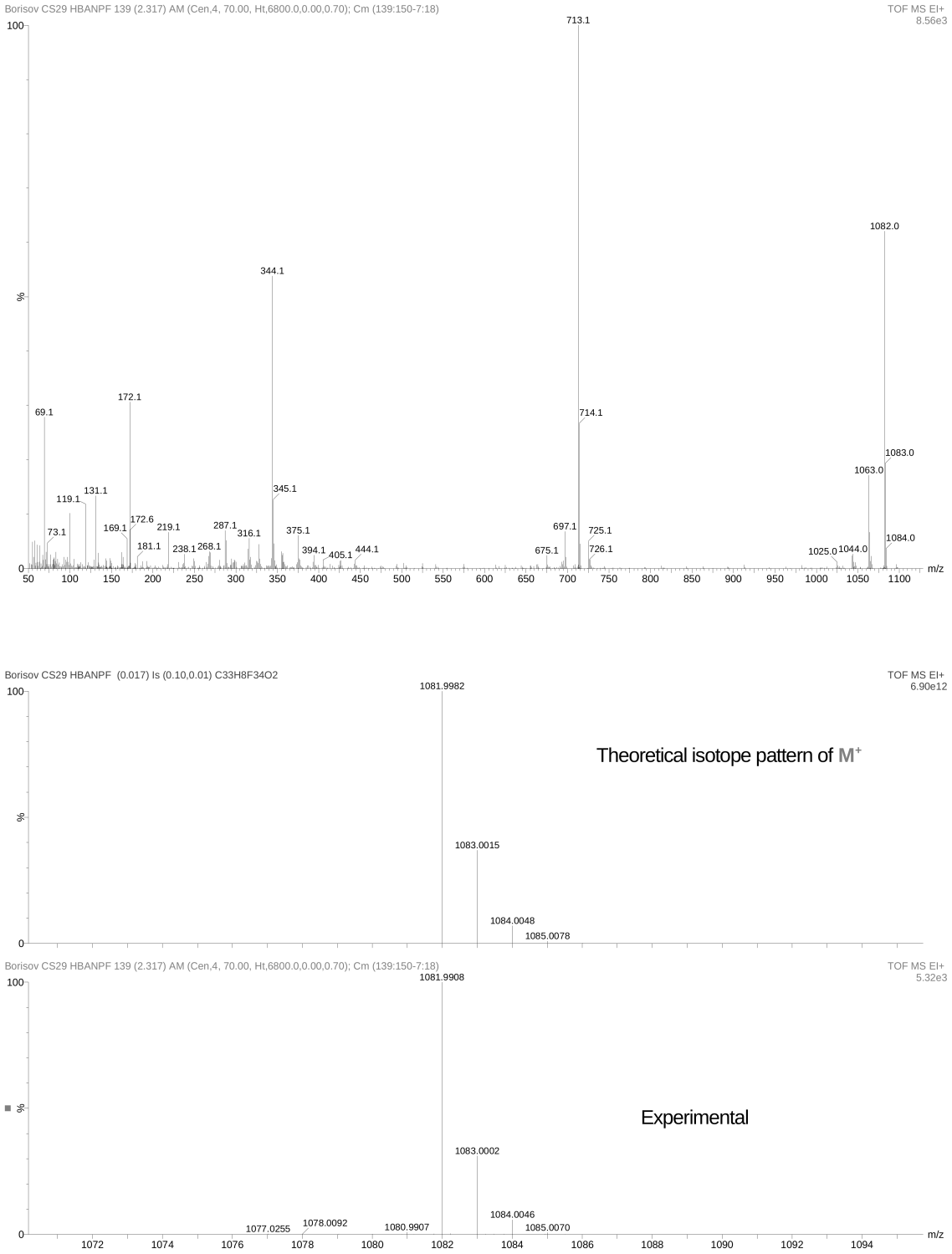

Figure 2.20: EI-DI-TOF spectrum of HBANPF

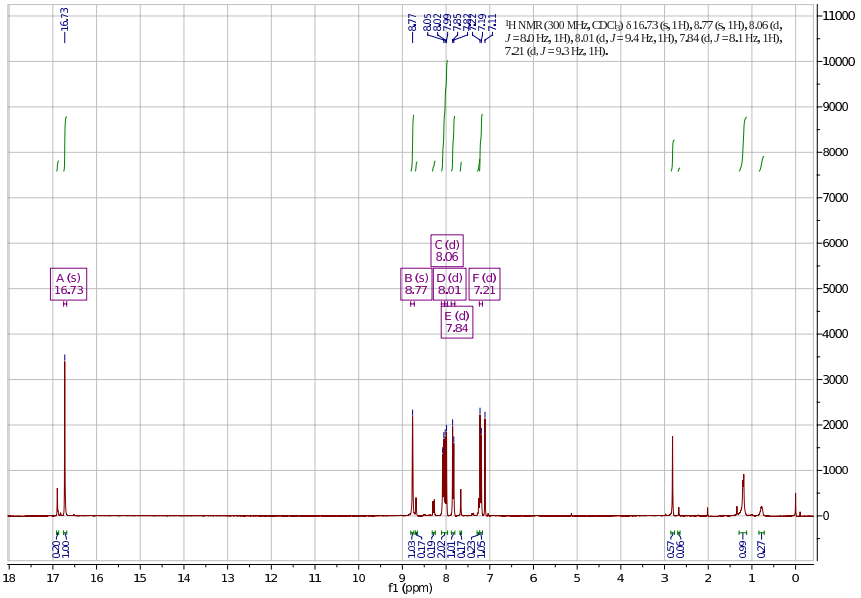

Figure 2.21: ^{1}H NMR spectrum (300 MHz, 112-trichlortrifluoroethan + $CDCl_3$) of HPhNPF (Free Ligand)

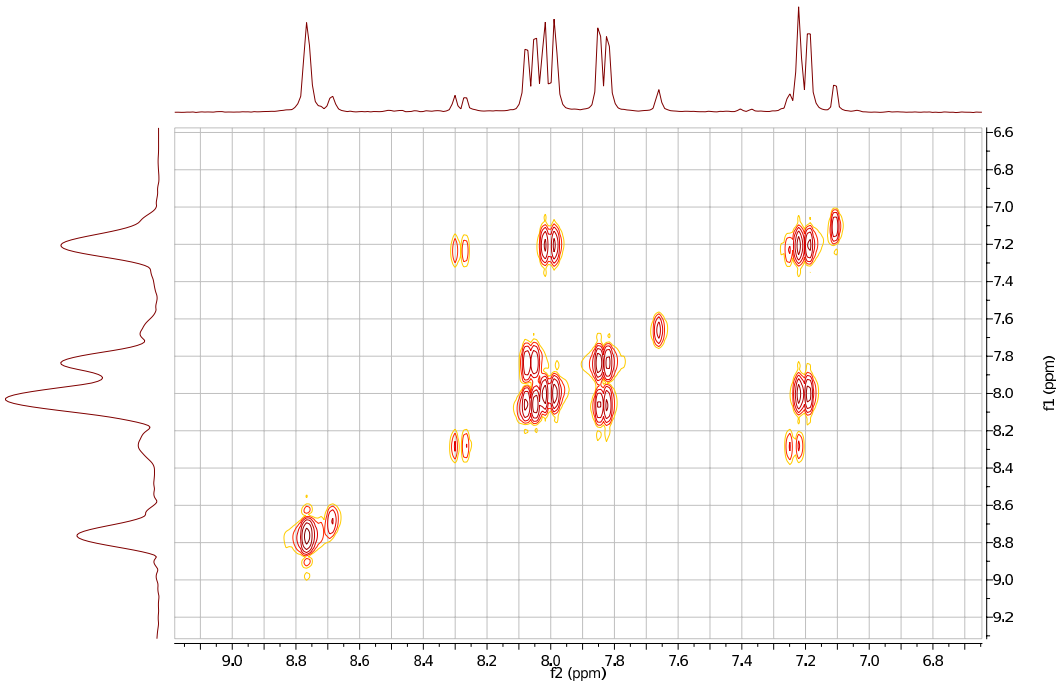

Figure 2.22: ^{1}H cosy NMR spectrum (300 MHz, 112-trichlortrifluoroethan + $CDCl_3$) of HPhNPF (Free Ligand)

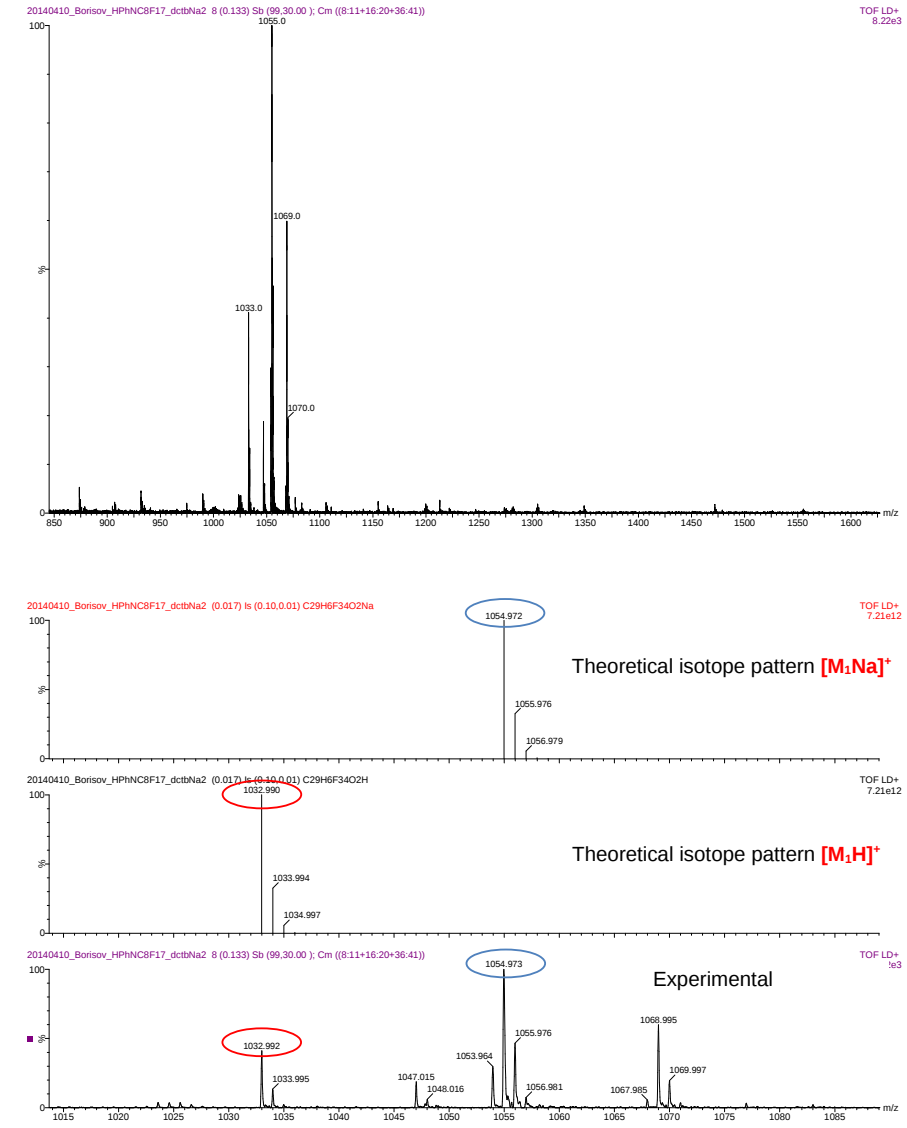

1

Figure 2.23: MALDI-TOF spectrum of HPhNPF

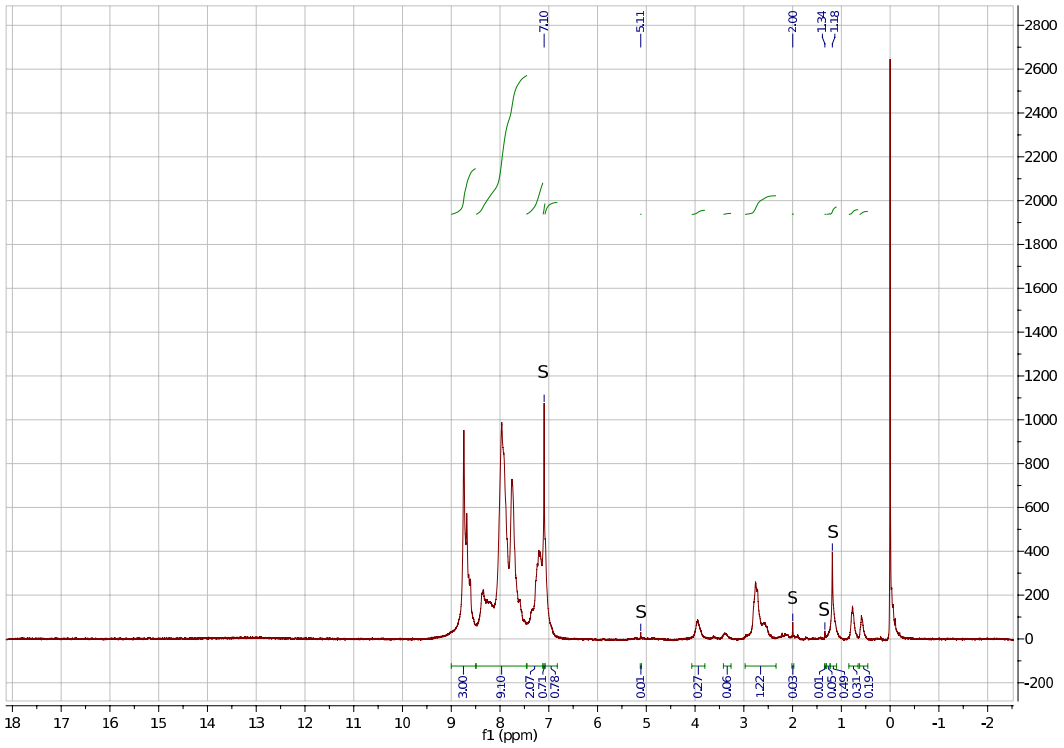

Figure 2.24: ^{1}H NMR spectrum (300 MHz, 112-trichlortrifluoroethan + $CDCl_3$) of $Al(HPhNPF)_3$. Impurities are highly visible due to a high molar mass to hydrogen ratio of the product, estimated purity: 99.5 %.

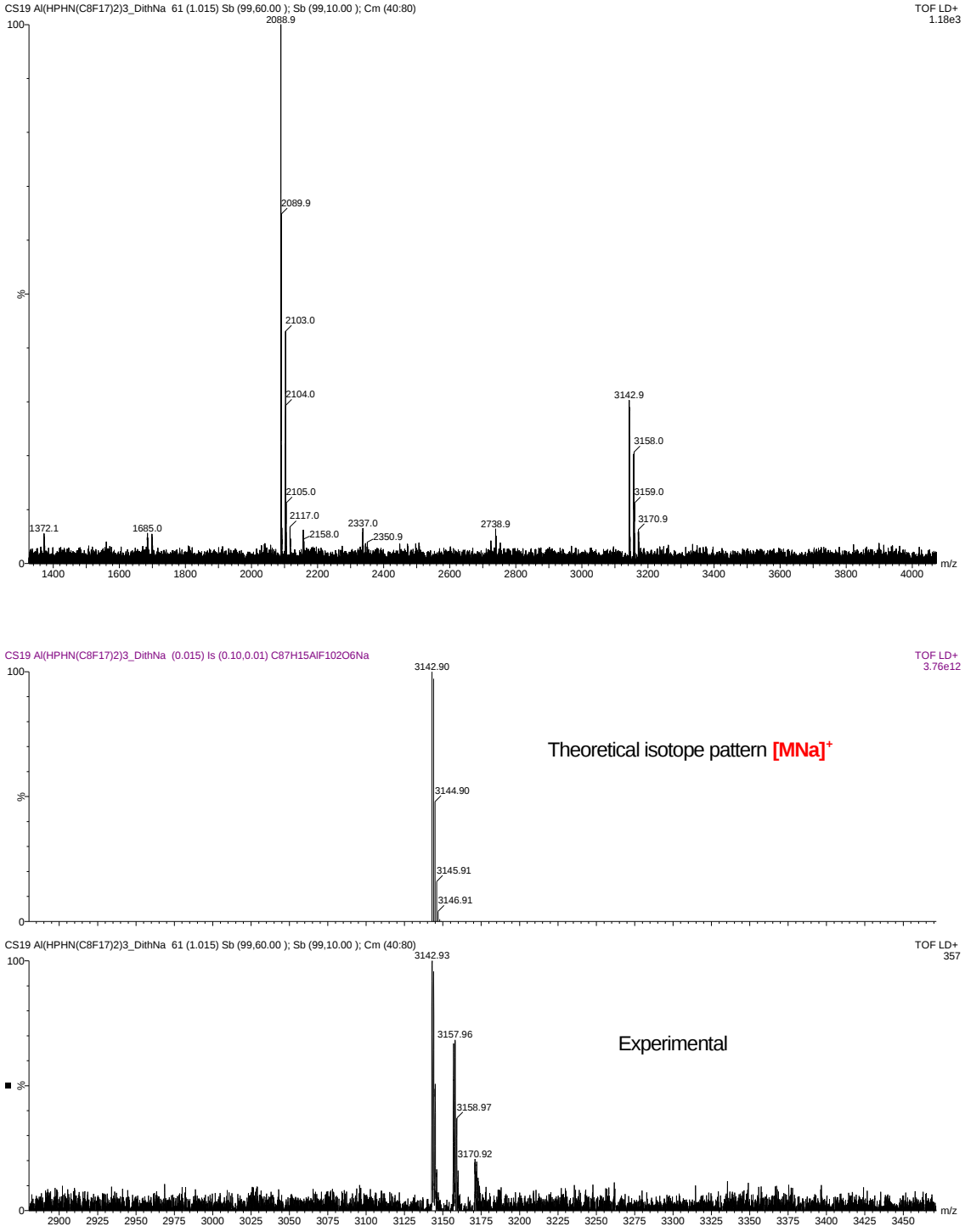

Figure 2.25: MALDI-TOF spectrum of $Al(HPhNPF)_3$

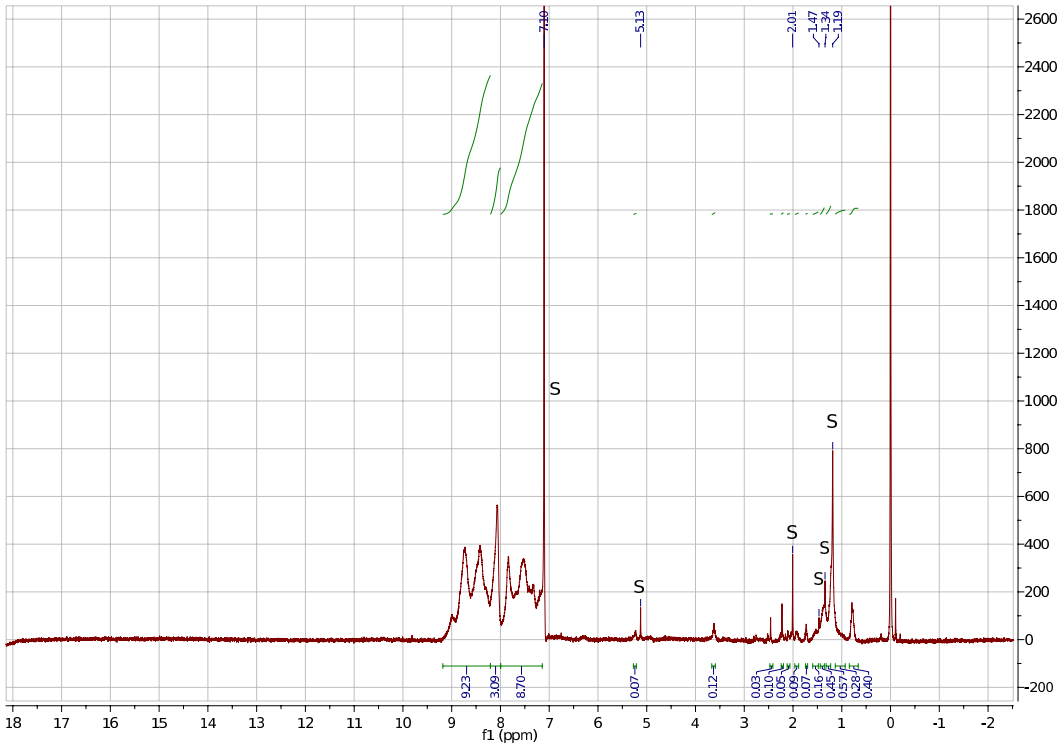

Figure 2.26: ^{1}H NMR spectrum (300 MHz, 112-trichlortrifluoroethan + $CDCl_3$) of $Al(HBANPF)_3$. Impurities are highly visible due to a high molar mass to hydrogen ratio of the product, estimated purity: 99.5 %.

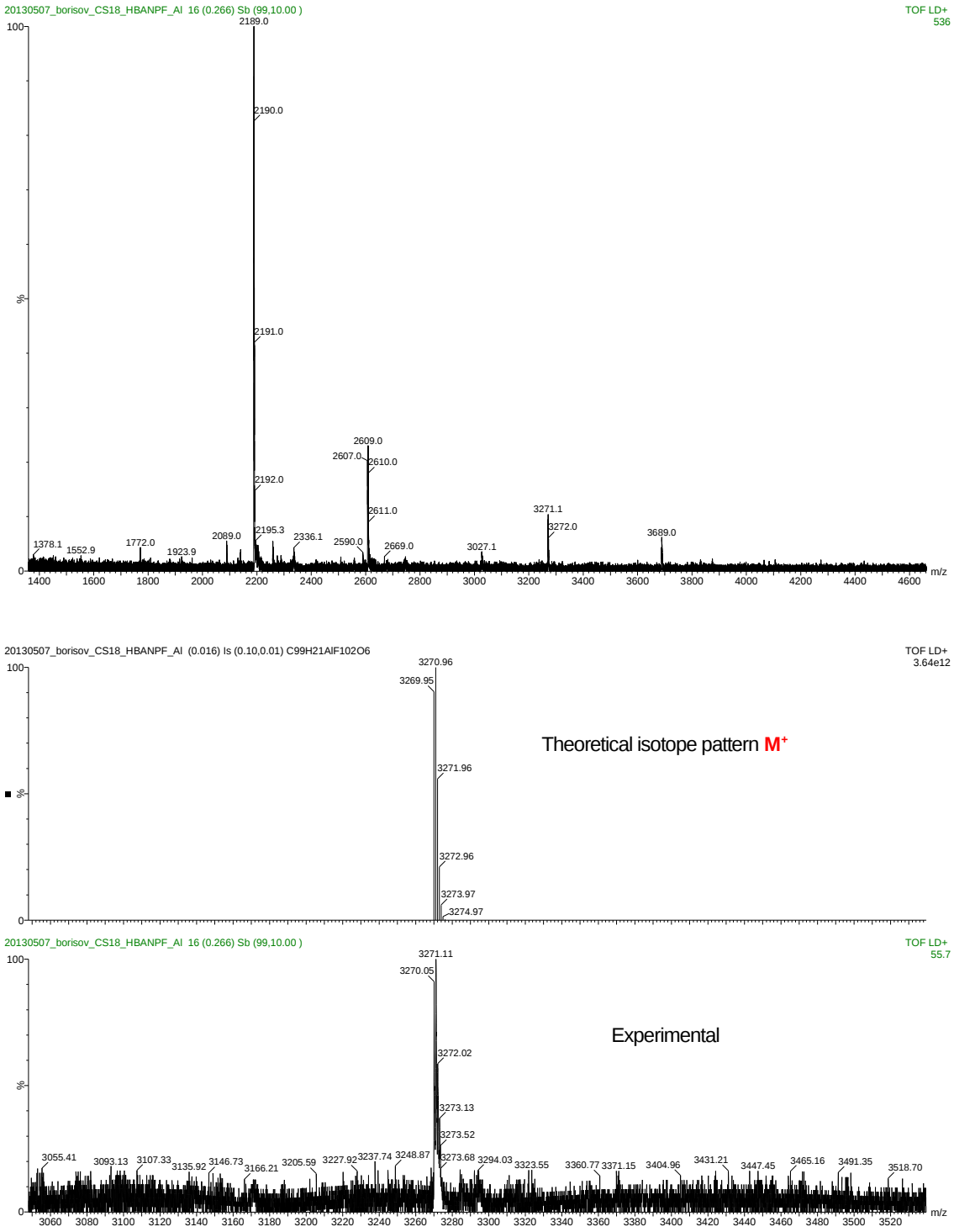

Figure 2.27: MALDI-TOF spectrum of Al(HBANPF)$_3$

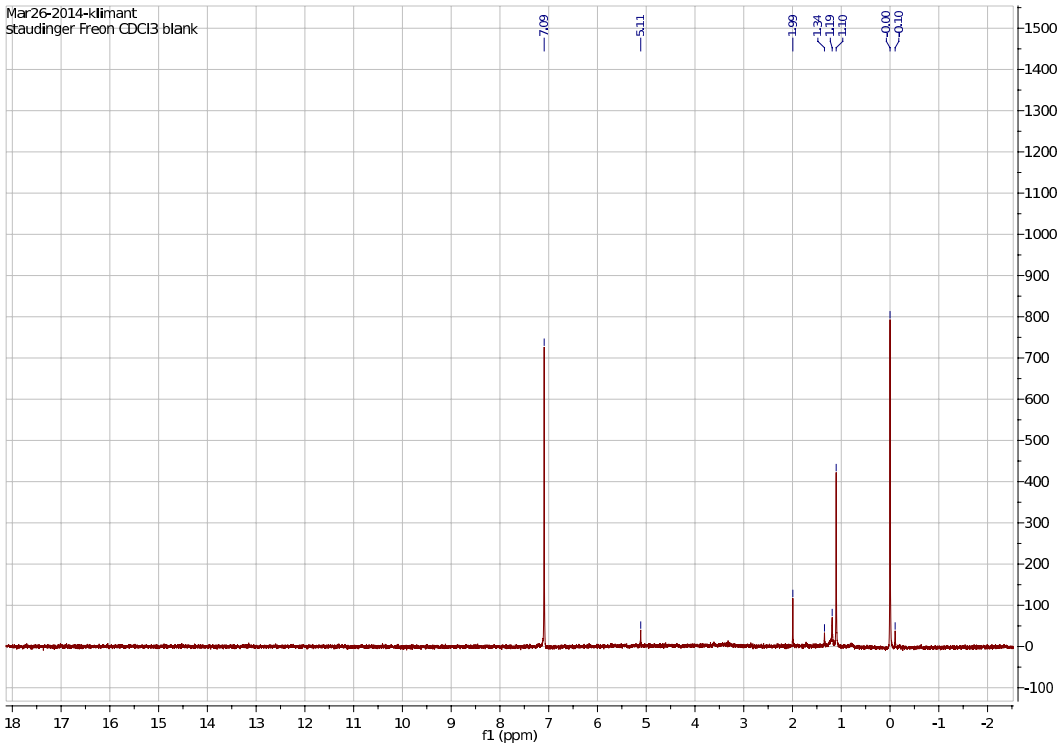

Figure 2.28: ^{1}H NMR Solvent Blank of 112-trichlortrifluoroethan + $CDCl_3$

2.8.4 Isomer Identification

To identify the exact structures of the main components of HPhNPF and HBANPF ^{1}H and COSY NMR spectra were recorded. Thereby the possible structures could be narrowed down to 5 different substitution patterns in case of HPhNPF (Figure 2.29). Furthermore NOESY spectra were recorded and no adjacencies between the duplets and singlets were found. A HMBC spectra of HPhNPF was used to identify the exact structure of its main component (Figure 2.30). The second observed substitution pattern could not be determined due to its small content and interferences in the spectra with the main component. The substitution pattern of HBANPF is very likely similar to the main component of HPhNPF because ^{1}H and COSY spectra showed no substitution on the benzannealed ring.

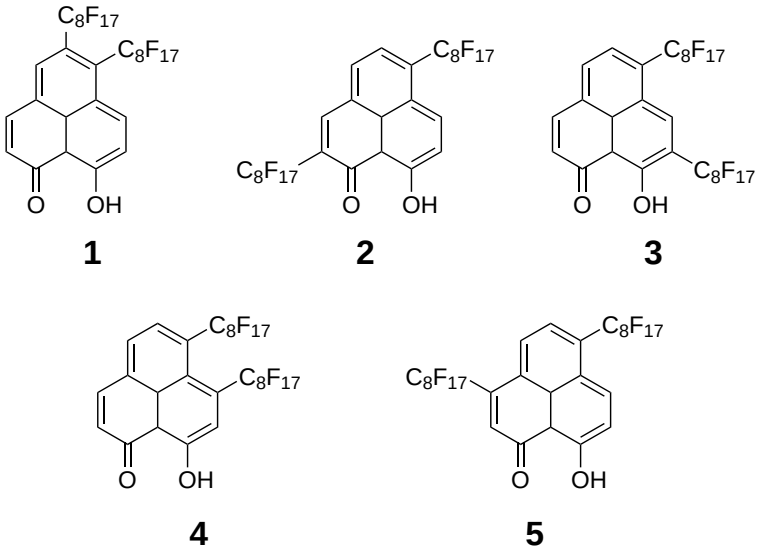

Figure 2.29: Possible Structures as determined by COSY

The interesting properties of the dyes are exhibited by the core structure of the ligands and not its perfluoroalkyl chains, which were only intruduced for solubility reasons. Furthermore no significant change in the optical properties of the dyes could be observed after substitution. Therefore and because a separation of the isomers was impossible due to their very similar properties the mixture of the isomers was utilized to synthesize the dyes.

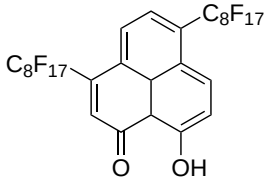

Figure 2.30: Final structure as determined by NOESY and HMBC

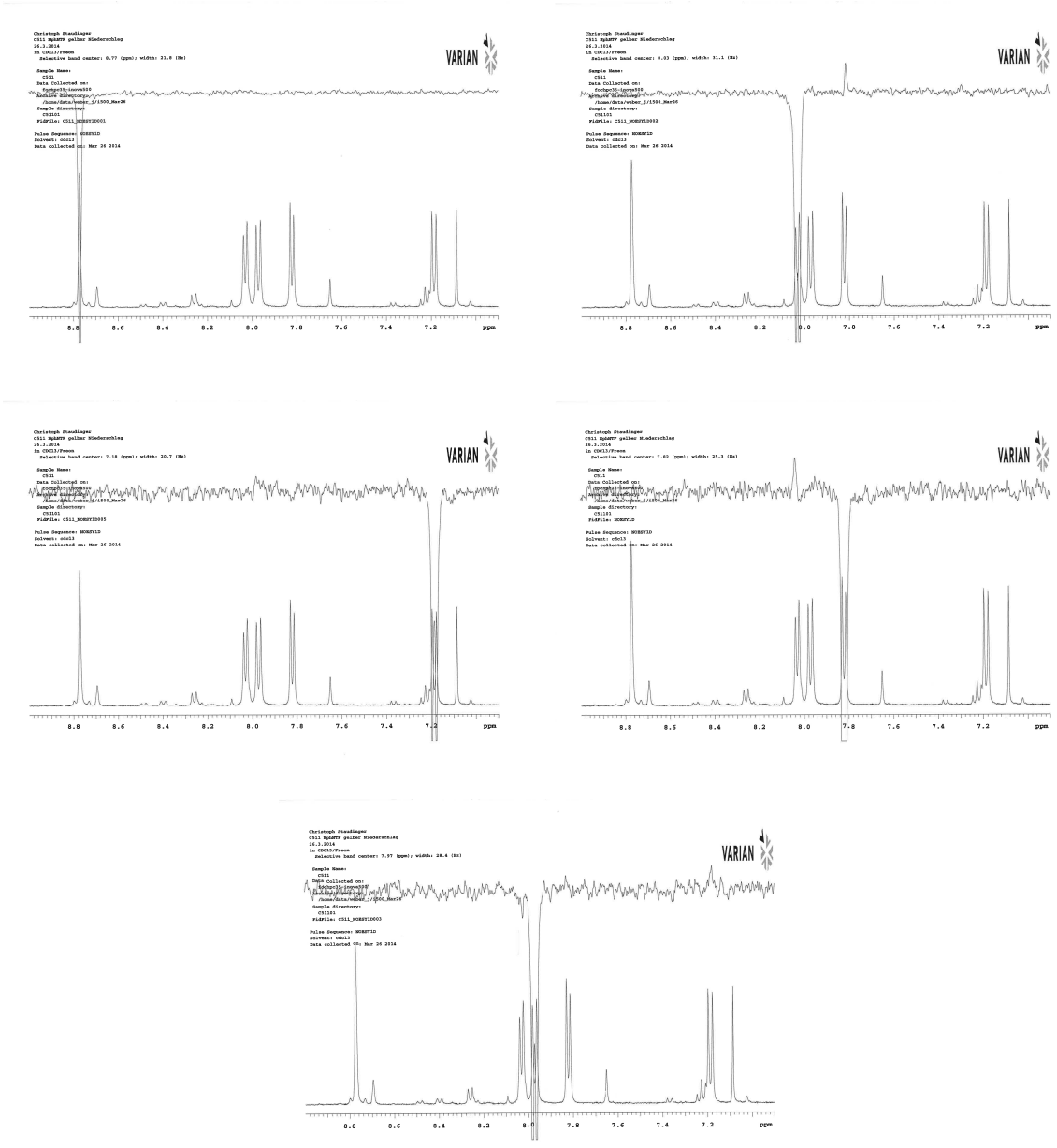

Figure 2.31: ^{1}H NOESY NMR of HPhNPF (Free Ligand)

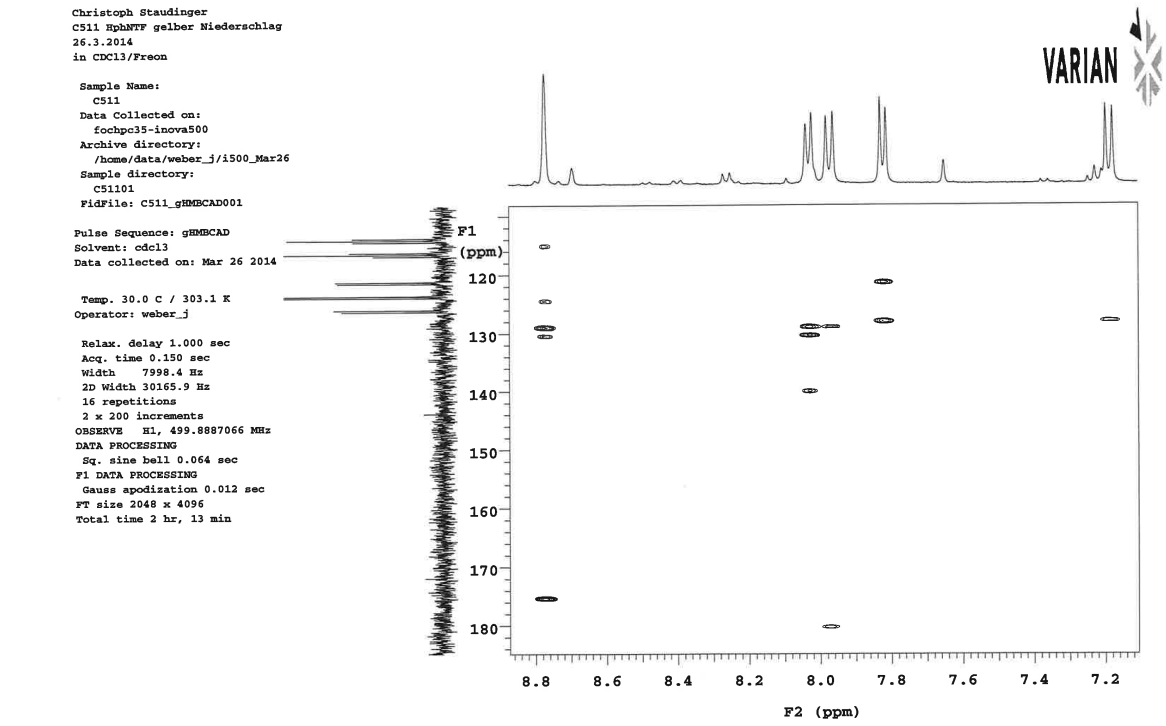

Figure 2.32: ^{1}H - ^{13}C HMBC NMR of HPhNPF (Free Ligand)

3 Intrinsic artifacts in optical oxygen sensors - How reliable are our measurements?

Philipp Lehner[1], Christoph Staudinger[1], Sergey M. Borisov[1], Johannes Regensburger[2] and Ingo Klimant[1]

[1]Institute of Analytical Chemistry and Food Chemistry, Graz University of Technology, NAWI Graz, Stremayrgasse 9, 8010 Graz, Austria.

[2]Department of Dermatology, University of Regensburg, Franz Josef Strauss Allee 11, 93053 Regensburg, Germany

Corresponding Author:
Sergery M. Borisov
tel: +43 316 873 32516
email: sergey.borisov@tugraz.at

Published in: **Chemistry - A European Journal**
Recieved: 10. Nov 2014
Published: 28. Jan 2015
doi: 10.1002/chem.201406037

3.1 Abstract

Optical oxygen sensing is of broad interest in many areas of research, such as medicine, food processing and micro- and marine biology. The operation principle of optical oxygen sensors is well established and they are routinely employed in lab and field experiments. Ultra trace oxygen sensors, which enable measurements in the sub nanomolar region (dissolved oxygen) are becoming increasingly important. Such sensors prominently exhibit phenomena that complicate calibration and measurements. However, these phenomena are not constrained to ultra trace sensors. Rather, they are inherent to the way optical oxygen sensors work and may influence any optical oxygen measurement when certain conditions are met. This is especially true for applications that deal with high excitation light intensities, such as microscopy and microfluidic applications. Herein we present various effects that we could observe in our work with ultra trace oxygen sensors and discuss the reasons for their appearance, the mechanism by which they influence measurements and how to best reduce their impact. The phenomena discussed are: oxygen photoconsumption in the sensor material, depletion of the dye ground state by high excitation photon fluxes, which can compromise both intensity- and ratiometric-based

measurements, triplet triplet annihilation, and singlet oxygen accumulation, which affects measurements at very low oxygen concentrations.

3.2 Introduction

A chemical sensor can be defined as „a miniaturized analytical device that can deliver real-time and online information on the presence of specific compounds or ions in complex samples“.[1] An ideal sensor is sensitive to the intended parameter only and does not influence or alter the measured system in any way. Optical sensors rely on the change of optical properties of a probe molecule in presence of the analyte.[2, 3] In the case of optical oxygen sensors that is the quenching of luminescence by molecular oxygen.[4] This change is then detected either as a difference in lifetime or emission intensity and equated to an oxygen concentration. For ideal systems, the relation of oxygen concentration to luminescence intensity and lifetime is described by the Stern-Volmer equation, which was derived almost a century ago.[5]

$$\frac{I_0}{I} = 1 + K_{SV} \cdot [Q] \tag{3.1}$$

With I_0 and I, τ_0 and τ being the measured luminescence intensity and lifetime, without and with quencher, respectively; K_{SV} is the Stern Volmer constant and $[Q]$ is the concentration of the quencher. The linear behavior established by this equation is rarely observed in experiments and an extension - the two site model[6, 7] - if often used instead. It assumes the occurrence of at least two distinct dye environments, or sites, with their own set of material constants and therefore different K_{SV} values.

$$\frac{I}{I_0} = \frac{f}{1 + K_{SVa} \cdot [Q]} + \frac{1 - f}{1 + K_{SVb} \cdot [Q]} \tag{3.2}$$

Where f is the relative amount of the dye contained in the first domain. Although K_{SV} is considered a material constant, it is still dependent on environmental parameters. The influence of temperature is well known[8, 9, 10, 11] and compensation is routinely employed in commercial applications. However there is an additional non-linear dependency on excitation- and ambient light intensity (or photon flux), which cannot be eliminated by ratiometric or lifetime measurements. This results in an additional cross-sensitivity to a parameter that is much harder to quantify and therefore compensate for. However, changes in ambient- and excitation light intensities are often neglected as well, because they are generally considered unnoticeably small for most common sensing systems. Nevertheless, the influence of photon flux changes can become quite noticeable and even prevalent, for instance if systems use rather high excitation intensities, dyes that have very high absorption coefficients or very long lifetimes, or deal with very low concentrations of oxygen in the sensor matrix. Particularly, a number of important methods, like fluorescence microscopy[12, 13, 14, 15] and micro fluidic applications[16, 17] are bound to suffer from the effects presented in this work. Because of the employed high excitation light intensities, that are necessitated by low dye concentrations and comparably low signal collection efficiency often encountered in these applications. Further, trace oxygen sensors are also strongly affected, because of the required long lifetimes and inherently low oxygen concentrations. While most oxygen sensors and probes are designed to be used in the physiological range (20 % - 1 % oxygen)[2, 18, 19] there is an emerging field of sensors designed for trace (<1 %)[20, 21, 22] and ultra-trace (<1 ppmv)[23, 24, 25] applications. These are interesting for various systems currently actively investigated by marine biologists[26, 27] and could become valuable to other fields, such as surface treatment[28] or industrial process

control.[29] Sensor systems designed for such applications necessarily combine some or all of the photo-physical and material properties mentioned above. One recent example are sensor materials based on aluminium chelates embedded in perflourinated matrices, that enable the measurement of very low oxygen concentrations down to the picomolar (DO) range.[25] These sensors feature exceptionally long luminescence lifetimes, efficient inter system crossing and good absorption coefficients. This enables their use as ultra trace sensors, but also leads to a very strong excitation photon flux dependency. Other oxygen sensing systems are similarly affected, but the same magnitude is only reached if they feature very high excitation intensities, such as during irradiation with laser light[30] (e.g. in microscopy applications) or at the tip of a tapered fibre.[31] In this work, materials based on boron and aluminium complexes were used to quantify the influence of excitation photon flux on K_{SV} and provide insights into the different contributing effects. We also highlight the unique challenges these dependencies imposed on ultra trace measurements.

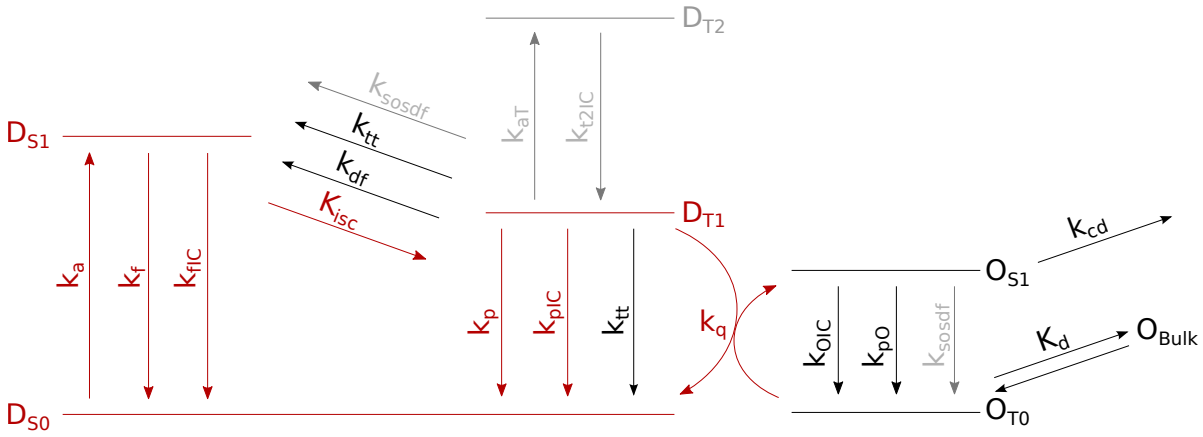

Figure 3.1: Extended Jablonski diagram of the possible states of dye and quencher molecules in an oxygen sensing material. Black lines represent components classically utilized to describe such a system, with dye ground- and excited singlet and triplet states (D_{S0}, D_{S1}, D_{T1}) and matching rate and equilibrium constants for absorption (k_a), fluorescence (k_f), inter-system-crossing (k_{isc}), phosphorescence (k_p), bimolecular quenching (k_q) and radiation-less decay constants (k_{fIC}, k_{pISC}). Solid grey lines denote additional components considered relevant for the investigated system, with oxygen ground- and excited state (O_{T0} ($^3\Sigma_g^-$), O_{S1} ($^1\Delta_g$)) and additional constants for reverse inter system crossing which results in delayed fluorescence (k_{df}), triplet-triplet annihilation (k_{tt}), physical deactivation of singlet oxygen (k_{Oisc}, k_{pO}), chemical consumption of singlet oxygen (k_{cd}) and diffusional equilibrium between sensor and bulk oxygen concentrations (K_d). And finally, dashed grey lines, which are expected to have only a minor influence on excitation photon flux dependence, with the second excited dye triplet state (D_{T2}), absorption (k_{aT}) and deactivation (k_{t2IC}) rates of the D_{T2} state and singlet oxygen sensitized delayed fluorescence(k_{sosdf}).

3.3 Results and Discussion

The Jablonski diagram in figure 3.1 shows the various states involved in an optical detection scheme based on oxygen quenching. The readout parameters typically used for oxygen determination are phosphorescence intensity ($r_p = k_p \cdot D_{T1}$) and lifetime, which depend on oxygen concentration through the quenching rate ($r_q = k_q \cdot D_{T1} \cdot O_{T0}$). In an idealized system

O_{T0} depends only on the bulk concentration (the intended measurements parameter) and D_{T1} depends linearly on the excitation intensity. For many common applications this idealized description of the physical system is sufficient. However, as seen in figure 3.1, a multitude of additional pathways exist, and if their contribution significantly alters state concentrations, the idealized model no longer holds true. This results in a non linear dependence of the readout parameters on the excitation intensity which significantly complicates measurements. Most experiments in this work were executed with excitation light photon fluxes of less than 1 mmol m^{-2} s^{-1} (20 mW cm^{-2} at 600 nm). For comparison, direct sunlight has a photon flux of approximately 1.5 mmol m^{-2} s^{-1} (30 mW cm^{-2} at 600 nm),[32] while at the tip of a tapered optical fibre the photon density can be as high as 1000 mmol m^{-2} s^{-1} (20 W cm^{-2} at 600 nm),[31] and densities can be up to three magnitudes higher in confocal laser microscopy.[33] To better understand the experimental data, we created a mathematical model (available as mathematica notebook or .cdf file in the supporting information) that describes the system summarized in figure 3.1 in a steady state and can therefore be used to simulate the effects of different changes in the system.

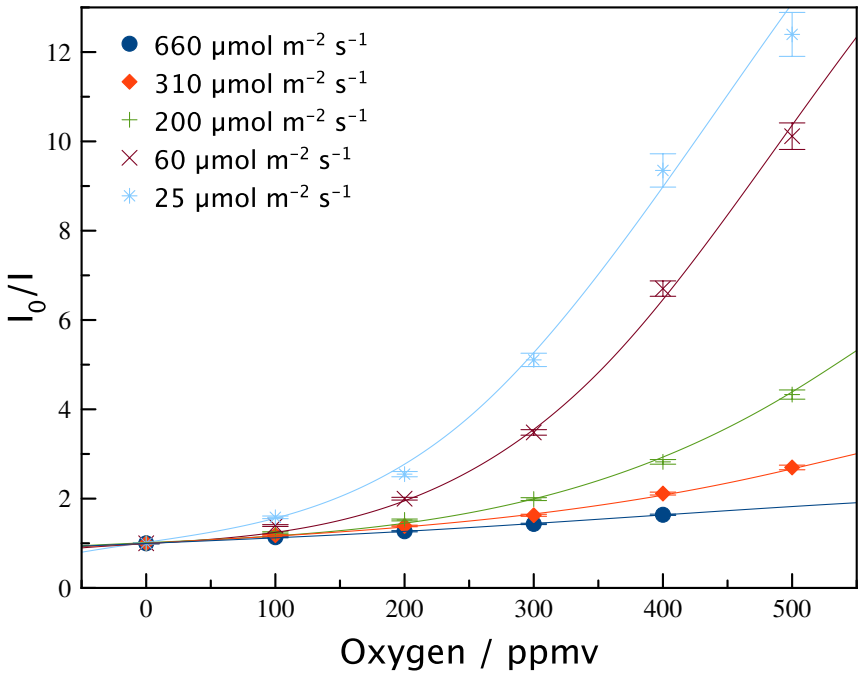

Figure 3.2: Intensity based calibration curves of 0.5 % (w/w) BF_2HPhN in polystyrene, acquired at 20 °C at different excitation photon fluxes. The calibration curves show a drastic decrease of sensitivity at higher light intensities and generally a characteristic upward curvature. This curvature is the result of the influence of oxygen photoconsumption decreasing at higher oxygen concentrations so that the curves show linear areas where the slope is identical. The area where the curve becomes linear again is shifted to higher oxygen concentrations at higher excitation light intensities.

3.3.1 Photoconsumption of Oxygen

An easily overlooked error in optical oxygen measurements is that the measured oxygen concentration does not necessarily relate to the bulk concentration through a simple solubility ratio but actually depends on a formed diffusional equilibrium of oxygen. Normally the oxygen concentration in the sensor material will conform to the solubility ratio (after the materials specific response time), but this is no longer a valid assumption if oxygen is actively consumed in the sensor layer, thereby shifting the diffusional equilibrium. An often cited advantage of optical oxygen sensors in respect to other methods, such as Winkler titration or the Clark electrode, is that they do not consume the analyte. However, singlet oxygen, which is formed in the photo-physical deactivation process, is known to be a highly reactive species. If the matrix, impurities, or the dye itself, are prone to oxidation a certain part of the generated oxygen will be chemically consumed and is therefore no longer available for further photo-physical interactions.[34, 35] The amount of singlet oxygen, and therefore its reaction rate, is directly proportional to the amount of probe molecules in the excited state (and therefore excitation light density). In the case of oxygen photoconsumption the dependence on excitation light intensity is observed as a characteristic change in the form and K_{SV} of the calibration curve. In Figure 3.2 intensity based calibrations of the sensor material BF_2HPhN in PS are shown (see figure 3.9 for structures and spectra of BF_2HPhN). Polystyrene is widely regarded as a very stable and suitable matrix for optical oxygen sensors. However, in trace sensor systems even the comparably small reactivity of polystyrene[34] has a large impact on the sensors response. One can observe a drastic decrease in sensitivity at higher excitation photon fluxes and an upward bend that is characteristic for oxygen photoconsumption. The calibrations are curved at first and then transition to steeper linear curves that have an almost parallel offset to a theoretical ideal calibration (compare with figure 3.10 and the model file). This is a result of the quenching rate (r_q) reaching saturation because of a limited supply of D_{T1}, while the diffusion rate increases linearly with rising oxygen concentrations. As predicted, the calibrations further show a dependence on the excitation light photon flux, due to the mentioned direct correlation of excited dye concentration and oxygen consumption rate. Because this effect changes the actual oxygen concentration in the sensor film it is observed in both intensity and lifetime measurements (figure 3.11).

Figure 3.3 shows the luminescence response of such a sensor material over time. One can see that the luminescence intensities are comparable at the start of the measurement. But in a timeframe of a couple seconds the system transitions to a new steady state defined by the equilibrium constant of oxygen consumption and diffusion rates. This results in the different K_{SV}s observed in figure 3.2 (which were obtained after enough time has passed to transition to the new equilibrium). Such behaviour has been reported previously, but not to this extent.[22] In this previous work the consumption was the result of volatile compounds embedded in the matrix which could be removed under vacuum or oxidized to achieve stable sensors. Of course in this current case, it is most likely the matrix itself that is the oxidizable compound. So while continuous irradiation, and therefore generation and subsequent reaction of singlet oxygen with reactive groups in the polymer, can reduce the effect over time (Figure 3.12), a true equilibrium is not easy to reach. In addition, the matrix properties might change significantly once all available groups have been brought to reaction with oxygen. Still, such a „conditioning“ of the sensor material does increase K_{SV} values obtained at high light intensities, as seen in figure 3.13. Basically, in this scenario, the sensor material changes its calibration characteristics not only with excitation light intensity but also during the measurement in a timescale of seconds and additionally slightly with each measurement. This, of course, results in either

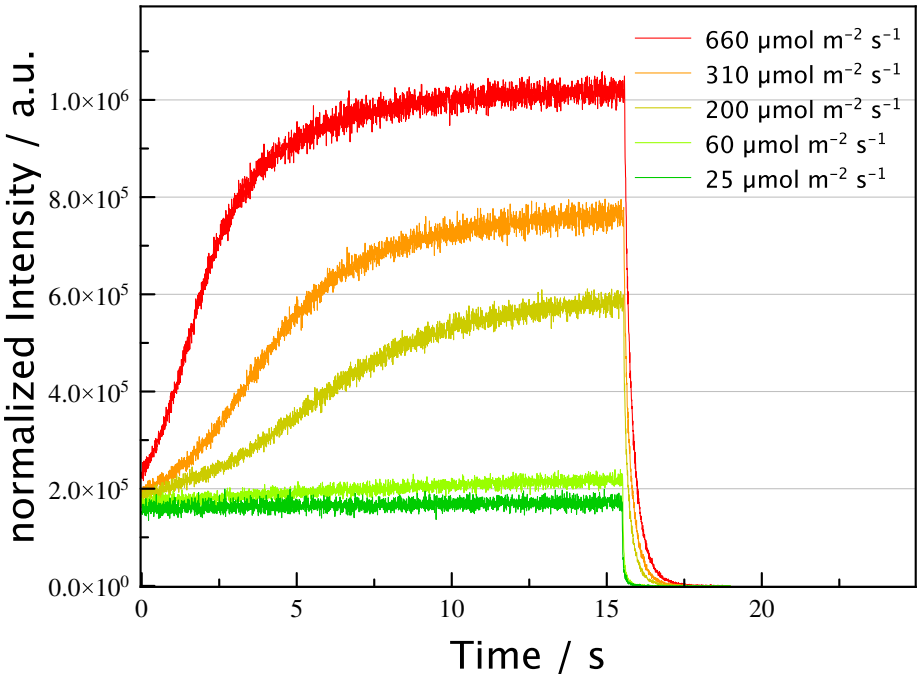

Figure 3.3: Time resolved response of the 0.5 % (w/w) BF_2HPhN in PS material at 20 °C to illumination with different photon fluxes at a fixed oxygen concentration of 500 ppmv. The formed equilibrium is dependent on the reaction rate of singlet oxygen and therefore the deviation from ideal behaviour becomes smaller at lower photon fluxes. Plotted intensity is normalized to excitation intensity.

unreliable measurements or almost unreasonably tedious calibration and correction efforts from a prospective end user. While this effect is arguably minor in most measurements in the physiological range, it is definitely not restricted to the investigated ultra-trace dyes (compare figure 3.3 to figure 3.14). Especially for measurements in very low concentration ranges the effect of oxygen photoconsumption has to be eliminated. The ideal matrix in this case are materials like Hyflon and Teflon AF, which are perfluorinated polymers that are chemically inert and have very high oxygen permeabilities.[36, 37] For such materials perflourinated dyes like $Al(HPhNPF)_3$ have to be used (for structure and photo-physical properties of $Al(HPhNPF)_3$ see figure 3.15-3.17). While the resulting sensors are very sensitive, they are also inherently more difficult to calibrate, because minuscule amounts of oxygen contaminating the setup already have a large effect on resulting calibrations. Therefore, Cytop A was chosen as an oxidation stable matrix for the experiments performed in this work, as its lower permeability (comparable to PS) made obtaining calibrations decisively easier, while enabling investigation of the remaining phenomena in absence of oxygen photoconsumption.

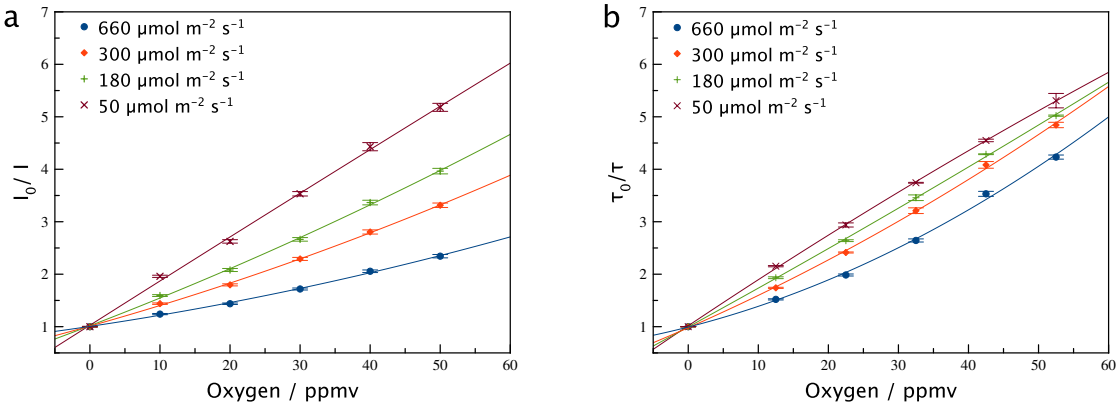

Figure 3.4: Calibration of $Al(HPhNPF)_3$ 0.2 % w/w in Cytop A at 20 °C, both intensity (a) and time domain based (b). Because of ground state depletion the dependency is larger in intensity based calibrations.

3.3.2 Depletion of the Dye Ground State

Even if oxygen photoconsumption is eliminated there exist a number of other effects that result in a dependence of the sensor sensitivity on excitation photon flux. One such effect is the depopulation of the dye ground state. The underlying principle is that the relationship between excitation light photon flux and excited dye concentration is not linear but instead, in accordance with the principles established in figure 3.1, follows a saturation curve. This is a trivial result of the dye only being in finite supply. It is, however, often overlooked or ignored because the concentration of the excited state is usually much smaller than the concentration of the ground state. In these cases the relation is therefore very close to being linear. However, if a significant amount of dye is excited, either as a result of high light intensities like they are common in e.g. microscopy applications or due to other factors that increase triplet state concentration, such as long lifetimes or high molar absorption coefficients, the effect becomes very noticeable in intensity-based or ratio metric measurements. As the lifetime is not dependent on the actual concentration of the excited triplet state, lifetime

measurements are unaffected by this phenomenon. However, as was shown,[31] this is only true for time- domain measurements, frequency domain and shark fin measurements are still affected because they include the rise time in their signal determination. Figure 3.4 compares intensity-based calibrations of $Al(HPhNPF)_3$ in Cytop A at different excitation photon fluxes, the observed difference in the intensity calibration is predominantly caused by ground state depletion. To verify that the use of Cytop A instead of Hyflon AD 60 for the rest of the experiments is legitimate, the same calibrations were performed with $Al(HPhNPF)_3$ in Hyflon (figure 3.18) which show the same general phenomena. To further verify that ground state depletion is significant, absorption experiments were performed in a photometer with additional excitation through a high intensity light source. Unfortunately, casting the thick films required for absorption measurements proved difficult with the perflourinated dyes embedded in Hyflon or Cytop A. Therefore, the boron complex of HBAN (for structure and spectral properties see figure 3.19) embedded in polystyrene was used for this experiment, the results of which are shown in figure 3.5. It unambiguously shows the reduction of ground state absorption at higher light intensities and the formation of a broad triplet absorption peak. In addition, one can see that the effect is higher at lower dye concentrations, which can be attributed to the lower efficiency of triplet-triplet annihilation that results in longer triplet state lifetimes. Interestingly, the high amount of ground state depletion exhibited by this system can be used to create a material that responds to oxygen concentration increase by an increase in fluorescence intensity, albeit at a lower resolution compared to the phosphorescence band. This is a direct result of regular oxygen quenching, which repopulates the dye ground state. An example of this phenomenon can be seen in figure 3.20. We also applied the developed steady-state model to the experimental data and it shows good correlation to experimental results, as can be seen in figure 3.21. Although the effect of ground state depletion is not visible in lifetime measurements and the overall influence of excitation light photon flux is therefore greatly reduced for this type of measurements, a significant dependency still remains. This dependency is presumably an effect of the remaining phenomena discussed in this work, which do influence luminescence lifetimes: triplet-triplet annihilation and singlet oxygen accumulation.

3.3.3 Triplet-Triplet Annihilation

Triplet-Triplet Annihilation: Triplet-triplet annihilation is a well studied process, whose efficiency directly depends on the excited triplet state concentration of the dye, as it is a bimolecular quenching reaction of two excited dye molecules. The collision leads to the deactivation of one dye molecule and the elevation of the other into the excited singlet state, from which deactivation follows the regular pathways. This is an intended process in so called up- conversion systems,[38, 39] and offers certain application specific advantages. In regular phosphorescence-based measurements it is an unwanted influence as it removes the independence of the lifetime on triplet state concentration. As such, the easiest way to minimize the influence of triplet triplet annihilation is to reduce exited triplet state concentration, either by reducing overall dye concentration or by lowering photon flux. Figure 3.6 shows the dependency of τ_0 on both dye concentration and photon flux for the $Al(HPhNPF)_3$ embedded in Cytop A sensor material. Surprisingly, the influence of dye concentration is more significant than the influence of light intensity. That influence is too small to explain the remaining excitation light dependence of the sensor in figure 3.4b, which suggests that there is an additional phenomenon affecting lifetime based calibrations.

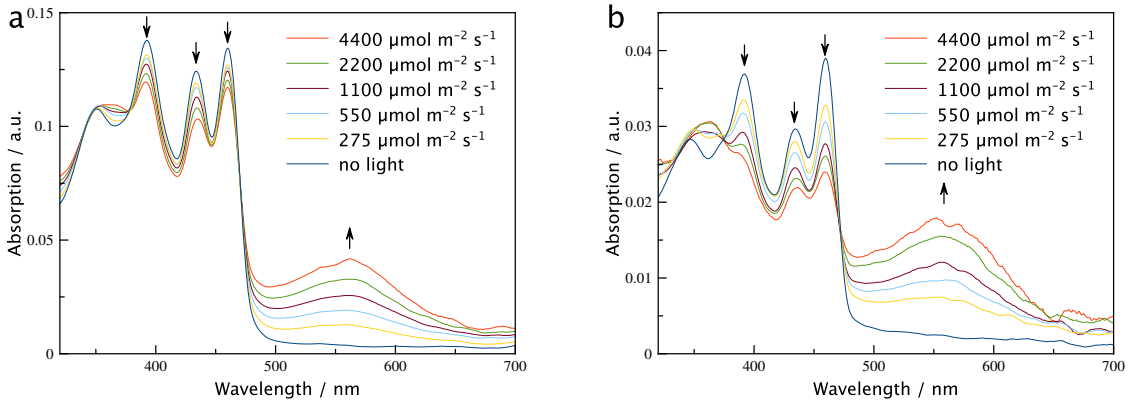

Figure 3.5: „Flash photolysis“ experiments of BF_2(HBAN) 0.5 % (a) and 0.1 % (b) (w/w) embedded in a polystyrene matrix at room temperature. At higher light intensities ground state absorption is noticeably reduced and a broad triplet absorption peak appears. This effect is smaller at higher dye concentrations due to the mitigating effect of triplet-triplet annihilation, which repopulates the dye ground state. A deoxygenated sensor sheet was placed in a photometer and continuously illuminated by a variable light source at a 45 degree angle. A schematic drawing of the setup is shown in figure 3.22.

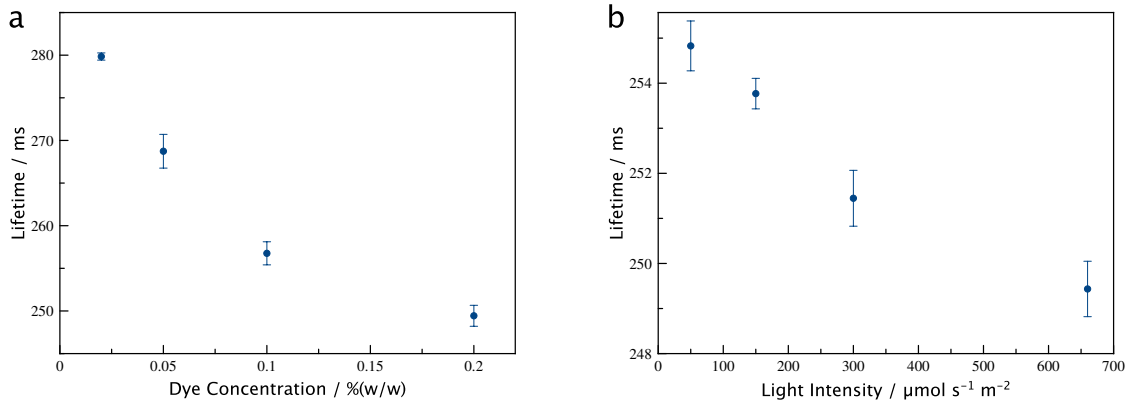

Figure 3.6: The influence of dye concentration on the lifetime of Al(HPhNPF)$_3$ in Cytop A at 660 µmol m^{-2} s^{-1} photon flux, 20 °C and deoxygenated conditions (a); of photon flux at constant dye concentration of 0.2 % (w/w) Al(HPhNPF)$_3$ in Cytop A, at 20 °C and deoxygenated condition (b). Both parameters influence triplet state concentration and therefore also influence triplet state lifetime, as triplet-triplet annihilation is a bimolecular reaction.

3.3.4 Singlet Oxygen Accumulation

This additional influence, which, to the best of our knowledge has never been reported, is very likely specific for measurements in the ultra trace region. To understand this effect, one has to consider the actual amount of the involved dye and oxygen molecules. The experiment in figure 3.4 was performed with a dye concentration of 0.2 % (w/w) in respect to the matrix, which translates to a dye concentration of roughly 2 mM, whereas the concentration of oxygen in the matrix at 10 ppmv oxygen corresponds to roughly 100 nM. If the population of the excited triplet state is significant, the amount of excited dye molecules is at least one magnitude higher than the oxygen concentration in the sensor film (probably more if one considers figure 3.5). This means that, if one ignores diffusional exchange from the bulk, one oxygen molecule has to quench tens or hundreds of dye molecules during one decay period in a time domain based lifetime determination. Additionally, the amount of dye molecules which a single ground-state oxygen molecule can quench is not only governed by quenching probability and diffusion rates but also by the time it takes for the oxygen molecule to return to the ground state between quenching events. Unfortunately, the lifetime of singlet oxygen can be very long, it is around 4 μs in water but can be in the order of several milliseconds or longer in perfluorinated solvents, apparently this is caused by the lack of hydrogen atoms and therefore the absence of high energy C-H and O-H vibrations that can participate in electronic to vibrational energy transfer quenching of singlet oxygen.[40] Our measurements show that the lifetime of singlet oxygen in polystyrene is approximately 30 μs whereas in Hyflon it is at least 1.2 ms (see figure 3.23 and 3.24). The increase is caused most likely by the lack of hydrogen atoms in perfluorinated matrices. While perfluorinated matrices are an absolute necessity for ultra-trace oxygen sensors due to their excellent oxidation stability, they amplify the effect of oxygen ground state depletion in the sensor matrix. To illustrate these effects, the steady state model was used as a starting point and expanded to a time-dependent system that simulates state concentrations during a decay process as it is observed during a time domain measurement (see the supporting material). Figure 3.7 shows the results obtained for a simulation of the used sensor system at different light intensities.

This model ignores diffusional interchange between bulk and sensor material in the timeframe of the measurement which, due to the high permeability of the used polymers, reduces the impact of this problem but also adds potential additional dependencies on film thickness, flow velocity, etc. However, comparison of the results of the lifetime measurements in figure 3.4 with the triplet-triplet induced changes in τ_0 in figure 3.6 leads to the conclusion that there has to be an additional effect linking excitation photon flux to K_{SV}. We propose that this is the result of singlet oxygen accumulation. Another theoretically possible explanation would be singlet oxygen sensitized delayed fluorescence (SOSDF),[41] but the effect is unlikely to be very efficient at such unfavourable ratios of dye and oxygen concentrations. However, considering the overall small amount of delayed fluorescence generated by this effect it was not possible for us rule it out, as the used dyes already exhibit strong *e*-type delayed fluorescence, and the influence of SOSDF (if any) could therefore not be quantified. To reduce the effect of singlet oxygen accumulation, one needs to minimize the ratio of dye excited state to oxygen ground state either by lowering excitation intensities or lowering overall dye concentration, thereby imposing a limit on achievable signals for ultra trace sensor materials. Figure 3.8 shows two sensor materials with lower dye concentrations than the one used in figure 3.4 and their respective calibration curves for different excitation photon fluxes. It is apparent that the dependency of calibration curves on the excitation photon flux decreases for lifetime-based measurements at lower dye concentrations. Not surprisingly, for intensity-based measurements

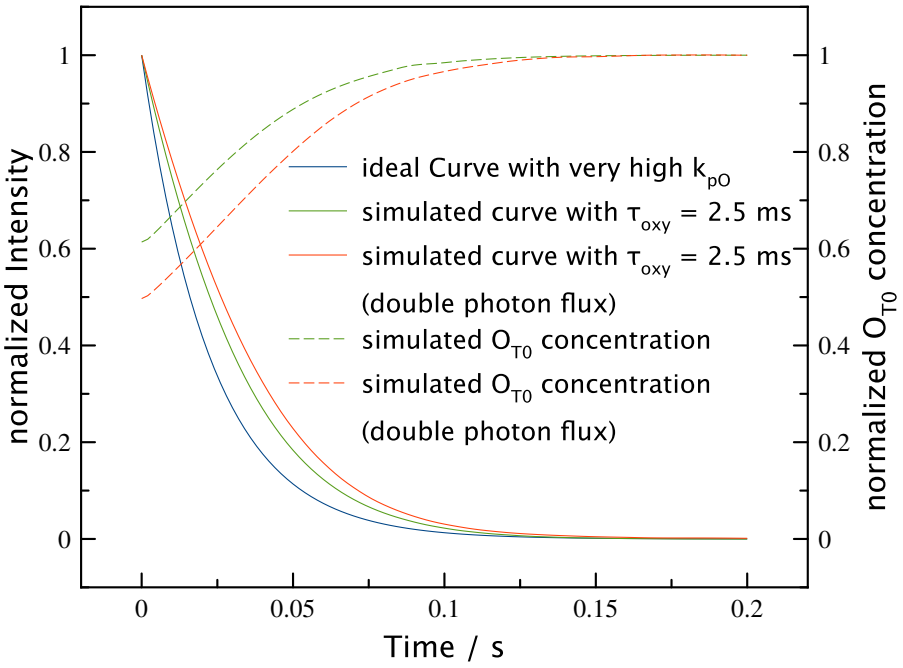

Figure 3.7: Qualitative simulation of decay curves obtained for different light intensities at an approximate oxygen concentration of 1 ppmv, the singlet oxygen lifetime has been doubled from the experimentally determined value to make the effect more visible.

it remains mostly the same, as the influence in these measurements is dominated by the effects of dye ground state depletion. Interestingly, our measurements suggest that an introduced dye can act as a quencher for singlet oxygen (figure 3.23). Given the high chemical stability of the porphyrin dye used for this experiment the deactivation process is most likely based on physical deactivation through the introduced C-H bonds. This implies, that the introduction of a physical quencher like the ones proposed by Enko et. al.[34] might help reduce singlet oxygen lifetimes and therefore the magnitude of this phenomenon. Unfortunately these compounds are usually not soluble in perflourinated matrices.

3.4 Conclusion

We demonstrated that oxygen measurements become much more challenging if measurement conditions require either high excitation photon fluxes, extraordinary dye properties or low oxygen concentrations. For trace and ultra-trace oxygen sensor materials, the demonstrated phenomena have a prominent influence on obtained calibration curves. In accordance with our results, chemical consumption of oxygen in the sensor layer has to be completely eliminated to obtain reproducible measurements. Time domain-based measurements are preferable to intensity or ratio metric measurements, due to the eliminated influence of ground state depletion. However, even time domain based measurements are not completely independent of excitation photon flux. To counter both triplet-triplet annihilation and singlet oxygen accumulation based influence, minimizing dye concentration or excitation photon flux are the best options. In real world measurement systems, this is limited by the sensitivity of the corresponding read-out

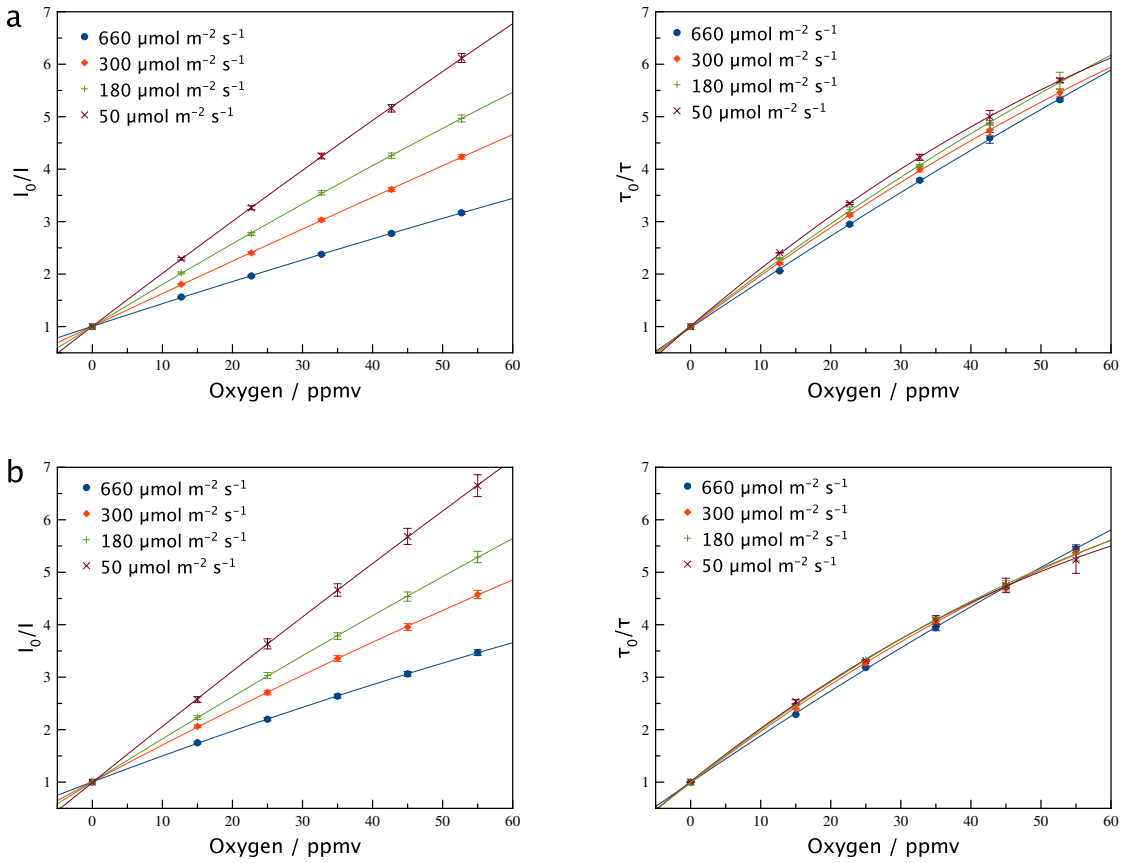

Figure 3.8: Calibration of Al(HPhNPF)$_3$ 0.1 % (a) and 0.05 % (b) w/w in Cytop A at 20 °C, both intensity (left) and time domain based (right). Because of ground state depletion the dependency is larger in intensity based calibrations. The excitation light intensity dependence in lifetime based calibrations is dominated by singlet oxygen accumulation. As the magnitude of this effect is directly dependent on triplet state concentration, it decreases for lower dye concentrations. Please note that for lifetime measurements the signal gain was chosen so that the signal intensity is constant for all datapoints as there is a slight dependency of fit quality on initial signal amplitude. In the lifetime plot of 0.05 % (w/w) Al(HPhNPF)$_3$ in Cytop A the signal could not be kept constant for the two highest oxygen concentrations of the two lowest excitation intensities as the instrument was operating at its limit. The apparent effect that calibration curves cross at higher oxygen concentrations should therefore be treated with caution and is likely an artefact. The most likely scenario for calibration curves is to converge at concentrations high enough for singlet oxygen consumption to be negligible.

device. Thicker films help to keep the concentration low and still achieve moderate signal intensities, although this results in a trade-off leading to longer response times and possibly increased singlet oxygen accumulation. Reflector films and optimized readout geometry are additional tuning factors to increase signal. In the end a balance has to be found for specific applications. An interesting further implication of our work is, that if the excitation photon flux can be exactly known, sensor sensitivities are effectively tuneable by changing excitation photon fluxes, and for intensity based measurements even a probe that shows fluorescence increase with oxygen concentration is feasible. Finally, the computational model we prepared to simulate the experimentally observed effects shows good correlation with results (figure 3.21, avg. $R^2 = 0.986$) and is capable of qualitative prediction of different photo physical phenomena. In summary, when doing measurements with optical oxygen sensors under extreme conditions, one should carefully consider the photophysical processes involved and what influence they might have on results. The extraordinary properties of such systems result in the dye concentration no longer being insignificantly small compared to the oxygen concentration, or the bulk oxygen concentration no longer being directly proportional to the concentration in the sensor material. This manifests as a dependence of K_{SV} on the intensity of excitation light. The various experiments performed in this work highlight the different macroscopic reasons for this dependence such as using dyes with high absorption coefficients and/or long lifetimes, when employing high excitation light intensities, measuring low oxygen concentrations or having an environment that readily reacts with singlet oxygen. These effects are not easy to distinguish from each other and materials and experiments in this work were carefully chosen to highlight specific influences. For most users of optical sensors minimizing all these influences or at least quantifying them will be enough. It should be kept in mind that keeping excited dye concentration low drastically reduces the impact of all the effects presented in this work. If obtaining high enough signals is a problem for a given setup and "sensing chemistry", improving the emission collection efficiency is the preferable approach to increasing of the excited dye concentration. Of course, synthesis of new dyes with higher quantum yields will also help to further minimize the undesirable effects.

3.5 Experimental Section

3.5.1 Materials

Nitrogen (99.9999 % purity) and test gases (1,000 ppmv O_2, rest N_2; and 20 ppmv O_2, rest N_2) were obtained from Linde Gas (Austria; www.linde.at), Hyflon AD 60 was obtained from Solvay (USA; www.solvayplastics.com). Cytop A was from Asahi (Japan, www.agc.com). Silicon E4 from Wacker (Germany; www.wacker.de). PS (MW 250 000) was obtained from Fisher Scientific. Aquaphobe CF was bought from ABCR (Germany; www.abcr.de). Sodium sulphite was obtained from Carl Roth (www. carlroth.com). Acetone and ethanol were acquired from Brenntag (Germany; www.brenntag.de), and remaining solvents were from VWR (Austria; www.at.vwr.com). Pyrenbutyric acid was from Sigma Aldrich. Platinum(II)-5,10,15,20-tetrakis-(2,3,4,5,6-pentafluorphenyl)-porphyrin (Pt-PFPP) and Palladium(II)-5,10,15,20-tetrakis-(2,3,4,5,6-pentafluorphenyl)-porphyrin (Pd-PFPP) were from Frontier Scientific (UK, www.frontiersci.com), BF_2HPhN, BF_2HBAN and Al(HPhNPF)$_3$ were synthesized according to the literature procedure.[25]

3.5.2 Preparation of the polystyrene-based sensor material films

The sensor films were prepared by dissolving the appropriate amount of dye in a solution of polystyrene 5 % (w/w) in chloroform. This „cocktail“ was subsequently knife-coated with a 75 µm spacer onto a glass substrate. The substrates were then dried in a vacuum oven.

3.5.3 Preparation of the Cytop A and Hyflon-based sensor material films

The sensor films were prepared by dissolving the appropriate amount of dye in a solution of either Cytop A or Hyflon AD (5 % (w/w) respectively) in octafluorotoluene. Cytop A is only available as solution in a specialized solvent and has to be dried before it can be redissolved in octafluorotoluene. This „cocktail“ is then knife-coated with a 75 µm spacer onto a glass substrate that has been treated with Aquaphobe CF. The substrates were then dried in a vacuum oven.

3.5.4 Preparation of the BF_2HBAN in PS sensor films for „flash photolysis“ experiments

The appropriate amount of dye is dissolved in a solution of PS (10 % w/w) in chloroform. The resulting „cocktail“ is then knife coated onto specially cut, 1 cm wide glass substrates using a 75 µm spacer with an additional spacer of 200 µm, resulting in a total thickness of the wet film of approximately 275 µm. The substrates were then dried in a vacuum oven.

3.5.5 Measurements

Absorption spectra were acquired on a Cary 50 UV-VIS spectrophotometer from Varian and the emission spectra and intensity calibrations were acquired on a Fluorolog 3 fluorescence spectrometer from Horiba Scientific equipped with a R2658 photomultiplier from Hamamatsu. The luminescence decay time calibrations were performed with the Fluorolog 3 spectrometer in kinetic acquisition mode. Calibrations were obtained using a temperature controlled flow-through cell combined with a gas-mixing device from Voegtlin (Switzerland; www.red-y.com), which was used to mix nitrogen with 1,000 ppmv O_2 testgas for polystyrene and Cytop A based sensors and 20 ppmv O_2 test gas for Hyflon AD 60 based sensors. Calibrations for the Cytop A and Hyflon measurements were further corrected for impurities in the nitrogen gas by a standard addition method. The lifetime in oxygen free sodium sulfite solution was used in combination with the lifetime under nitrogen to calculate intrinsic contamination. All calibration points of a measurement were corrected for this offset. To achieve different photon fluxes, neutral density filters from qioptiq (Germany, www.qioptiq-shop.com) were placed in the excitation beam path of the Fluorolog 3. „Flash Photolysis“ Experiments were performed in the Cary spectrophotometer with a 455 nm high power LED obtained from Roithner Lasertechnik, arranged according to the schematic in figure 3.22. Photon fluxes were determined with a LI 250A Lightmeter from LI-COR. Simulations were created in Mathematica from Wolfram. Please see the supporting information for more details about the model. Time resolved singlet oxygen measurement were performed as described in the literature,[42] with the following settings: Pt-PFPP in Teflon and Hyflon was excited at 505 nm with 11 mW for 10 seconds, pyrenbutyric acid was excited at 347 nm with 9 mW for 10 seconds, 0.1 % Al(HPhNPF)3 in Hyflon was excited at 462 nm with 10 mW for 30 seconds and the different concentrations of Pt-PFPP in Hyflon were excited for 30 seconds at 505nm and 10mW. All measurements were repeated at least three times using the same sensor material. For oxygen photoconsumption experiments

different areas of the same sensor sheet were used for repeated experiments. When intensity and lifetime calibrations are presented for the same material they were also obtained using the same sensor sheet.

3.6 Acknowledgement

The work was financially supported by the European Research Council (Project 'Oxygen', N 267233).

3.7 References

[1] Otto S Wolfbeis. "Editorial: Probes, Sensors, and Labels: Why is Real Progress Slow?" In: *Angewandte Chemie International Edition* 52.38 (Aug. 2013), pp. 9864–9865.

[2] Xu-Dong Wang and Otto S Wolfbeis. "Optical methods for sensing and imaging oxygen: materials, spectroscopies and applications." In: *Chemical Society Reviews* 43.10 (May 2014), pp. 3666–3761.

[3] Colette McDonagh, Conor S Burke, and Brian D MacCraith. "Optical Chemical Sensors". In: *Chemical reviews* 108 (2008), pp. 400–422.

[4] Michela Quaranta, Sergey M Borisov, and Ingo Klimant. "Indicators for optical oxygen sensors." In: *Bioanalytical reviews* 4.2-4 (Dec. 2012), pp. 115–157.

[5] Otto Stern and Max Volmer. "Über die Abklingzeit der Fluoreszenz". In: *Physikalische Zeitschrift* 20 (Sept. 1919), pp. 183–188.

[6] ER Carraway and JN Demas. "Photophysics and Photochemistry of Oxygen Sensors Based on Luminescent Transition-Metal Complexes". In: *Analytical Chemistry* 63 (1991), pp. 337–342.

[7] J N Demas, B A DeGraff, and Wenying Xu. "Modeling of Luminescence Quenching-Based Sensors: Comparison of Multisite and Nonlinear Gas Solubility Models". In: *Analytical Chemistry* 67.8 (Apr. 1995), pp. 1377–1380.

[8] Christof Grewer and Hans Dieter Brauer. "Temperature dependence of the oxygen quenching of .pi..pi.*-singlet and .pi..pi.*-triplet states of singlet oxygen sensitizers". In: *The Journal of Physical Chemistry* 97.19 (May 1993), pp. 5001–5006.

[9] Carlos Baleizão, Stefan Nagl, and Michael Schäferling. "Dual Flourescence Sensor for Trace Oxygen and Temperature with Unmatched Range and Sensitivity". In: *Analytical Chemistry* 80 (July 2008), pp. 6449–6457.

[10] S M Borisov, A S Vasylevska, Ch Krause, and O S Wolfbeis. "Composite Luminescent Material for Dual Sensing of Oxygen and Temperature". In: *Advanced Functional Materials* 16.12 (Aug. 2006), pp. 1536–1542.

[11] B Zelelow, G E Khalil, G Phelan, and B Carlson. "Dual luminophor pressure sensitive paint: II. Lifetime based measurement of pressure and temperature". In: *Sensors and Actuators B* (2003), pp. 1–11.

[12] Alina V Kondrashina, Ruslan I Dmitriev, Sergey M Borisov, Ingo Klimant, Ian O'Brien, Yvonne M Nolan, Alexander V Zhdanov, and Dmitri B Papkovsky. "A Phosphorescent Nanoparticle-Based Probe for Sensing and Imaging of (Intra)Cellular Oxygen in Multiple Detection Modalities". In: *Advanced Functional Materials* 22.23 (July 2012), pp. 4931–4939.

[13] Sara Prior, Ara Kim, Toshitada Yoshihara, Seiji Tobita, Toshiyuki Takeuchi, and Masahiro Higuchi. "Mitochondrial respiratory function induces endogenous hypoxia." In: *PloS one* 9.2 (2014), e88911.

[14] Juan López-Gejo, David Haigh, and Guillermo Orellana. "Relationship between the microscopic and macroscopic world in optical oxygen sensing: a luminescence lifetime microscopy study." In: *Langmuir* 26.3 (Feb. 2010), pp. 2144–2150.

[15] Mohammad A Yaseen, Vivek J Srinivasan, Sava Sakadzić, Weicheng Wu, Svetlana Ruvinskaya, Sergei A Vinogradov, and David A Boas. "Optical monitoring of oxygen tension in cortical microvessels with confocal microscopy." In: *Optics express* 17.25 (Dec. 2009), pp. 22341–22350.

[16] Samantha M Grist, Lukas Chrostowski, and Karen C Cheung. "Optical oxygen sensors for applications in microfluidic cell culture." In: *Sensors (Basel, Switzerland)* 10.10 (2010), pp. 9286–9316.

[17] Christopher J Ochs, Junichi Kasuya, Andrea Pavesi, and Roger D Kamm. "Oxygen levels in thermoplastic microfluidic devices during cell culture." In: *Lab on a chip* 14.3 (Feb. 2014), pp. 459–462.

[18] Yutaka Amao. "Probes and Polymers for Optical Sensing of Oxygen". In: *Microchimica Acta* 143.1 (Sept. 2003), pp. 1–12.

[19] Andrew Mills. "Controlling the sensitivity of oxygen sensors". In: *Sensors and Actuators B* 51 (Nov. 1998), pp. 60–68.

[20] Guoqing Zhang, Gregory M Palmer, Mark W Dewhirst, and Cassandra L Fraser. "A dual-emissive-materials design concept enables tumour hypoxia imaging." In: *Nature materials* 8.9 (Sept. 2009), pp. 747–751.

[21] Yutaka Amao, Keisuke Asai, Ichiro Okura, Hiromi Shinohara, and Hiroyuki Nishide. "Platinum porphyrin embedded in poly (1-trimethylsilyl-1-propyne) film as an optical sensor for trace analysis of oxygen". In: *The Analyst* 125.11 (2000), pp. 1911–1914.

[22] Sergey M Borisov, Philipp Lehner, and Ingo Klimant. "Novel optical trace oxygen sensors based on platinum(II) and palladium(II) complexes with 5,10,15,20-meso-tetrakis-(2,3,4,5,6-pentafluorphenyl)-porphyrin covalently immobilized on silica-gel particles." In: *Analytica Chimica Acta* 690.1 (Mar. 2011), pp. 108–115.

[23] Stefan Nagl, Carlos Baleizão, Sergey M Borisov, Michael Schäferling, Mário N Berberan-Santos, and Otto S Wolfbeis. "Optical sensing and imaging of trace oxygen with record response." In: *Angewandte Chemie (International ed. in English)* 46.13 (2007), pp. 2317–2319.

[24] Sven Kochmann, Carlos Baleizão, Mário N Berberan-Santos, and Otto S Wolfbeis. "Sensing and imaging of oxygen with parts per billion limits of detection and based on the quenching of the delayed fluorescence of (13)C70 fullerene in polymer hosts." In: *Analytical Chemistry* 85.3 (Feb. 2013), pp. 1300–1304.

[25] Philipp Lehner, Christoph Staudinger, Sergey M Borisov, and Ingo Klimant. "Ultra-sensitive optical oxygen sensors for characterization of nearly anoxic systems". In: *Nature Communications* 5 (July 2014), pp. –.

[26] N P Revsbech, L H Larsen, J Gundersen, T Dalsgaard, O Ulloa, and B Thamdrup. "Determination of ultra-low oxygen concentrations in oxygen minimum zones by the STOX sensor". In: *Limnol Oceanogr Methods* 7 (2009), pp. 371–381.

[27] Daniel A Stolper, Niels Peter Revsbech, and Donald E Canfield. "Aerobic growth at nanomolar oxygen concentrations." In: *Proceedings of the National Academy of Sciences of the United States of America* 107.44 (Nov. 2010), pp. 18755–18760.

[28] Takeo Nakano, Ken'ichiroh Hoshi, and Shigeru Baba. "Effect of background gas environment on oxygen incorporation in TiN films deposited using UHV reactive magnetron sputtering". In: *Vacuum* 83.3 (Oct. 2008), pp. 467–469.

[29] Henry Berger. "Contamination due to process gases". In: *Microelectronic Engineering* 10.3-4 (Feb. 1991), pp. 259–267.

[30] Felix Friedl, Nils Krah, and Bernd Jähne. "Optical sensing of oxygen using a modified Stern–Volmer equation for high laser irradiance". In: *Sensors and Actuators B: Chemical* 206 (Jan. 2015), pp. 336–342.

[31] Christoph Larndorfer, Sergey M Borisov, Philipp Lehner, and Ingo Klimant. "The effect of high light intensities on luminescence lifetime based oxygen sensing". In: *Analyst* (2014), pp. –.

[32] R W Thimijan and R D Heins. "Photometric, radiometric, and quantum light units of measure: a review of procedures for interconversion". In: *HortScience* 18.6 (1983), pp. 818–822.

[33] T Bernas, M Zarebski, R R Cook, J W Dobrucki, and P R Cook. "Minimizing photobleaching during confocal microscopy of fluorescent probes bound to chromatin: role of anoxia and photon flux." In: *Journal of microscopy* 215.Pt 3 (Sept. 2004), pp. 281–296.

[34] Barbara Enko, Sergey M Borisov, Johannes Regensburger, Wolfgang Bäumler, Georg Gescheidt, and Ingo Klimant. "Singlet oxygen-induced photodegradation of the polymers and dyes in optical sensing materials and the effect of stabilizers on these processes." In: *The journal of physical chemistry. A* 117.36 (Sept. 2013), pp. 8873–8882.

[35] Aleksander S Golub and Roland N Pittman. "PO2 measurements in the microcirculation using phosphorescence quenching microscopy at high magnification." In: *American journal of physiology. Heart and circulatory physiology* 294.6 (June 2008), H2905–16.

[36] Vincenzo Arcella, Alessandro Ghielmi, and Giulio Tommasi. "High Performance Perfluoropolymer Films and Membranes". In: *Annals of the New York Academy of Sciences* 984.1 (Mar. 2003), pp. 226–244.

[37] Stuart M Nemser and Ian C Roman. "Perfluorodioxole Membranes". Pat. Sept. 1991.

[38] Jianzhang Zhao, Shaomin Ji, and Huimin Guo. "Triplet–triplet annihilation based upconversion: from triplet sensitizers and triplet acceptors to upconversion quantum yields ". In: *RSC Advances* 1.6 (2011), pp. 937–950.

[39] Rony S Khnayzer, Jörg Blumhoff, Jordan A Harrington, Alexandre Haefele, Fan Deng, and Felix N Castellano. "Upconversion-powered photoelectrochemistry." In: *Chemical communications (Cambridge, England)* 48.2 (Jan. 2012), pp. 209–211.

[40] Francis Wilkinson, W Phillip Helman, and Alberta B Ross. “Rate Constants for the Decay and Reactions of the Lowest Electronically Excited Singlet State of Molecular Oxygen in Solution. An Expanded and Revised Compilation”. In: *Journal of Physical and Chemical Reference Data* 24.2 (1995), p. 663.

[41] Marek Scholz, Roman Dědic, Thomas Breitenbach, and Jan Hála. “Singlet oxygen-sensitized delayed fluorescence of common water-soluble photosensitizers.” In: *Photochemical & photobiological sciences : Official journal of the European Photochemistry Association and the European Society for Photobiology* 12.10 (Oct. 2013), pp. 1873–1884.

[42] Alena Knak, Johannes Regensburger, Tim Maisch, and Wolfgang Bäumler. “Exposure of vitamins to UVB and UVA radiation generates singlet oxygen.” In: *Photochemical & photobiological sciences : Official journal of the European Photochemistry Association and the European Society for Photobiology* 13.5 (May 2014), pp. 820–829.

3.8 Supporting Figures

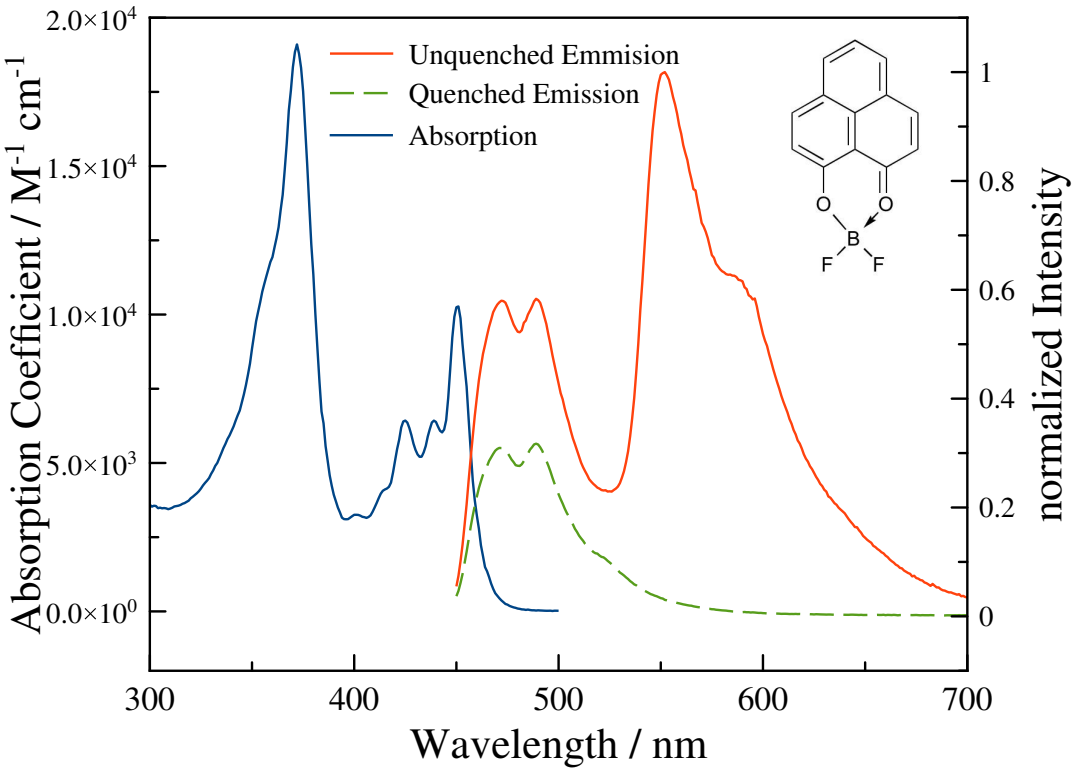

Figure 3.9: Spectral properties and structure of BF2HPhN in PS

The sensor systems used in this work consist of BF_2HPhN in PS, BF_2HBAN in PS and Al(HPhNPF)$_3$ embedded in a Cytop A as matrix. This last material combination has not been previously used due to comparably low sensitivities, but for this application it is ideal as it also shows some of the effects of ultra trace sensors while still being comparably easy to obtain calibrations with.

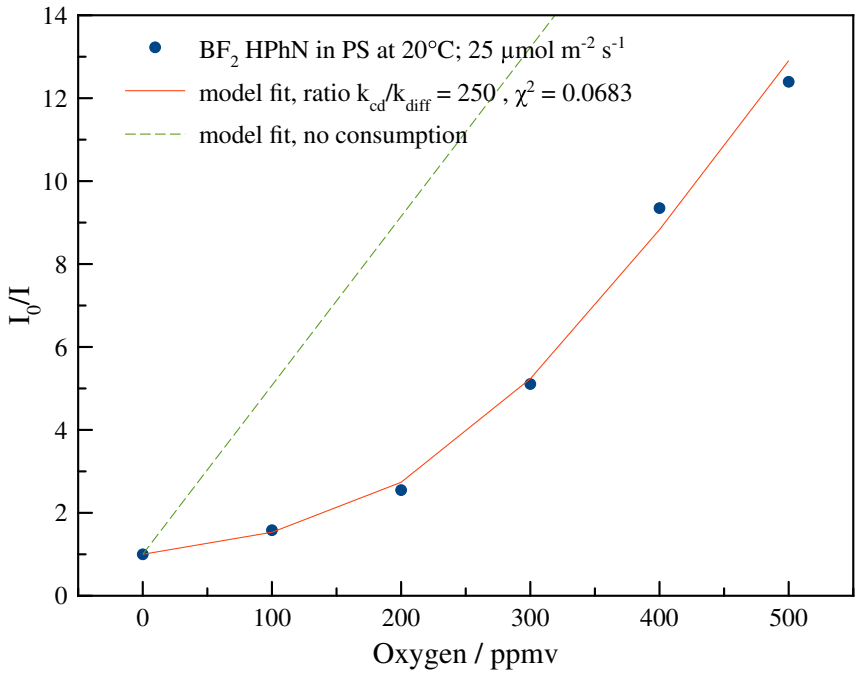

Figure 3.10: Simulation of chemical oxygen depletion. Notice how - in accordance with experiments - the fit for the calibration is nearing a line that is parallel with a theoretical ideal calibration at higher oxygen concentrations (green dashed line, also see the supplementary model file). Unfortunately the approximations the model makes in respect to diffusion, render it unusable to quantitively fit the experimental results. The model assumes a homogeneous distribution of oxygen in the sensor material, but in the case of oxygen photoconsumption there most-certainly is a concentration gradient over the sensor film.

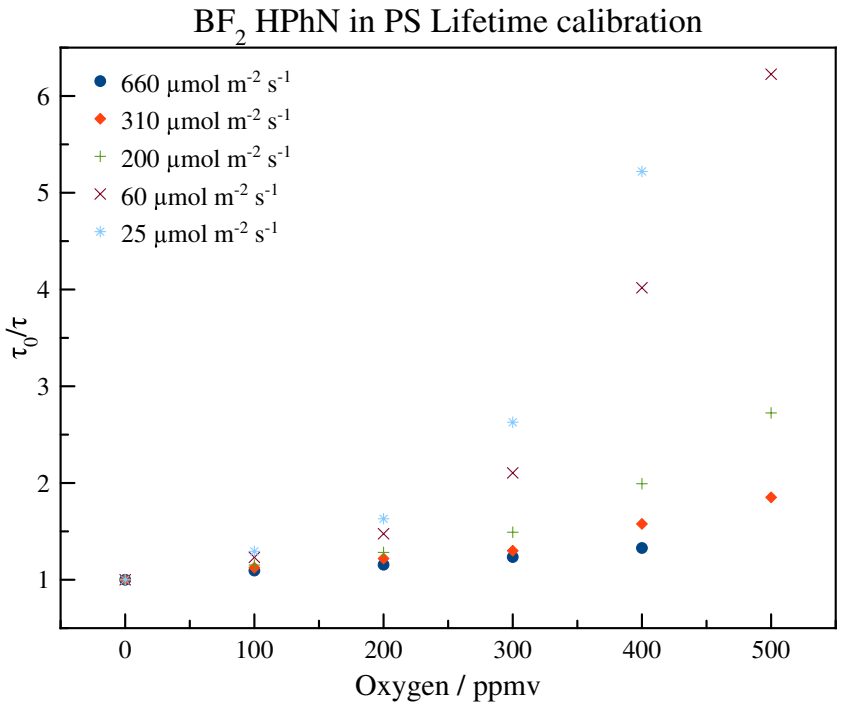

Figure 3.11: Calibration curves for BF_2HPhN in polystyrene based on lifetimes measured in the time-domain, acquired at 20 °C.

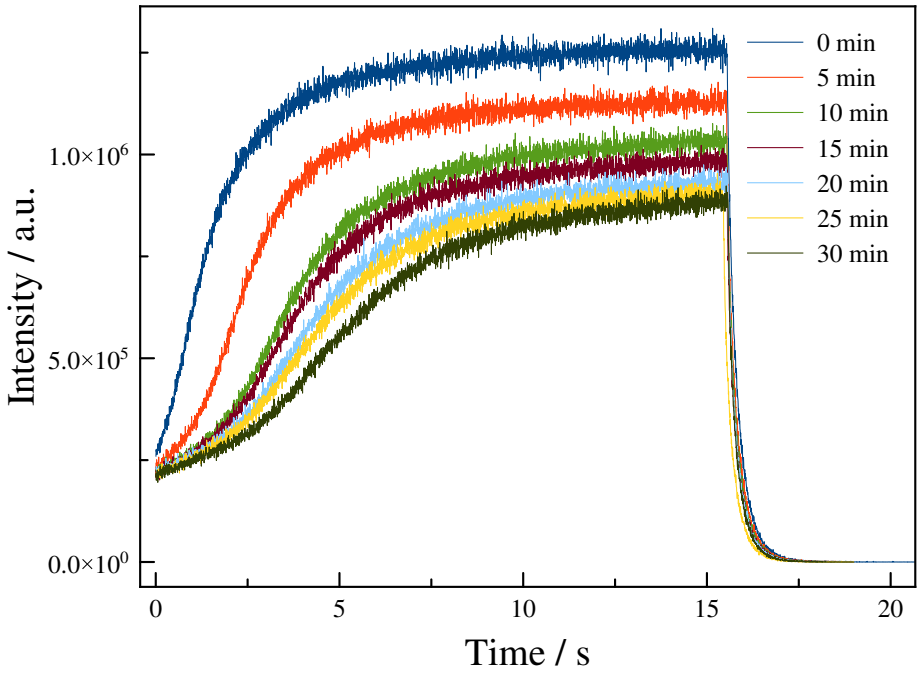

Figure 3.12: Change in the time-resolved response of the sensor at 500 ppmv oxygen and 660 µmol m^{-2} s^{-1}. Excitation light was switched off after 15 s. In between measurements the material was exposed to air and irradiated with strong UV light to speed up the chemical saturation of reactive centers.

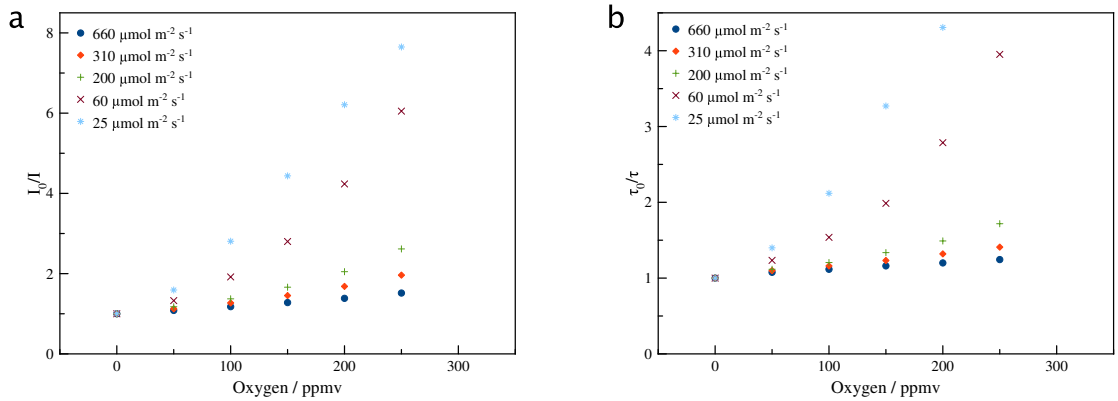

Figure 3.13: Calibration curves of BF_2HPhN in polystyrene based on intensity measurements (a) and lifetime measurements (b). Obtained at 20 °C after the air-equilibrated sample has been irradiated with UV light for 30 minutes.

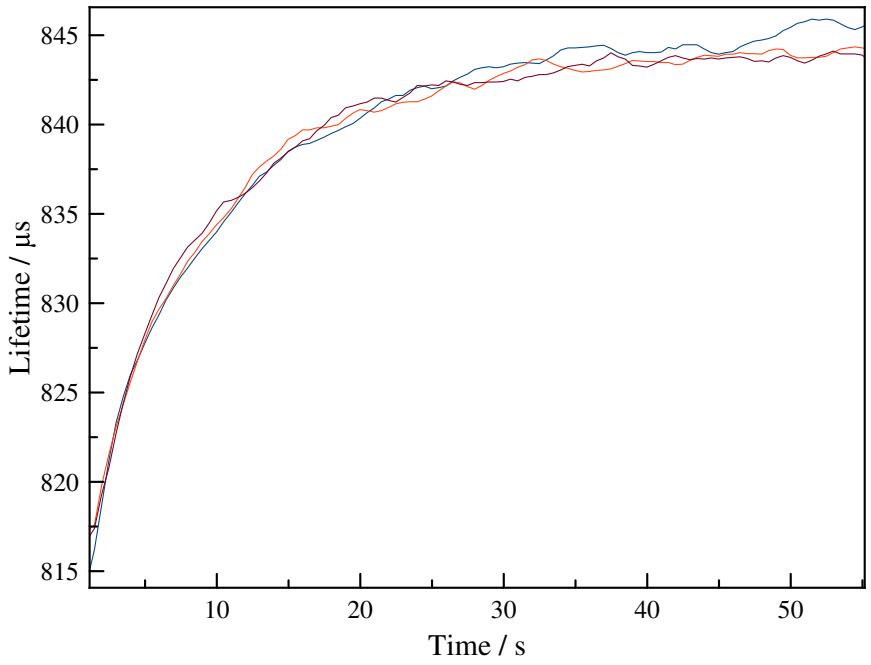

Figure 3.14: Change of the steady state equilibrium observed in a Pd-PFPP in PS sensor material at 500 ppmv, that reacts to a 4 fold increase in light intensity. In the experiment a 25 % neutral density filter was removed from the excitation source at t=0. The three lines represent three repetitions of the experiment.

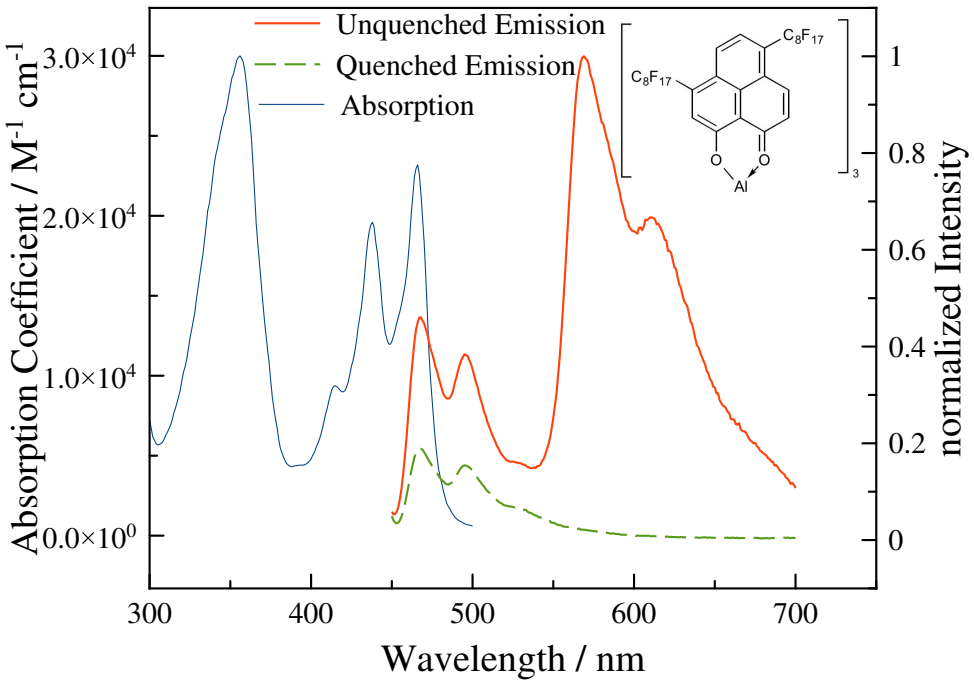

Figure 3.15: Structure and spectral properties of $Al(HPhNPF)_3$ in Hyflon AD 60

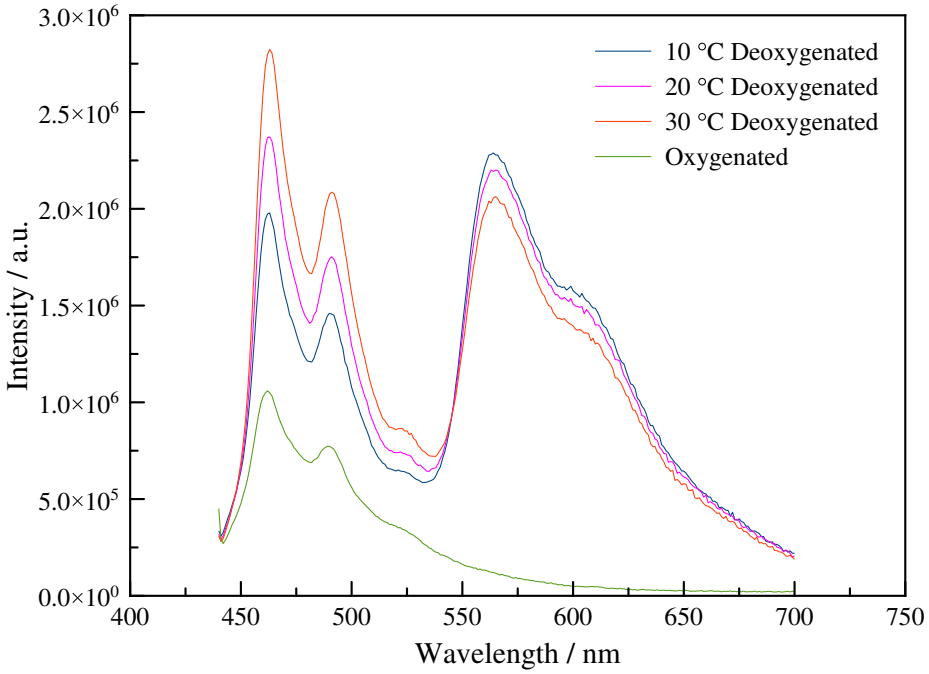

Figure 3.16: Temperature dependence of the emission spectra of the used $Al(HPhNPF)_3$ in CytopA sensor, caused by e-type delayed fluorescence

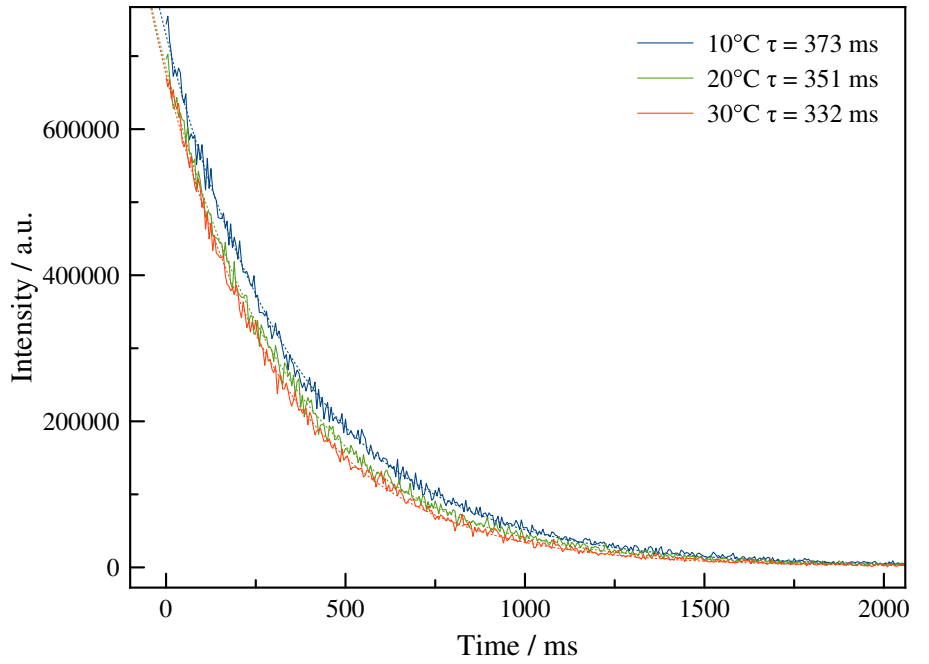

Figure 3.17: Decay curves of the used $Al(HPhNPF)_3$ in CytopA sensor

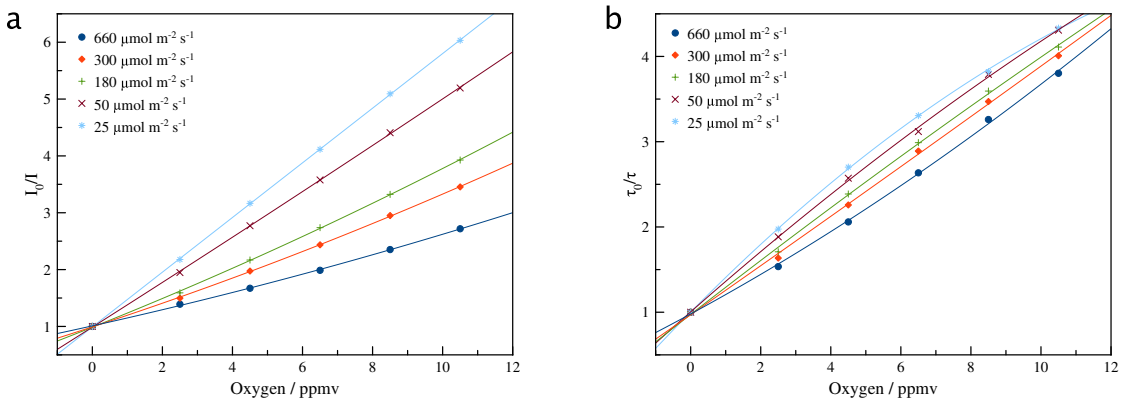

Figure 3.18: Calibration of Al(HPhNPF)$_3$ 0.1 % w/w in Hyflon AD 60 at 20 °C, both intensity (a) and time domain based (b). The observed phenomena appear to be comparable in magnitude to the experiments performed with Cytop A as matrix material.

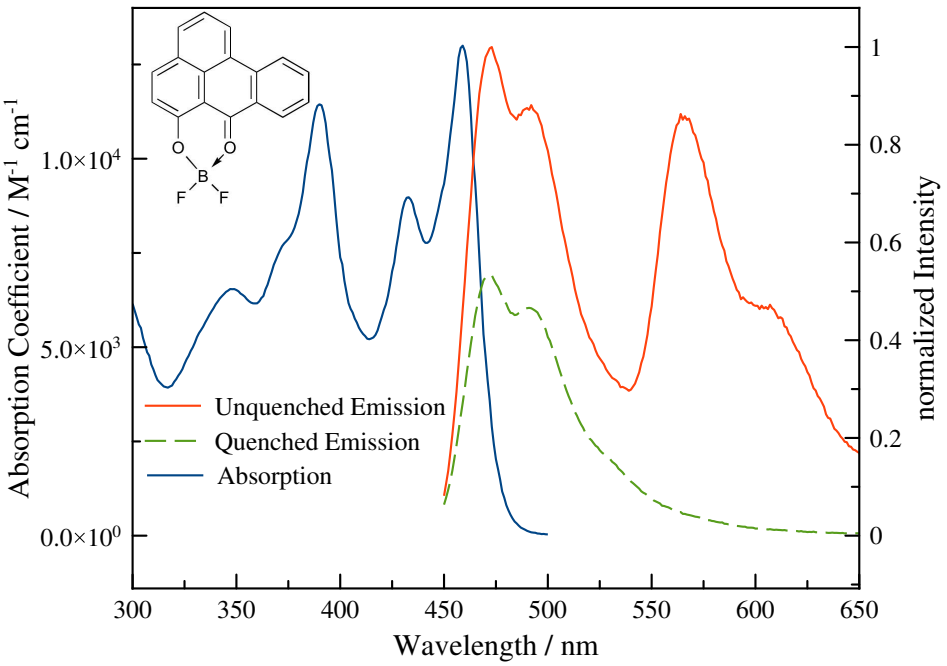

Figure 3.19: Spectral Properties and Structure of BF_2HBAN in PS

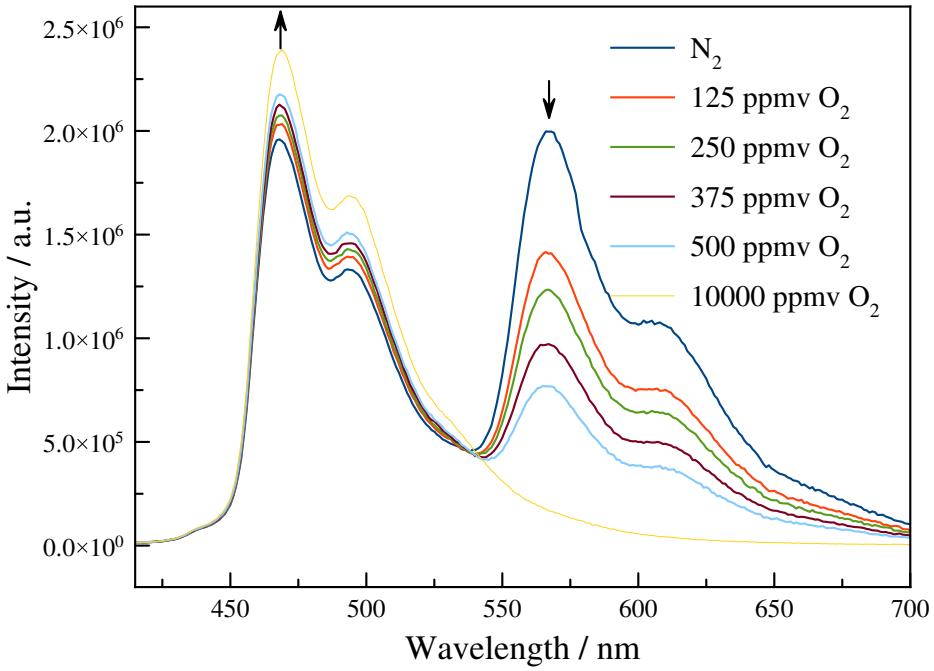

Figure 3.20: Spectra of BF_2HBAN 0.1 % (w/w) in PS, obtained at high light intensities (2 mmol m^{-2} s^{-1}) at 05 °C. The low temperature was used to decrease the mitigating influence of delayed fluorescence.

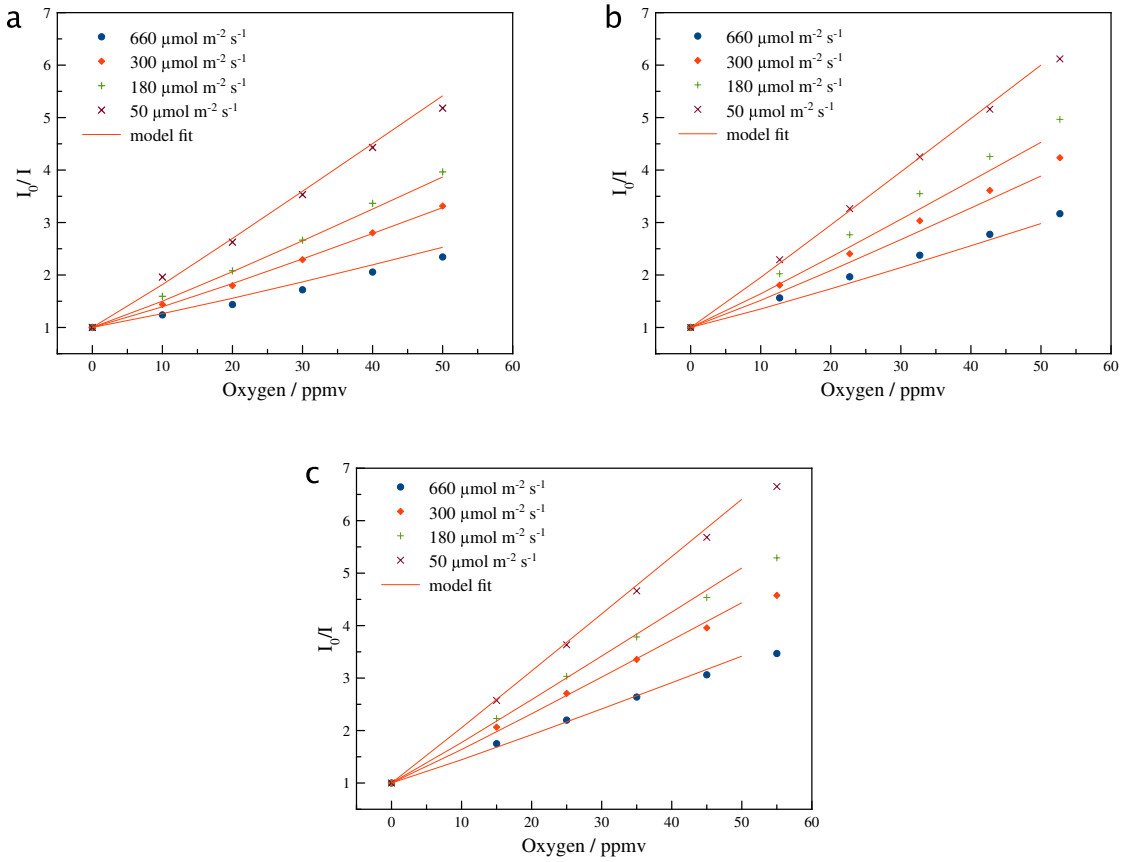

Figure 3.21: Fits of the developed steady state model for experimentally obtained intensity based calibration curves for the Al(HPhNPF)$_3$ in Cytop A sensor material at 0.2 % (a), 0.1 % (b), and 0.05 % (c) (w/w) dye content. One set of constants was used to fit all three datasets. R^2 values for individual fits range from 0.930 to 0.999 with an average $R^2 2$ value of 0.986. Please refer to the supplementary model file for specifics about the fit and used constants.

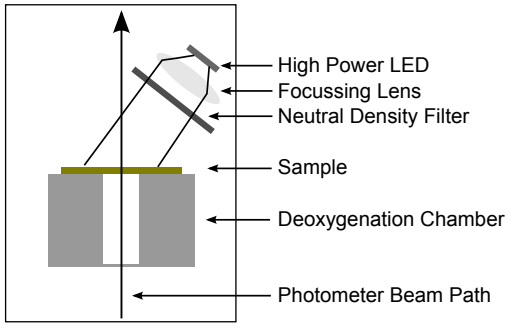

Figure 3.22: Schematic of the experimental setup of the „flash photolysis“ experiments performed in a regular photometer.

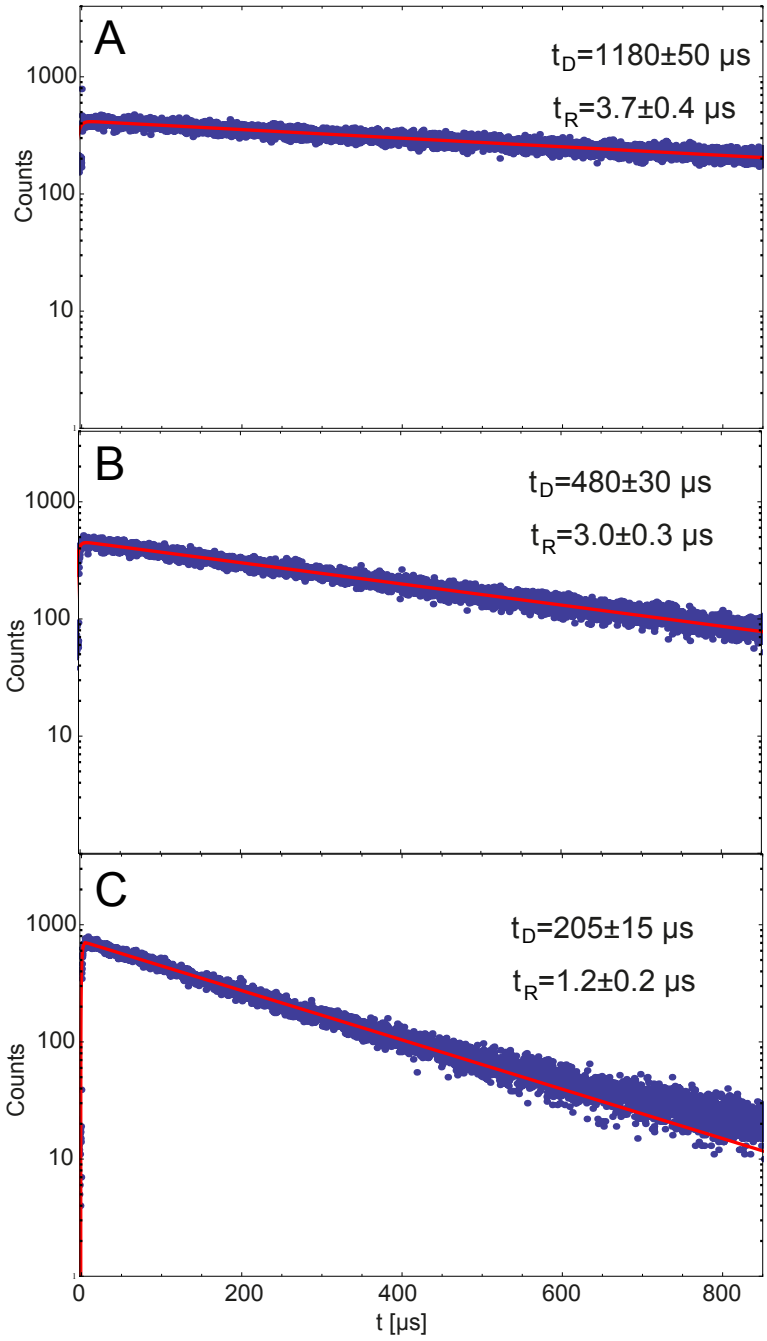

Figure 3.23: Time resolved singlet oxygen luminescence signal generated with different Pt-PFPP-concentrations in Hyflon (A = 0.04 % , B = 0.2 %, C = 1 % (w/w)) (P = 10 mW, λ = 505 nm, 30 sec). Red lines represent the result of the used Levenberg-Marquardt-algorithm fit.

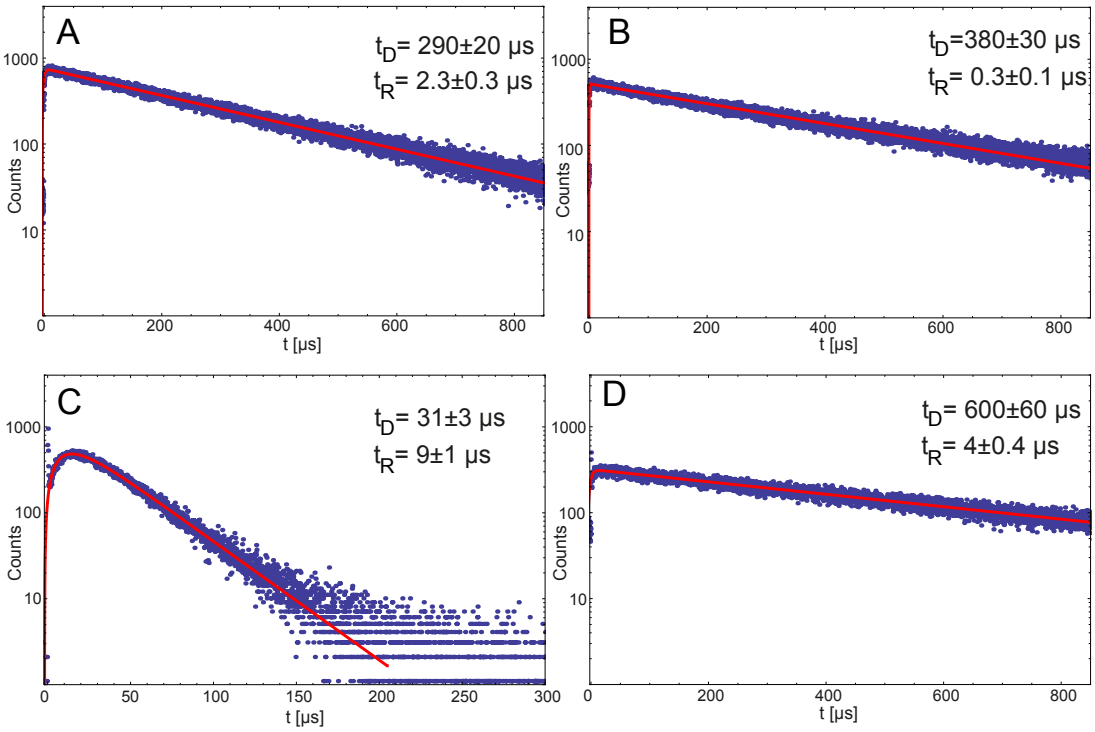

Figure 3.24: Time resolved singlet oxygen luminescence of different sensitizers in different materials (A: 0.5 % (w/w) Pt-PFPP in Hyflon, B: 0.5 % (w/w) Pt-PFPP in Teflon, C: 0.5 % (w/w) pyrene-butyric acid in PS, D: 0.1 % (w/w) $Al(HPhNPF)_3$ in Hyflon). Red lines represent the result of the used Levenberg-Marquardt-algorithm fit.

3.9 COSSMo

Computational **O**xygen **S**teady **S**tate **Mo**del

The content of this section is transcribed from a mathematica notebook and is available in interactive format (CDF or Mathematica notebook) from the author or as supporting information from the corresponding journals website.

3.9.1 Background

Description

This model is used to simulate photochemical processes in a oxygen sensor system, which can be used to correlate and validate experimental results. It uses a steady state model, which assumes that the different states shown in Figure 3.25 are in equilibrium with each other.

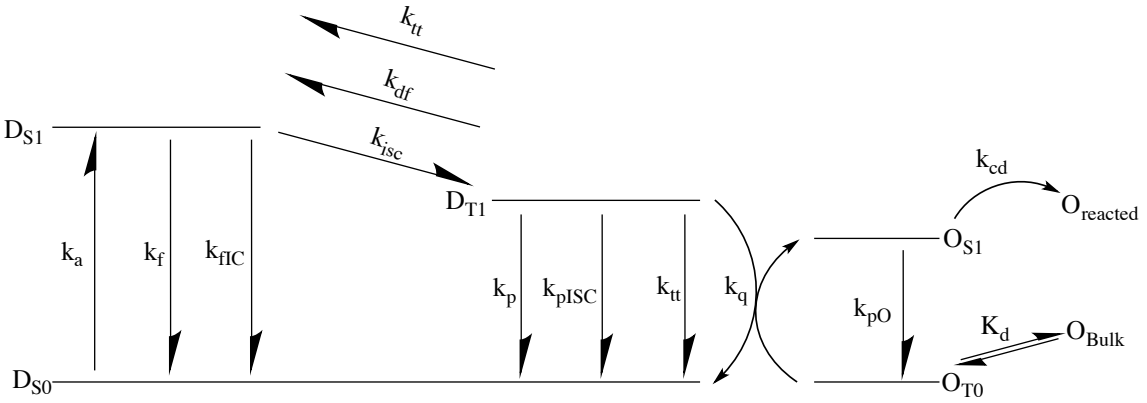

Figure 3.25: The Steady State described in this model

The two systems interacting with each other are that of the Dye with D_{S0} being its ground state and that of the Quencher (in this specific case: Oxygen) with O_{T0} as its ground state. Incoming light is absorbed by a ground state dye molecule according to the rate k_a into the singlet excited state where it will either fallback to the ground state through fluorescence or internal conversion (k_f, k_{fIC}) or it can cross over into the much more stable triplet state through inter-system-crossing (k_{isc}). The triplet state is the one of analytical interest as it is directly responsible for the measured signal ($k_p \times D_{T1}$), but is unfortunately not only influenced by the deactivation through quencher collision ($k_q \times D_{T1} \times O_{T0}$) but also by other phenomena like triplet triplet annihilation ($D_{T1}^2 \times k_{tt}$), thermally activated reverse inter-system-crossing which results in delayed fluorescence ($k_{df} \times D_{T1}$) and indirectly by the fact that overall dye concentration is not endless and may therefore reach saturation in the meta-stable state D_{T1}. Further, the measured oxygen concentration ($k_q \times O_{T0}$) is not necessarily directly proportional to O_{Bulk} (the intended parameter). For one, because diffusion into the sensor is in equilibrium with other possible reactions like chemical consumption ($O_{S1} \times k_{cd}$). And also, as physical deactivation of Singlet oxygen ($O_{S1} \times k_{pO}$) is not infinitely fast the oxygen ground state can be depleted just like the dye ground state. To differentiate between the two types of ground state

depletion, the oxygen depletion will be called singlet oxygen accumulation in the rest of the document.

State Equations

The systems state is described by the six following (non-)linear equations, where the last two can be omitted in a state without quencher:

$$\begin{aligned}
0 &= -D_{S0}k_a + D_{S1}(k_f + k_{fIC}) + D_{T1}(k_p + k_{pISC} + D_{T1}k_{tt} + k_q O_{T0}) \\
0 &= D_{S0}k_a - D_{S1}(k_f + k_{fIC} + k_{isc}) + D_{T1}(k_{df} + D_{T1}k_{tt}) \\
0 &= D_{S1}k_{isc} - D_{T1}(k_{df} + k_p + k_{pISC} + 2D_{T1}k_{tt} + k_q O_{T0}) \\
0 &= -C_{Dye} + D_{S0} + D_{S1} + D_{T1} \\
0 &= k_{diff}K_{sol}O_{Bulk} - O_{T0}(k_{diff} + D_{T1}k_q) + k_{pO}O_{S1} \\
0 &= D_{T1}k_q O_{T0} - O_{S1}(k_{cd} + k_{diff} + k_{pO})
\end{aligned} \tag{3.3}$$

The diffusion of oxygen from the bulk into the sensor layer is simplified to a rate constant (k_{diff}) for diffusion in and out of the sensor with the concentration in the bulk corrected with the solubility ratio Bulk/Sensor (K_{sol}) to account for the difference in concentration at equilibrium conditions. While this approximation is adequate to simulate effects that are not dominated by diffusion, it is inadequate to describe a system with strong concentration gradients inside the sensor layer, as would be the case with significant oxygen consumption. Overall, the system uses a number of simplifications and assumptions:

- No gradient of dye excitation (as a result of absorption) is considered
- No gradient of oxygen inside the sensor layer is considered
- A homogeneous dye environment is assumed
- O_{Bulk} is considered constant
- Temperature is considered constant
- Concentration depend diffusion influence on k_{tt} is ignored
- Excitation into the D_{S2} state is omitted
- Excitation into the D_{T2} state is omitted

Time-dependent extension for prediction of decay curves

Another method of measurement is to use the change in exited triplet state lifetime instead of the steady state intensity as the readout parameter. To determine the lifetime in a time-resolved way, irradiation light is switched off and a decay curve is captured which is then fitted with an exponential equation resulting in a lifetime value. The obvious advantage is that this lifetime value is governed by $\frac{1}{D_{T1}k_{tt}+k_{df}+k_q O_{T0}+k_p+k_{pISC}}$, so it no longer relies on the initial population of D_{T1} (if triplet-triplet annihilation is negligible). But, as this method is no longer steady

state, it has to be extended using the following system of differential equations, describing the dependence of dye triplet concentration on time if irradiation is switched off:

$$\begin{aligned} \frac{\mathrm{d}D_{T1}}{\mathrm{d}t} &= -D_{T1}(k_{df} + k_q O_{T0} + k_p + k_{pISC}) \\ \frac{\mathrm{d}O_{T0}}{\mathrm{d}t} &= k_{pO} O_{S1} - D_{T1} k_q O_{T0}) \\ O_{Total} &= O_{S1} + O_{T0} \end{aligned} \tag{3.4}$$

This extension relies on initial values supplied by the steady state model and then computes the changes in dye triplet concentration over time. It does so by assuming a closed system, i.e. there's no diffusional exchange with the bulk. For ultra-trace sensors, where diffusion coefficients are high and lifetimes are long diffusional exchange with the bulk may not be entirely negligible. It is however not practial to include a diffusion dependent term into the above equation, as it will be either very simplified (like in the steady state model) or very complex to integrate. For qualitative predictions this model should be sufficient.

3.9.2 Calculations

Numerical solution

Obtaining an exact algebraic solution to the above system is neither easy nor practical, a numerical solution though can be obtain with adequate speed and precision, this section explains how such a numerical solution is obtained within Mathematica. A numerical solution has some other implications, for example that it has to be resolved whenever a value changes. As a result you will find this code in all model figures presented in this notebook. First an equation set has to be defined for Mathematica to solve, as there are five variables, five equations have to be defined, the equation describing the sate of D_{S1} can be omitted as it contains no unique constants. Therefore the following code describes the used equation system:

```
stateEquation=
  { 0==ka (-DS0)+DS1 (kf+kfIC)+DT1 (DT1 ktt+kq OT0+kp+kpISC),
    0==DS1 kisc-DT1 (2 DT1 ktt+kdf+kq OT0+kp+kpISC),
    0==OBulk kdiff Ksol-OT0 (DT1 kq+kdiff)+kpO OS1,
    0==DT1 kq OT0-OS1 (kcd+kdiff+kpO),
    0==-CDye+DS0+DS1+DT1 }
```

Example Calculation

The resulting equation can then be numerically solved by Mathematica if values for all constants are supplied:

```
numericalStateEquation = stateEquation /.
  { CDye → 100, OBulk → 10, ka → 0.1, kf → 30000000, kp → 1.5,kfIC → 30000,
    kpISC→ 0.1, kpO → 1000, kq → 40, kdf→ 0, kisc → 30000000, ktt → 0,
    kdiff → 1000, Ksol → 10, kcd → 0 }
```

Finally `NSolve` is used to numerically solve the equation for the five states:

```
NSolve[Join[Rationalize[numericalStateEquation],
  { DS0 ≥ 0, DS1 ≥ 0, DT1 ≥ 0, OT0 ≥ 0, OS1 ≥ 0 }],
  { DS0, DS1, DT1, OT0, OS1 }, Reals]
```

Yielding the following solution for the five states:
$\{D_{S0} \rightarrow 99.9988, D_{S1} \rightarrow 1.66581 \times 10^{-7}, D_{T1} \rightarrow 0.00124889, O_{T0} \rightarrow 99.9975, O_{S1} \rightarrow 0.00249772\}$

Relation to obtainable values

To estimate the magnitudes of rate constants the following relations to experimentally obtainable values can be used:

- Excitation Light Intensity: k_a is directly dependent on the excitation light intensity and can be estimated through the Lambert Beer equation. One should note though that Lambert Beer integrates absorption over the film thickness, while the model assumes a constant absorption throughout the entire film.

- Fluorescence Quantum Yield: Is defined as absorption vs emission and therefore is experimentally valid only for a very specific set of border conditions. Fluorescence QY is the most usable one as $\Phi_f = D_{S1}k_f/(D_{S0}k_a)$ which represents the model in fully quenched condition.

- Phosphorescence QY: It's defined as $\Phi_p = D_{T1}k_p/(D_{S0}k_a)$ which is only measurable under deoxygenated conditions in a system where triplet triplet annihilation and delayed fluorescence are negligible. Which is true at low temperatures, unfortunately the temperature dependence is not trivial to estimate.

- Delayed Fluorescence Quantum Yield together with the other QYs can be used to estimate k_df

- k_q can be estimated from calibrations and obtained K_{SV} values

- Decay time: $\tau_0 = (D_{T1}k_{tt} + k_{df} + k_p + k_{pISC} + k_qO_{T0})^{-1}$ is calculated at specific points to validate the parameters entered into the model.

- Oxygen decay time: As this is only dependent on $(k_{cd} + k_{pO})^{-1}$ it might be suitable as a directly supplied value, but is currently also only calculated for validation purposes.

3.9.3 Model

Simulation of expected behavior

In the following set of simulations the system uses coefficients that are reasonable guesses and are expected to be in the same order of magnitude as coefficients for a dye that shows fluorescence and phosphorescence with roughly 250 ms lifetime, all of the effects described in the next section "Cases with non-linear behavior" are purposefully reduced to a minimum in this section through choosing low values for k_a, k_{tt}, k_{df} and a high value for k_{diff} and k_{pO}.

Figure 3.27 shows a simulated calibration curve obtained under ideal conditions, although physically not sensible (as k_q is constant for a given dye-matrix combination), this plot allows to see the direct dependence of K_{SV} on k_q:

Dye Properties			Oxygen Properties		
Constant	Value	Unit	Constant	Value	Unit
Dye Content	0.1	% (w/w)	Concentration	1	nM
MW	3142.9	g mol^{-1}	k_{pO}	830	s^{-1}
k_a	0.1	s^{-1}			
k_f	30 000 000	s^{-1}	Matrix Properties		
k_{fIC}	30 000	s^{-1}	Constant	Value	Unit
k_{isc}	30 000 000	s^{-1}	Density	1.93	g L^{-1}
k_p	3.8	s^{-1}	k_q	22 000 000	s^{-1} mol^{-1}
k_{pISC}	0.1	s^{-1}	K_{sol}	10	
k_{df}	0	s^{-1}	k_{diff}	0.1	s^{-1}
k_{tt}	0	s^{-1} mol^{-1}	k_{cd}	0	s^{-1}

Table 3.1: Constant values applied to the model in section 3.9.3 as initial state

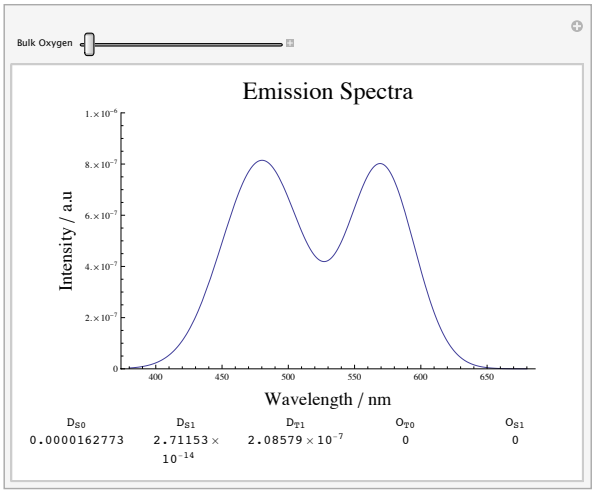

Figure 3.26: Simulated Emission Spectra of an idealized system with minimal non-linearities occurring, just to prove that the model actually works

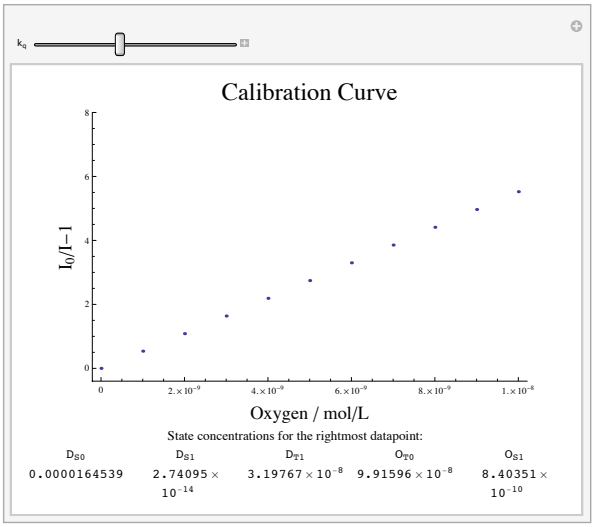

Figure 3.27: Simulated Calibration Curve for the same ideal system also applied in figure 3.26

Cases with non-linear behavior

In the following chapter, rate constants purposefully ignored in the ideal state are varied to show the different effects explained by the model. While the rate constants were kept within sensible bounds for most cases, some of the effects presented are exaggerated in the model compared to a real system.

Chemical Oxygen Consumption

As singlet oxygen is much more reactive than it's triplet counterpart there can be significant oxygen depletion through chemical reaction, dependent on the matrix' stability to oxidation and the presence of other oxidize able species. If depletion through oxidation is significant, the actual concentration of oxygen in the sensor becomes a function of the equilibrium between reaction and diffusion from the bulk, which results in a deviation of the measured signal to actual bulk oxygen concentration.

Ground state depletion

The observed phosphorescence intensity is often assumed to have a linear dependence to excitation light intensity. If the sensor is exposed to very high irradiation - especially if the dye has an exceptionally long-living triplet state or high absorption coefficients - there might be significant depletion of the dye ground state so that it's value can no longer be assumed constant. Then, saturation behavior can be observed and, as the unquenched state is much more prone to this effect as a partially quenched state, quenched intensities are less affected and therefore higher. As a result, the ratio I_0/I is reduced and sensor appears less sensitive. Note that this effect is not observable in phosphorescence lifetimes as it does not influence the triplet state reaction rates.

Triplet-Triplet Annihilation

Triplet-triplet annihilation is directly dependent on triplet state concentration and as such has an influence on sensor sensitivity that can be minimized. Because of this direct dependence is

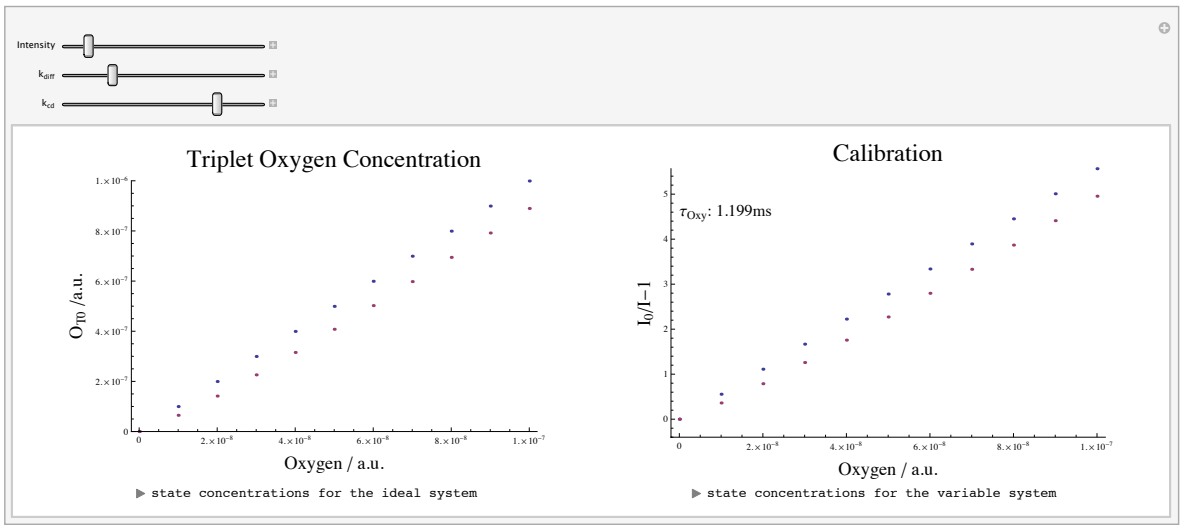

Figure 3.28: Simulated calibration curves for an ideal system (blue) and a system with chemical oxygen depletion (red), resulting in a scenario where the measured concentration becomes diffusion dependent

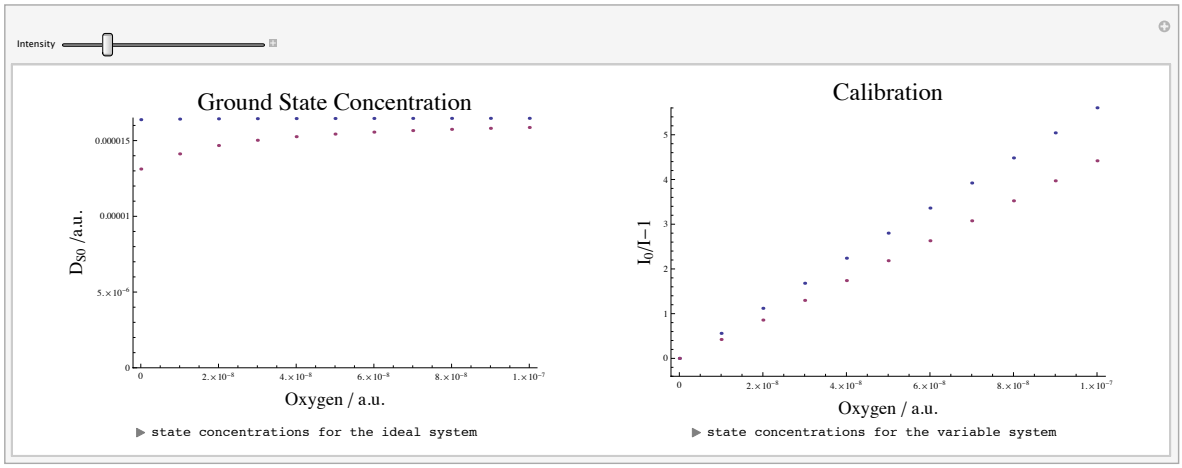

Figure 3.29: Simulated calibration curves for an ideal system(blue) and a system with variable irradiance(red), resulting in ground state depletion

also influenced by excitation light.

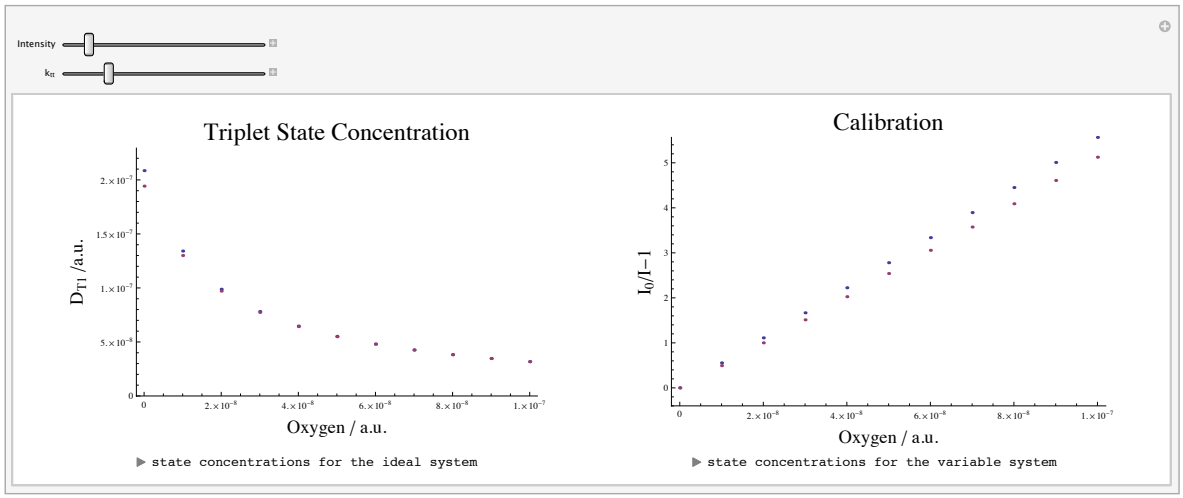

Figure 3.30: Simulated calibration curves for an ideal system(blue) and a system with triplet triplet annihilation(red), resulting in lower decay times

Singlet Oxygen Accumulation

If the lifetime of the oxygen singlet state is long enough and the concentration of dye triplet state is also high, there is the possibility that a non negligible quantity of oxygen is actually present as the non-detectable singlet state and therefore not measurable. But as it's still part of the oxygen diffusion equilibrium the direct proportionality between the oxygen concentration in the sensor and in the bulk is no longer true.

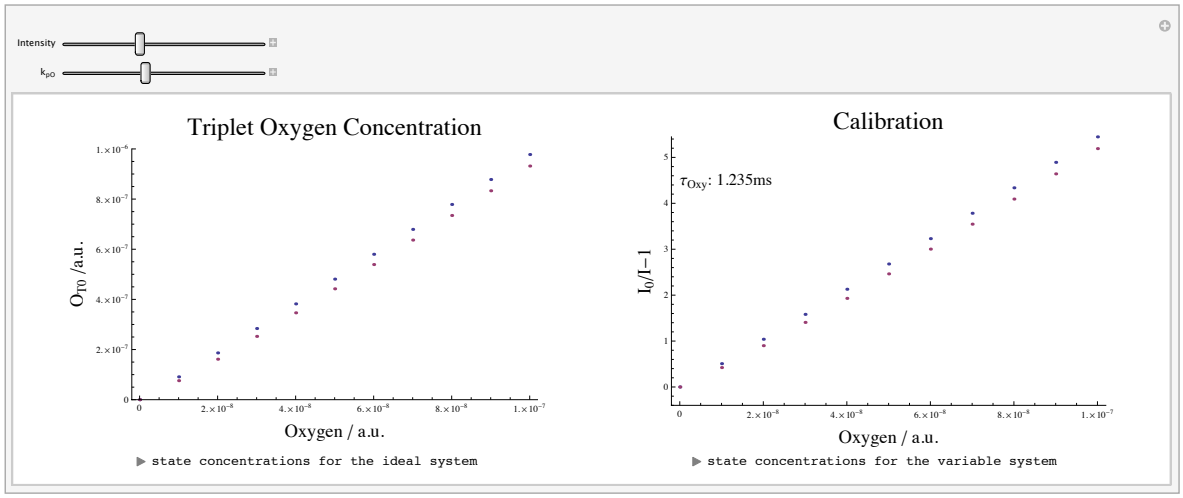

Figure 3.31: Simulated calibration curves for an ideal system(blue) and a system with singlet oxygen accumulation(red), resulting in a lower concentration of detectable ground state oxygen

In Figure 3.32 the results of solving the time dependent extension of the model for D_{T1} as a function of time are shown. As expected high values for k_{pO} result in little deviation from ideal

behavior, whereas with lower values the curve start to become distorted from a pure single exponential decay.

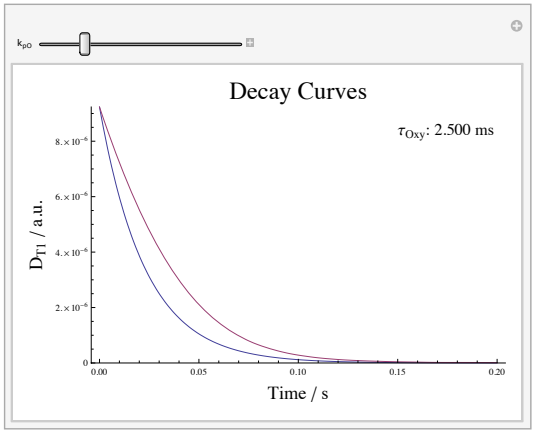

Figure 3.32: Simulated decay curves for an ideal system(blue) and a system with simulated singlet oxygen accumulation(red), the higher the excited singlet state lifetime of oxygen, tho more pronounced the effect appears.

3.9.4 Experimental correlation of BF_2HPhN Results

Dye Properties			Oxygen Properties		
Constant	Value	Unit	Constant	Value	Unit
Dye Content	0.5	% (w/w)	Concentration	1	nM
MW	244.05	g mol^{-1}	k_{pO}	830	s^{-1}
k_a	8	s^{-1}			
k_f	30 000 000	s^{-1}	Matrix Properties		
k_{fIC}	30 000	s^{-1}	Constant	Value	Unit
k_{isc}	30 000 000	s^{-1}	Density	1.05	g L^{-1}
k_p	3.8	s^{-1}	k_q	490 000	s^{-1} mol^{-1}
k_{pISC}	0.1	s^{-1}	K_{sol}	10	
k_{df}	0	s^{-1}	k_{diff}	0.02	s^{-1}
k_{tt}	0	s^{-1} mol^{-1}	k_{cd}	5	s^{-1}

Table 3.2: Constant values applied to the model in section 3.9.5 as initial state

Applying fits to experimental data of calibrations with variable excitation flux and unknown oxygen consumption rate

To demonstrate the applicability of the model to chemical oxygen consumption, the measured photon fluxes are converted into a ratio, and then the prediction of the model is compared to the results. As is apparent in Figure 3.33, while the form of the curve can be made to fit the curvature of the calibration results, it is not possible to fit all five curves at once with the same coefficients (only varying excitation photon flux). This is most likely a result of the described

inadequacy of the diffusion system used in the model. It is very likely that during active oxygen consumption in the layer, the oxygen concentration is very Inhomogeneous throughout the film.

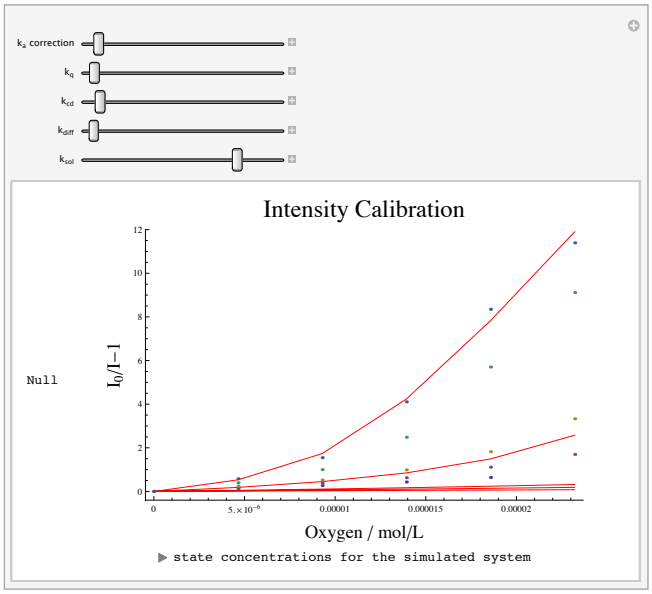

Figure 3.33: Fitting the model to the actual Calibration curves of BF_2HPhN 0.5 % in PS

3.9.5 Experimental correlation of Al(HPhNPF)$_3$ Results

Dye Properties			Oxygen Properties		
Constant	Value	Unit	Constant	Value	Unit
Dye Content	0.1	% (w/w)	Concentration	1	nM
MW	3142.9	g mol^{-1}	k_{pO}	830	s^{-1}
k_a	0.45	s^{-1}			
k_f	30 000 000	s^{-1}	Matrix Properties		
k_{fIC}	30 000	s^{-1}	Constant	Value	Unit
k_{isc}	30 000 000	s^{-1}	Density	1.93	g L^{-1}
k_p	3.3	s^{-1}	k_q	930 000 s^{-1}	mol^{-1}
k_{pISC}	0.1	s^{-1}	K_{sol}	10	
k_{df}	0	s^{-1}	k_{diff}	0.02	s^{-1}
k_{tt}	450 000	s^{-1} mol^{-1}	k_{cd}	5	s^{-1}

Table 3.3: Constant values applied to the model in section 3.9.5 as initial state

Applying fits to experimental data of calibrations with variable excitation flux

Another way to apply the model is to fit the experimental data obtained for different excitation fluxes and dye concentrations. The ratio of excitation photon fluxes and dye concentrations is fixated and constants (especially k_{tt} and k_q) are chosen, so that all results can be fitted with

the same set of constants. Figures 3.34-3.36 show that for ground state depletion and triplet triplet annihilation (two effects where the aforementioned problem of diffusional simulation is less of a problem) the model provides very good fits to experimental data.

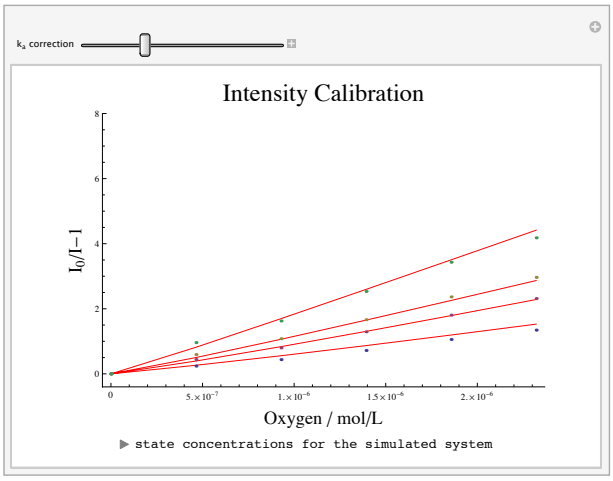

Figure 3.34: Fitting the model to the actual Calibration curves of Al(HPhNPF)$_3$ 0.2 % in Cytop A at 20 °C

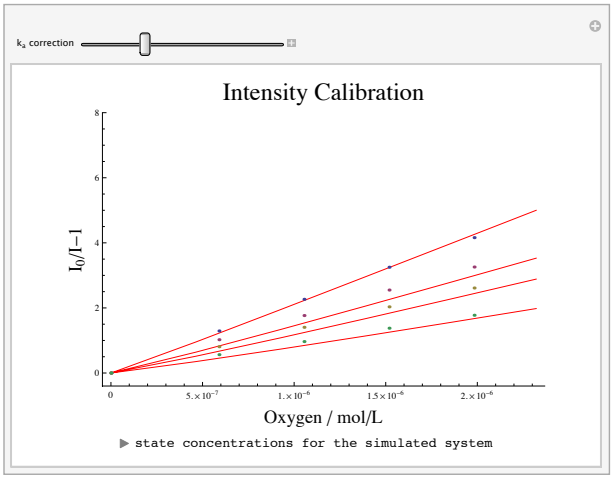

Figure 3.35: Fitting the model to the actual Calibration curves of Al(HPhNPF)$_3$ 0.1 % in Cytop A at 20 °C

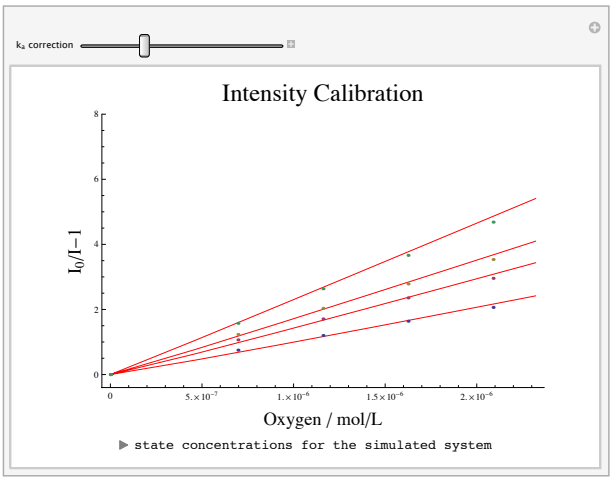

Figure 3.36: Fitting the model to the actual Calibration curves of $Al(HPhNPF)_3$ 0.05 % in Cytop A at 20 °C

4 Lumos – a sensitive optode system for measuring oxygen in the nanomolar range

Philipp Lehner[1], Christoph Larndorfer[1], Emilio Garcia-Robledo[2], Morten Larsen[3], Sergey M. Borisov[1*], Niels-Peter Revsbech[2], Ronnie N. Glud[3], Donald E. Canfield[3] and Ingo Klimant[1]

[1]Institute of Analytical Chemistry and Food Chemistry, Graz University of Technology, NAWI Graz, Stremayrgasse 9, 8010 Graz, Austria.
[2]Department of Biosciences, Aarhus University, 8000 Aarhus, Denmark
[3]Nordic Center for Earth Evolution, University of Southern Denmark, 5230 Odense M, Denmark

Corresponding Author:
Sergery M. Borisov
tel: +43 316 873 32516
email: sergey.borisov@tugraz.at

Submitted to: **Plos One**

4.1 Abstract

Most commercial available optical oxygen sensors target the measuring range of 300 to 2 µmol L^{-1}. However these are not suitable for investigating the nanomolar range which is relevant for many important environmental situations. We therefore developed a miniaturized phase fluorimeter based measurement system called the Lumos (Luminescene Measuring Oxygen Sensor). It consists of a readout device and specialized sensing chemistry that relies on commercially available components. The sensing chemistry consists of palladium(II)-5,10,15,20-tetrakis-(2,3,4,5,6-pentafluorphenyl)-porphyrin embedded in a Hyflon AD 60 polymer matrix and has a K_{SV} of 6.25 × 10^{-3} $ppmv^{-1}$. The applicable measurement range is from 1000 nM down to a detection limit of 0.5 nM. A second sensor material based on the platinum analogue of the porphyrin is spectrally compatible with the readout device and has a measurement range of 20 µM down to 10 nM. The Lumos device is a dedicated system optimized for a high signal to noise ratio, but in principle any phase flourimeter can be adapted to act as a readout device for the highly sensitive and robust sensing chemistry. The presented sensor system exhibits lower noise, higher resolution and higher sensitivity than the electrochemical STOX sensor previously used to measure nanomolar oxygen concentrations. Examples of oxygen contamination in common sample containers has been tested and microbial or enzymatic oxygen consumption at nanomolar concentrations is presented.

4.2 Introduction

Online determination of oxygen concentration is extensively applied in many areas of science and technology[1, 2, 3], as oxygen is an important oxidant in both chemical and biological reactions. Monitoring oxygen concentration in the micromolar range is well established and a multitude of commercial sensor systems, both electrochemical and optical, exist. There are, however, numerous applications where lower concentrations of oxygen need to be monitored, such as in industrial process control[4], and corrosion protection[5]. Also, a significant number of aerobic or facultative anaerobic organisms grow in conditions with oxygen concentrations significantly below 1 µM (DO) [6, 7, 8, 9]. An area of research where low-concentration oxygen monitoring is especially relevant is the investigation of oceanic oxygen-minimum zones (OMZ) containing huge volumes of anoxic or near-anoxic water[10, 11], such as the eastern tropical north pacific OMZ[12]. The range of sensor systems that can determine oxygen concentrations in the nano molar range are currently very limited. One such sensor, the electrochemical STOX sensor[13], can be applied both in the laboratory and for in-situ investigations and can reliably measure concentrations down to about 10 nM. Its sensitivity compares favorably to other commercially available in-situ devices such as the Seabird and Aanderraa dissolved oxygen sensor, but it is difficult to make and very fragile, which limits its availability and applicability – especially in laboratory setups requiring multiple sensors. A viable alternative to such electrochemical sensors are luminescence based optical sensors[14, 15, 16]. They work by detecting a change in luminescence lifetime or intensity that is caused through physical quenching of a probe by molecular oxygen. These sensors have the benefit that they do not consume the analyte (oxygen). In addition they can be miniaturized and can be applied „contact-free“, i.e., the measurement can be performed through an optical window. The contact-free read-out is an important characteristic when working with low oxygen concentrations as the 21 % oxygen in the atmosphere easily contaminates the sample by the insertion of electrochemical sensors.

We here present the Lumos (short for Luminescence Measuring Oxygen Sensor). It is a measurement system that combines a robust sensing chemistry of very high sensitivity with a miniaturized phase fluorometry readout device. We furthermore demonstrate how the Lumos can be used to monitor trace oxygen dynamics in various laboratory settings.

4.3 Materials and Methods

4.3.1 Material

Platinum(II)-5,10,15,20-tetrakis-(2,3,4,5,6-pentafluorphenyl)-porphyrin (PtTFPP) and palladium(II)-5,10,15,20-tetrakis-(2,3,4,5,6-pentafluorphenyl)-porphyrin (PdTFPP) were obtained from Frontier Scientific (UK, frontiersci.com). Hyflon AD 60 and polystyrene were from Solvay (USA, solvay-plastics.com) and Fisher Scientific, respectively. Poly(phenylsilsesquioxane) 3.5-6.5 % OH (PPSQ) and octafluorotoluol were acquired from ABCR (Germany, abcr.de). Other required solvents were purchased at VWR (Austria, at.vwr.com). Circular 8 mm diameter, 1 mm thick sand blasted glass substrates were custom ordered from Hilgenberg (Germany, hilgenberg-gmbh.de), aluminum casings were fabricated in house and anodized by Heuberger Eloxal (Austria, heuberger.at). DT Blue interference and RG 630 color filters were obtained from Qioptiq (Germany, qioptiq.de). Bright Red foil filters were from LEE Filters (UK, leefilters.com) 405 nm UV LEDs (Bivar) and ultrabright red LEDs were obtained from RS (Austria, at.rs-online.com) and LumiTronix (Germany, leds.de), respectively. Glucose oxidase (GOx) from Aspergillus niger, Tris Buffer and $HgCl_2$ were obtained from Sigma-Aldrich (Swiss,

sigmaaldrich.com), α-D-glucose was from Roth Chemicals (Austria, carlroth.com).

4.3.2 Readout Device

The Lumos readout device is optimized for package size and signal to noise ratio (SNR). The electronic and optical components are contained in a 33 mm diameter cylindrical anodized aluminum casing that is 24 mm high and features a mini USB plug for easy connection to a PC using the USB 2.0 standard. The Lumos is, in essence, a miniaturized phase fluorimeter with optical components specifically tuned to maximize SNR for the selection of sensing materials it is used in combination with. It generally consists of an excitation circuit that can emit modulated light, an optics block that delivers light to and from the external sensor material, a photodetector that converts the sensor response into an output signal, and a digital signal processor (DSP) that performs the calculations, performs the signal conversion from analog to digital (and vice-versa) and handles the measurement execution and timing. This DSP communicates via an universal asynchronous receiver transmitter interface (UART) to a separate printed circuit board (PCB), which then handles the USB communication protocol (with the industry standard USB controller FT232) to the PC, with compatible software. Any alternative readout device that can be tuned to the spectral properties of the dyes and is capable of resolving lifetimes in the range of microseconds to a few milliseconds is suitable to be used in combination with the presented sensor chemistry.

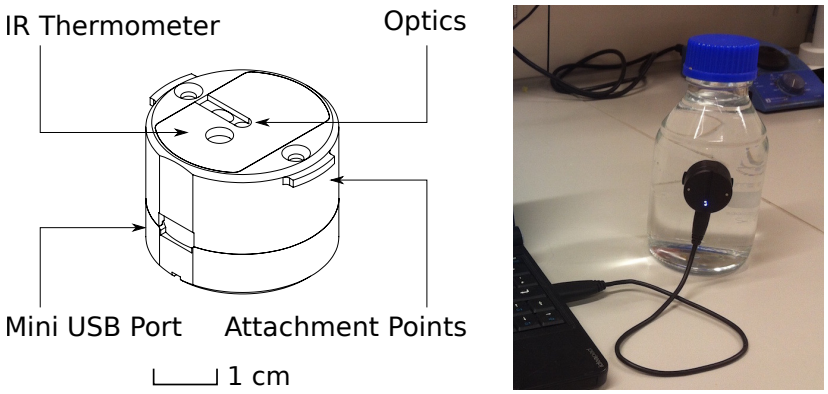

Figure 4.1: Device Characteristics. A representation of the Lumos readout device and sensor spot substrates. The Lumos casing features small notches than can be used as attachment points for mechanical mounting of the device to a vessel wall. The flat front surface is also very well suited for using adhesive tape for mounting. To the right is shown a picture of the Lumos together with a 1 Euro coin for size comparison.

4.3.3 Sensor Substrate spray coating

Substrates for the Lumos sensing sheets consist of 8 mm diameter, 1 mm thick glass disks that are sand blasted on one side to facilitate adhesion of the sensing chemistry. For best results and uniformity the sheets were coated onto the substrates using a spray-coating technique using a custom build device. The spray-coating device consists of an industrial grade airbrush from Efbe Airbrush (Germany, efbe-airbrush.de) fixed to an x-y-z table actuated by stepper motors from Isel (Germany, isel-gmbh.com). The motors are controlled by a Triple Beast Driver from Benezan Electronics (Germany, benezan-electronics.de), which also drives a fourth

axis extension for the airbrush needle valve and a solenoid valve by SMC(USA, smcusa.com) for airflow switching. The spraying procedure was automated using G-Code and LinuxCNC (linuxcnc.org).

For spraying the respective dye (PdTFPP for trace sensors, PtTFPP for high range sensors, 0.01 % (w/w) with respect to the solvent) was dissolved with Hyflon AD 60 (2 % (w/w) with respect to the solvent) in octafluorotoluene and filled into the airbrush reservoir. The Airbrush was then led over each substrate in spirals consisting of 6 half circles with 5 repetitions, adequate film thickness is verified using signal intensity measurements with the readout device.

4.3.4 Other possible methods of sensor preparation

It is paramount for sensor performance that the sensing sheets are on top of a glass substrate, as polymer substrates can act as a buffer for oxygen and therefore influence results. In our case, where a large quantity of individual sensor spots were created spray-coating was the best option. For smaller batches of spots, however, knife-coating yields very good results as well. For knife-coating the respective dye (0.025 % (w/w) with respect to the solvent) was dissolved with Hyflon AD 60 (5 % (w/w) with respect to the solvent) in octafluorotoluene. The resulting 'cocktail' is then coated on a glass substrate, for example microscopy glass slides. For best homogeneity and adhesion the substrate should be treated with Aphaphobe CF or a similar hydrophobizing agent prior to the coating. The ideal film-thickness depends on the used readout device, but using a 175 µm spacer yields good results for most setups. The sensing sheets need to be dried at 60 °C for at least an hour after coating.

4.3.5 Glucose oxidase (GOx) oxygen consumption experiments

A solution of 1 g of glucose and 2 g TRIS buffer in 500 ml distilled H_2O was adjusted with 0.1 M HCl to pH 8. At the beginning of the experiment 0.5 mg GOx in 1 ml distilled H_2O was added and the reaction was performed in a closed and stirred glass vessel where the oxygen consumption was monitored with a Lumos device fixed to the side.

4.3.6 Respiration experiments

Laboratory incubations were performed in custom-made 1.1 L glass bottles described in Tiano et al.[17]. The bottles were equipped with a port for the insertion of a STOX sensor[13] and a long pressure compensation tube. In addition, a flat circular glass window (4 cm of diameter) was built in the bottle wall in order to attach the sensor disk in the inner part and to hold the Lumos device more easily in the outer part of the bottle. Two respiratory experiments were conducted, using tap-water from Aarhus (Denmark) and water from the Eastern Tropical North Pacific (ETNP) OMZ. Experiments in the OMZ were performed during the Oxygen Minimum Zone Microbial Biogeochemistry Expedition 2 (OMZoMBiE2) cruise (R/V New Horizon; cruise NH1410; May 10-June 8, 2014). Here, water samples from 100 m depth were collected with a rosette of Niskin bottles at cruise station 16 (N 20.05734, W 107.04884; approx. 160 km offshore Manzanillo, Mexico), where the in situ oxygen concentration was below 20 nM as deduced from in situ STOX measurements[18].

Water samples for both experiments were collected in a 20 L glass bottle and treated as follows. The oxygen concentration in the water samples was first reduced to approximately 100 nM by vigorously bubbling with N_2 gas for 15-20 minutes. After this period, samples were transferred to the incubation bottles under a continous flow of N_2 gas to avoid oxygen contamination. A glass-coated magnet inside the bottle driven by external magnetic stirrer

ensured the homogenization of the sample during the incubation. Samples were maintained at controlled temperatures of 20 °C and 14 °C for the tap-water and OMZ incubations, respectively. Oxygen concentration was simultaneously monitored during the incubation by STOX sensors as described previously[17, 12] and by Lumos sensors. For demonstration purposes, the oxygen consumption rates of the applied tap-water was stimulated by the injection of 0.1 mL of sieved (20 µm) liquefied cattle manure, thereby adding both organic matter and bacteria.

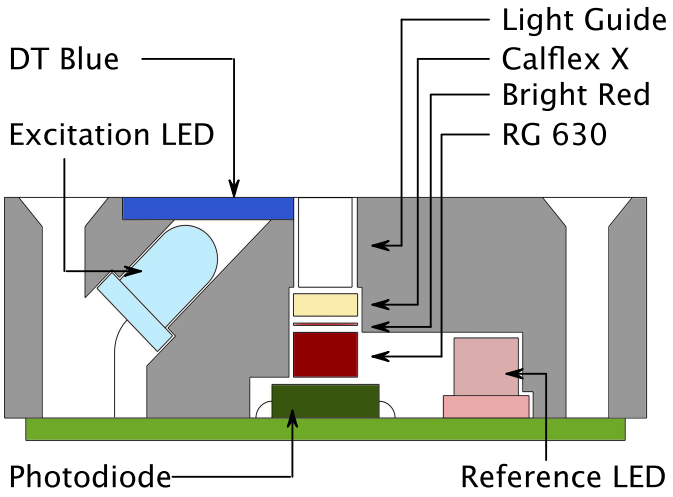

Figure 4.2: Optical Setup of the Lumos. A cross section of the Lumos' optical assembly. To maximize signal gain and simplify manufacturing a 45° angle layout is employed. The ideal distance of the sensor sheet from the top of the device is about 2-4 mm which is consistent with measurement through a vessel wall. Emission of the sensor is gathered in a short 3 mm fibre light guide and reaches the photodiode through a set of filters designed to reduce ambient and excitation light interference. The reference LED is positioned so that its light can directly reach the diode.

4.3.7 Oxygen intrusion experiments

To test for the intrusion of O_2 into standard laboratory incubations, we performed a series of tests applying the Lumos in combination with the trace range sensors (Pd-TFPP in Hyflon) described above. For experiments that mention headspace treatment a 2 ml or 20 ml headspace (He) was introduced into Exetainer® vials (Labco, UK) or serum bottles, respectively and the vials/bottles were shaken for 15 seconds. After this the headspace was flushed and the procedure was repeated two more times. Twelve ml Exetainer® vials were filled with degassed (He) MilliQ water spiked with 0.1 % (v/v) saturated HgCl2 solution. The Exetainer® vials were then closed with caps containing a butyl-rubber septum. These were either untreated caps or „deoxygenated“ caps that had been kept under helium atmosphere for one month prior to use. The serum bottle experiments were performed in 120 ml serum bottles which were filled with the same degassed water solution and applying stoppers that were either untreated or „deoxygenated“ by boiling for 15 min and then stored under a He atmosphere for three months.

For all experiments the vials/bottles were placed on a small rocking table – gently shaking the vials/bottles for 15 min per hour, data points acquired during shaking are not included in the graphs because of electrical interference from the rocking table.

4.4 Results and Discussion

4.4.1 Structure and Function of the Readout Device

The Lumos is a phase fluorimeter in a miniaturized package, designed to work with sensor sheets coated on glass substrates (Figure 4.1). The excitation circuit consists of a main 405 nm light emitting diode (LED) and a second 630 nm reference LED. Tests showed that both types of diodes have similar temperature dependence of their properties. Both LEDs are controlled by LED Driver Circuits that use operational amplifiers to convert the micro controllers digital to analog converter (DAC) output to a current between 0 and 94 mA. Operation amplifiers and the metal oxide semiconductor field-effect transistors (MOSFET) were chosen for low energy consumption and fast transition times, facilitating modulation of the excitation output in the kHz region. The optical components are enclosed in a machined anodized aluminum casing that optically isolates the different light pathways and acts as a support (Figure 4.2).

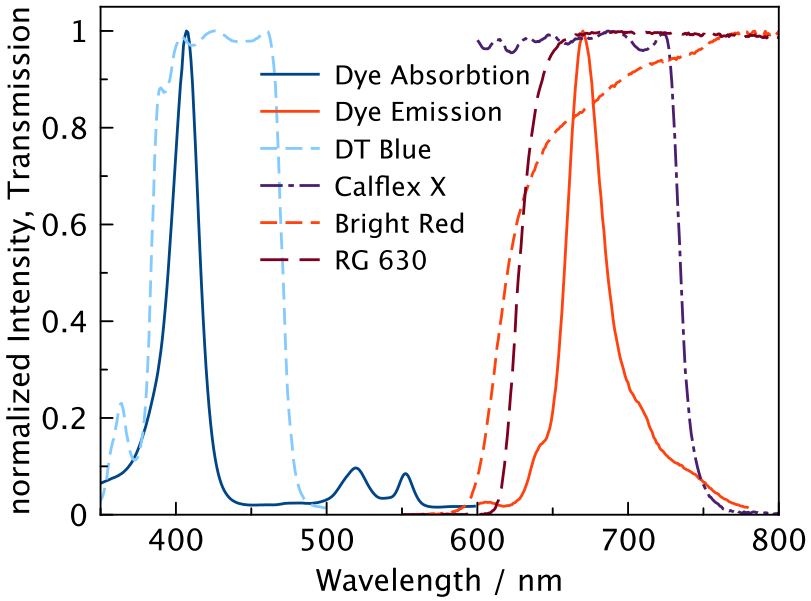

Figure 4.3: Spectral properties of the indicators and optical components. Transmission and normalized intensity spectra of the optical filters and the PdTFPP dye. A 405 nm LED is used to excite the dye and a DT Blue interference filter (the shown spectrum is the transmission at a 45° angle) is used to ensure that no excitation light is in the relevant detection region. A stack of Bright Red and RG 630 color filters combined with a Calflex X interference filter form a band pass for the interesting emission region. The Bright Red filter is used to minimize fluorescence inherent to the RG 630 color filter.

The main LED is fixed at an angle which results in an optimal overlap of excitation and detector light pathways 2 - 4 mm outside of the device. In front of the LED a DT Blue shortpass interference filter assures that almost no light ($< 0.1\,\%$) from the main LED can

directly reach the photodetector circuit. Light that is emitted from the sensor material is collected in a cylindrical light fibre and guided through a Bright Red and RG 630 long-pass color filter combined with a short-pass Calflex X IR blocker to greatly reduce ambient light interference and background to under 0.5 % (Figure 4.3). The emission light is then detected by a photodiode which is „bootstrapped“, resulting in reduced capacitance that improves the bandwidth of the amplifier, and a small reverse bias that reduces temperature dependence of the photodiode.

The current output of the photodiode is amplified using a 25 MOhm variable gain amplifier, and the resulting voltage is input to the micro controllers analog to digital converter (ADC). Because of the low modulation frequencies required for phosphorescence readout, all the signal processing can be done digitally and the need for an analog lock-in amplifier is eliminated, allowing for the small form factor of the device. Instead of a lock-in amplifier a digital single frequency Fourier transform algorithm is applied to the ADC input and in conjunction with coherent averaging the phase shift at the excitation frequency is then computed.

In a typical measurement the DAC outputs a sine wave represented by 64 points per period repeated over a sampling interval of 128 ms. This output is used to drive the main LED which in turn emits violet light that excites the dye in a sensing layer fixed in front of the device (usually inside a glass container, to which the readout device is attached on the outside). The luminescence response of the dye, which is phase shifted with respect to the excitation light, is guided to the photodiode, and the resulting current is amplified and read into the ADC as a voltage. Afterwards the reference LED is activated with the same DAC output, and because of the special geometry its emission light is directly guided to the photodiode. Any phase shift measured is thus solely due to electronic lag time. This reference value in conjunction with a previously performed zero calibration and the phase shift measured in the previous step are used to obtain the real phase shift value for the sensor material. This phase shift value can then be converted into a luminescence lifetime τ (assuming mono-exponential behavior of the decay curve) with the formula:

$$\tau = \frac{\tan \Phi}{2\pi f} \tag{4.1}$$

where f is the frequency of the modulation and Φ is the phase shift. A calibration can then be applied for obtaining oxygen concentration values. For temperature compensation purposes an IR temperature sensor is also included in the package: it measures thermal emission in the µm wavelength range (where glass has an emissivity close to 1), and therefore allows for online temperature compensation. The obtained phase shift and temperature values are placed into registers and can be read out by any protocol conforming software on an attached PC. The communication is based on a virtual com port provided via a UART to USB interface chip by FTDI. This chip is contained on a printed circuit board separate to that of the measurement circuitry and also controls advanced behavior like providing a hard reset and JTAG Interface for debugging and interfacing with the micro controllers boot loader for firmware updates. This separate board also contains the power control circuit that supplies the measurement circuit with a stabilized voltage.

4.4.2 Sensing Chemistry

Reaching detection limits in the low nano molar region is not a trivial task. There are multiple factors that influence the performance of a sensor, some of them inherent to the dye used and some to the matrix in which the dye is usually immobilized in. Both of these components have to be optimized to create sensor materials for measuring trace oxygen concentrations.

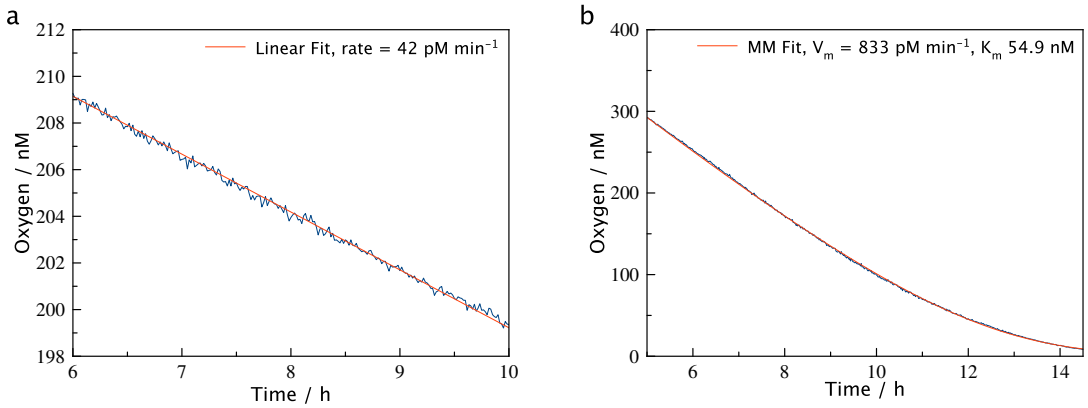

Figure 4.4: Respiration Experiments. Selected regions of a microbial respiration in tap-water (a) and tap-water with a little added manure (b). The more active sample shows considerably higher consumption rates and in both samples the low noise of the Lumos is evident. In (a) a linear fit (red line) is applied, but in (b) with manure amended water a Michealis-Menten fit (red line) can be applied due to the larger concentration range being analyzed.

Generally the sensitivity of an optical sensing material has to be estimated, acknowledging that permeability of the matrix multiplied by luminescence lifetime is directly proportional to sensitivity.[19] Using highly permeable matrices and dyes with long luminescence decay times is therefore the most reliable way to reach high sensor sensitivity.

A variety of dyes with very long decay times exist, with porphyrin based dyes being very popular[20, 21]. Especially benzoporpyrin based dyes are known for their high photostability and high molar absorption coefficients[22, 23]. There are two viable choices of porphyrin dyes: 1) benzoporphyrins and 2) pentafluorophenyl substituted porphyrins. Benzoporphyrins feature absorption maxima in the blue and red region of the electromagnetic spectrum and luminescence in the NIR region. The lifetimes of Pd (II) benzoporphyrin complexes are usually in the range of 200-400 µs, depending on substitution pattern and solubility in a given matrix. Because of their prominent absorption maximum in the red region they can be excited with ∼600nm LED light, which has some application specific advantages like higher transmission through tissue and lower risk of light induced biofouling compared to excitation with UV light. Due to the NIR luminescnece, visible light can be removed by filters and ambient light interference is therefore minimized. They show very good solubility in standard matrices like polystyrene.

Pentaflourophenyl substituted porphyrins feature high absorption in the violet region and luminescence in the red region. They have even longer lifetimes than most benzoporphyrins; up to 1200 µs in Hyflon AD 60 for the Pd based metal complex. They are also soluble in most standard matrices, but in addition, their perfluorinated substituents render them excellently soluble in highly permeable perfluorinated polymers like Hyflon and Teflon AF.

A sensor system could have been realized with both types of dyes, but the Lumos ultimately was designed to be compatible with the pentafluorphenyl porphyrins Pd-TFPP and it‘s spectrally comparable counterpart Pt-TFPP. The higher susceptibility to ambient light interference was considered a justifiable trade-off considering the expected 2-fold increase in sensitivity due to longer luminescence decay times alone. Also Pd-TFPP and Pt-TFPP are available commercially and can be embedded in the required high permeability matrices without further chemical modification.

Regarding the matrix for the sensing material, the choices were rather limited. Polystyrene is often used as a standard material, and combined with Pd-TFPP it would feature adequate sensitivity (although 10× lower than the chosen material, Figure 4.9a), with a detection limit already in the nM region. However, due to oxygen consumption in the sensor film itself, which is caused by the matrix not being stable enough against the very reactive singlet oxygen species generated during quenching, polystyrene could not be used for the sensor[24]. Other possible materials include ormosils, which have been shown to feature higher oxygen permeabilities[25, 26]. Indeed using poly(phenylsilsesquioxane) (PPSQ) as material increased the resulting sensors sensitivity 4-fold (Figure 4.9b). However, adsorption onto silica gel surface promised even higher sensitivities, and while this approach requires covalent grafting of the dye onto the surface, the resulting sensors are still the most sensitive based on that specific dye known to us[27]. Unfortunately there are some drawbacks to this approach, like low batch-to-batch reproducibility of sensor properties, more complex sensor preparation and lower long-term stability, due to chemical degradation of the more accessible dye. As a result, perfluorinated matrices such as Hyflon AD 60 (P $\approx$ 170 $\times$ 10^{-16} mol^{-1} m^{-1} s^{-1} Pa^{-1} ,ref. [28]) and Teflon AF 1600 (P $\approx$ 1200 $\times$ 10^{-16} mol^{-1} m^{-1} s^{-1} Pa^{-1},ref. [29]) were chosen, as they feature excellent chemical stability and are also commercially available. While sensors based on Teflon AF could potentially feature sensitivities comparable to silica-gel based sensors, it was concluded that the much cheaper Hyflon AD 60, in which the dyes also show better solubility and lower temperature dependence, should be used as the matrix material.

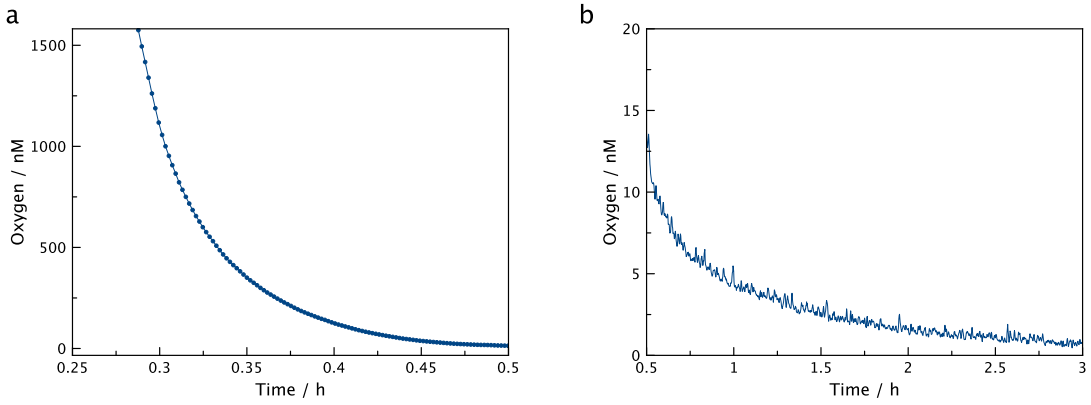

Figure 4.5: Enzymatic oxygen consumption. Oxygen consumption of GOx in buffered glucose solution showing the fast initial consumption (a) and slower consumption at low nM concentrations (b).

The final sensor materials thus consisted of Pd-TFPP embedded in Hyflon AD 60 (trace range), and Pt-TFPP embedded in Hyflon AD 60 (high range). These two sensors can be used to achieve an overall higher dynamic range and both are compatible with the Lumos readout device by just changing the excitation frequency (171 Hz for PdTFPP, 1500 Hz for PtTFPP). Both sensors feature very low temperature crosstalk in τ_0 and negligible temperature crosstalk in K_{SV}. Their calibration curves are not linear, but can be fitted using the two-site Stern-Volmer model[30, 31], yielding the calibration information shown in figure 4.10 and 4.11. K_{SV} is about 6.25 *times* 10^{-3} $ppmv^{-1}$ for the trace material and 0.29 *times* 10^{-3} ppmv-1 for the high range material, which corresponds to detection limits of 0.5 nM and 10 nM, respectively (assuming a minimal detectable phase shift change of 0.05°). The upper range limits are approximately

1000 nM and 20.000 nM for the trace and high range sensing material, respectively (assuming a cut-off at $tau_0/\tau \approx 4$).Both sensors are usable in even higher ranges but noise levels will increase noticeably. The low detection limits combined with low noise and high sampling frequency make the Lumos ideally suited for monitoring rates and oxygen levels in the low nano molar region.

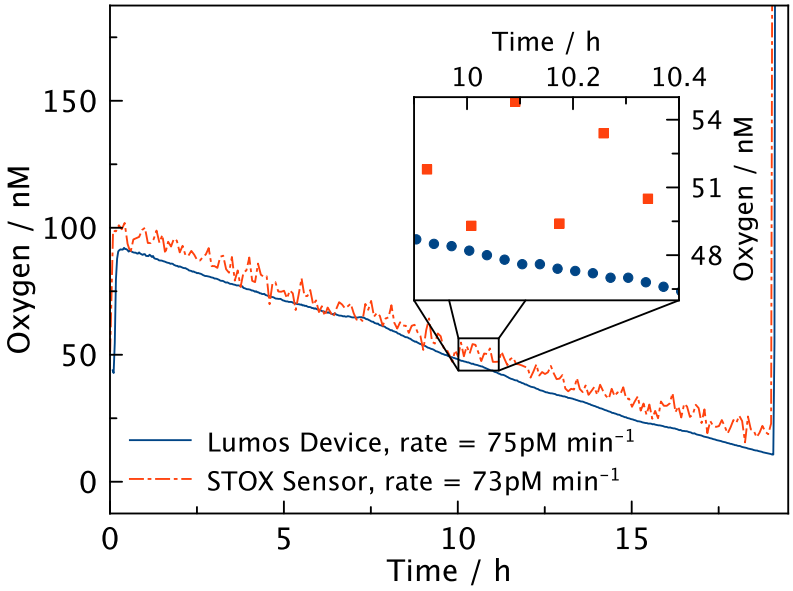

Figure 4.6: Comparison of the Lumos and STOX sensor. Respiration in a deep sea sample monitored with both Lumos and a STOX electrochemical sensor simultaneously. Both sensors detect comparable rates but the much lower noise of the Lumos is evident.

4.4.3 Applications

The device was developed as a tool for marine biologists and as such has been employed in a number of laboratory and field experiments. Presentation of the many data obtained with the Lumos is outside the scope of this manuscript and will be published separately. Here we include some sample results as a dempnstration of sensor performance during some representative applications. Figure 4.4 shows measurements in tap-water before and after amendment with diluted cattle manure (figure 4.4a, 4.4b). Prior to manure addition the oxygen decline was linear reflecting a consumption rate of 42 pmol L^{-1} min^{-1}. The microbial activity was greatly stimulated after manure addition and the acquisition of a larger part of the curve allowed for direct fitting of an integrated Michaelis Menten kinetic[32], resulting in a V_m of 833 pmol L^{-1} min^{-1} and a K_m of 54.9 nM. Noise was below one nanomolar.

Another example of oxygen consumption in the trace oxygen region is depicted in Figure 4.5. Here the oxygen consumption of glucose oxidation catalyzed by glucose oxidase was monitored. The data quality is similar to the example above, and demonstrate for fast low-noise determination of oxygen concentrations over three orders of magnitude. Michaelis Menten fits did, however, result in poor correlation coefficients, presumably as glucose was not available in excess and no catalase was present. Electro-chemical STOX sensors have previously been applied in aquatic studies of trace oxygen dynamics[13]. Figure 4.6 presents the results of a

parallel measurement of respiration rates using Lumos and a STOX sensor in a sea water sample from near anoxic OMZ deep water. Both devices show comparable rates and parallel trends and the slight parallel shift might be a result of differences in calibration procedures. However, the better signal to noise ratio of the Lumos is evident. Even though neither of the devices operate at their maximum sampling frequencies the Lumos has a distinct advantage in supplying a virtually continuous oxygen reading whereas the STOX sensor only yields one value for every measuring cycle that typically takes 0.5 - 5 min. A measuring cycle of a STOX sensor consists of a period where oxygen is allowed to enter the sensor followed by a period where oxygen is prevented from reaching the sensing cathode, representing the control of zero signal. This switching results in the somewhat lower response time, but is also the feature that allows for comparatively better resolution at low concentrations as compared to other electrochemical oxygen sensors[18].

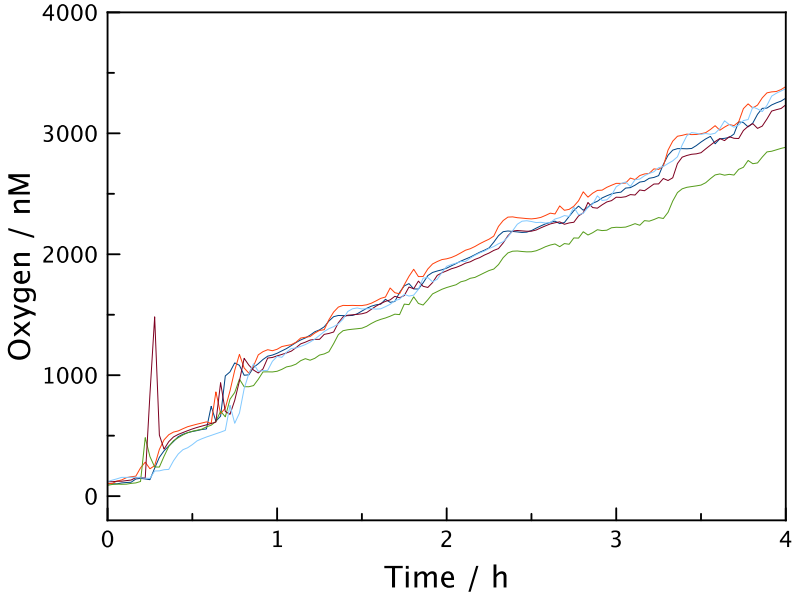

Figure 4.7: Oxygen Level in Exetainer® vials. Measurement of the oxygen intrusion into 12 ml Exetainer® vials that were used without special preparations to reduce oxygen contamination. The initial low oxygen concentration quickly rises to above 1 µM in less than an hour. The five lines represent five simultaneous measurements in separate vessels.

Due to the capability of the Lumos to measure through transparent walls of an experimental vessel, the device could be used to assess the ingress of oxygen into the type of containers that are routinely used to experimentally incubate samples from low oxygen environments. The results of these measurements can be seen in Figure 4.7 where a glass vial with a butyl rubber septum (Exetainer®) was filled with degassed water amended with $HgCl_2$ to inhibit any microbial activity. Vials were placed at constant temperature and exposed to air. No special precautions like the ones described by De Brabandere et al.[33] were taken to avoid oxygen contamination and multiple Lumos setups were applied in parallel. After just one hour, oxygen levels within the vials had increased to approximately 1 µM, and after 4 h the concentrations were around 3 µM. As such vials are routinely used for measuring anaerobic metabolism the 3 µM contaminating oxygen is worrisome as this would be sufficient oxygen to sustain aerobic metabolism and possibly inhibit anaerobic metabolism. For the water samples presented in

figure 4.6, 3 µM corresponds to 30 days of respiration. The experiment was subsequently repeated using: i) caps that had been stored under helium atmosphere for one month and ii) an additional 2ml headspace of He introduced into the vials. Figure 4.8 shows that both experiments exhibit drastically reduced oxygen contamination rates, suggesting that the main reason for contamination is diffusion from the oxygen contained in the rubber seal. Especially the vials containing the additional headspace show a constant low level of oxygen for up to 50 hours, making this method of preparation the preferred method to store samples with very low oxygen content. In Figures 4.12 and 4.13 the experiments were repeated with 120 ml serum bottles, and although overall oxygen contamination was lower due to the higher volume, the same general trend can be observed and the contamination was still significant.

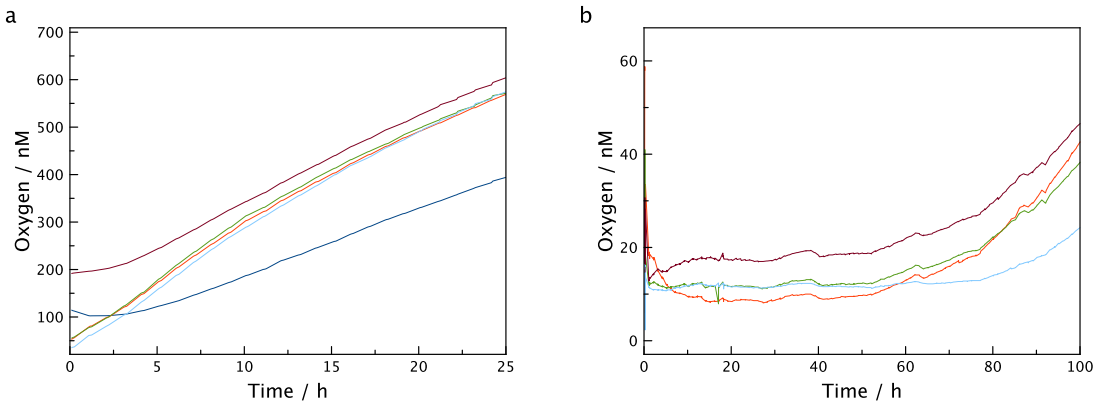

Figure 4.8: Oxygen Level in Exetainer® vials with oxygen contamination reducing preparations. Measurement of the oxygen contamination in 12 ml Exetainer® vials using rubber seals that were stored under helium atmosphere for one month (a) and additional introduction of a 2 ml He headspace (b). Both experiments show significantly reduced oxygen ingress.

4.5 Conclusions

We developed a combined system of specialized sensing materials and an optimized readout device that allows for high resolution oxygen sensing in the 0.5 -1000 nM range. This set up is ideal for studying respiration rates and microbial activity at trace amounts of oxygen. A second sensor material that is also compatible with the readout device can be used for higher concentration regions of 10 - 20.000 nM. As a result the whole system is small, modular, flexible, robust and easy to use, making it a valuable tool for researchers.

4.6 Acknowledgement

The work was financially supported by the European Research Council (Project ‘Oxygen’, N 267233).

4.7 References

[1] Tibor Anderlei and Jochen Büchs. “Device for sterile online measurement of the oxygen transfer rate in shaking flasks”. In: *Biochemical Engineering Journal* 7.2 (Mar. 2001), pp. 157–162.

[2] Atul Gupta and Govind Rao. “A study of oxygen transfer in shake flasks using a non-invasive oxygen sensor.” In: *Biotechnology and Bioengineering* 84.3 (Nov. 2003), pp. 351–358.

[3] Otto S Wolfbeis. “Materials for flourescence-based optical chemical sensors”. In: *Journal of Materials Chemistry* 15 (July 2005), pp. 2657–2669.

[4] Henry Berger. “Contamination due to process gases”. In: *Microelectronic Engineering* 10.3-4 (Feb. 1991), pp. 259–267.

[5] Kazuo Tanno. “An Automatic Recording Analyzer for the Determination of Dissolved Oxygen in Boiler Feed Water”. In: *Bulletin of the Chemical Society of Japan* 37.6 (Feb. 1964), pp. 804–810.

[6] Daniel A Stolper, Niels Peter Revsbech, and Donald E Canfield. “Aerobic growth at nanomolar oxygen concentrations.” In: *Proceedings of the National Academy of Sciences of the United States of America* 107.44 (Nov. 2010), pp. 18755–18760.

[7] I S Longmuir. “Respiration rate of bacteria as a function of oxygen concentration.” In: *The Biochemical journal* 57.1 (May 1954), pp. 81–87.

[8] F J Bergersen and G L Turner. “Bacteriods from Soybean Root Nodules: Respiration and NFormula-Fixation in Flow-Chamber Reactions with Oxyleghaemoglobin”. In: *Proceedings of the Royal Society B: Biological Sciences* 238.1293 (Jan. 1990), pp. 295–320.

[9] M J Johnson. “Aerobic microbial growth at low oxygen concentrations.” In: *Journal of bacteriology* 94.1 (July 1967), pp. 101–108.

[10] A Paulmier and D Ruiz-Pino. “Oxygen minimum zones (OMZs) in the modern ocean”. In: *Progress in Oceanography* 80.3-4 (Mar. 2009), pp. 113–128.

[11] Osvaldo Ulloa, Donald E Canfield, Edward F DeLong, Ricardo M Letelier, and Frank J Stewart. “Microbial oceanography of anoxic oxygen minimum zones.” In: *Proceedings of the National Academy of Sciences of the United States of America* 109.40 (Oct. 2012), pp. 15996–16003.

[12] Laura Tiano, Emilio Garcia-Robledo, Tage Dalsgaard, Allan H Devol, Bess B Ward, Osvaldo Ulloa, Donald E Canfield, and Niels Peter Revsbech. “Oxygen distribution and aerobic respiration in the north and south eastern tropical Pacific oxygen minimum zones”. In: *Deep Sea Research Part I: Oceanographic Research Papers* 94 (Dec. 2014), pp. 173–183.

[13] N P Revsbech, L H Larsen, J Gundersen, T Dalsgaard, O Ulloa, and B Thamdrup. “Determination of ultra-low oxygen concentrations in oxygen minimum zones by the STOX sensor”. In: *Limnol Oceanogr Methods* 7 (2009), pp. 371–381.

[14] Xu-Dong Wang and Otto S Wolfbeis. “Optical methods for sensing and imaging oxygen: materials, spectroscopies and applications.” In: *Chemical Society Reviews* 43.10 (May 2014), pp. 3666–3761.

[15] Michela Quaranta, Sergey M Borisov, and Ingo Klimant. “Indicators for optical oxygen sensors.” In: *Bioanalytical reviews* 4.2-4 (Dec. 2012), pp. 115–157.

[16] Colette McDonagh, Conor S Burke, and Brian D MacCraith. “Optical Chemical Sensors”. In: *Chemical reviews* 108 (2008), pp. 400–422.

[17] Laura Tiano, Emilio Garcia-Robledo, and Niels Peter Revsbech. “A new highly sensitive method to assess respiration rates and kinetics of natural planktonic communities by use of the switchable trace oxygen sensor and reduced oxygen concentrations.” In: *PloS one* 9.8 (2014), e105399.

[18] Niels Peter Revsbech, Bo Thamdrup, Tage Dalsgaard, and Donald Eugene Canfield. “Construction of STOX oxygen sensors and their application for determination of O2 concentrations in oxygen minimum zones.” In: *Methods in enzymology* 486 (2011), pp. 325–341.

[19] J Crank and G S Park. *Diffusion in Polymers*. Ed. by P Neogi. Marcel Dekker Inc., Feb. 1996.

[20] Y Amao and T Miyashita. “Novel optical oxygen sensing material: platinum octaethylporphyrin immobilized in a copolymer film of isobutyl methacrylate and tetrafluoropropyl methacrylate”. In: *Reactive and Functional Polymers* 47 (2001), pp. 49–54.

[21] M Trinkel. “Optical sensors for trace oxygen analysis”. PhD thesis. Karl Franzens University Graz: University of Graz, Jan. 1998.

[22] S M Borisov, G Nuss, and I Klimant. “Red Light-Excitable Oxygen Sensing Materials Based on Platinum(II) and Palladium(II) Benzoporphyrins”. In: *Analytical Chemistry* 80.24 (Dec. 2008), pp. 9435–9442.

[23] Sang-Kyung Lee and Ichiro Okura. “Photostable Optical Oxygen Sensing Material: Platinum Tetrakis(pentafluorophenyl)porphyrin Immobilized in Polystyrene”. In: *Analytical Communications* 34.6 (1997), pp. 185–188.

[24] Barbara Enko, Sergey M Borisov, Johannes Regensburger, Wolfgang Bäumler, Georg Gescheidt, and Ingo Klimant. “Singlet oxygen-induced photodegradation of the polymers and dyes in optical sensing materials and the effect of stabilizers on these processes.” In: *The journal of physical chemistry. A* 117.36 (Sept. 2013), pp. 8873–8882.

[25] X Chen, Z Zhong, Z Li, Y Jiang, and X Wang. “Characterization of ormosil film for dissolved oxygen-sensing”. In: *Sensors and Actuators B* 87 (2002), pp. 233–238.

[26] Ingo Klimant, Falk Ruckruh, Gregor Liebsch, Achim Stangelmayer, and Otto S Wolfbeis. “Fast Response Oxygen Micro-Optodes Based on Novel Soluble Ormosil Glasses”. In: *Microchimica Acta* 131.1-2 (June 1999), pp. 35–46.

[27] Sergey M Borisov, Philipp Lehner, and Ingo Klimant. “Novel optical trace oxygen sensors based on platinum(II) and palladium(II) complexes with 5,10,15,20-meso-tetrakis-(2,3,4,5,6-pentafluorphenyl)-porphyrin covalently immobilized on silica-gel particles.” In: *Analytica Chimica Acta* 690.1 (Mar. 2011), pp. 108–115.

[28] Vincenzo Arcella, Alessandro Ghielmi, and Giulio Tommasi. “High Performance Perfluoropolymer Films and Membranes”. In: *Annals of the New York Academy of Sciences* 984.1 (Mar. 2003), pp. 226–244.

[29] Stuart M Nemser and Ian C Roman. “Perfluorodioxole Membranes”. Pat. Sept. 1991.

[30] E R Carraway, J N Demas, and B A DeGraff. “Photophysics and oxygen quenching of transition-metal complexes on fumed silica”. In: *Langmuir* 7.12 (1991), pp. 2991–2998.

[31] J N Demas, B A DeGraff, and Wenying Xu. “Modeling of Luminescence Quenching-Based Sensors: Comparison of Multisite and Nonlinear Gas Solubility Models”. In: *Analytical Chemistry* 67.8 (Apr. 1995), pp. 1377–1380.

[32] Chetan T Goudar, Jagadeesh R Sonnad, and Ronald G Duggleby. “Parameter estimation using a direct solution of the integrated Michaelis-Menten equation”. In: *Biochimica et Biophysica Acta (BBA) - Protein Structure and Molecular Enzymology* 1429.2 (Jan. 1999), pp. 377–383.

[33] Loreto De Brabandere, Bo Thamdrup, Niels Peter Revsbech, and Roshan Foadi. “A critical assessment of the occurrence and extend of oxygen contamination during anaerobic incubations utilizing commercially available vials.” In: *Journal of microbiological methods* 88.1 (Jan. 2012), pp. 147–154.

4.8 Supporting Figures

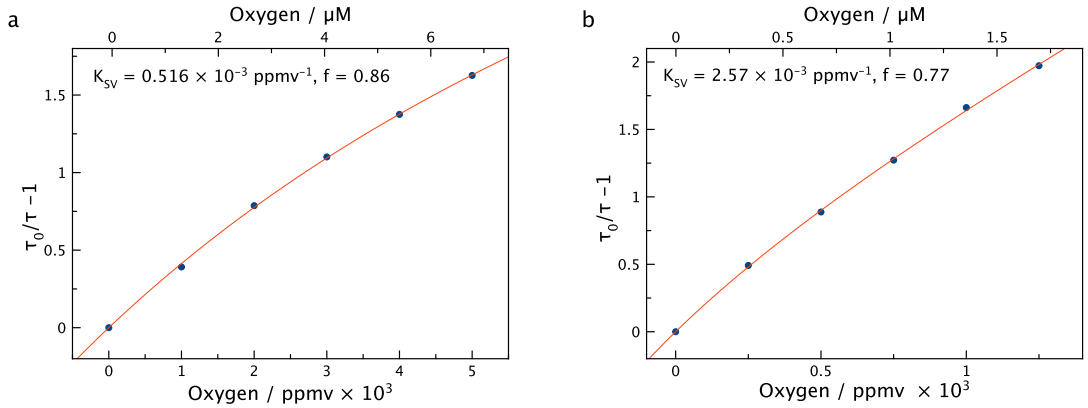

Figure 4.9: Calibrations in standard matrices. Calibrations of PdTFPP in polystyrene (a) and PPSQ (b) at 20 °C.

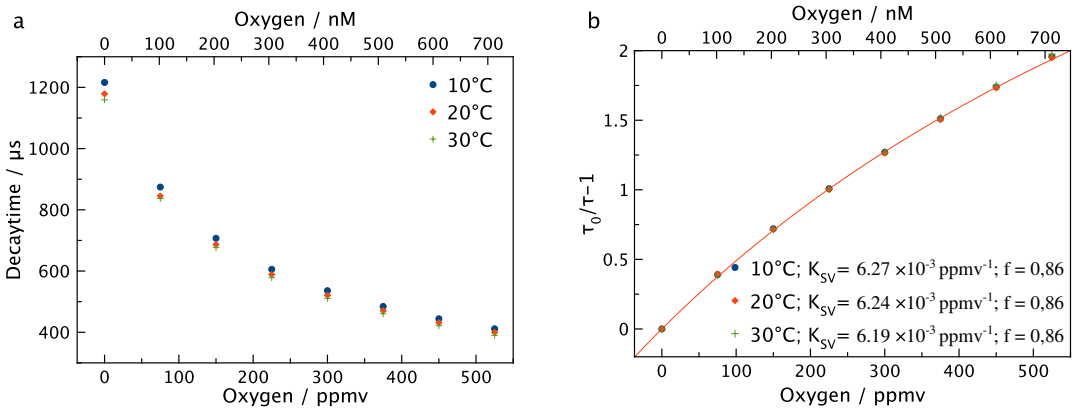

Figure 4.10: Calibrations of PdTFPP in Hyflon AD 60. Calibration of the Lumos trace sensor material (PdTFPP in Hyflon AD 60) at different temperatures. Notice the high sensitivity and low temperature crosstalk in τ_0(a), as well as the negligible temperature crosstalk in K_{SV}(b). Calibration curves show a slight curvature, that is common for polymer based matrices and can be fitted using the two-site Stern-Volmer model.

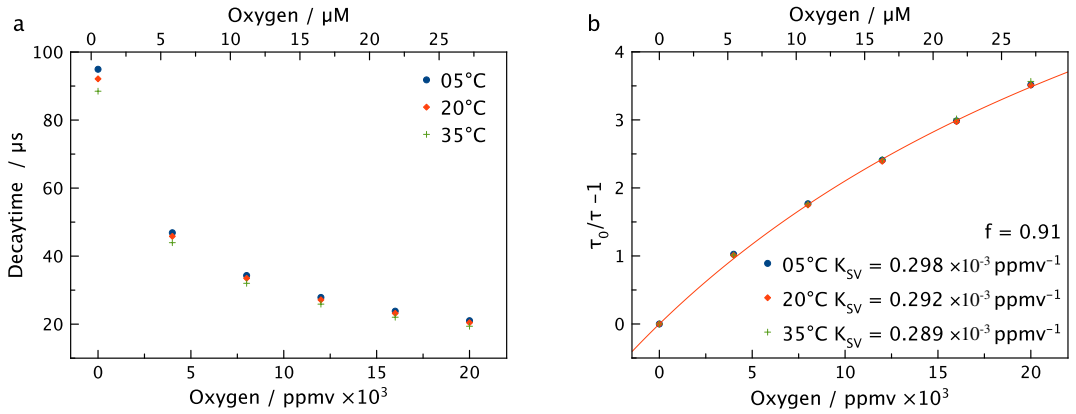

Figure 4.11: Calibrations of PtTFPP in Hyflon AD 60. Calibration of the Lumos high range sensor material (PtTFPP in Hyflon AD 60) at different temperatures. This material also shows very low dependencies of τ_0 (a) and K_{SV} (b) on temperature. The sensitivity of this material is around twenty fold smaller than the trace material and provides a larger dynamic range for measurements at higher oxygen concentrations.

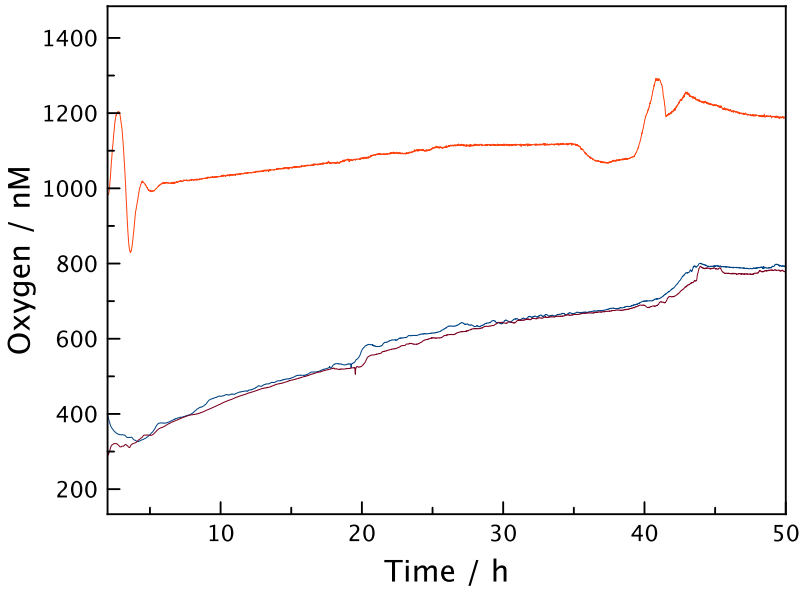

Figure 4.12: Oxygen Level in Serum Bottle. Measurement of the oxygen intrusion into samples contained in three 120 ml serum bottles that were used without special preparations to reduce oxygen contamination. While oxygen intrusion is smaller compared to Exetainer® vials, in part due to the larger volume to exposed surface ratio, intrusion is still significant.

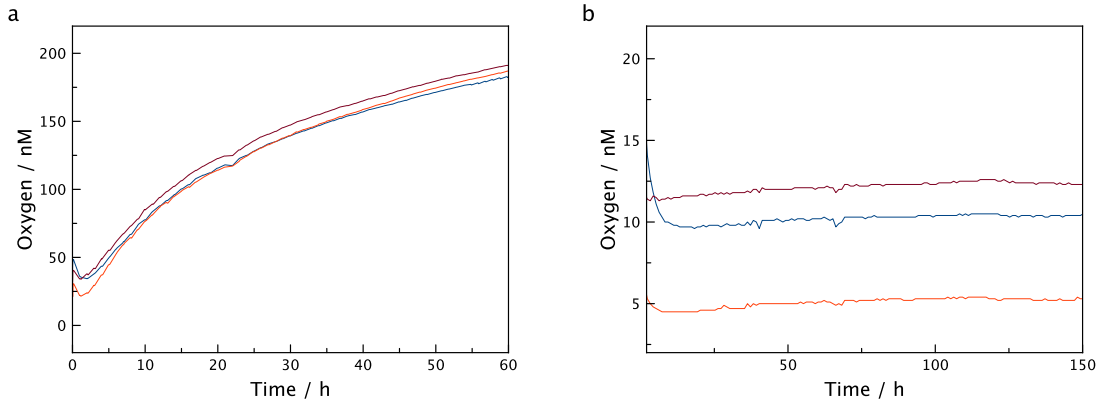

Figure 4.13: Oxygen Level in Serum Bottle with oxygen contamination reducing preparations. Measurement of oxygen intrusion into samples contained in 120 ml serum bottles capped with stoppers that were kept under helium atmosphere for 3 months (a) and an additional 20 ml He headspace (b). In the same trend as figure 4.8, oxygen intrusion is vastly reduced especially for the bottles with headspace.

5 Other Work

In contrast to the content of previous chapters, many additional results were not published in peer reviewed journals. Because they are still of interest and were part of or were a direct result of work on Project Oxygen, such results are summarized and presented in this chapter.

5.1 Optical Oxygen Imaging using an iPhone

5.1.1 Introduction

Simplification and cost-reduction of measurement equipment is a common trend in many applied sciences, whether it is for point-of-care devices in medicine[1] or other analytical tools for application in development regions or for home users.[2] Many such strategies involve smart phones,[3, 4] because they are widely available and combine the processing power of modern computers with open standards and other amenities like built-in charge-coupled-device (CCD) cameras and microphones. The sensor materials presented in chapter 2 feature extraordinarily long luminescence decay times, so long in fact that any ordinary video camera, even the ones embedded in most modern smartphones are sufficient to capture time-domain based decay curves directly. It is therefore possible to measure oxygen concentrations or even perform oxygen imaging with just a smartphone, specialized software and a matching sensor material.

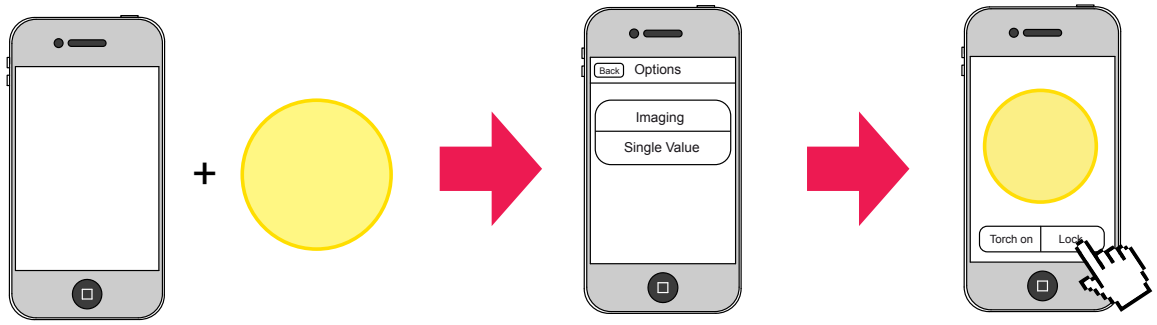

Figure 5.1: Scheme of the iPhone Application

5.1.2 Methods

The smart phone used for experiments was an Apple iPhone 4 with built in CCD Camera and LED Flash. Software was written in Objective-C using the iPhone developer SDK in XCode and a publishing license supplied by Graz University of Technology. Imaging results were obtained with Matlab and the imaging toolbox. The sensors employ the boron complex based oxygen indicator dyes described in section 2. Specifically BF_2HBAN was used for its higher brightness, higher temperature dependence and longer decay time. BF_2HBAN was synthesized as described in chapter 2, poly(vinylidenchloride-co-acetonitrile) (PVDC/PAN) was purchased

from ABCR (Austria, www.abcr.de) and circular 3 cm diameter teflon filters were purchased from Merck Millipore (Germany, emdmillipore.com).

Sensor Material Preparation

BF_2HBAN (1 % (w/w) in polymer) and PVDC/PAN ((5 % (w/w) in solvent) were dissolved in acetone. The resulting "cocktail" was knife coated using a 175 µm spacer onto Mylar® foil. While the film was still wet a teflon filter was placed on the substrate and the resulting material was dried at 60 °C for 30 minutes.

iPhone Program

The software for the iPhone was programmed utilizing Model-View-Controller architecture. When the software initializes access to the device's camera is requested and upon successful capture a live-feed is shown on the phones display. Superimposed on that feed are the controls and an aiming reticule that shows which area of the video feed is going to be used for readout. Through the controls the user can toggle the LED flash on and off (to check positioning) and engage the exposure and focus lock. This last step is necessary before a measurement to disable auto exposure control of the phone, which would result in the acquisition of unusable datasets.

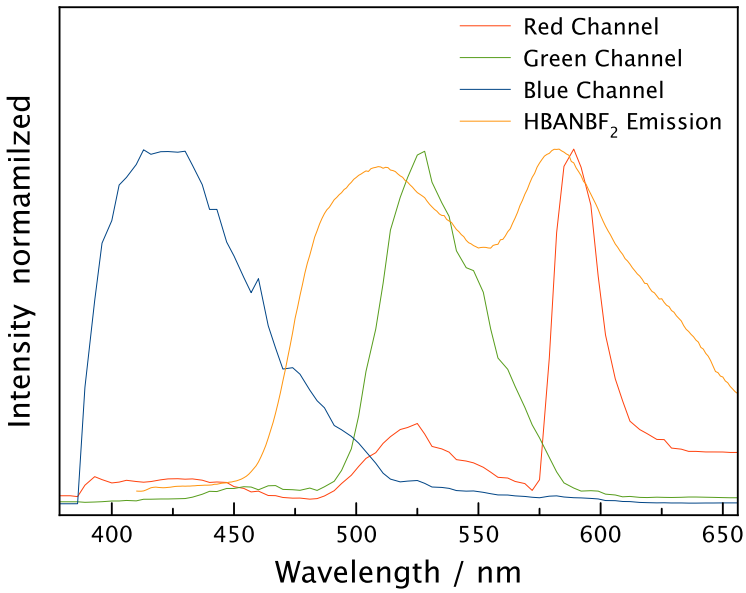

Figure 5.2: iPhone CCD and dye spectral overlap. Fluorescence of the dye is visible in the blue and green channels of the iPhone's CCD chip, phosphorescence is visible in the red channel.

The user can also access an options menu where the type of acquisition (single value or imaging), output format, calibration values and some debug settings can be chosen. Once the lock is engaged the user is presented with the option to start a measurement. A schematic representation of how the system might be used is presented in figure 5.1. If single value acquisition is enabled once the measurements starts, the software will compile an XQuartz shader for the included graphics chip that automatically integrates an area of 200x200 pixels and returns a single intensity value at 30 frames per second (FPS). The internal LED Flash

is switched on for 1 second and then a decay curve is captured and analyzed using rapid lifetime determination and using the calibration values from the options menu an oxygen value is computed and displayed on the screen. While the iPhone certainly has enough processing power to handle imaging applications as well (though most likely not in realtime), for this proof-of-concept imaging analysis was performed on videos captured by the iPhone at 30 FPS using the imaging toolbox from Matlab, on a desktop computer that was already available.

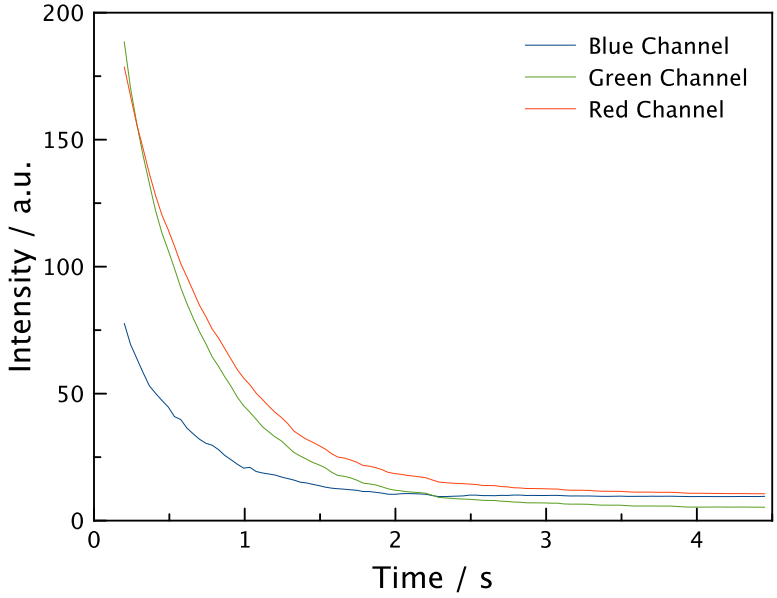

Figure 5.3: Data acquired with an iPhone 4 at 25 °C. The sensor was purged with nitrogen to obtain the maximum signal intensity, all three channels are shown.

5.1.3 Results and Discussion

The matrices described in chapter 2 yield very sensitive sensors that would have severely complicated data acquisition. Therefore PVDC/PAN copolymer was used that is highly impermeable, and is in fact often used as a barrier material for oxygen. In combination with these ultra sensitive dyes though, the resulting sensor material is sensitive to oxygen in the physiological region. To improve response times and signal intensity teflon filters were soaked in the sensing cocktail to provide a higher surface and more backscatter of luminescence. The sensor material is uniquely suited to be read out with any common video camera, such as the one contained in an iPhone, because the emission of the dye overlaps nicely with the different channels of a CCD Chip. Figure 5.2 shows the spectral overlap of the iPhone's CCD channels with the dye emission spectrum. Most of the fluorescence peak is contained in the blue and green channels, whereas the phosphorescence peak is almost exclusively contained in the red channel.

If the iPhone is used to capture data it should be held very steadily. Note that due to the integration of an area single point acquisition should be less prone to errors resulting from small movements than imaging applications. Still, for best results the iPhone was mounted on a tripod for all data presented herein. Figure 5.3 shows the decay curves obtained for all three channels when measuring the sensor material under deoxygenated conditions. Notice

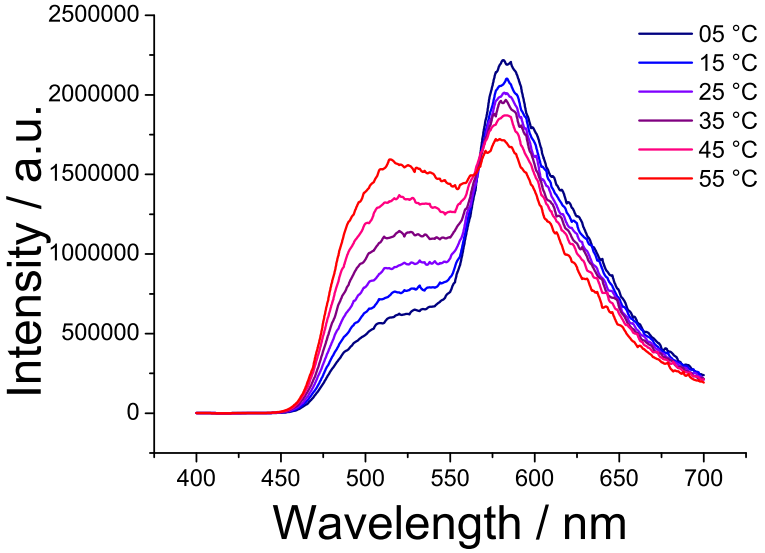

Figure 5.4: Temperature dependent delayed luminescence spectra of the sensor material acquired with a Fluorolog 3 spectrometer and a delay of 5 ms under deoxygenated conditions.

how all three channels show roughly the same lifetime even though the intensities are different. That is because the sensor material also exhibits e-type delayed fluorescence that is picked up by the blue and green channels and has the same lifetime as the material's phosphorescence by definition. E-type delayed fluorescence is thermally activated and therefore has a strong dependence on temperature. Interestingly this means that the signal intensity of the different channels also depends on temperature. Figure 5.4 shows how the delayed luminescence spectrum of BF_2HBAN in PVDC/PAN changes at different temperatures.

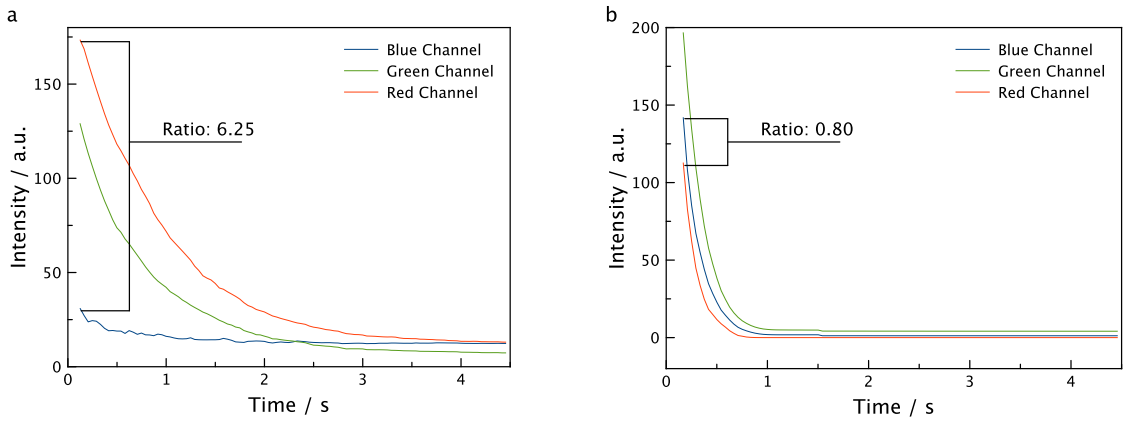

Figure 5.5: Data acquired with an iPhone 4 at 05 °C (a) and 55 °C (b) under deoxygenated conditions. Note the large difference in both initial channel intensity ratio and lifetime.

In theory it should be possible to use the ratio of delayed fluorescence and phosphorescence intensity to measure temperature independently of oxygen concentration (assuming the sensor material is not fully quenched of course). Figure 5.5 shows how two measurements obtained

with the iPhone compare at different temperatures. Obviously the ratio changes significantly with temperature and could theoretically be used to correct the equally temperature dependent lifetime, leading to a self referenced oxygen determination method. Unfortunately, as is also evident in figure 5.5 the temperature dependence of the lifetime is also quite significant. This means that at least with the limited capabilities of an iPhone, such a self referenced compensation is not feasible, at least not with current consumer technology. Given the steep development and integration trend in consumer electronics a device with the necessary capabilities might soon be available. Indeed the currently available iPhone 6 features image acquisition at 240 FPS which would improve temporal resolution by a factor of 8.

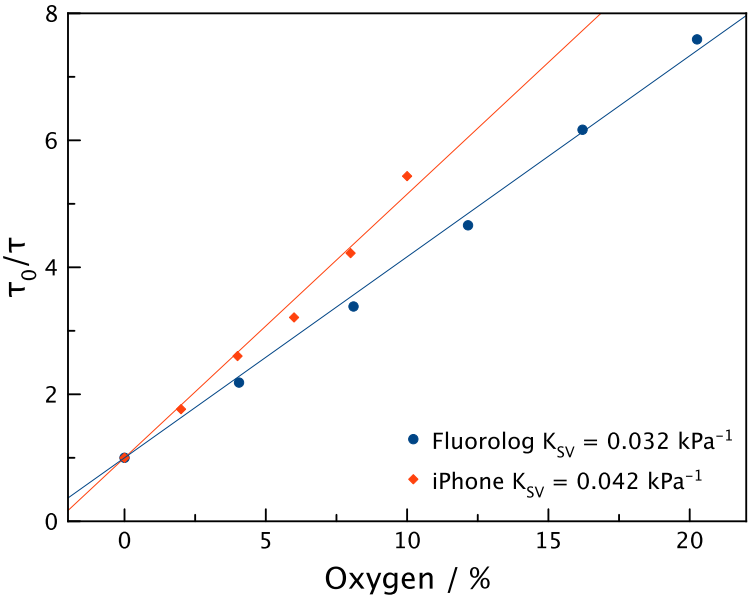

Figure 5.6: Calibration of BF_2HBAN with an iPhone 4 and Fluorolog Spectrometer at 25 °C.

To prove that – regardless of temperature compensation capabilities – the iPhone and sensing material are usable as an oxygen sensor, a calibration curve was obtained using a gas mixing device described in previous chapters. The calibration curve was obtained with both the iPhone and the Fluorolog 3 spectrometer in kinetic acquisition mode under the same conditions to test whether calibrations would be reliable. Figure 5.6 shows calibrations obtained with both the iPhone and the Fluorolog spectrometer. The two methods generally show comparable results, the discrepancy between the two methods might originate from timing differences, the different methods used for obtaining a lifetime value or from non-linearities described in chapter 3 that are caused by the different illumination intensities of the iPhones LED flash and the Spectrometer's xenon lamp. As the intended goal was to reach a proof-of-concept this result is more than adequate. For many applications readout is likely not required to be very specific. One such application could be the monitoring of anaerobe fermentation in multiple vessels in a dark or red-light room. If a sensor spot is mounted in each vessel just holding the iPhone to the sidewall of the vessel and recording a single datapoint could be used to quickly check if oxygen levels are still below a certain threshold. In a more simplified approach the iPhone might be removed altogether and just quickly switching the light on and off in the room could be used to qualitatively identify vessels that are no longer anaerobe (where no afterglow is visible to the naked eye).

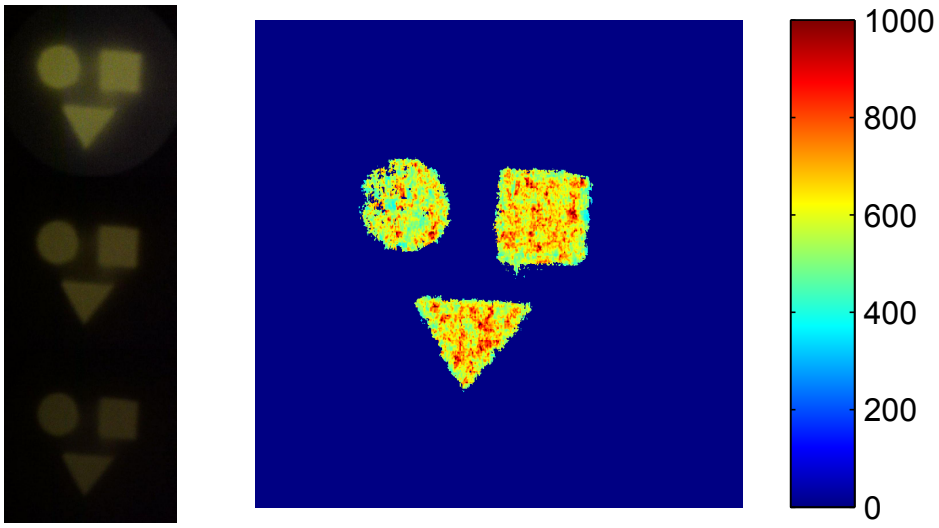

Figure 5.7: Imaging data acquired with an iPhone 4 at 25 °C, the video captured with the iPhone was analyzed using the Matlab imaging toolbox. The computed lifetime values were normalized and a cutoff was used to eliminate low values.

To highlight the last proposed application – oxygen imaging – a mask was cut from Mylar® foil and glued onto a regular sensor sheet. This allowed for the nitrogen flow to only deoxygenate exposed areas, therefore a spatially different oxygen concentration could be achieved, which could then be resolved using oxygen imaging. Figure 5.7 shows the results obtained by using the Matlab imaging toolbox on a desktop PC to analyze the video footage acquired with an iPhone. Evidently this very simple example shows that this setup can in fact be used to monitor oxygen concentrations in imaging applications.

5.1.4 Conclusion

The very long decay times of the dyes presented in chapter 2 enable the readout of the dyes with a common video camera operating at 30 FPS such as the one built into an iPhone and other smart phones. It was shown that an iPhone can be used with specialized sensing sheets to use time-domain based lifetime determination to acquire oxygen readings in the physiological region. The calibration obtained correlates with a calibration obtained with another method for the same material. Because of the special dependence of delayed fluorescence and phosphorescence intensity on temperature a direct compensation of the signal for temperature is theoretically possible but requires mere sensitive detectors than are available in the iPhone. While all experiments were performed with an iPhone the same results should be obtainable with any video camera capable of recording at least 30 FPS and a suitable excitation light source. In fact the sensor material can even be used for qualitative assessment of oxygen contamination with the naked eye.

5.2 Ultra Trace Readout Device

5.2.1 Introduction

The ultra trace oxygen materials presented in chapter 2 were read out with a Fluorolog 3 in kinetic acquisition mode. They are intended, however, for application by marine researchers to investigate microbial oxygen respiration close to anoxic conditions. It is not feasible for this application to require a high-end fluorescence spectrometer for readout, especially – as was shown in this chapter – readout of the sensor is theoretically possible with even a common smart phone CCD camera. Because of that a dedicated readout device should be constructed that – much in the same way as the Lumos (described in chapter 4) – is constructed specifically for use with the $Al(HPhN)_3$ in Hyflon AD 60 ultra trace sensing material. Such a device needs to fulfill very specialized requirements: It needs to have a better temporal resolution than a common CCD camera, a sampling frequency of about 1 kHz is ideal. Further it needs to keep the sample in absolute darkness and must be very sensitive, so the concentration of the sensing dye can be kept as low as possible to avoid the non-linearities described in chapter 3. It can, however, have a very simplified optical setup, because excitation and measurement are temporally separated.

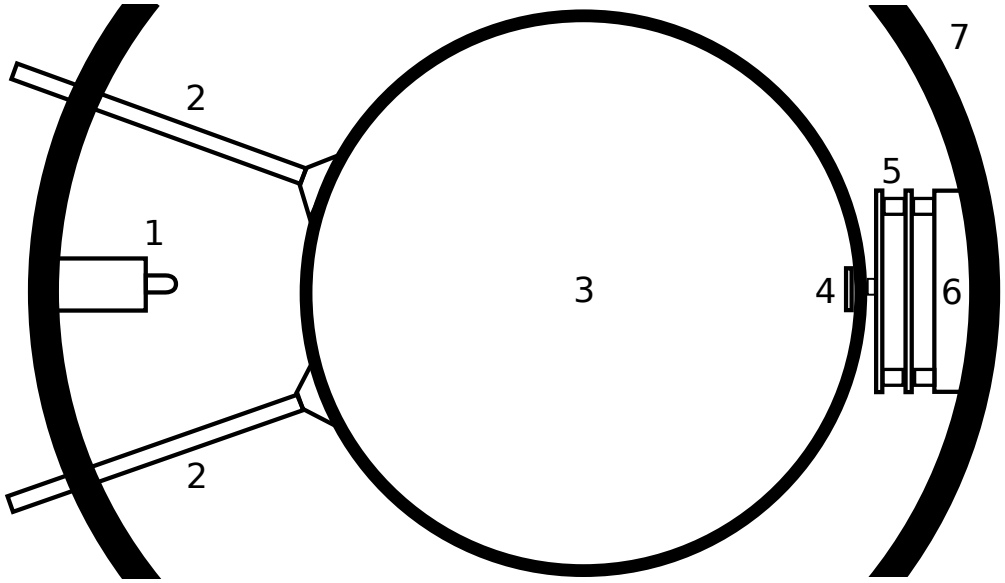

Figure 5.8: Cross-section of the ultra trace readout device. The device consists of a excitation LED (1), two set screws (2) to hold a measurement vessel (3) – with sensor spot (4) fixed inside – in front of the readout circuit board (PCB) (5). The readout PCB is mounted to an adapter (6) that is itself fixed to the inside of a 160 mm diameter polymer tube (7). The tube acts as support and protects against interference from ambient light.

5.2.2 Device

The device is in prototype stage as of the time of this writing. Figure 5.8 shows a schematic of what the finished device should look like. To avoid the mentioned non-linearities, the concentration of the dye in the matrix will be kept as low as possible. For that to be feasible

the photodiode needs to be able to gather as much light as possible from the sensing layer. Therefore the photodiode is placed directly in front of the outer vessel wall to minimize the distance to the sensor spot. As a result the excitation light source is moved to the other side of the vessel and excitation happens through the bulk medium. Optical filters are not necessary because of the temporal separation of excitation and detection. The experimental vessel is placed inside the outer tube enclosing the measurement chamber. It is positioned so that the applied sensor spot is directly in front of the photodiode and held in place by set screws. The outer tube is necessary because of the filter-less setup and because of the non-linearities described in chapter 3, which necessitate the absolute absence of ambient light. The read out part of the setup consists of 2 printed circuit boards (PCB). One contains the measurement and background-compensation photodiodes and the other contains an amplifier, 12 bit analog to digital converter (ADC), a random access memory (RAM) chip and a micro controller unit (MCU). The signal of the measurement and background photodiode gets amplified by the variable gain amplifier read into the MCU through the ADC and the results are then stored in the RAM chip. The RAM chip is required because the MCUs internal storage is not big enough to hold the values generated during 3 seconds of 1 kHz sampling. The MCU contains custom firmware that controls the measurement procedure. First the excitation LED is switched on for 1 second, then after a 5 ms delay the MCU starts sampling the ADC output at a 1 kHz rate and writes the data into the external RAM chip. When the measurement is finished the data can be read out and transferred over an UART connection to the accompanying software.

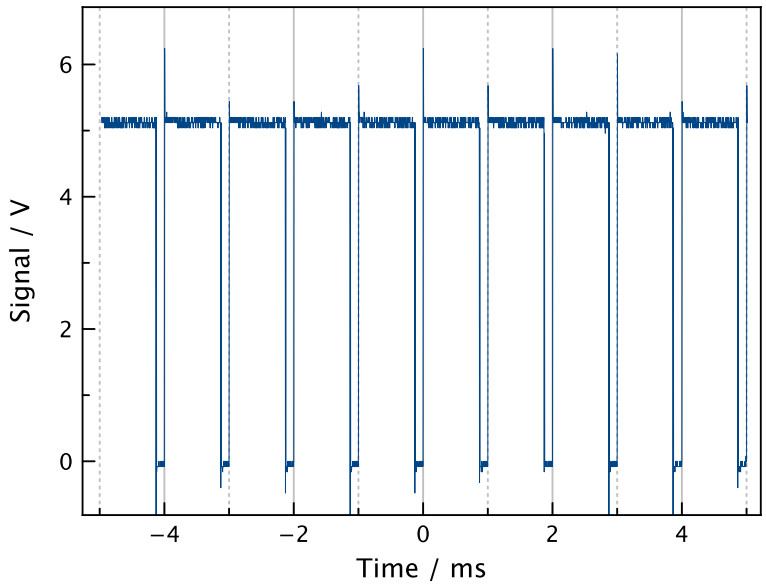

Figure 5.9: Verification of the 1 kHz sampling interval using an oscilloscope

It is very important to verify that the MCU is in fact capable of recoding data points at a reliable 1 ms interval as results would otherwise be unreproducible. Figure 5.9 shows the results of a sampling experiment conducted with an oscilloscope.

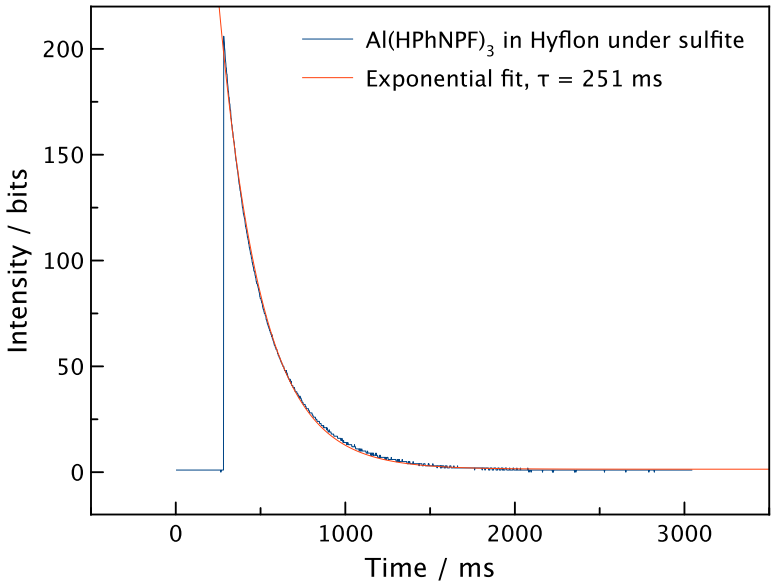

Figure 5.10: First test results with the prototype device, sampling the sensor material under deoxygenated conditions.

Using a prototype device, its capability of recording the sensor materials response was demonstrated in a simple experiment. Figure 5.10 shows the decay curve captured for a sensor layer fixed to the side wall of a vessel containing deoxygenated sodium sulfite solution. The exponential fit shows good correlation with the lifetimes obtained for the same material in previous chapters, and noise of the signal is very low. This is especially important because the low dye concentrations and resulting low emission intensities require strong amplification of the signal.

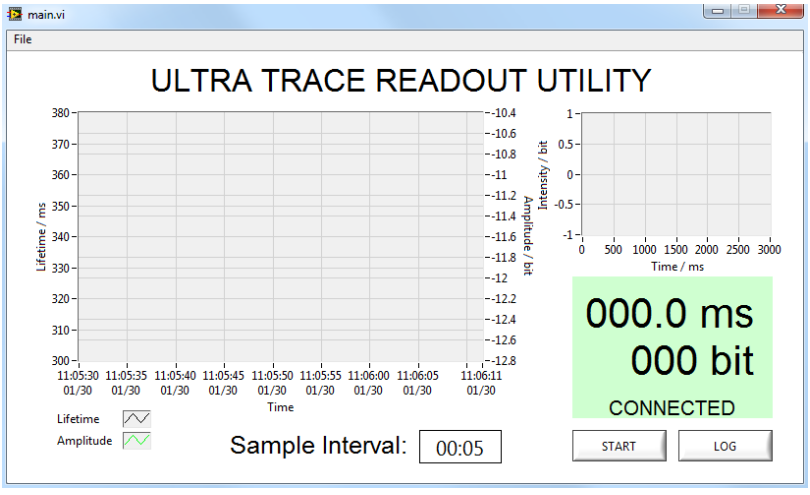

Figure 5.11: Software Interface of the Ultra Trace Reader

5.2.3 Software

Software to control the device and record measurement data on a connected computer was created using LabView. The software is designed to operate as a state-machine. Depending on user and device input the software changes its internal state to perform data-operations or update the graphical user interface (GUI). The GUI of the software is presented in figure 5.11, it is kept simplistic as to be easily usable. The user might change the sample interval, and activate and stop measurement and logging of data. Currently the software displays the results of the last measurement in the top right corner and uses either rapid lifetime determination or a direct exponential fit (users-choice) to extract a lifetime value from the measurement data. The lifetime values captured over time are then displayed in the large graph on the left. For future versions of the software it is planned to add direct conversion of lifetime values to oxygen concentrations through an user defined calibration curve.

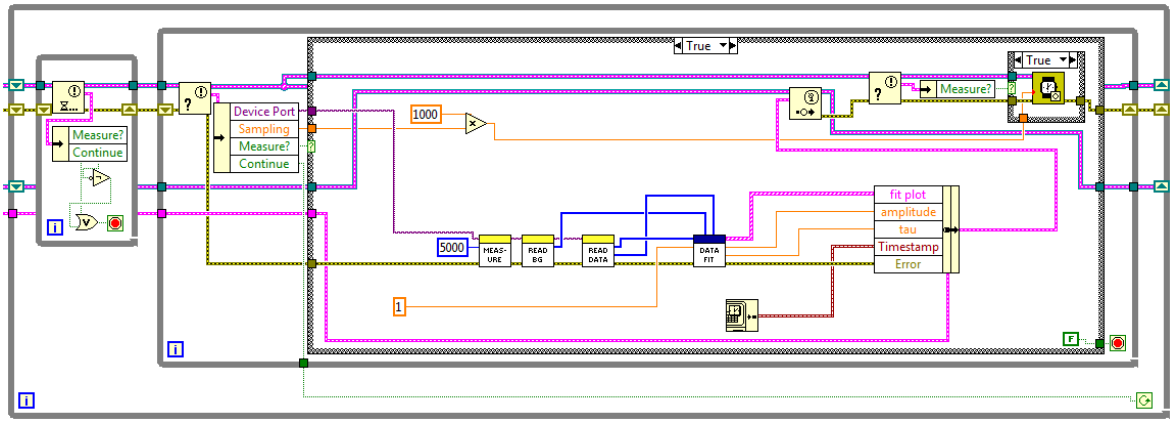

Figure 5.12: Measurement Loop of the Ultra Trace Reader Software as displayed in LabView

When the software is started, it automatically starts searching for connected compatible devices, if one is found the software switches into the active state and waits for user input. The software is designed using two main loops, one being the aforementioned state-machine handling all user interaction and data handling and the second being a dedicated measurement loop tasked with acquiring data points in a timely manner. The state-machine controls the measurement loop through a LabView class called 'occurrence' which informs other code executed in parallel of any changes made to itself. If the user clicks on START for example the occurrence changes its internal state to 'measure' and the measurement loop which has been idle up to this point recognizes this change and starts acquiring data. A scheme of the measurement loop as it is displayed in LabView is depicted in figure 5.12. Gray borders indicate loops and rectangles indicate 'SubVIs' which are comparable to functions in other programming languages, the colored lines represent the propagation of variables through the program. The execution of the loop starts on the left, where it is kept inside the first smaller loop until the occurrence changes its state to measure. The execution then switches into the second loop, where parameters like sampling interval, the type of fit to be performed etc., are read out and implemented to perform a measurement. The device takes about 3 seconds to capture a sample and the resulting curve is then fitted using the selected method and the result is sent to the main state-machine where it triggers a refresh of the GUI to display the newly acquired data.

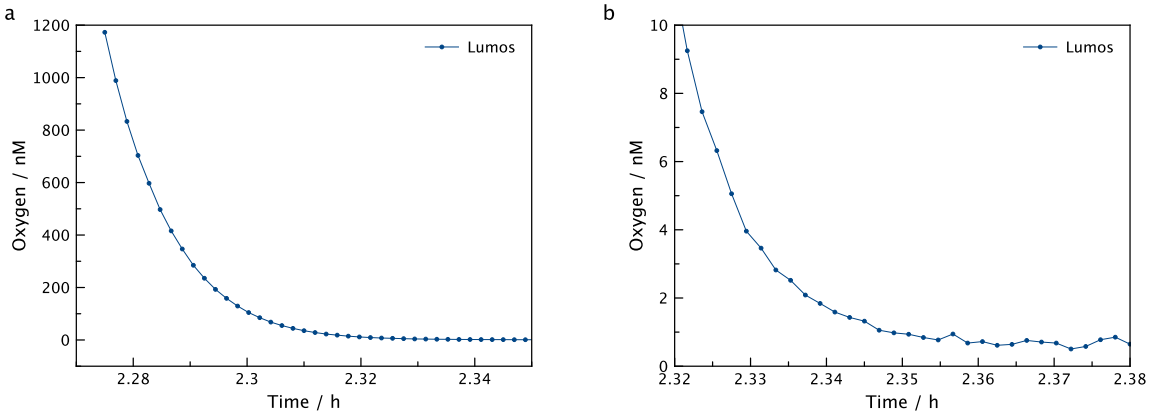

Figure 5.13: Monitoring E.Coli Oxygen Consumption with the Lumos, (a) and (b) show different regions of the same measurement dataset and highlight the sub nanomolar resolution of the Lumos sensor.

5.2.4 Results with Fluorolog Setup

Even though the device is currently in development, an existing setup consisting of the Fluorolog 3 spectrometer mentioned in earlier chapters and specialized glass bottles could be used to obtain measurements with the ultra trace sensor material of biological samples. How these measurements were performed is detailed in the appendix in section 9.4. Because the software from which the fluorolog spectrometer is operated is not designed for this type of data acquisition setting up correct sampling is a bit complicated. Measurements are, of course, expected to be easier to perform with the newly designed device. Nonetheless some first results of measuring the oxygen consumption of e. coli by both Lumos and ultra trace sensors is presented in this section. Figure 5.13 shows the initial consumption as captured with the Lumos device, once again the low noise and capabilities of the Lumos to measure single digit nano molar concentrations is evident. However, the Lumos is not capable of resolving concentrations below one nano molar, as is evident from figure 5.14a.

In figure 5.14a Lumos and ultra trace data is presented together on a logarithmic scale, and while the Lumos does not resolve any changes in concentration the ultra trace sensor does continue to resolve oxygen consumption in the measurement vessel. Figure 5.14b shows the ultra trace data by its own and evidently the ultra trace sensor monitored the consumption of oxygen by e. coli in the range of 1 nM down to 200 pM. For the ultra trace material this range lies in the upper area of its dynamic range, but unfortunately the Fluorolog 3 spectrometer used as a readout device for these measurements has a limit as to how much data in can acquire before ceasing to function. In future measurements with the finished ultra trace readout device we hope to capture the whole consumption curve down to its endpoint.

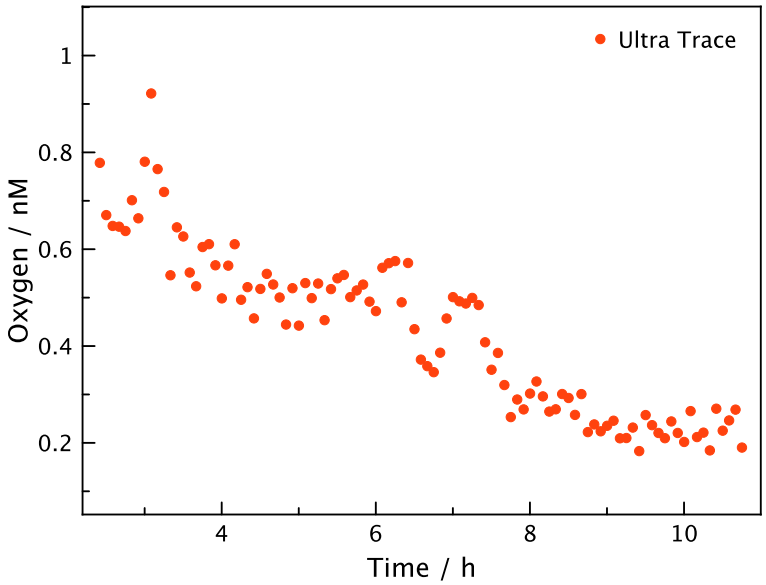

Figure 5.14: Monitoring E.Coli Oxygen Consumption with the Fluorolog and Ultra Trace Material

5.3 Investigating the Influence of Pressure on Sensing Materials

5.3.1 Introduction

When oxygen sensors are employed for in-situ measurements in the ocean, they are exposed not only to a harsh environment but also to large changes in hydrostatic pressure. Such changes in pressure can alter the sensors properties, because the matrix and – as a consequence – the dyes environment could be mechanically altered. Matrices with large internal volumes, like they are common for trace sensing applications, may be compressed and therefore show lower permeability for oxygen. Compression may also bring dye molecules closer together, thereby increasing the efficiency of interaction.

How exactly changes in ambient hydrostatic pressure change the sensing properties and calibration of various sensing materials is currently unknown. Because sensors will be deployed for in-situ measurements as part of project oxygen we decided to investigate the pressure dependence of sensor properties and calibrations and therefore built a setup that can be used to measure the sensor response at different hydrostatic pressures.

5.3.2 Setup and Artifacts

The setup consists of a pressure chamber constructed from a stainless steel tube capped with stainless steel fittings that are connected by hardened metal bolts. The bottom fitting has a connector for a hand pump to control the hydrostatic pressure and the top has openings that are used for fiberoptic feedthroughs by pyro science. The sensors can be fixed inside the pressure container and read-out from the outside by pyro science phase fluorimeter modules attached to the fiberoptic feedthroughs. The pressure is monitored by an electronic pressure gauge and can be regulated through manipulation of the manual pump. The system was tested

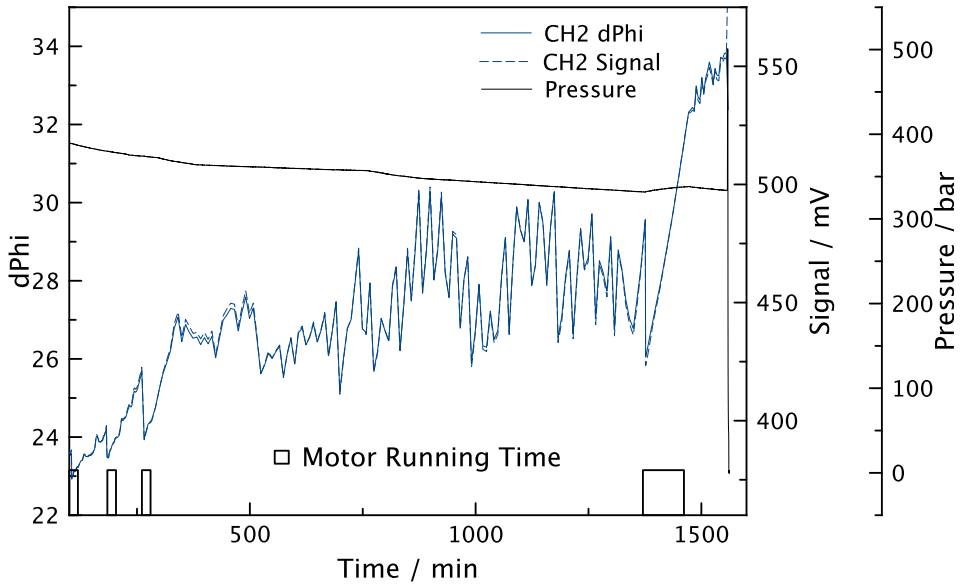

Figure 5.15: Artifacts due to inhomogeneity of the pressure compartment. The used sensor consists of a platinum(II)benzoporphyrin dye embedded in polystyrene. The water was air saturated.

with a standard oxygen sensing material consisting of a platinum(II)benzoporphyrin embedded in polystyrene. Initial measurements showed that the medium inside the pressure container is very inhomogeneous that is why a brushless motor was added to the setup. Figure 5.15 shows the results obtained from a continuous measurement at roughly 350 bar hydrostatic pressure. Evidently the system is very inhomogeneous. If the motor is switched on, the large fluctuations disappear, but unfortunately – as is also evident – the motor does consume oxygen while in use. As a result a second submersible, pressure stable stirring mechanism was constructed using a brushless motor with a strong magnet attached to its axle fixed inside a closed, silicon oil filled tube with shielded electronic connectors that has a magnetic stirring bar attached at the outside. With this setup oxygen consumption and fluctuation inside the measurement chamber could be significantly reduced. However, in the following experiments another artifact could be identified.

Figure 5.16 shows a measurement of the beginning of a pressure cycle. Interestingly there is a peak in signal and lifetime at the very first time pressure is applied to the system. At first, this peak was observed at initial pressure jumps of 50 bar, but figure 5.16 undeniably shows that even a pressure difference of just 1 bar triggers the peak in sensor signal and lifetime. The reason for this peak is as of yet unknown, while this peak being an artifact caused in some way by the optical setup seems likely, the fact that both signal and lifetime are affected equally contradicts that explanation.

5.3.3 Outlook

While the system still exhibits unexplained artifacts it can not be used for measuring sensor properties and calibrations. However, future measurements will likely determine the real cause of this last artifact. If it is indeed the result of the optical setup, just measuring the same material with a different setup should already yield important insight. As the jump is observed

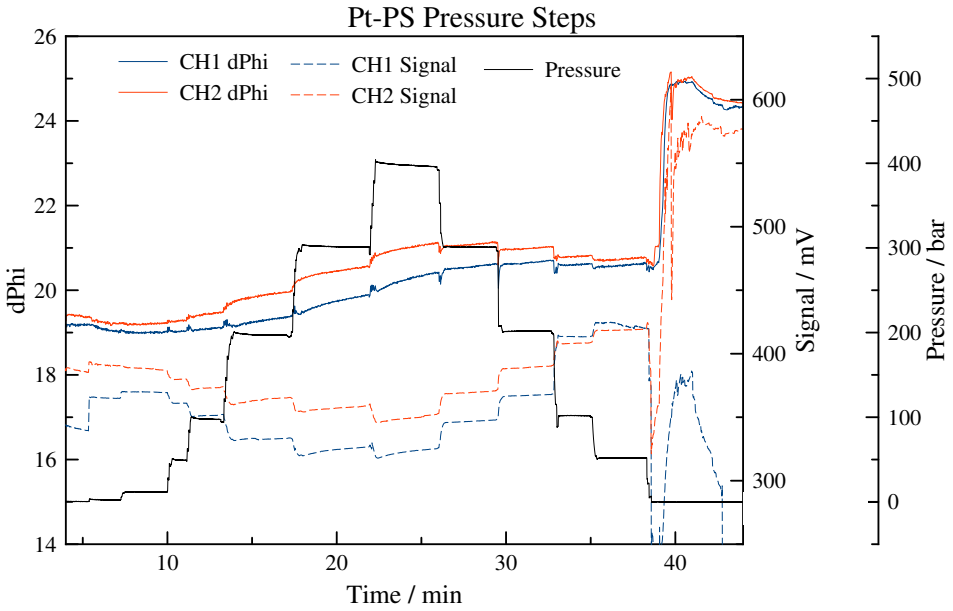

Figure 5.16: A measurement of the very beginning of a pressure cycle showing a yet unidentified artifact. The sensor material used was the same as in figure 5.15. The water was air saturated.

already at a 1 bar jump in hydrostatic pressure, this experiment could likely be repeated in a regular round bottom flask with a measurement through the side wall. Because this measurement would not include a fibre optic feedthrough any unexpected response that is also visible in this test cannot be caused by the optical setup and is therefore either caused by the sensor material itself or by pressure dependent activity on the sensors surface, like the collapse of tiny bubbles. An argument that speaks against the theory of surface changes is that the same peak was also observed by colleagues in Denmark that performed their experiments under deoxygenated conditions. They therefore could not have observed an actual change in oxygen partial pressure caused by the collapse of bubbles. The appendix contains a list of sensing materials that might be interesting to investigate once the setup is fully operational.

5.4 References

[1] Luc Gervais, Nico de Rooij, and Emmanuel Delamarche. “Microfluidic chips for point-of-care immunodiagnostics.” In: *Advanced Materials* 23.24 (June 2011), H151–76.

[2] Ali Kemal Yetisen, Muhammad Safwan Akram, and Christopher R Lowe. “Paper-based microfluidic point-of-care diagnostic devices.” In: *Lab on a chip* 13.12 (June 2013), pp. 2210–2251.

[3] Seung Ah Lee and Changhuei Yang. “A smartphone-based chip-scale microscope using ambient illumination.” In: *Lab on a chip* 14.16 (Aug. 2014), pp. 3056–3063.

[4] Li Shen, Joshua A Hagen, and Ian Papautsky. “Point-of-care colorimetric detection with a smartphone.” In: *Lab on a chip* 12.21 (Nov. 2012), pp. 4240–4243.

6 Conclusion

In this work we presented new sensor materials based on boron and aluminium complexes of rigid aromatic analogues of β-diketones, that are imbedded in highly permeable per-fluorinated matrices like Hyflon AD 60 and Teflon AF 1600. The used dyes feature exceptionally long decaying phosphorescence as well as e-type delayed fluorescence. As a result, the materials exhibit oxygen sensitivities that were previously unreachable. Some of the presented materials feature detection limits as low as 5 pM, which is a 20-fold increase in sensitivity compared to other state-of-the-art materials. Additionally the dual emission of the dyes potentially allows for direct temperature compensation of the read-out signal. Measuring oxygen concentrations in such low regions is, however, very challenging and we presented an in-depth study of the various photo-physical phenomena that can have an influence on calibration curves and therefore measurement results. We found that time domain based measurements are preferable to ratiometric approaches as they eliminate at least some of the dependence of calibration curves on excitation light intensity. Intensity based measurements are heavily influenced by non-linear behavior resulting from the depopulation of a dyes electronic ground state. But even with this influence removed there are still some other ways in which K_{SV} is dependent on excitation light. One such way which has to be eliminated under any circumstances is chemical oxygen consumption, that is why for trace oxygen measurements only very oxidation stable highly per-fluorinated matrices are used. These matrices introduce a new problem, however. Singlet oxygen requires compounds with very specific vibrational energy levels such as the C-H bond to deactivate through collision. The absence of such compounds in per-fluorinated matrices results in drastically longer lifetime of singlet oxygen that results in a depletion of ground-state oxygen in the sensor material and therefore also in a change of calibration. We also presented a mathematical model simulating these influences that shows good correlation with experimental results. As a consequence, dye concentrations have to be kept very low and specialized read-out equipment had to be constructed to interface these ultra trace sensors. The device presented in this work is currently in the prototype stage and will no doubt be further improved in the future. Another device that was built as part of Project Oxygen is the Lumos. It is also presented in this work. The Lumos is a specialized phase fluorimeter designed to read-out matching sensing materials that come in two versions and are capable of resolving oxygen in the ranges of 0.5 -1000 nM and 10 - 20.000 nM. These systems have been employed for marine research and some of the results obtained are also presented.

In conclusion, we developed sensing materials and a corresponding readout device for the nano molar range that is currently extensively used by our colleagues in Aarhus and Odense. We also developed ultra trace sensing materials that can resolve oxygen down to single digit pico molar concentrations and performed some initial experiments in monitoring microbial oxygen consumption with these materials. A dedicated read-out device is currently in the prototype stage. Further we investigated the influence of excitation light changes on K_{SV} and modeled and measured the various photo-physical phenomena that are responsible. In addition some smaller projects that were investigated are also presented.

7 List of Figures

8 List of Tables

9 Appendix

9.1 Dual Lifetime Referencing

In this method a reference dye is chosen so that its luminescence properties are also not affected by the analyte. But its excitation and emission wavelength are showing a significant overlap with the corresponding regions of the indicator dye. Additionally this reference dye needs to have a lifetime significantly different from the indicator dye. If all these requirements are met, the normalized intensity of the indicator dye can be calculated by measuring the whole systems phase shift (according to the principles described in the next section). This works by assuming the response signal to be a linear combination of both indicator and reference signals, i.e.:

$$\begin{aligned} A_m \cos \Phi_m &= A_{ind} \cos \Phi_{ind} + A_{ref} \cos \Phi_{ref} \\ A_m \sin \Phi_m &= A_{ind} \sin \Phi_{ind} + A_{ref} \sin \Phi_{ref} \end{aligned} \tag{9.1}$$

where A is the amplitude and Φ is the phase shift. As the reference dye's decay time is much longer than the indicator dye's decay time and can be considered constant, equation 9.1 can be simplified to:

$$\begin{aligned} A_m \cos \Phi_m &= A_{ind} + A_{ref} \cos \Phi_{ref} \\ A_m \sin \Phi_m &= A_{ref} \sin \Phi_{ref} \end{aligned} \tag{9.2}$$

Dividing the two expressions in equation 9.2 yields equation 9.3.

$$\frac{A_m \cos \Phi_m}{A_m \sin \Phi_m} = \cot \Phi_m = \cot \Phi_{ref} + \frac{A_{ind}}{\sin \Phi_{ref} A_{ref}} \tag{9.3}$$

As the reference dye's properties are considered to remain constant, Φ_m is therefore proportional to A_{ind}/A_{ref} and can be used as a normalized readout signal.

9.2 PIMs - polymers with intrinsic microporosity

9.2.1 Introduction

Polymers with intrinsic microporosity (PIMs)[1, 2, 3] are a relatively young area of research. They are based on rigid backbone alternating ladder co polymers of various spiro- and aryl compounds. Their rigidity prevents folding of the chains in the drying polymer film into an optimally dense structure and instead forms a kinetically stable continuum of nanometer sized pores. Such PIMs show very high permeabilities for different gases[4] and because of the large difference in permeability for e.g. oxygen and carbon dioxide they are being investigated for their application as gas separation membranes.[5] While they are comparable in permeability to other highly permeable polymers like Teflon AF, they have an important advantage: they are incredibly cheap to synthesize. Because of that fact PIMs were investigated for their usability as matrix material for ultra trace oxygen sensors.

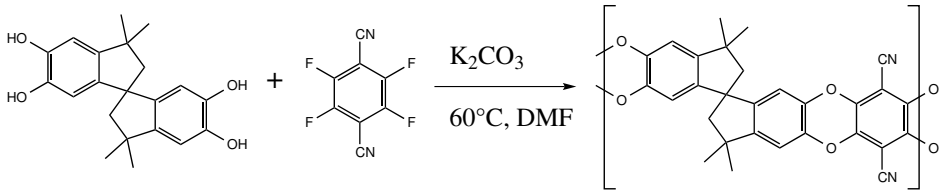

Figure 9.1: Synthesis of PIM 1

9.2.2 Experimental and Preliminary Results

To investigate their suitability as matrix material for ultra trace oxygen sensors PIM 1 was synthesized according to literature procedures (figure 9.1, ref. [1]). The resulting polymer is brittle and bright yellow, it also shows intense green fluorescence. The polymer is readily soluble in tetrahydrofuran. Figure 9.2 shows the absorption and emission spectra of PIM 1. Because of that emission the material might be suitable for use as a matrix with inherent reference characteristics in ratiometric sensors. Unfortunately, PIM 1 is not suitable as a matrix for trace oxygen sensing, because tests showed that it consumes a lot of oxygen, presumably due to the cyanide groups that are readily oxidized.

PIM 1 which is comprised of spirobisidane and dicyano benzene monomers is not the only possible polymer with intrinsic microporosity that can be created using the same synthetic strategy. Figure 9.3 shows some other monomers that might be used instead of the dicyano benzene monomer to form comparable compounds. Tests with the perfluoro biphenyl monomer (structure 1, figure 9.3) yielded a highly cross linked polymer that could not be dissolved in various solvents. As is apparent from the structure there are enough binding sites on the perfluoro biphenyl monomer to cause this high level of crosslinking. Literature suggests[1] that obtaining a soluble product is possible with these educts, owing possibly to a thermodynamic preference of single substitution on each ring, we were ,however, not able to reproduce these results. The PIM comprised of spirobisidane and octafluorotoluene (structure 2, figure 9.3) was also synthesized, but yielded a very brittle polymer with very short chain lengths. Apparently the lack of a second electron withdrawing substituent on the benzene ring hindered the progress of chain growth.

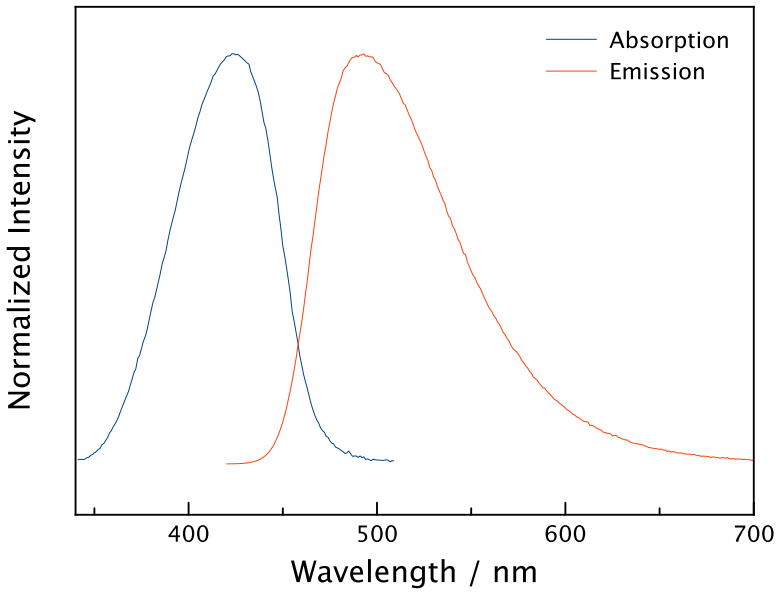

Figure 9.2: Spectral properties of PIM 1

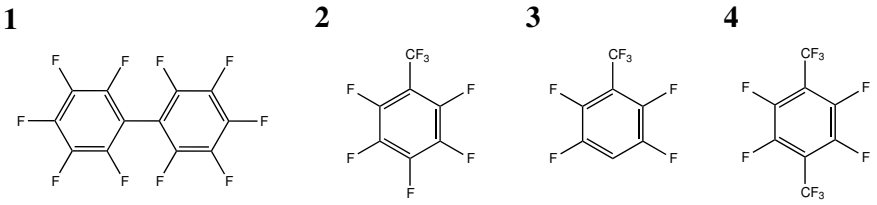

Figure 9.3: Other possible educts for PIM synthesis

9.2.3 Conclusion and Outlook

While PIMs are interesting polymers because of their rigid backbone structure, microporosity and easy synthesis, the two PIMs investigated are not inherently suitable for trace oxygen sensors. This is because of their low oxidation stability (PIM 1) and their lack of solubility in common solvents (PIM 2). PIM 1 might still be interesting to use as sensor material for physiological range ratiometric sensors because of its inherent fluorescence. This was not further investigated, though. A wide variety of other possible monomers to use as PIM educts exists. However, investigation of PIM matrices stopped once Hyflon AD 60 was found to be well suited as a cheaper alternative to Teflon AF. Hyflon AD 60 is not only less expensive than Teflon AF, it also has a comparable sensitivity and many dyes show better solubility in Hyflon than in Teflon AF. Furthermore, because it is commercially available it can be obtained with consistent batch to batch reproducibility.

Although Hyflon proved to be the easier choice for ultra trace sensors, PIMs still show a lot of promising possibilities. For example the 3-hydro perfluoro toluene monomer (structure 3, figure 9.3) might be used in conjunction with bromo-substituted dyes to perform direct arylation of the dyes according to the reaction described by Lafrance et al[6] (figure 9.4). The product of this reaction might then be used in conjuction with the spirobisidane and a 3-(trifluoromethyl) perfluorotoluoene (structure 4, figure 9.3) to form a PIM with covalently linked dye that should – in theory – be very oxidation stable. However, due to time constraints, this possibility could not be investigated and might be interesting for further research.

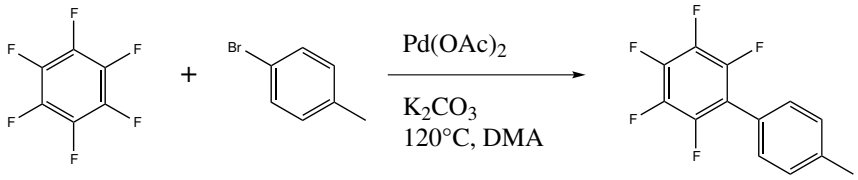

Figure 9.4: Aryl Coupling reaction as described by Lafrance et al.

9.3 References

[1] Peter M Budd, Bader S. Ghanem, Saad Makhseed, and Neil B McKeown. *Polymers of intrinsic microporosity (PIMs): robust, solution-processable, organic nanoporous materials.* Jan. 2004. URL: http://pubs.rsc.org/en/content/articlepdf/2004/CC/B311764B.

[2] Neil B McKeown and Peter M Budd. "Exploitation of Intrinsic Microporosity in Polymer-Based Materials". In: *Macromolecules* 43.12 (June 2010), pp. 5163–5176.

[3] CG Bezzu, D Fritsch, BM Kariuki, and NB McKeown. "Hexaphenylbenzene-based polymers of intrinsic microporosity". In: *Chem Commun ...* (2011).

[4] Peter M Budd, Neil B McKeown, and Detlev Fritsch. "Free volume and intrinsic microporosity in polymers". In: *Journal of Materials Chemistry* 15.20 (2005), pp. 1977–1986.

[5] PM Budd, NB McKeown, and BS Ghanem. "Gas permeation parameters and other physicochemical properties of a polymer of intrinsic microporosity: Polybenzodioxane PIM-1". In: *Journal of Membrane Science* (2008).

[6] Marc Lafrance, Christopher N Rowley, Tom K Woo, and Keith Fagnou. "Catalytic Intermolecular Direct Arylation of Perfluorobenzenes". In: *Journal of the American Chemical Society* 128.27 (July 2006), pp. 8754–8756.

9.4 How Fluorolog Readout of the Ultra Trace Sensors is accomplished

Sensor cocktails for both Lumos and the $(HPhNPF)_3Al$ based ultra-trace sensor materials are prepared according to the descriptions contained in the respective sections. Measurements in the ultra-trace regions need to be performed in special glass bottles that have a capillary for pressure compensation and a glass seal. Because the neck of these bottles is only 7.5 mm wide, standard Lumos sensor spots cannot be used in conjunction with these bottles. Instead 0.1 mm thin glass slides are treated with Aquaphobe CF and are cut into 7 × 10 mm pieces. These are then drop coated with the respective cocktails, dried and coated on the backside with hot-melt adhesive (HMA). The optimal way to do so is to cut a small rectangular piece (about 3 × 4 × 1 mm) from the HMA and place the piece of glass with the backside up and the rectangular piece of HMA on top in a 80 °C oven for 5-10 minutes.

To place the sensor spots in the glass bottle, the room temperature spots are introduced into the bottle placed at the right height and distance on the inside wall of the bottle (about one third of the height off the bottom of the bottle and 90° apart). The bottle is then heated in the oven at 80 °C for about 10 minutes until the HMA has liquified. The sensor spots are then gently pushed into their final position using a curved spatula and the bottle is left to cool at room temperature. To replace the sensor spots they can be easily removed using organic solvents and a little force.

The prepared bottle then needs to be placed in the Fluorolog sampling compartment. For that the cuvette holder (including its legs) is removed from the sampling compartment and a small magnetic stirrer is introduced. Depending on the placement of the sensor spots inside the bottle the height of the stirrer might need to be adjusted by placing distance material under the stirrer. A Lumos readout device is then placed on the outside wall of the bottle over the corresponding sensor spot by using double sided adhesive tape. One should make sure not to cover any part of the Lumos readout device's optical components. The bottle can then be filled with a liquid sample. For best results in microbial respiration experiments it is advisable to remove a large part of the contained oxygen through nitrogen bubbling prior to transference of the liquid into the measurement bottle.

In case of e. coli experiments a vessel containing culture medium diluted 1:10 (for the available 10× concentrated medium that means a dilution of 1:100) with milli-q water is used. The vessel is then bubbled with nitrogen and transferred through a capillary into the measurement vessel. Once the vessel is situated inside the sampling compartment of the Fluorolog 20 µL of the e. coli sample is introduced into the bottle through the capillary using a special needle.

Before the measurement can be started, the Fluorolog needs to be set up for automated data acquisition. The Fluorlog's acquisition mode needs to be set to "kinetic" and the monochromators should be set to 435 nm (excitation) and 580 (emission). Optimal slit width depends on film thickness of the sensor, an excitation slit width of 4 nm coupled with a 25 % neutral density filter placed in the beam path of the excitation light and a 10 nm emission slit should yield good results. This needs to be confirmed for a given sensor though, by using sodium sulfite solution to measure the maximum signal achievable with the current setup and settings. The settings should be tuned to achieve a signal under sulfite of about 2 million raw counts.

Once the ideal settings have been found the measurement routine should be saved and started once so it is set as the active configuration. The Flurolog supports batch collection of data, because of various shortcomings of the software it should not be used though. Instead a user input simulation software like ghost mouse should be used to trigger measurements. Before a

measurement, it has to be confirmed that the settings of the input simulator are correct. The software needs to simulate a click on the rerun measurement button (play icon) of the Fluorolog software and then after a few seconds on the close shutter button of the software (to acquire the decay curve). These two steps have to be repeated each time the sampling interval passes. The Flurolog software will then collect data until the file is too large to save at which point the software crashed, which is usually after around 10 hours. The data acquired up to this point can then be exported to individual files using an export script and the data can then be analyzed using custom software.

9.5 Preparing Pressure Test substrates

The pressure testing setup still exhibits some unexplained properties that render it unusable for extensive testing of sensor materials. Once these problems are solved, however, there is a large number of interesting matrices that should be investigated for their pressure dependence. Such matrices are for example matrices with high intrinsic free volume, particle based materials, but also common matrices or functionalized derivatives. For future reference this section contains a list of possibly interesting matrices along with instructions on how to prepare a sensor "cocktail" from these materials.

Polystyrene

Polystyrene is a standard material used for optical oxygen sensors and can act as a baseline for comparing the performance and pressure dependence of other materials. To prepare a polystyrene "cocktail" one should dissolve 1 % (w/w) in respect to the polymer of regular platinum(II)benzoporphyrin dye and 10 % (w/w) in respect to the solvent of the polymer in chloroform and dry at 60 °C after dip-coating.

Bromopolystyrene

Testing bromopolystyrene could give insights into how functionalization and therefore change in steric properties influences pressure dependence. Sensor preparation is the same as for regular polystyrene.

Polystyrene with entrapped diamond powder

Polystyrene with entrapped diamond powder is used in sensing applications because the scattering of emission light results in higher signal intensities. It would be interesting to investigate if the addition of particles affects the matrices pressure response. To prepare a sensing cocktail one has to add 2 % (w/w) in respect to the polymer of diamond power to a "cocktail" prepared in the same way as for regular polystyrene.

Teflon AF 1600

Teflon AF features a very high permeability, which is in part a result of its high internal free volume. Because this material and other comparable materials like Hyflon are going to be used for in-situ trace sensing, it is very important to determine the influence high pressures have on the sensors performance. Unfortunately regular benzoporphyrins are not soluble in highly perfluorinated matrices, therefore a special perfluoroalkylated variant has to be used. To prepare a "cocktail" for dip-coating 0.5 % (w/w) in respect to the polymer of the perfluoroalkylated dye and 5 % (w/w) in respect to the solvent of the polymer should be dissolved in octafluorotoluene. The coated fibre should then be dried at 60 °C.

Silicone E4 directly doped with dye

Silicone is often used as a support material for particle based sensors, it is usually a very elastic material and the effect of deformation under pressure on sensor performance is of great interest. Preparing sensor coatings is unfortunately not easy, the approach to just dissolve silicon E4 and dye in hexane yielded only questionable results. A more promising approach is to coat the

fibre tip directly with silicone, let it cure over night and then let the layer coated on the fibre swell in a solution of the dye for migration of the dye into the silicon layer.

Crosslinked polystyrene beads in Teflon AF

Of course particle based systems are also going to be of interest, polystyrene beads embedded in silicone are a common sensing scheme and determining how such particle based systems are affected and how they compare to regular polymer film based sensors is of interest. To prepare a sensor "cocktail" 50 % (w/w) in respect to the silicone of the dye infused particles are dispersed in a solution of 5 % (w/w) Teflon AF 1600 in cytop solvent.

Crosslinked polystyrene beads in Silicone E4

The same particles can also be dispersed in silicone E4, a comparison with the particles dispersed in Teflon AF will hopefully show if the surrounding material that normally intended only for mechanical stabilization of the film has any influence on the sensing properties of the material. To prepare the sensor 50 % (w/w) of particles are dispersed directly in silicone E4 without additional solvent and then coated directly onto the fibre and cured over night.

Polyphenylsilsesquioxane particles in Silicone E4

To compare how different particle environments affect a sensors pressure response polyphenylsilsequioxane (PPSQ) is an interesting additional material. To prepare sensor films PPSQ is dissolved in chloroform and and dried and sintered at 120°C for 3 hours. The material is then pulverized and put in a solution of 0.5 % benzoporphyrin dye in chloroform which is slowly evaporated under stirring until the material is dry and the dye is adsorbed on the surface of the particles. 50 % (w/w) of the particles are then dispersed directly in silicone E4 and coated onto the fibre for over night curing.

Silicagel particles in Silicone E4

Porous silica gel particles dispersed in a flexible support like silicone might me especially interesting as the viscous silicone might migrate into the pores of the particles and therefore change sensor properties irreversibly. In the same way as for PPSQ, silica gel particles are dispersed in a solution of 0.5 % benzoporphyrin dye in chloroform which is slowly evaporated under stirring until the material is dry and the dye is adsorbed on the surface of the particles. 50 % (w/w) of the particles are then also dispersed directly in silicone E4 and coated onto the fibre for over night curing.